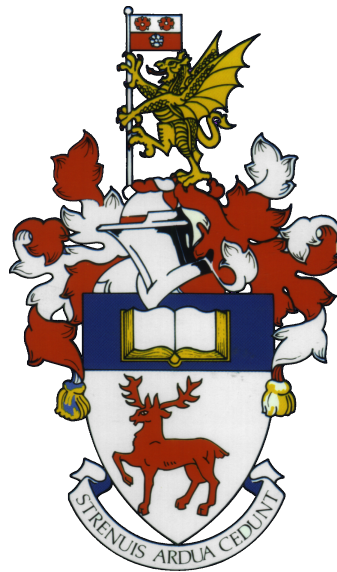# UNIVERSITY OF SOUTHAMPTON

FACULTY OF NATURAL AND ENVIRONMENTAL SCIENCES

School of Ocean and Earth Science

SEDIMENTARY PROCESSES IN SUBMARINE CANYONS

by

William O. Symons

Thesis for the degree of Doctor of Philosophy

October 2017

UNIVERSITY OF SOUTHAMPTON

<u>ABSTRACT</u>

FACULTY OF NATURAL AND ENVIRONMENTAL SCIENCES
School of Ocean and Earth Science

<u>Doctor of Philosophy</u>

SEDIMENTARY PROCESSES IN SUBMARINE CANYONS

by William O. Symons

Submarine canyons are one of the most dramatic morphological features on continental margins and enable sediment transport from the shelf to the deep sea; however, the exact processes operating within submarine canyons are poorly understood. Much of our understanding of the dynamics of sediment-laden flows in submarine canyons results from making inferences from the deposits that they leave behind in the geological record. This thesis aimed to better understand what deposits can reveal about flow processes and ultimately to test the validity of this approach for reconstructing flow dynamics. This aim was achieved by 1) analysing seafloor bedforms, 2) the detailed lithological and ichnological analysis of submarine canyon deposits, and 3) utilising turbidity current monitoring data. Construction and analysis of a global database of seafloor bedforms suggests that bedforms across all scales and a wide variety of settings can be generated by supercritical flows. The most complete dataset of monitored turbidity currents in a submarine canyon was combined with precisely located vibracores collected in Monterey Canyon. The combination of these datasets demonstrates that deposits can be used to accurately infer flow properties, and the data were further used to develop a new three-part model for turbidity current behaviour: 1) flows begin as thin, high-concentration highly energetic flows; 2) the flows become more dilute with an expanding head; and 3) the flow rapidly thickens along its length. This new model of turbidity current behaviour, along with understanding the frequency of these events, explains the distribution of benthic communities in Monterey Canyon based on the biogenic sedimentary structures identified within the sedimentary cores.

Contents

List of Figures

List of Tables

Declaration of Authorship

I, William O. Symons, declare that the thesis entitled *'Sedimentary processes in submarine canyons'* and the work presented in the thesis are both my own, and have been generated by me as the result of my own original research. I confirm that:

- this work was done wholly or mainly while in candidature for a research degree at this University;

- where any part of this thesis has previously been submitted for a degree or any other qualification at this University or any other institution, this has been clearly stated;

- where I have consulted the published work of others, this is always clearly attributed;

- where I have quoted from the work of others, the source is always given. With the exception of such quotations, this thesis is entirely my own work;

- I have acknowledged all main sources of help;

- where the thesis is based on work done by myself jointly with others, I have made clear exactly what was done by others and what I have contributed myself;

- parts of this work have been published as:

Symons, W.O., Sumner, E.J., Talling, P.J., Cartigny, M.J.B., and Clare, M.A., 2016. Large-scale sediment waves and scours on the modern seafloor and their implications for the prevalence of supercritical flows. Marine Geology 371, 130-148.

Symons, W.O., Sumner, E.J., Paull, C.K., Cartigny, M.J.B., Xu, J., Maier, K.L., Lorenson, T.D., Talling, P.J., 2017. A new model for turbidity current behavior based on integration of flow monitoring and precision coring in a submarine canyon. Geology 45, 367-370

Signed:..

Date:..

Acknowledgements

I would firstly like to thank my supervisors Esther Sumner, Matthieu Cartigny, Pete Talling and Mike Clare, for your continued support, encouragement and guidance throughout the last four years. Esther has been a fantastic supervisor, always being available to talk through problems and guide me through academic life, even when 5000 miles away in Monterey. I would like to thank all of the supervisors for going beyond the call of duty many times, including providing field work opportunities and reading what seemed like endless drafts of manuscripts; without that time and effort I would not be in the position I am today and this thesis would not be as strong. I would also like to thank Charlie Thompson who acted as panel chair and provided invaluable guidance for the preparation of this thesis, NERC for funding this studentship (NE/L501657/1) and GSNOCS for the opportunity to study here. Also, I would like to thank Ian Kane and John Marshall for examining my thesis and providing helpful comments in a great discussion to improve this work.

Special thanks go to Charlie Paull. Charlie's generosity provided the foundation for this project and without his support this would not have been possible. Additionally, I would like to thank Charlie and Mary for taking me in for six weeks, allowing me to use their home as my own and making my stay even more enjoyable. I would also like to thank all of the people at MBARI who made my visits out to California unforgettable. Thanks specifically go to Krystle Anderson, Roberto Gwiazda, Eve Lundsten, the crew of the *R/V* Western Flyer, and the pilots of ROV *Doc Ricketts* for helping with data collection, interpretation, and presentation. Katie Maier, Tom Lorenson, Angela Tan, Mary McGann, Danny Brothers (all USGS) and Jingping Xu (Ocean University of China) have all been instrumental in data collection and have significantly improved this thesis by providing more data and ideas.

Thanks also go to my office mates, past and present, for offering your time for discussions both work and non-work related. The sedimentology and geohazards team have provided great science discussions, both at NOC and over a drink (or few) and I would like to thank Age, Alessandro, Ed, James, Jamie, Jenny, Josh, Maria, Millie, Sophie and Zoe.

The last four years would not have been nearly as enjoyable if I didnt get to spend it with the friends I made at NOC. The list of people that I would like to thank is countless, but Chris, Rich, Sam G and Sam P have been great friends and have provided much needed breaks from the PhD. I would particularly like to thank Dave Reading for letting me know the 'secret' of getting through the PhD unscathed and still being around for a weekly (if we were organised enough) lunch catch-up. To 'Soton Life', thank you for your much-needed friendship outside of NOC.

I would like to acknowledge my family. Without their unwavering support and encouragement I would not be where I am today. Finally, but in need of the biggest thanks, is Hannah. Hannah has been there throughout this PhD, always available to

talk through problems. Without her constant encouragement I wouldn't be where I am today, both with the PhD and outside of work.

Chapter 1

Introduction

1.1 Project rationale

The purpose of this study is to better understand the deposits from submarine canyons and what insights that they, along with the direct monitoring of sediment transport events, provide about the sedimentological processes that occur within submarine canyons.

Previous work into submarine canyon morphology and dynamics has identified them as one of the most important pathways for the transport of sediment and associated pollutants and organic matter to deep-sea fans (e.g. Shepard and Dill, 1966; Berner, 1982; van Weering et al., 2002; Paull et al., 2005; Canals et al., 2006; Arzola et al., 2008; Normark et al., 2009; Puig et al., 2014). Submarine gravity flows are proposed as the main mechanism that transports this sediment through submarine canyons (Twichell and Roberts, 1982). Unlike our knowledge of comparable environments in the terrestrial realm (e.g. rivers), the exact processes that transfer sediment through submarine canyons are not well understood (Paull et al., 2010a). The destructive nature of flows, difficult to access nature of submarine canyons and limitations of instrumentation makes monitoring difficult. As such, much of our understanding of submarine canyon processes comes from the analysis of the deposits that these flows leave behind in the geological record. Seafloor bedforms are a key feature for inferring flow processes as their morphological expression and internal character are directly related to the flow that creates and

maintains them. The discovery of seafloor bedforms, and specifically bedforms in the axis of submarine canyons, is becoming more prevalent as seafloor-mapping capabilities improve. The formation of these enigmatic bedforms is often debated and highlights that there is a lack of understanding of these deposits. Despite the reliance on deposits to infer flow processes, the validity of using seafloor deposits to infer flow dynamics remains to be tested against direct flow observations.

Developing our knowledge of turbidity currents (a type of sediment density flow) is important, as these flows dominate sediment transport into many parts of the deep-sea and have the potential to form some of the largest sediment accumulations on Earth (submarine fans) (Talling, 2014). Additionally, these flows are a potential hazard to seafloor infrastructure, including seafloor cables that transfer more than 95% of transoceanic data (Piper et al. 1999; Hsu et al. 2008; Carter et al., 2009; Cattaneo et al. 2012), and costly infrastructure used for recovering oil and gas (Barley, 1999). The highly variable seascapes and subsequent interplay between canyon morphology and oceanic processes also means that submarine canyons have vital ecological roles, with enhanced biodiversity and ecosystem functions, often across small spatial scales (Fernandez-Arcaya et al., 2017). It is clear that developing our understanding of physical processes within submarine canyons, and how sediment is transported through them, is essential for numerous applications.

Despite recent advances in our ability to monitor turbidity currents and the estimates of turbidity current concentrations, there are as yet no direct measurements of their concentration profiles (Xu, 2011). Powerful and destructive turbidity currents are inferred to possess a basal layer that has high sediment concentrations (Hughes Clarke, 2016), with laboratory observations, seafloor deposits, and movement and destruction of monitoring instruments providing evidence for these dense basal layers (Posta et al., 1988; Garcia, 1994; Hughes Clarke et al., 2016; Symons et al., 2017). Dense basal layers are important to understand because they pose a significant risk to seafloor infrastructure but also are fundamental in understanding turbidity current dynamics. Understanding the concentration and velocity profiles of these basal layers has not been possible with current monitoring efforts, and numerical models struggle to realistically model high-concentration parts of flows. The use of seafloor deposits and information gained from

field deployments therefore provides the most direct information (e.g. run-out distance of a coarse-grained high-concentration layer) about the potential destructive processes occurring at the base of turbidity currents.

1.1.1 Overarching thesis aim

The overarching aim of this thesis is to better understand submarine canyon deposits and ultimately what insights these deposits provide about the processes that transport sediment through submarine canyons. This study has benefited from access to the most comprehensive dataset of systematically and precisely collected core samples from a submarine canyon ever collected and this is combined with rare direct monitoring data from the same location. These datasets allow direct comparison of flow dynamics from monitored turbidity currents with resultant deposits in order to test the validity of using seafloor deposits to reconstruct flow characteristics.

To achieve the aim of better understanding flow processes, the thesis aims to address the following questions:

1. What do the morphological characteristics of seafloor bedforms reveal about the turbidity currents that created them?

2. How accurately do deposits represent the spatial and temporal evolution of turbidity currents?

3. What are the primary controls on the distribution of lithofacies and bioturbation within a submarine canyon?

1.1.2 Thesis structure

This thesis is presented as three key science chapters, each produced as a standalone scientific paper. As a result of each chapter being produced independently of the others, there will be overlapping content, primarily with the introduction of study sites and background. Chapters 2 and 3 are published and chapter 4 has been submitted. This section aims to highlight how each chapter serves in developing our understanding

of sediment transport processes in submarine canyons, the rationale behind each chapter, and how the chapters are linked.

In chapter 2 a comprehensive database, constructed from literature concerning bedforms on the modern seafloor is presented. The recognition of large-scale bedforms on the modern seafloor has increased over recent years as advanced seafloor mapping techniques have developed. Bedforms can reveal important information about flow processes because bedforms reflect the interaction between seafloor sediment and over-riding flows. The identification of bedforms specific to the axial channel of submarine channels and canyons, and the debate into the formation of these features highlights a gap in our knowledge of bedform generation and flow processes. By assessing seafloor bedforms globally, a more complete understanding of flow processes and bedform generation can be taken forward to better elucidate submarine canyon processes and specifically the dynamics of turbidity currents within submarine canyons. By grouping bedforms based on morphological and environmental characteristics, this chapter aims to understand whether groups of bedforms with similar wavelengths, wave heights, and locations are indicative of different formative processes.

In Chapter 3 a novel dataset of precisely located core transects from Monterey Canyon specifically collected for this project is presented. Coupled with these cores are some of the most detailed direct measurements from turbidity currents, which were collected by the US Geological Survey (USGS) in 2002 and published in Xu et al. (2014); the USGS dataset was analysed in further detail for this study. This chapter aims to evaluate how well deposits record the spatial and temporal evolution of turbidity currents within a submarine canyon by combining deposits with flow measurements. The combination of the two datasets also enables development of a new model for turbidity current behaviour. This chapter also considers the limitations of current monitoring data and hazards to the monitoring equipment.

In chapter 4, the aim is to assess the response of deep-sea fauna to the sedimentary processes operating within submarine canyons. The knowledge of turbidity current processes gained from chapter 3 is used in this assessment. Studying biogenic structures and the degree of bioturbation within sediments is an important tool for sedimentologists

as it can reveal environmental information beyond that gained from sedimentary structures and lithofacies alone. Despite a proposed link between ichnology and sedimentary facies, the conclusion that trace fossils vary according to the exact location within a submarine canyon or channel (e.g. thalweg, terrace, over-bank) remains untested in a modern, active system. This chapter therefore aims to visually and statistically analyse seafloor deposits to test the response of organisms and sedimentary deposits to active processes within a modern submarine canyon (outlined in chapter 3), ultimately assessing how seafloor deposits beyond just sedimentary facies reflect sediment transport processes in submarine canyons.

Chapter 5 serves to conclude the thesis, revisiting the research questions outlined in section 1.1.1, and present proposals for future work.

1.2 Submarine canyons: An introduction

Submarine canyons are among the most common and dramatic geomorphic features on both active (endogenetic) and passive (exogenetic) continental margins (Shepard, 1981; Twichell and Roberts, 1982). They are steep-walled incisions with V-shaped cross-sections that may develop down-slope to exhibit a shallower U-shaped channel (Daly, 1936; Lastras et al., 2009). Active margins contain more submarine canyons than passive margins, with canyons closer spaced and steeper on active margins, whereas the sediment thickness associated with passive margins is greater than those on active margins (Harris and Whiteway, 2011). In plan-view, submarine canyons typically follow a sinuous path and often display tributary canyon systems (Lastras et al., 2009; Huang et al., 2014), with average values of sinuosity not seen to differ between active and passive margin canyons (Harris and Whiteway, 2011). The shapes of canyons typically reflect the processes that transport sediment through them, deposit sediment within them, and erode into the underlying bedrock of the canyon (Paull et al., 2011). The accumulation of vast amounts of material downstream from canyons in deep-sea fans (Paull et al., 2013) highlights that submarine canyons are preferential conduits for sediment transport from the shelf to the deep sea (Puig et al., 2003). The ecological significance of submarine canyons should also be noted, as their complex morphology interacts with
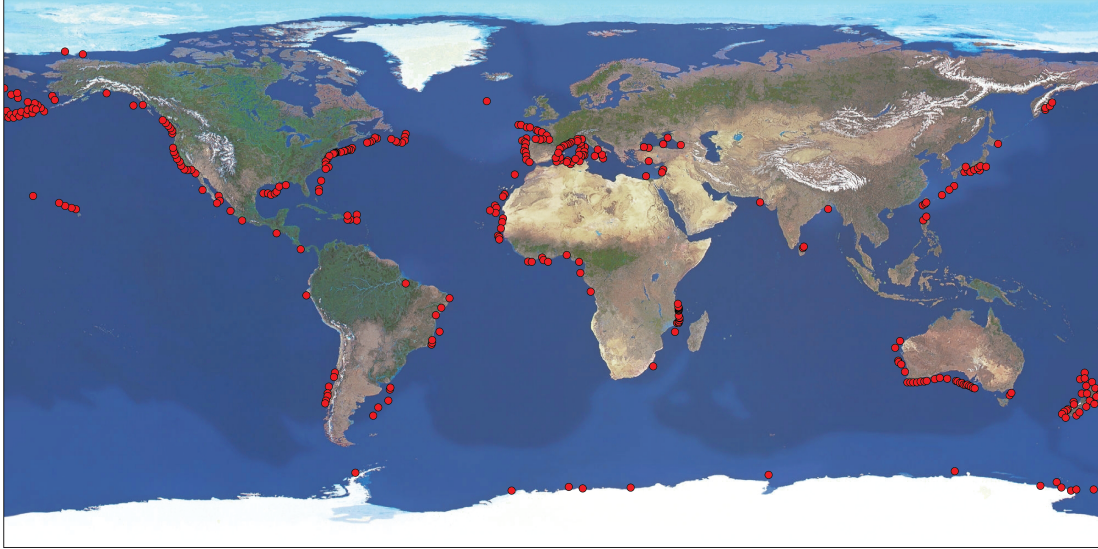
Figure 1.1: Global distribution of 660 submarine canyons (modified from De Leo et al., 2010).

ocean currents, tides and internal waves that lead to enhanced primary productivity and benthic biodiversity (Vetter and Dayton, 1998; De Leo et al., 2010; Huvenne and Davies, 2013; Huang et al., 2014). Although there has been significant advancement in knowledge of modern submarine canyon systems (e.g. Paull et al., 2003, 2005, 2010a, 2013; Mullenbach et al., 2004; Puig, 2004; Smith et al., 2005, 2007; Xu et al., 2004; Canals et al., 2006; Arzola et al., 2008; Xu, 2010, 2011; Babonneau et al., 2013; Puig et al., 2014; Sumner and Paull, 2014; Tubau et al., 2015; Symons et al., 2017), our understanding of the exact processes that transport sediment within canyons is limited and the subject of on-going investigation (Puig et al., 2014). The main limiting factor in our understanding is the limitations of the technology available (Paull et al., 2005) to sample, monitor and image such complex, hazardous and inaccessible environments (e.g. Inman et al., 1976; Prior et al., 1987; Khripounoff et al., 2003; Paull et al., 2003; Xu, 2011).

1.3   Sediment transport processes in submarine canyons

Many studies have shown that submarine canyons have greater suspended-sediment concentrations (e.g. Drake and Gorsline, 1973; Carson et al., 1986; Gardner, 1989; Durrieu de Madron, 1994), downward particle fluxes (e.g. Hung and Chung, 1998;

Puig and Palanques, 1998), and sediment accumulation rates (e.g. Carson et al., 1986; Sanchez-Cabeza et al., 1999; Arzola, 2008; Huh et al., 2009) than the surrounding open-slope regions (Puig et al., 2003), yet mechanisms involved in transporting sediment into and through submarine canyons are not fully understood (Puig et al., 2014). Since the 1950's there have been advances in understanding of sedimentary processes in deep-sea canyon and channel systems as a result of both field studies and modelling of the causes and processes of sediment flows in these environments (e.g. Heezen and Ewing, 1952; Bagnold, 1962; Menard, 1964; Shepard and Buffington, 1968; Komar, 1969; Shepard et al., 1969). Perhaps the most significant advance in our understanding of submarine sediment transport processes came from the development of oceanographic instrumentation in the late 1960's that could remain deployed for extended periods (Normak and Piper, 1991; Puig et al., 2014). Progress in the study of submarine canyon processes has also advanced with the ability to collect detailed bathymetric data to document seafloor morphology (Paull et al., 2011). For example, the identification of crescent shaped bedforms within the axial channel of Monterey Canyon from high-resolution bathymetric surveys (Paull et al., 2010a) has questioned our knowledge of submarine canyon processes, as different authors ascribe different formative processes to these features (Symons et al., 2016). Using knowledge gained from oceanographic monitoring and seafloor mapping, the following sections are dedicated to outlining the sediment transport mechanisms that have been proposed within submarine canyons.

1.3.1   Oceanographic Processes that transport sediment

Submarine canyons affect the movement of water masses laterally along continental margins and vertically within submarine canyons. It has long been established that the interaction of the open ocean with the topography of continental margins results in current oscillations of variable magnitude that have the ability to mobilise sediment (Petruncio et al., 1998).

1.3.1.1   Internal waves

Monitoring of tidal oscillations in submarine canyons highlight that they are a focus of enhanced internal-wave activity (e.g. Shepard 1975; Cacchione and Drake, 1986; Gardner, 1989; Petruncio et al., 1998; Kunze et al., 2002; Xu et al., 2002; Puig et al., 2004). Internal waves are oscillations along density boundaries within the water column and submarine canyons act as effective pathways for funnelling open-ocean internal wave energy to shallower waters (Gordon and Marshall, 1976). This focus within submarine canyons is likely a result of their slopes matching the angle at which the internal waves travel, therefore strengthening the internal wave (Zhang et al., 2008). Increased bottom shear stresses as a result of these intensified internal waves have the ability to re-suspend and subsequently transport sediment (Puig et al., 2004). A number of studies have demonstrated the role of internal waves in re-suspending and distributing sediment, e.g. Monterey Canyon (Petruncio et al., 1998; Kunze et al., 2002; Xu et al., 2002), Baltimore Canyon (Gardner et al., 1989), Guadiaro Canyon (Puig et al., 2004) and Nazaré Canyon (de Stitger et al., 2007).

1.3.1.2   Dense shelf-water cascading

Dense shelf-water cascading (DSWC) can transport sand and create high sediment fluxes within submarine canyons (e.g. Canals et al., 2006; Puig et al., 2008, 2014; palanques et al., 2009; Talling et al., 2014). This meteorologically-driven oceanographic process results from cooling and/or evaporation of shelf water. The dense water spills over the shelf edge and cascades downslope as a gravity-driven current until it reaches an equilibrium depth (Canals et al., 2006; Puig et al., 2014). These cascading events can be intensified by cold, dry winds, which cool and homogenise the shelf water column, facilitating dense water formation (Palanques et al., 2006). These low sediment concentration flows can be prolonged, lasting for days to several weeks, and reaching speeds of up to 85 cm/s (Canals et al., 2006; Talling et al., 2014).

1.3.2 Sedimentological processes that transport sediment

Sediment transport processes that occur in submarine canyons but are not directly a result of the oceanographic process outlined above are typically a result of sediment instability and failure. Whilst the presence of sediment within the head of a canyon may be linked to oceanographic processes, e.g. the canyon head intersecting the littoral transport of sediment (e.g. Paull et al., 2005), other preconditioning factors that reduce sediment stability lead to the failure and subsequent transport of sediment. Here, the sedimentological processes that are thought to transport sediment through submarine canyons and the origin of these processes are examined.

1.3.2.1 Debris flows

Debris flows are a common gravity flow in submarine canyons (e.g. Shepard, 1981; Mulder et al., 1997; Pickering et al., 2001; Arzola et al., 2008; Paull et al., 2010a; Brothers et al., 2013). Debris flows are typically cohesive flows with non-Newtonian (Bingham) rheologies (i.e. some initial yield strength must be overcome before movement occurs) (Mulder and Alexander, 2001). The main particle support mechanisms are reduced excess particle density, the yield strength of the sediment-water mixture and grain-to-grain collisions, (Iverson, 1997; Mulder et al., 1997, Talling et al., 2007). Whilst debris flows can exhibit weak turbulence, they are typically laminar (Iverson, 1997; Talling et al., 2007). Deposition from debris flows is commonly rapid, if not en masse as the entire sediment body freezes, resulting in ungraded, poorly sorted and structureless deposits (debrites) (Lowe, 1982; Mulder and Alexander, 2001).

1.3.2.2 Turbidity currents

The current paradigm is that turbidity currents are the dominant mechanism for transporting sediment through submarine canyons (e.g. Twichell and Roberts, 1982; Shanmugam, 2000; Paull et al., 2011), and as such will be described in more detail than debris flows (previous section). Turbidity currents have been classed as the dilute end member of gravity flows in which fluid turbulence is likely the main particle support

mechanism, although hindered settling and grain interaction may also contribute (Middleton and Hampton, 1973; Kneller and Buckee, 2000; Mulder and Alexander, 2001; Meiburg and Kneller, 2010). Turbidity currents have a Newtonian rheology, whereby
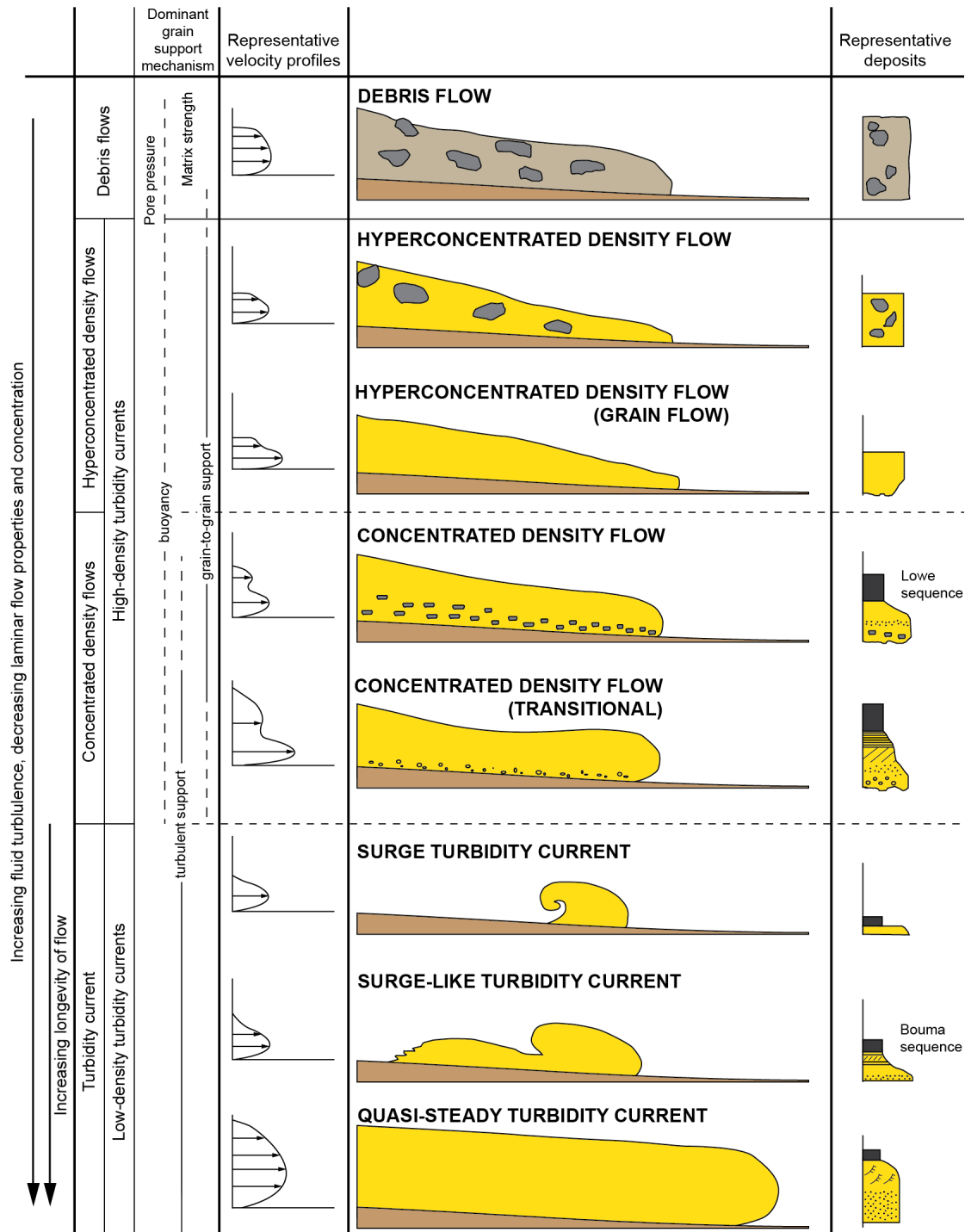
Figure 1.2: Schematic representation of subaqueous gravity flows, including dominant grain-support mechanisms, idealised velocity profiles, idealised flow shape amd schematic sedimentary logs (modified from Mulder and Alexander, 2001).

they begin to deform and flow upon the initial application of shear stress and their driving force is the density difference between the cloud of suspended sediment and the ambient water (Lowe and Guy, 2000; Meiburg and Kneller, 2010). Sediment concentrations within turbidity currents are estimated to range from 0.1% to 7% (Meiburg and Kneller, 2010), but can reach 9%, beyond which fluid turbulence can no longer be maintained and laminar flow processes become more dominant (Bagnold, 1962). Turbidity currents can be classified into high- and low-density turbidity currents (e.g. Kuenen and Migliorini, 1950; Lowe, 1982; Kneller and Branney, 1995; Stow et al., 1996; Cartigny et al., 2013), where sediment concentration and the degree at which grain settling is hindered near the bed (Talling et al., 2012) determine the classification. Some authors find the 'high-density turbidity current' classification contentious due to the lack of fluid turbulence and instead propose an intermediate classification of 'concentrated' and 'hyperconcentrated' density flows between turbidity currents and debris flows (Mulder and Alexander, 2001) (figure 1.2). The classification of Mulder and Alexander (2001) also describes three different types of turbulent flow: (1) surge, (2) surge-like, and (3) quasi-steady, where flow duration is a primary discriminator (figure 1.2). Shorter surge and surge-like flows are thought to initiate from an initial pulse of sediment whilst longer, quasi-steady flows result from a more continuous input of sediment. Many of the classifications for submarine density flows, and specifically turbidity currents, are based on experiments (laboratory and numerical) and outcrop. The difficulty with using these approaches is that key parameters that are needed to classify full-scale turbidity currents (e.g. flow speed, concentration, density) are unknown. The limited amount of monitoring work of turbidity currents highlights complexities that may not be resolved by previous classification methods. Studies from Monterey Canyon highlight that turbidity currents are able to move heavy ($\sim$45 kg) concrete monuments in the axis of Monterey Canyon along with mobilising the seafloor (Paull et al., 2010a), indicating that the dilute models for turbidity currents may not be appropriate for full-scale, natural events.

The deposits from turbidity currents (turbidites), unlike debrites, show evidence of progressive aggradation, ultimately recording the temporal evolution of the turbidity current at a given location (Amy and Talling, 2006). The structures of turbidites indicate whether turbulence was damped near the bed, whether sediment settling was hindered,

and the rates of bed aggradation (Talling et al., 2012). These deposits therefore indicate whether near-bed flow was relatively dense or dilute. The vertical deposit structure will also represent changing conditions of the parent flow experienced at that location through time (see Bouma (1962), Lowe (1982), Stow and Shanmugam (1980) for idealised structures of classic (medium-grained), coarse-grained, and fine-grained turbidites). On slopes, and within submarine canyons, turbidites typically taper in thickness and reduce in grain size with distance from their source (e.g. Talling et al., 2004; Symons et al., 2017).

1.3.2.3   Triggering of submarine flows

Turbidity currents, can be triggered in a number of ways, with Normark and Piper (1991) proposing three main triggers: hyperpycnal flows, slope failures, and storm-generated flows (Normark and Piper, 1991; Piper and Normark, 2009). Additional to these three triggers, and more specific to submarine canyons, are anthropogenic causes such as bottom trawling.

Hyperpycnal flows are specific to river-fed canyon systems. During significant periods of flooding, river discharge has the ability to carry large volumes of sediment directly into the canyon head. The excess density of the sediment-laden water results in the river discharge forming a dense underflow (providing concentration is greater than $\sim 1.3\%$ by volume; Mulder and Syvitski, 1995; Mulder and Syvitski, 2003; Talling, 2014), which plunges below the less-dense ambient seawater (Normark and Piper, 1991; Mulder et al., 2001; Mulder and Syvitski, 2003). Turbidity currents formed in this way have been observed in a number of locations, including the Var Canyon (Mulder et al., 2001; Khripounoff et al., 2009, 2012), and Gaoping Canyon (Carter et al., 2012; Liu et al., 2012). Hyperpycnal flows have not been recorded to extend beyond the continental slope (Talling, 2014).

Earthquakes have been suggested to generate turbidity currents in submarine canyons (e.g. Gaoping Canyon; Hsu et al., 2008; Monterey Canyon; Garfield et al., 1994). Ground movement caused by earthquakes can result in widespread slumping of unlithified sediment in the heads of canyons and en masse sediment movement (Normark and

Piper, 2009). Turbidity currents are generated in this manner from the transformation of an originally coherent slide/slump mass into an incoherent granular mass, evolving to a more dilute phase through entrainment of water (Piper and Normark, 2009). Large earthquakes have been suggested to cause both large-scale canyon-flushing events that periodically flush sediment from canyons to the deep ocean (Arzola et al., 2008; Talling, 2014); and also canyon-filling events as a result of a small volume of failed material that does not reach submarine fans (e.g. Goldfinger et al., 2003).

Large waves during storms may cause cyclic-loading that re-suspends sediment in the head of canyons and destabilise slopes (e.g. Inman, 1976; Okey, 1997; Xu et al., 2002, 2004; 2010; 2014; Paull et al., 2003; Puig et al., 2004; de Stigter et al., 2007; Puig et al., 2014, and references therein). The downslope ignition of this suspended material occurs as potential energy is converted to kinetic energy as the flow moves downslope (Parker 1982; Piper and Normark, 2009), generating a turbidity current. Based on current knowledge, these turbidity currents do not appear to reach slope fans or distal basin settings (Paull et al., 2005; de Stigter et al., 2007; Xu, 2011), and in the case of Monterey Canyon, it is rare for turbidity currents generated by large wave activity to extend beyond 2000 m water depth (Xu, 2011).

Turbidity currents can also be generated through anthropogenic activity, such as bottom trawling (e.g. Palanques et al., 2005; Puig et al., 2012). Trawling on the margins of submarine canyons suspends sediment that generates dilute, slow moving turbidity currents that overspill the canyon flanks and into the main canyon axis, depositing and infilling the submarine canyon (Puig et al., 2012).

1.4 Deposit analysis from submarine canyons

The lack of direct measurements of turbidity currents in submarine canyons has meant that historically, the analysis of seafloor deposits and outcrop has provided the greatest insight into these flows (Komar, 1985; Migeon et al., 2012; Postma and Cartigny, 2014), as the nature, thickness and location of the deposits are controlled by flow dynamics (Postma and Cartigny, 2014). The analysis of submarine canyon or channel deposits from outcrop is difficult however as only a few good examples have been

documented (e.g., Wheeler Gorge, California (Walker, 1975); Point Lobos, California (Clifton and Hill, 1987); Rasario Formation, Mexico (Morris and Busby-Spera, 1990); Stilo-Capo d'Orlando Formation, southern Italy (Cavazza and DeCelles, 1993); Pigeon Point, California (López-Gamundí, 1993); Cingöz Formation, southern Turkey (Satur et al., 2005); Black's Beach, California (May and Warme, 2007); San Fernando Canyon (Dykstra and Kneller, 2009); Wonoka Canyons (Giddings et al., 2010); Offida Canyon, central Italy (Di Celma, 2011); Karoo Basin, South Africa (Hodgson et al., 2011); Serra Mulara Formation, Italy (Zecchin et al., 2011)), as the scale of most canyons means their geometry and internal architecture are often lost in exposure (May and Warme, 2007). Also, good examples of submarine canyon outcrops are rare because their preservation potential is low (May and Warme, 2007); as canyon fill is uplifted, it is typically deformed and eroded and therefore does not retain the original depositional signature. As such, modern seafloor deposits often provide the greatest insights into canyon formation, maintenance, and sedimentological processes. Previous attempts have therefore been made to understand the behaviour of flows using channel morphology, seafloor bedforms and deposit characteristics e.g. grading patterns and lithofacies (e.g. Kneller and McCaffrey, 2003; Primez and Imran, 2003; Migeon et al., 2012; Postma and Cartigny, 2014).

1.4.1   Seafloor bedforms

The identification of seafloor bedforms (repeated undulations on the seafloor that can be positive or negative relief) can reveal important information about the dynamic processes that occur in submarine canyons, as bedforms reflect the interaction between seafloor sediment and over-riding flows (e.g. Wynn et al., 2002; Smith et al., 2005, 2007; Arzola et al., 2008; Paull et al., 2010a; 2011; Girardclos et al., 2012; Hill, 2012; Hughes-Clarke et al., 2012; Babonneau et al., 2013; Cartigny et al., 2014; Covault et al., 2014; Symons et al., 2016). The morphology (e.g. cross-sectional symmetry, wave-length and -height), grain size, location, migration direction and internal structure of such bedforms provide evidence for how they were formed and thus, the dynamics and evolution of the flows that formed them (e.g. Wynn and Stow, 2002; Cartigny et

al., 2011; Postma and Cartigny, 2014; Symons et al., 2016). The advent of advanced seafloor mapping techniques (Wynn et al., 2014) has revealed crescent-shaped bedforms unique to the axes of confined systems (e.g. Paull et al., 2008, 2010a; Babonneau et al., 2013; Covault et al., 2014). The formation of these coarse-grained bedforms that exhibit a crescent-shaped crest in plan view, and migrate upslope, has received a lot of discussion in the literature (Paull et al., 2010a; Kostic, 2011; Cartigny et al., 2011; Talling et al., 2013; Normandeau et al., 2015; Symons et al., 2016). Multiple formative processes have been proposed for these bedforms, e.g. internal tides (Xu et al., 2008), liquefaction and slumping of the axial channel fill (Paull et al., 2010a), and supercritical flows and cyclic steps (Taki and Parker, 2005). The lack of consensus as to how crescent shaped bedforms form demonstrates that there are gaps in our knowledge of canyon processes.

1.4.2 Lithofacies and grain sizes

The deposits within submarine canyons and channels reflect the processes that transport and deposit sediment within these systems (Hubbard et al., 2014; Symons et al., 2017; and section 1.3.2.2). A number of studies have used outcrops to reconstruct turbidity currents and constrain channel evolution (e.g. Kane et al., 2007; Dykstra and Kneller, 2009; Hubbard et al., 2014). However, comparatively few studies have used modern sediment cores to reconstruct detailed turbidity current behaviour in submarine canyons or channels (e.g. Pirmez and Imran, 2003; Migeon et al., 2012; Jobe et al., 2017). Below, three systems are briefly outlined that have used modern seafloor deposits to determine turbidity current dynamics and evolution through confined systems.

1.4.2.1 The Var Turbidite System

Migeon et al. (2012) reconstructed the vertical sediment distribution and velocity structure of turbidity currents flowing through the Var channel using bathymetric data, high-resolution seismic-reflection profiles, and sediment cores. The roughness and morphology of the seafloor within the channel allowed Migeon et al. (2012) to predict

flow dynamics, such as when the flow would be erosional or depositional. The distribution of grain sizes within the cores allowed Migeon et al. (2012) to estimate which grain sizes were supported at different elevations within the flow, they found: coarse sands at less than 50 m above the seafloor, medium to fine sands between 50 m and 200 m, and silt and mud were carried 300 m above the seabed. The vertical distribution of grain sizes also allowed a theoretical velocity profile to be deduced, which was in agreement with numerically modelled and theoretical velocity profiles (Migeon et al., 2012).

1.4.2.2   The Amazon Channel

The Amazon channel has been a key site to better understand the evolution of large turbidite systems. Normark and Damuth (1997; ODP 155) were able to identify 15 major sedimentary facies within 17 cores collected from the Amazon Channel and Fan. The distribution of these facies showed that the sand and clasts carried through the Amazon system by turbidity currents remain confined within the channel, even when the levee-crest to channel-floor relief is as little as 35 m, until reaching the active depositional lobe at the channel mouth. Additionally, Normark and Damuth (1997) were able to evaluate the amount of sediment that was deposited over-bank on levees compared to bypassing down-system by considering the channel relief. The cross-sectional area of the 650 km long Amazon Channel decreases from 0.8 km^2 to 0.05 km^2 down system, meaning that at the minimum area the upper 80% of the flow thickness will be stripped off and deposited overbank (Normark and Damuth, 1997).

Developing on the work of Normark and Damuth (1997), Pirmez and Imran (2003) identified that numerical models for reconstructing turbidity currents within the Amazon Channel required a number of assumptions, such as estimating flow density, water entrainment and acceleration. Other parameters such as flow velocity were a function of these estimated parameters and therefore created additional uncertainty (Pirmez and Imran, 2003). To better constrain the models, they were combined with ground-truth information from channel morphology and a suite of sediment cores. Sediment cores from channel axis, overbank and base-of-levee were analysed and grain-size patterns

were used to estimate cross-channel flow stratification (Pirmez and Imran, 2003). Turbidity currents that pass through the Amazon Channel are a mix of sand and mud (sand:mud ratio of 5-10%), yet only mud is found on the levees and overbank deposits, despite the thickness of the flow exceeding the relief of the channel. The lack of sand in the overbank therefore suggests the vertical stratification of grain sizes within the flow, with sand confined to the lower 20-30 m of the flow (Pirmez and Imran, 2003).

1.4.2.3 The western Niger Delta slope

By using high-resolution bathymetry, seismic reflection, and piston core data from a submarine channel on the western Niger Delta slope, Jobe et al. (2017) were able to ground truth an in-channel sedimentation model (simple formulation for turbidity currents flowing in a confined channel under steady and quasi-uniform flow conditions) that solved vertical concentration and velocity profiles of turbidity currents. They demonstrated from their core dataset that coarse-grained sands in the channel thalweg transition to thin, fine-grained, bedded sands and muds at the channel margin. The data also show that bed thickness and grain size decreases with distance from the thalweg (thickness decreases 5 times with 20 m elevation above the thalweg). With key inputs such as channel cross-section, flow depth, flow duration and grain size distribution defined, the trends from the channel dataset were reproduced in their model, therefore predicting velocity and suspended sediment concentration for turbidity currents on the Niger Delta slope. In addition the model was also able to predict where the flows were likely to be depositional and where they were erosional (Jobe et al., 2017).

1.4.3 Ichnology of deep-sea deposits

Seafloor deposits can reveal more about a turbidite system than lithological data alone. Perhaps one of the most under-utilised data types in sedimentological studies of modern and ancient turbidite systems is ichnology (Callow et al., 2014). The study of biogenic structures formed by the activity of an organism (Bromley, 1996) have been used in modern and ancient systems to reveal intricate details about (palaeo) environmental conditions, to identify significant stratigraphic surfaces, and to determine

proximity to source within turbidite systems (e.g. Kane et al., 2007; Heard and Pick-
ering, 2008; Wetzel, 2008; Cummings and Hodgson, 2011; Uchman and Wetzel, 2011;
Callow et al., 2013; Heard et al., 2014; Callow et al., 2014; Knaust et al., 2014). Many
deep-water ichnological studies are based on the ichnofacies paradigm of Seilacher (1964,
1967), whereby different organisms will produce similar burrows, and therefore trace-
fossil assemblages, that reflect specific environmental and/or taphonomic conditions,
and developed further by many subsequent studies (e.g. Frey and Seilacher, 1980; Frey
et al., 1984; Bromley et al., 1984; Uchman, 2001; McIlroy, 2004). Ichnofacies identified
for deep-water environments include *Zoophycos* (continental slope) and *Nereites* (basin
floor) (figure 1.3) (Callow et al., 2014). Workers have found that ichnofacies have broad
environmental ranges (e.g. water depth), therefore ichnosubfacies were developed to in-
crease the spatial resolution beyond that achievable using ichnofacies (e.g. Hubbard et
al., 2012). Ichnosubfacies examples include *Ophiomorpha rudis* (sand-rich channels and
channel-proximal lobes) and *Paleodictyon* (thin-bedded sand-rich turbidite lobe fringes)
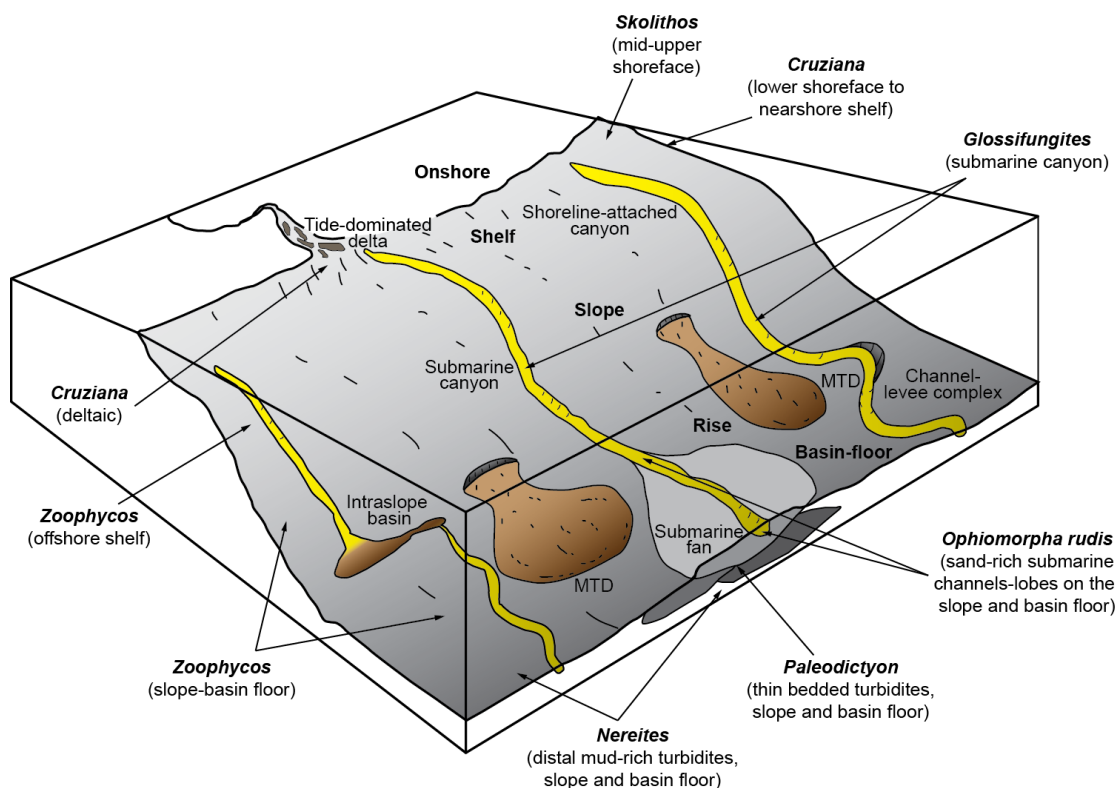
Figure 1.3: Diagram showing depositional environments from marginal marine
to the abyssal plains to highlight the distribution of marine ichno(sub)facies.
MTD = mass transport deposit (modified from Callow et al., 2014).

(Callow et al., 2014). In addition, workers have developed the ichnofabric approach to trace fossil analysis (Taylor and Goldring, 1993; Taylor et al., 2003; McIlroy, 2004). This approach lends itself to a fully integrated sedimentary fabric and ichnological analysis that incorporates lithology, bioturbation intensity, burrow size, ichnodiversity, abundance, cross-cutting relationships and depth of burrowing to classify deposits (Bromley and Ekdale, 1986; Taylor and Goldring, 1993; Taylor et al., 2003; McIlroy, 2004, 2008; Callow et al., 2014).

1.5 Direct observations and monitoring of sediment transport processes in submarine canyons

Despite difficulties in directly monitoring submarine flows (e.g. challenges and cost in deploying instrumentation, infrequency of events, hazardous nature of the events), a number of monitoring efforts in recent years have made major advances and provided valuable insights into the processes that transport sediment in channelised settings (e.g. Paull et al., 2003, 2005; Khripounoff et al., 2003; Xu et al., 2004, 2013, 2014; Vangriesheim et al., 2009; Xu, 2010, 2011; Cooper et al., 2012; Hughes-Clarke et al., 2016).

Unlike the days- or month-long data series that could be collected during initial monitoring of submarine canyons (Shepard et al., 1979), modern instrumentation can be deployed for long periods of time (e.g. Palanques et al., 2005; Xu, 2010; Khripounoff et al., 2012). Additionally, modern technological advances means that multiple moorings can be deployed simultaneously with a whole suite of instruments. Despite these advances, temporal resolution of the data are limited due to the instruments being battery powered and needing slower sampling frequencies during longer deployments (Xu et al., 2014; Sumner and Paull, 2014). Perhaps the most significant development in flow measuring technologies is the acoustic Doppler current profiler (ADCP). The onset and widespread use of ADCPs, mounted on ships, seafloor platforms and moorings, has allowed researchers to attempt to constrain arguably the two most important parameters of turbidity currents: the vertical profiles of (1) velocity, and (2) sediment concentration (e.g. Xu et al., 2004, 2014; Xu, 2010, 2011; Cooper et al., 2012; Hughes-Clarke et al., 2016). The recent monitoring efforts of Xu et al. (2010, 2013, 2013), Hughes-Clarke et

al. (2012, 2016), Cooper et al. (2012), Khripounoff et al. (2003, 2012), Vangriesheim et al. (2009) and Ayranci et al. (2012) have estimated sediment concentrations for turbidity currents from ADCP backscatter values (Talling et al., 2015). However, significant uncertainties still remain when estimating concentration because the grain-size distribution within the flow is typically unknown. Nevertheless, these concentration estimations, along with ADCP velocity profiles, sediment trap samples and water-column measurements provide a significant step forward in understanding the timing, triggering and internal structure of turbidity currents. The most complete visual observation of a natural turbidity current was acquired during a remotely operated vehicle (ROV) dive in Mendocino Canyon, Northern California (Sumner and Paull, 2014). During this dive the ROV was caught within a dilute turbidity current. Through multiple ascents and descents through the water column, unique insights about the thickness, density structure, concentration (from transmissometer measurements and grain size calibrations), velocity, and duration of the turbidity current were gained.

1.6   Monterey Canyon: A natural laboratory

Monterey Canyon is the study area for chapters 3 and 4 and whilst a brief introduction to the system is provided within each chapter, a general overview is provided here. This section serves to introduce the geological setting, morphological expression and overall controls on the shape of Monterey Canyon.

Monterey Bay is home to the extensive Ascension-Monterey canyon system that includes Monterey Canyon, one of the largest submarine canyons on the Pacific coast of North America (Greene et al., 2002), and five other major canyons (Ascension, Año Nuevo, Cabrillo, Soquel and Carmel) (figure 1.4). Monterey Canyon begins in the littoral zone just offshore Moss Landing and follows a sinuous path east to west for ∼470 km into >4000 m water depth on the Monterey Fan (Greene et al., 2002; Paull et al., 2011). The Pajaro River to the north and Salinas River to the south provide sediment to the shelf during high discharge events, which is subsequently transported to the head of the canyon (Paull et al., 2006). Monterey Canyon was previously connected to the

Salinas river (Smith et al., 2007) but the river was redirected due to earthquake activity. Soquel and Carmel Canyons are two main tributary canyons, intersecting Monterey Canyon at 980 m and 1970 m water depth respectively.
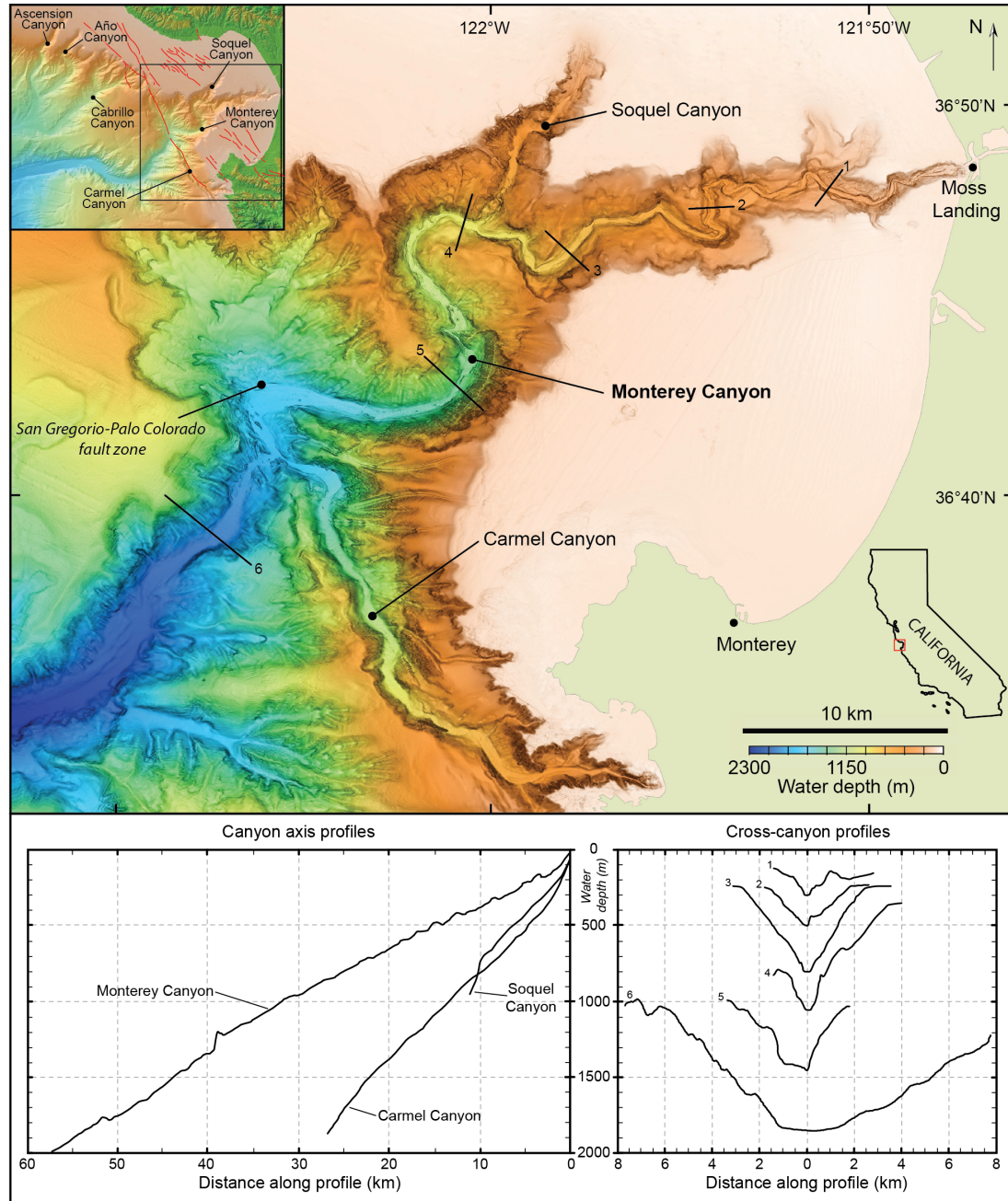
Figure 1.4: Map showing the bathymetry of Monterey Bay and Monterey Canyon, offshore California (USA) (modified after Paull et al., 2010). Inset map shows location of Monterey Bay with respect to California. The bottom panel shows the longitudinal thalweg profile of upper Monterey Canyon, and Carmel and Soquel Canyons for comparison. Select cross-sectional canyon profiles are shown to highlight the morphological evolution of Monterey Canyon down system.

The Ascension-Monterey canyon system has a complex origin and evolution due to the diverse tectonic history of the Californian margin. Monterey Canyon (possibly) began as a subaerial valley eroded into Cretaceous granitic rocks of the Salinian block (Salinia) during the Oligocene to early Miocene (Greene, 1977). At this time ($\sim$21 Ma) this structural block is estimated to have been at least 350 km south of its present location (Graham, 1976; Page and Englebretson, 1984), and still being influenced by subduction and tectonic uplift. As the margin shifted from being dominantly collisional to oblique strike-slip along the San Andreas Fault, Salinia moved north (Greene and Hicks, 1990). During this passage northwards, Salinia experienced periods of emergence and submergence, which ultimately developed the canyon morphology beyond its subaerial valley origin and produced a succession of regressive and transgressive sedimentary units (Greene, 1977). During times when the tectonic block was deeply submerged below sea level, sediments were deposited within the canyon but never to an extent where the morphological depression was lost (Greene and Hicks, 1990). At times when Salinia was elevated to sea level or above, the canyon system developed steep walls through renewed erosion. Whilst the canyon shape can be attributed to erosional processes and mass-wasting features, large scale meanders and linear canyon sections that reflect the gross-canyon morphology are likely the tectonic offset of a long-lived canyon system (Greene and Hicks, 1990; Greene et al., 2002). The structural control on the overall canyon morphology results from the proximity of Monterey Canyon to the western margin of the San Andreas Fault system, which extends NNW-SSE across Monterey Bay. Two fault zones are seen to significantly control the morphology of Monterey Canyon: (1) the San Gregorio-Palo Colorado fault zone, and (2) the Monterey Bay fault zone (Greene and Hicks, 1990; Greene et al., 2002; Paull et al., 2011).

Extensive mapping of Monterey Canyon show that the main axial channel (thalweg) of the canyon is relatively flat (Greene et al., 2002; Paull et al., 2005, 2011; Smith et al., 2005) and varies between 100 m and 350 m wide in the upper canyon, increasing in width to $\sim$1000 m at $\sim$1850 m water depth (Paull et al., 2011). Beyond $\sim$1850 m water depth the canyon cross-section changes from V-shaped to U-shaped. The overall slope of the channel is relatively uniform, averaging 1.7° between 200 m and 1200 m water depth (Paull et al., 2005). Terraces (raised plateaus between the incised thalweg

and canyon wall) are common within the canyon and slope gently toward the thalweg (Paull et al., 2005). The walls of Monterey Canyon typically have slopes of between 10° and 25°, but locally can reach 45° (Greene et al., 2002; Paull et al., 2005).

Field studies carried out in Monterey Canyon between 1993 and 2007 highlight that it is a sedimentologically active system, and provide some of the most extensive observations and measurements of turbidity currents in a natural system (e.g. Greene et al., 2002; Xu et al., 2002, 2004, 2013, 2014; Paull et al., 2003, 2005, 2010). These turbidity currents are likely responsible for the features such as bedforms, knick points, and intra-canyon meanders that are restricted to the morphologically complex canyon thalweg (Greene et al., 2002; Paull et al., 2011; Symons et al., 2016).

Multiple turbidity currents occur in Monterey Canyon each year (Xu et al., 2004), yet it is rare for them to extend beyond 2000 m water depth (Xu, 2011); it was ~150 years ago that a turbidity current went beyond 3400 m water depth (Johnson et al., 2005). In addition to Monterey Canyon, other canyons on the Californian margin are active systems, including Oceanside, Carlsbad, La Jolla, Hueneme, Redondo, Newport, Eel, and Mendocino canyons (Covault et al., 2007; Normark et al., 2009; Sumner and Paull, 2014; Paull et al., 2014), and more than half of the submarine fans on the Californian Borderland are active during the present sea-level highstand (Normark et al., 2009). This activity contradicts the sequence-stratigraphic models (e.g. Postamentier et al., 1991) that suggest activity and growth of submarine fans predominantly occur during sea-level lowstands where rivers reach the outer continental shelf. These sequence-stratigraphic models are primarily based on passive margins where continental shelves are relatively wide (Covault et al., 2007). On the tectonically active Californian margin, where the continental shelf is narrow, the heads of canyons are able to intersect littoral cells or connect to rivers (Covault et al., 2007; Normark et al., 2009). In the case of Monterey Canyon, the sediment that generates the sub-annual turbidity currents is sourced from the intersection of the canyon head with the local littoral cell, supplying an estimated 400,000 m^3 of sediment into Monterey Canyon each year (Paull et al., 2003).

Chapter 2

Large-scale sediment waves and scours on the modern seafloor and their implications for the prevalence of supercritical flows

Symons, W.O[1]., Sumner, E.J[1]., Talling, P.J[2]., Cartigny, M.J.B[2]., and Clare, M.A[2]., 2016. Large-scale sediment waves and scours on the modern seafloor and their implications for the prevalence of supercritical flows. Marine Geology 371, 130-148.

[1]*School of Ocean and Earth Science, University of Southampton*
[2]*National Oceanography Centre, Southampton*

Abstract

Large-scale (20 m to 7 km wavelength) bedforms are common on the seafloor, yet there is a lack of consensus on how they form and thus what to call them. We conducted statistical analysis on a dataset of 82 seafloor bedforms that span a range of water depths and environments. The data form three distinct groups: 1) small-scale (20-300 m wavelength) sediment waves with mixed relief made of medium sand to cobble-sized sediment that form in confined settings, which we call small sediment waves; 2) large-scale (300-7000 m wavelength) sediment waves with mixed relief made of fine-grained sediment that form in relatively unconfined settings, which we call large sediment waves; and 3)

large-scale fully enclosed depressions in the seafloor, which we call scours. There is a statistically significant data gap in the size of bedforms between small sediment waves and large sediment waves that does not appear to be a sampling artefact. This data gap probably results from the environments in which sediment waves form being either confined (e.g. channel or canyon) or unconfined (e.g. open slope). Bedform migration direction is available for 36% of the data and includes small and large-scale sediment waves; of these examples all are shown to migrate up-current. Up-current migration is indicative of supercritical flow; thus this data suggests that supercritical flows operate in a wide range of environments and can generate both small and large sediment waves. Therefore, we suggest that small and large sediment waves form by similar processes despite the gap in bedform wavelength and sediment size. The migration direction for scours remains unknown. Scours may form from similar processes to small and large sediment waves, or alternatively they may be a completely separate bedform type that form when erosive flows exploit pre-existing defects in the seafloor. This novel statistical analysis of a global database shows that up-current migrating bedforms associated with supercritical flow are unusually widespread, and are recognised at two distinct scales.

2.1   Introduction

Sediment-laden flows in the ocean are poorly understood because there are few direct observations of these types of flows (Talling et al., 2015). As a result, much of what is known about sediment-laden flows is based upon the analysis of deposits that they leave behind in the geological record and on the modern seafloor. Large-scale (up to 7.2 km wavelengths), undulating bedforms, are one of the most distinct, widespread, and frequently described features on the deep seafloor (Flood and Shor, 1988; Piper and Savoye, 1993; Wynn and Stow, 2002; Gong et al., 2012) (figure 2.1). Despite abundant literature on these seafloor features there is a general lack of consensus on how they should be interpreted, what the bedforms reveal about how they are formed, or indeed how they should be classified.

The recognition of large-scale bedforms on the deep seafloor has increased over
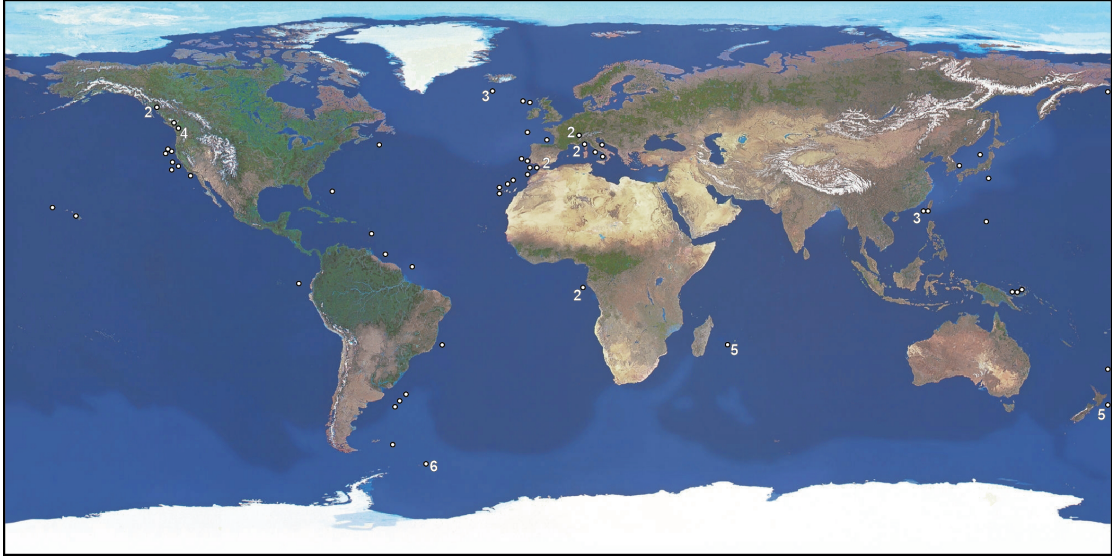
Figure 2.1: Map showing global distribution of seafloor bedforms used in this study.

the last six decades due to the advent of advanced seafloor mapping techniques (Wynn et al., 2014). The last global review of seafloor bedforms was conducted in 2002 (Wynn and Stow, 2002); however, in the last 13 years technology has progressed sufficiently for numerous, mainly shallower water examples (<500 m water depth) of bedforms to be identified and studied (e.g. Paull et al., 2010a; Babonneau et al., 2013; Hughes Clarke et al., 2014) along with many additional examples in deep water (e.g. Arzola et al., 2008; Gong et al., 2012).

Here we conduct a global analysis of seafloor bedforms using a much larger dataset than any previous study. In an attempt to avoid bias, we initially make no assumptions about how the bedforms formed but instead compile a dataset of observable bedform parameters (wave height, wavelength, slope angle, environmental setting, system size, water depth and crest shape). This dataset is then analysed visually and statistically to define clusters of bedforms with similar characteristics, which forms the basis for a classification scheme. We go on to use our dataset to infer how the different groups of bedforms were formed.

2.1.1   Terminology

A wide range of terms have been used to describe seafloor bedforms; however, there is no general consensus on terminology. For example, the same bedform may be classified differently by different authors (e.g. sediment waves versus crescent shaped bedforms for the same features in Monterey Canyon; Smith et al., 2007; Paull et al., 2010a). Below, we outline a set of terms that we will use throughout this contribution

Figure 2.2: Classification of seafloor bedforms based on their origin, migration direction, grain size, and crest shape.

(figure 2.2).
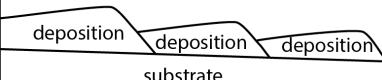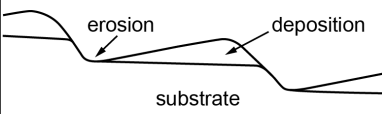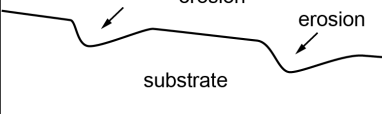
We define a ***topographic feature*** as any morphological feature on the seafloor. A ***bedform*** is formed by interaction of a gravity current with the seafloor, including turbidity currents, thermohaline bottom currents, and saline gravity currents (Wynn and Stow, 2002; Gong et al., 2012; Sumner et al., 2013). The term *bedform* encompasses seafloor features of any scale that span the range from negative to positive relief in relation to the overall seafloor. We define slope creep bedforms as features that form by deformation of the seabed under the influence of gravity, which may be initiated by events such as earthquakes (Lee et al., 2001).

We further classify flow bedforms as ***sediment waves*** or ***scours*** according to the prevalence of erosion. Sediment waves are typically tens of metres to a few kilometres in wavelength and several metres in wave height (Wynn et al., 2000b). Sediment waves are created by a combination of deposition and erosion, and their crests are positive relative to the surrounding region of seafloor. Before any investigation is made, we propose that a whole range of bedform relief with relation to the local seafloor is possible so that sediment waves can be further divided into: 1) depositional bedforms, where deposition is dominant and the majority of the bedform is elevated above the regional seafloor, and 2) mixed bedforms if the sediment wave is formed from a combination of erosion and deposition (figure 2.2). The grain size of sediment waves is variable, ranging from mud-size (Lewis et al., 1998), through sand-size (Kenyon and Belderson, 1973) to gravel-size (Shor et al., 1990). We use the term sediment wave to encompass all of the above forms regardless of grain size. Sediment waves have been documented globally and in a range of different submarine environments including continental shelves (e.g. Cattaneo et al., 2004), continental slopes and rises (e.g. Ediger et al., 2002), basin floors (e.g. Flood and Giosan, 2002), deltas (e.g. Hill, 2012; Hughes Clarke et al., 2014), canyons and channels (e.g. Arzola et al., 2008) and volcanic flanks (e.g. Wright et al., 2006). Sediment waves can be further classified according to their grain size and the type of flow that formed them (Wynn and Stow, 2002). *Coarse-grained turbidity current sediment waves* are commonly formed by confined flows in submarine canyons or channels, or from expanding flows in channel-lobe transition zones (Mulder and Alexander, 2001; Faugères et al., 2002; Wynn and Stow, 2002b; Arzola et al., 2008). *Fine-grained turbidity current*

sediment waves have been inferred to form beneath unconfined turbidity currents, most notably on the backslopes of channel levees (Lewis et al., 1998; Migeon et al., 2000; Nakajima and Satoh, 2001; Normark et al., 1980, 2002). Both coarse- and fine-grained bottom current sediment waves form in unconfined settings where bottom currents are prevalent (Lonsdale and Malfait, 1974; Flood and Shor, 1988; Manley and Caress, 1994; Cunningham and Barker, 1996; Gong et al., 2012; Kuang et al., 2014).

Scours are predominantly erosional bedforms, although they may have localised areas of deposition. They are characterised by enclosed depressions, which cut into (and lie below) the surrounding region of seafloor. Scours are predominantly found in deep-water settings on the margins and at the mouths of submarine canyons and channels, such as the Eel Fan (Lamb et al., 2008; Paull et al., 2014), Agadir Canyon Mouth (Huvenne et al., 2009; Macdonald et al., 2011), Horseshoe Valley (Terrinha et al., 2009; Duarte et al., 2010; Macdonald et al., 2011), Setúbal Canyon Mouth (Lastras et al., 2009; Macdonald et al., 2011), and Whittard Channel margin (Macdonald et al., 2011). Shallower water examples of scours have been found on channel levees and back slopes, such as the Monterey East Channel (Fildani et al., 2006). Scours can occur as linear trains (Fildani et al., 2006; Covault et al., 2013; Zhong et al., 2015), individual isolated depressions (Macdonald et al., 2010; Paull et al., 2014), or form areas of complex erosion (Macdonald et al., 2010).

The crests of flow bedforms typically migrate over time. The direction of migration provides insight into the flow-state (sub or supercritical) and type of flow that created the bedform. Crests can migrate along slope, upslope (towards the flow source), or downslope (away from flow source). The planform crest shape of flow bedforms can vary between individual bedforms within a system and can be linear, crescentic (with limbs pointing up or downslope), or sinuous.

The term **crescent shaped bedform** was recently introduced to describe coarse-grained bedforms that have a crescent shaped crest in plan view (Paull et al., 2010a). Crescent shaped bedform has subsequently been used to describe bedforms with a broader range of characteristics (Covault et al., 2014). To avoid confusion we do not use the term crescent shaped bedform in our terminology but note that crest shape is an important discriminator between bedform types.

2.1.2   Previous classification of seafloor bedforms

As discussed above, there is a lack of consensus as to how to classify seafloor bedforms. The most detailed existing study to classify seafloor bedforms was limited to deep-water (up to 4825 m water depth (Ercilla et al., 2002; Wynn and Stow, 2002)) sediment waves. The sediment waves were classified based on grain size (sand and gravel or mud and silt) with inferences made about formative processes; resulting in the following classification scheme (Wynn and Stow, 2002):

  i. Fine grained bottom current sediment waves that can be up to 10 km in wavelength (trough to trough) and 150 m wave height (maximum relief).

 ii. Coarse grained bottom current sediment waves reaching 200 m in wavelength and a few metres wave height

iii. Fine grained turbidity current sediment waves reaching 7 km in length and 80 m wave height.

 iv. Coarse grained turbidity current sediment waves reaching 1 km in length and up to 10 m wave height.

Evidence to support this four-fold classification came from knowledge of the environment, bedform morphology, sediment size, wave migration direction, and inferring wave forming processes.

Wynn and Stow (2002) were able to classify deep-water sediment waves by morphology, using values for the upper limits of dimensions and grain size. By providing characteristics of internal morphology and migration patterns for the different sediment wave categories they were also able to link the product to the formation process - a step that few studies have been able to provide. Wynn and Stow (2002) summarised previous work that attributed sediment wave formation to antidunes and internal waves (Normark et al., 1980), lee waves (Flood, 1988) and discussed how amplification of an initial seafloor defect may enable bedform growth (Kubo and Nakajima, 2002).

In the decade since Wynn and Stow (2002) published this study far more data, and higher resolution data, have become available for a wider range of seafloor bedforms.

Wynn and Stow (2002) used 14 examples in their contribution, and this study includes 82 examples. Additionally, Wynn and Stows' (2002) use of grain size as a discriminator between bedforms is restrictive; particularly as accurate grain size data are rarely reported. Finally, Wynn and Stow (2002) focussed only on deep-water sediment waves, whereas it is now apparent that similar bedforms are present in a wide range of water depths and environments (figure 2.1). Thus, it is appropriate to test and expand the classification scheme of Wynn and Stow (2002) using the much larger dataset that is now available, using a novel statistical approach and expanding the interpretation underlying the classification into supercritical flow processes.

2.1.3 Aims

Seafloor bedforms are common and occur in a wide range of submarine environments (figure 2.1). However, the existing classification scheme (Wynn and Stow, 2002) is based on a small dataset and limited to examples in deep water. This study uses data from a much wider range of water depths and settings. It aims to provide a holistic analysis of available published data on seafloor bedforms in order to:

i. define groups of bedforms based on key characteristics and environmental settings, supported with appropriate statistical analysis, to test the significance of relationships,

ii. consider whether these groups are indicative of different formative processes, and

iii. test whether the conclusions of Wynn and Stow (2002) are valid for a much larger dataset and wider range of environments than was used in their study.

2.2 Methods

A global database of 82 examples of seafloor bedforms (table 2.1) was created to document their key characteristics. Examples were chosen based on the quality of the data available and not by the formative mechanism. As a result the database includes

bedforms that have been attributed to formation by turbidity currents, bottom currents and slope creep, albeit those formed by turbidity currents form the majority. These specific examples were chosen because the papers included high-resolution images of the bedforms and information regarding bedform dimensions and environmental factors (water depth and seafloor slope angle) as well as interpretations of formative mechanisms (for differentiation between turbidity current and bottom current formed bedforms). The database was analysed visually and statistically to establish groups of bedforms based on their morphological characteristics and environmental distribution.

2.2.1 Data

Eight characteristics were used to define the dimensions and characteristics of the bedforms in each study: (i) wavelength, (ii) wave height, (iii) seafloor slope angle, (iv) minimum and maximum water depth of bedform occurrence, (v) confinement, (vi) environment, (vii) planform crest shape, and (viii) cross-sectional shape. Information was also documented on previously published interpretations of potential formative processes and environmental setting of the bedforms. For each dataset the following were extracted: (i) minimum bedform dimensions, (ii) maximum bedform dimensions and, if sufficiently high-resolution data were available (iii) measurements of an individual bedform (measurements were possible in 32 of the 82 examples).

To constrain bedform morphology beyond just scale, the planform crest shape and cross-sectional shape were determined for each bedform. The planform crest shape of the bedforms was defined as one of the following: (i) crescentic (where the two ends of the crest clearly point downslope or upslope), (ii) sinuous, (iii) straight, and (iii) unknown (where no reference was made to crest shape or there were no suitable planform figures to determine the crest shape of the bedforms) (figure 2.3). The cross-sectional shape of a bedform was defined as one of the following: (i) upslope asymmetric (where the downslope limbs are longer and shallower), (ii) downslope asymmetric (where the upslope limbs are longer and shallower), (iii) symmetric, (iv) asymmetric (no orientation - reference was made to asymmetry in the literature but no reference was made to orientation). Additionally there is the distinction between positive and negative relief

(figure 2.3). All cross-sectional shapes other than scours are at least partially positive in their relief (an aggraded feature in relation to the overall slope) unless stated. Scours are defined as mainly comprising enclosed depressions, which may be circular, elliptical or crescent shaped. Scours may be further subdivided into isolated scours, linear trains of scours, or fields of scours (multiple individual scours spread over an area of seafloor).

Table 2.1: Table of bedform examples used in this study, along with abbreviations. * denotes bedforms that display up-current migrating crests or reference is made to up-current migrating crests within the literature. † denotes volcanic bedforms. Volcanic bedforms are either directly on a volcanic slope, formed through volcanic processes, or inferred to be composed of volcaniclastic grains. ‡ denotes bedforms that are interpreted to be formed by bottom currents.

Location	Code	Key reference
Adriatic shelf*‡	AS	Cattaneo et al., 2004
Adventure Island†	AI	Leat et al., 2013
Agadir	A	Macdonald et al., 2011
Amazon Fan*	AF	Normark et al., 2002
Barra Fan*	BF	Howe, 1996
Blake-Bahama Ridge‡	BBR	Flood, 1994
Bristol Island	BI	Leat et al., 2013
Carnegie Ridge	CR	Lonsdale and Malfait, 1974
Cilaos canyons*†	CC	Sisavath et al., 2011
Cilaos Distal Fan	CDF	Sisavath et al., 2011
Cilaos Proximal Fan*†	CPF	Sisavath et al., 2011
Dakataua Caldera - New Britain†	DC	Silver et al., 2009
Eel Canyon	EC	Lamb et al., 2008
Eel Fan	EF	Lamb et al., 2008
El Julan Channel*†	EJC	Wynn et al., 2002
Espirito Santo Basin*	ESB	Heinio and Davies, 2009
Etang-Sal Sector - La reunion†	ESS	Babonneau et al., 2013
Ewing Drift‡	ED	Flood and Shor, 1988
Falkland Trough*‡	FT	Cunningham and Barker, 1996
Fraser River Delta (outer southern channel margin)*	FRD-SCM	Hill, 2012
Fraser River Delta (slope)*	FRD-S	Hill, 2012

Continued on next page

Table 2.1 – *Continued from previous page*

Location	Code	Key reference
Fraser River Delta (southern channel margin interior)*	FRD-SCI	Hill, 2012
Fraser River Delta (tributary channels)*	FRD-TC	Hill, 2012
Gardar Drift Area A‡	GDA	Manley and Caress, 1994
Gardar Drift Area B‡	GDB	Manley and Caress, 1994
Gardar Drift Area C‡	GDC	Manley and Caress, 1994
Gulf of Cadiz low velocity zone‡	GDD	Habgood et al., 2003
Gulf of Cadiz medium to high velocity zone‡	GC-MH	Habgood et al., 2003
Gulf of Cadiz medium velocity zone‡	GC-M	Habgood et al., 2003
Haleakala Volcano†	HV	Eakins and Robinson, 2006
Hawaiian Ridge†	HR	Moore et al., 1994
Horseshoe Valley	HSV	Macdonald et al., 2011
Humboldt Slide*	HS	Lee et al., 2002
Kahouanne Seamounts†	KS	Lebas et al., 2011
Kimbe and Hixon Bay†	KHB	Silver et al., 2009
La Jolla Canyon system*	LC	Paull et al., 2013
La Palma*†	LP	Wynn et al., 2000
Landes Plateau (Bay of Biscay)*	LP BB	Faugres et al., 2002
Laurentian fan	LF	Piper et al., 1985
Lower Nazare Canyon*	LNC	Arzola et al., 2008
Macaulay Island†	McI	Wright et al., 2006
Margin of Gabon - Lower Slope*	MGLS	Lonergan et al., 2013
Margin of Gabon - Upper Slope*	MGUS	Lonergan et al., 2013
Montagu Island†	MI	Leat et al., 2013
Monterey Canyon*	MC	Paull et al., 2010a
Monterey East*	ME	Fildani et al., 2006
Moroccan continental rise*	MCR	Jacobi et al., 1975
Navarinsky Canyon*	NC	Karl and Carlson, 1982

Table 2.1 – *Continued from previous page*

Location	Code	Key reference
Noeick River Delta Lower-slope	NRDL	Bornhold and Prior, 1990
Noeick River Delta Mid-slope*	NRDM	Bornhold and Prior, 1990
Orinoco Valley*	OV	Ercilla et al., 2002
Rhone Levee	RL	Girardclos et al., 2012
Rhone main delta channel	RDC	Girardclos et al., 2012
Rockall Trough*	RT	Howe, 1996
Saint-Etienne sector - La reunion†	SSS	Babonneau et al., 2013
San Mateo*	SM	Covault et al., 2014
Selvage (NE Atlantic)*	S	Wynn et al., 2000b
Setubal Canyon	SC	Arzola et al., 2008
South Candlemas Embayment†	SCE	Leat et al., 2010
South China Sea Wave Field 1*	SCS1	Gong et al., 2012
South China Sea Wave Field 2	SCS2	Gong et al., 2012
South Korea Plateau	SKP	Lee and Chough, 2001
South Taiwan Channel*	STC	Kuang et al., 2014
Southern Hikurnagi trough (Drift/toe of the Chatham Rise)‡	SHT DT	Lewis and Pantin, 2002
Southern Hikurnagi trough (Foot of the Chatham Rise)	SHT F	Lewis and Pantin, 2002
Southern Hikurnagi trough (foredeep to trench transition)	SHT FT	Lewis and Pantin, 2002
Southern Hikurnagi trough (left-bank levee)*	SHT L	Lewis and Pantin, 2002
Southern Hikurnagi trough (overbank plain)	SHT OP	Lewis and Pantin, 2002
Squamish Delta*	SD	Hughes Clarke et al., 2012
Stromboli Volcano†	STV	Casalbore et al., 2010
Sumisu volcano†	SV	Tani et al., 2007
Tiber Pro-delta slope*‡	T	Trincardi and Normark, 1988
Tolokiwa Island†	TI	Silver et al., 2009
Toyama deep-sea channel*	TDSC	Nakajima and Satoh, 2001
Var Fan*	VF	Piper and Savoye, 1993

Table 2.1 – *Continued from previous page*

Location	Code	Key reference
Var Sedimentary Ridge*	VSR	Migeon et al., 2001
West Dongsha Channel*	WDC	Kuang et al., 2014
West Mariana Ridge	WMR	Gardner, 2010
West Penghu Channel*	WPC	Kuang et al., 2014
West Taiwan Channel*	WTC	Kuang et al., 2014
Whittard Channel Margin	WCM	Macdonald et al., 2011
Zapiola Drift*‡	ZD	Flood and Shor, 1988
Zavodovski (north fan)†	ZN	Leat et al., 2010
Zavodovski (south)†	ZS	Leat et al., 2010

The environmental setting for each bedform was defined as follows: (i) delta, (ii) canyon/channel, (iii) open slope, and (iv) levee. These environmental settings were further subdivided based on water depth and confinement: (i) delta open (where there are no containing walls), (ii) delta channel, (iii) shallow open slope, (iv) shallow channel, (v) unconfined continental slope, and (vi) continental slope channel. A straight-line distance between the beginning and end of the system was used to constrain canyon and channel system sizes. The systems were grouped based on the straight-line distance into the following: (i) small systems (<10 km long), (ii) medium systems (10-50 km long), and (iii) large systems (>50 km long).

The migration direction of the bedforms was noted as migrating down current or up current. For migration direction to be used clear seismic images had to be presented in the literature. Additionally, the position of the bedforms crest had to be able to be traceable between different reflectors. Information on bedform migration was available for 29 of the 82 examples.

2.2.2 Statistical analysis

Principal component analysis (Joliffe, 2002) was used to understand which of the variables (e.g. wavelength, amplitude, water depth) best explains the variance in the data. We first determined how many principal components best explain the variance in the data through a dimensionless analysis. We then determined the correlation between

CROSS-SECTION SHAPE

CREST SHAPE (PLANFORM)

A. Downslope asymmetric

1. Crescentic

B. Upslope asymmetric

2. Sinuous

C. Symmetric

3. Straight

D. Asymmetric, negative relief
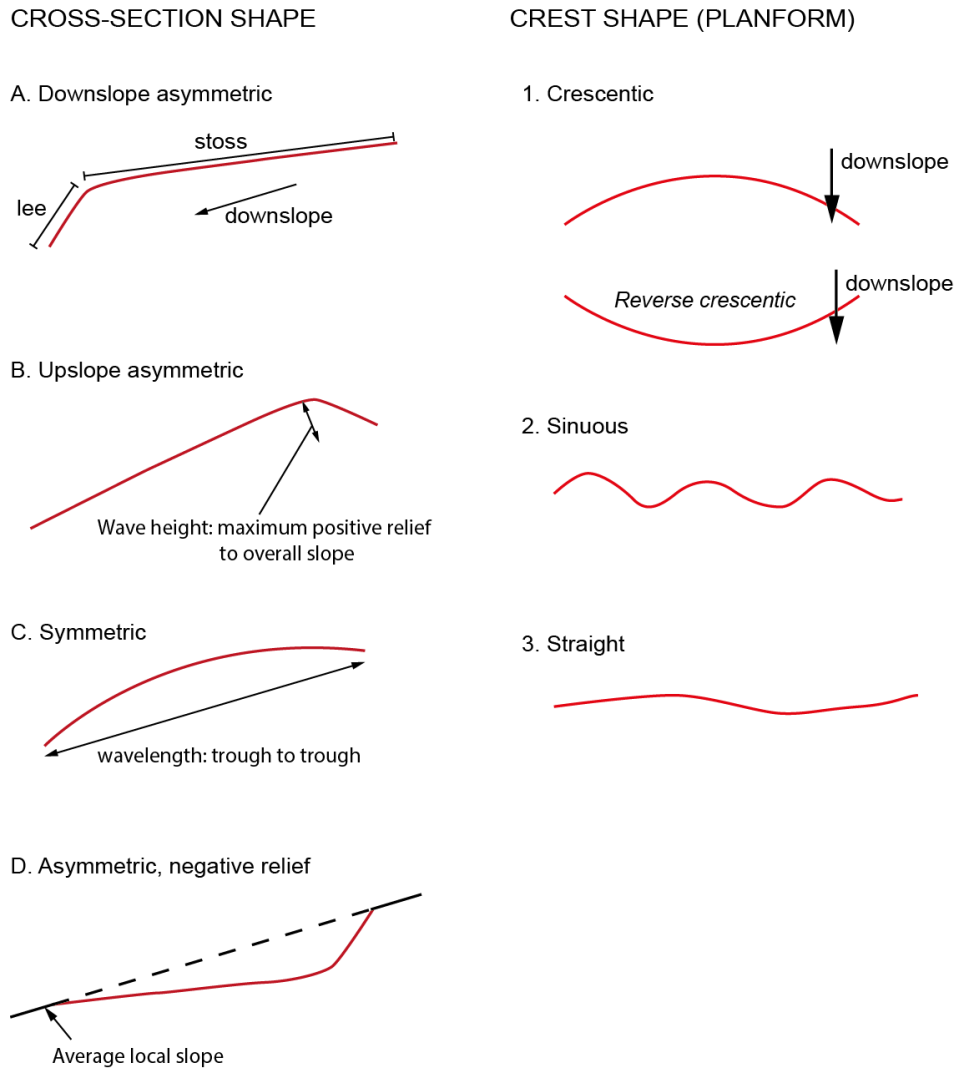
Figure 2.3: Line drawings showing terms used for bedform cross-section geometry and planform crest shape.

the variables and the principal components to understand which variables we should consider for further analysis. A correlation coefficient of 1 is perfectly correlated, -1 is perfectly negatively correlated, and 0 shows no correlation. We set a threshold limit of 0.5 (more than 50% of the data are explained by a principal component) for determining which variables to analyse further. Finally, we compared the results of principal component analysis with cluster analysis, to understand which variables may affect clustering observed in the data.

Cluster analysis was conducted using a Gaussian finite mixture model (Fraley et al., 2012) in order to determine whether groups are statistically significant. The Gaussian finite mixture model performs multiple tests to determine the best fit for different

parameter scenarios to characterise the distribution of data (where and how the clusters are distributed and centred). Parameters considered by the model include the number of clusters, their central point (as defined by the mean), and their orientation in relation to coordinate axes, cluster volume and shape. The clusters are ellipsoidal, centred at the mean values, while the covariance of the data determines the other genetic features (Fraley et al., 2012).

The data were tested using the Mclust function in R, which allows testing of all possible variations of the above parameters (Fraley et al., 2012), and compares Bayesian Information Criterion (Konishi and Kitigawa, 2008) values for the best-fit parameterisations for up to nine clusters. The Bayesian Information Criterion is the maximised log-likelihood value (Dempster et al., 1977; Fraley et al., 2012). The greater the unexplained variation in the variables (e.g. wave height and wavelength) and/or the greater the number of parameters (e.g. due to number of clusters), the greater the Bayesian Information Criterion and the more complex the model. Therefore, the closer to zero the Bayesian Information Criterion value, the stronger the support for that number of clusters (Fraley et al., 2012). Thus, this method can be used to determine which model best explains the distribution of clusters and how many clusters are most likely according to the complexity that exists within the dataset.

2.2.3 Data analysis

Data were plotted and analysed for both visual and statistical trends. Bedform wavelength versus wave height was plotted for three data sets that comprised; (i) minimum bedform dimensions stated in the literature, (ii) maximum bedform dimensions stated in the literature, and (iii) specific measured dimensions from images in the literature. The plots were then annotated with planform and cross-sectional shapes using a number and letter system. Wave height was taken as the maximum positive or negative relief relative to the local seafloor (figure 2.3).

2.3   Results

2.3.1   Controlling parameters on bedforms - principal component analysis

Principal component analysis was used to determine the main controlling parameters on bedform dimensions and which components to focus our further analysis on. The first, second and third principal components account for 41%, 29% and 16% (table 2.2) of the variance in the database respectively (column 2, table 2.2), hence we focus on these three principal components in the following analysis. The first principal component, which explains 41.1% of the total variance, is strongly correlated with wavelength (correlation coefficient of 0.878) and water depth (0.794) and to a lesser degree, grain size (0.590; table 2.2). The first principal component increases with increasing wavelength and water depth, which are themselves strongly positively correlated. The second principal component explains a further 29.2% of the total variance and is strongly negatively correlated with wave height (-0.827) and gradient (-0.824; table 2.2; which are themselves positively correlated). The third principal component explains a further 16.3% of the total variance and is negatively correlated with grain size (-0.736; table 2.2). Water depth (0.480; table 2.2) is almost significant but does not exceed the 0.5 threshold correlation score and is inversely correlated to grain size.

The strongest correlations were observed for wavelength (0.878 for principal component 1) and wave height (-0.827 for principal component 2); hence, we focus on these for further analysis. Subsequently, when wavelength and wave height are plotted on a logarithmic graph, groups of bedforms are apparent with respect to both morphology and setting. The same trends are recognised for all three datasets (minimum, maximum and specific examples), and are supported by statistical analysis. For brevity, in the main text we only present figures showing the maximum dimensions of bedforms; plots showing minimum and specific examples are available in appendix A.

		Correlation Coefficient				
Principal Component	Proportion of variance	Wavelength	Wave Height	Water Depth	Gradient	Grain Size
PC1	0.4113	**0.878**	0.384	**0.7934**	-0.400	**0.590**
PC2	0.2919	-0.161	**-0.827**	-0.337	**-0.824**	0.264
PC3	0.1634	0.085	-0.017	0.479	-0.105	**-0.736**
PC4	0.068	-0.175	-0.240	0.326	0.326	0.199
PC5	0.065	-0.407	0.289	0.179	-0.207	0.035

Table 2.2: Correlation coefficients determined from principal component analysis. Values above 0.5 are highlighted as being significantly correlated results. The proportion of variation for each principal component is also shown.

2.3.2 Classification based on scale and relief

Three groups are recognised based on the scale and relief of the bedform relative to the overall slope (figure 2.4). These groups are: (i) small-scale sediment waves with mixed relief, (ii) large-scale sediment waves with mixed relief, and (iii) large-scale scours that mainly comprise enclosed depressions (figure 2.4). Each of the above groups is described in further detail below.

Small-scale sediment waves with mixed relief (16 bedforms) have wavelengths from 20 m to 300 m and wave height between 0.5 m and 8 m (blue group; 2.4). Where data on cross-sectional shape is available, the small-scale bedforms are asymmetric in a downslope orientation to symmetric. When data on sediment size is available, these small dimension bedforms are composed of coarse grain sizes, up to cobble size. Planform crest shape is variable with the smaller bedforms in the small-scale sediment wave group exhibiting downslope crescentic crests and larger bedforms within the group having more sinuous crests.

Large-scale sediment waves with mixed relief (59 bedforms) (green group; figure 2.4) have wavelengths ranging from 300 m to 7200 m and wave height from 5 m to 220 m. Their cross-sectional shapes are more variable than other groups with shapes from downslope asymmetric, through symmetric, to upslope asymmetric.

Large-scale scours that comprise enclosed depressions (seven bedforms) exhibit wavelengths from 550 m to 3500 m, and wave heights from 20 m to 200 m (red
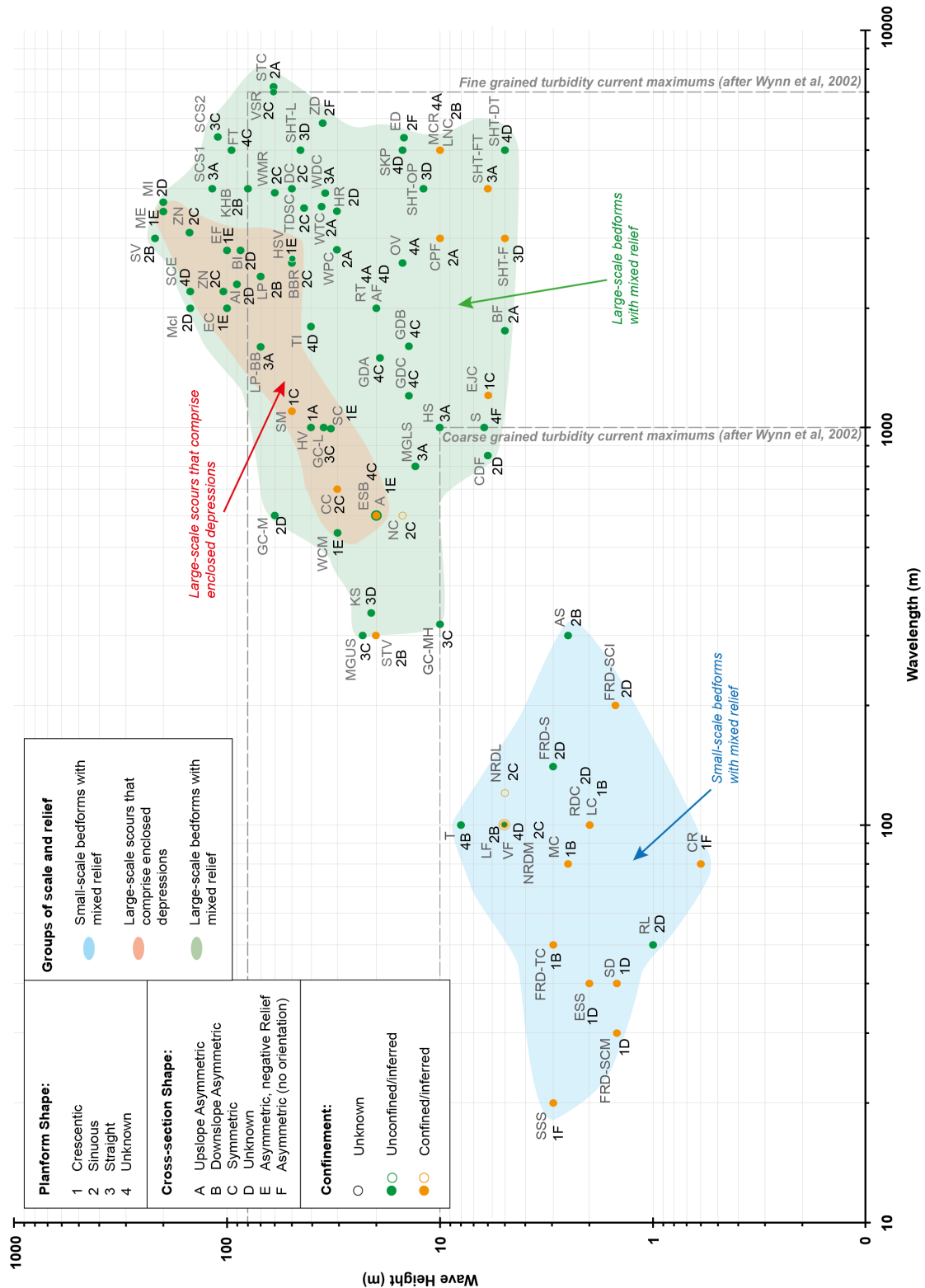
Figure 2.4: (Caption next page.)

Figure 2.4: *(Previous page)* Plot of wavelength versus amplitude with logarithmic axes for global bedform examples. This plot highlights bedform groupings based on geomorphological classification. Points indicate confinement (filled green = unconfined; open green = inferred to be unconfined from literature; filled orange = confined; open orange = inferred to be confined from literature). Letter and number coding denotes cross-sectional and crest/planform shape: 1 – crescentic, 2 – sinuous, 3 – straight, 4 – unknown; a – upslope asymmetric, b – downslope asymmetric, c – symmetrical, d – unknown, e – asymmetrical, negative relief, f – asymmetrical (unknown orientation).

group; figure 2.4), which overlaps the dimensions of the large-scale bedforms with mixed relief. However, in contrast to the large-scale bedforms with mixed relief, these bedforms comprise enclosed depressions that have negative relief relative to the local slope. Large-scale scours that comprise enclosed depressions are typically associated with silt with grain size maximums of fine sand.

2.3.3 Classification based on environment

Three main groups are defined based on environment: (i) deltas; (ii) open slopes; and (iii) channels and canyons (figure 2.5).

Delta bedforms range from 30 m to 300 m in wavelength and from 1 m to 8 m wave height and display crescentic or sinuous crests. Where reference is made to cross-sectional shape of delta bedforms, it is typically downslope-asymmetric. The delta environment can be further subdivided into (i) unconfined delta environments (purple area; figure 2.5); and (ii) confined delta environments (blue; figure 2.5).

Unconfined delta bedform wavelengths are between 50 m and 300 m and wave heights are from 1 m to 8 m. To classify confined systems further, sizes were assigned to each example. Small confined systems are <10 km in length; medium systems are 10-50 km long; and large systems are >50 km long. Confined delta environments (i.e. delta channels) are all small systems. Wavelengths of bedforms in *confined delta* environments range between 30 m and 200 m. Their wave heights are much less variable than their unconfined counterparts, ranging from 1.5 to 3 m.

Continental slope slope bedforms range from 80 to 7200 m in wavelength and 0.5 to 220 m in wave height. Planform crest shapes of continental slope bedforms
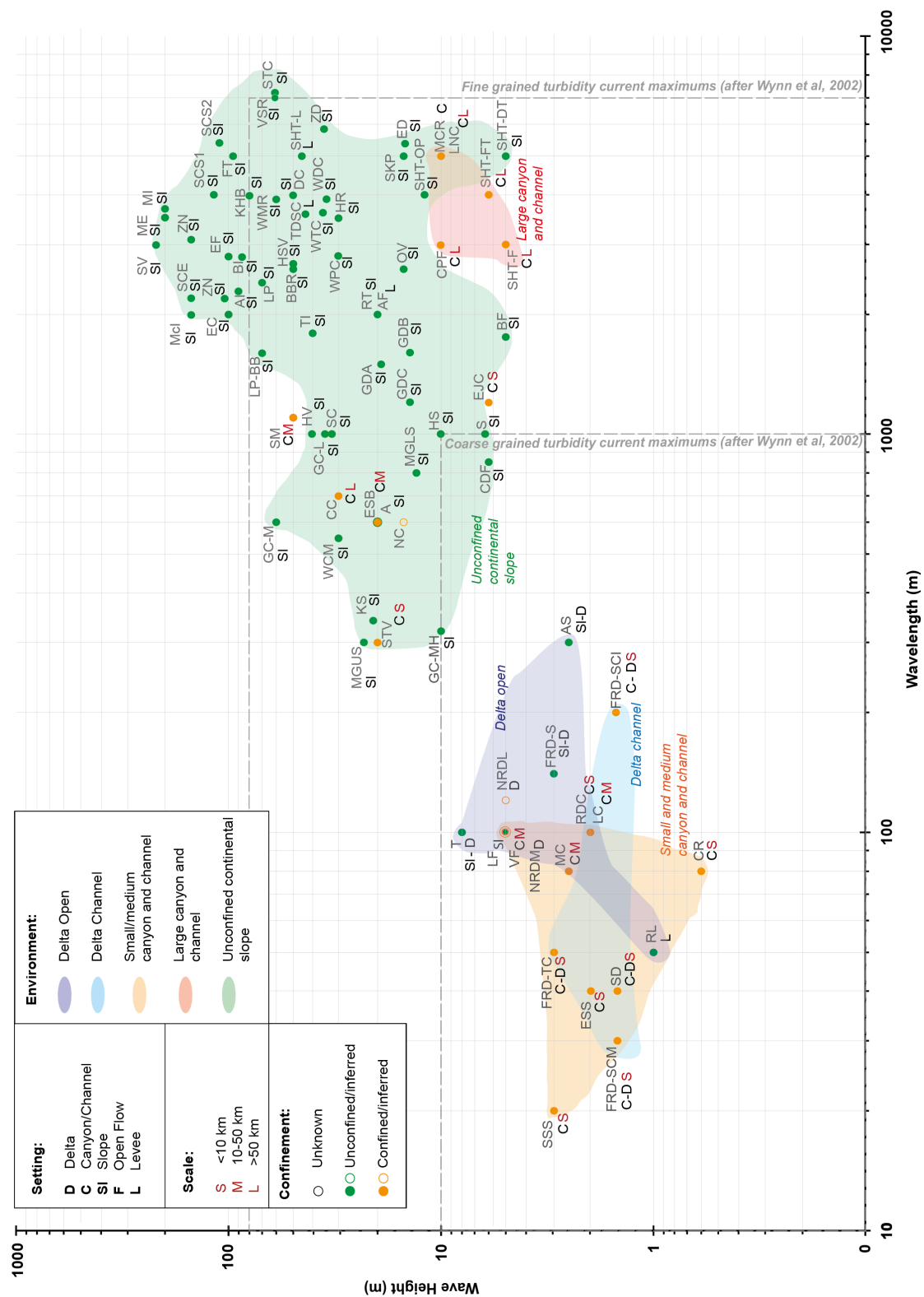
Figure 2.5: (Caption next page.)

Figure 2.5: *(Previous page)* Plot of wavelength versus amplitude with logarithmic axes highlighting groupings based on setting. Points indicate confinement (filled green = unconfined; open green = inferred to be unconfined from literature; filled orange = confined; open orange = inferred to be confined from literature). Black letter coding defines setting: D – Delta, V – Volcanic, C – Canyon/channel, Sl – Slope, L – Levee. Red letter coding defines scale of system: S – small (<10 km), M – medium (10-50 km), L – large (>50 km).

range from crescentic, through sinuous, to straight. Where reference is made to cross-sectional shape of continental slope bedforms, they include both upslope and downslope asymmetric and symmetric. The continental slope environment can be further subdivided into (i) unconfined continental slope environments (green area; figure 2.5), and (ii) confined continental slope environments (orange and red areas; figure 2.5).

Unconfined continental slope bedforms span a wide range of dimensions, with wavelengths from 320 m to 7200 m and wave heights between 5 m and 220 m (green area; figure 2.5) and have crests that are straight or sinuous. All unconfined continental slope bedforms that define this group are found in water depths that are greater than 500 m. Unconfined continental slope bedforms in water depths shallower than 500 m are associated with the unconfined delta bedforms.

Confined continental slope bedforms exhibit wavelengths from 80 m to 5000 m and wave heights from 0.5 m to 10 m. By assigning each canyon and channel a category of small, medium, or large, the canyon and channel group can be further subdivided into: (i) small (<10 km) and medium (10-50 km); and (ii) large (>50 km) canyons and channels. Small and medium canyons and channels contain small dimension bedforms ranging from 20 m to 100 m in wavelength and 0.5 m to 5 m in wave height (orange area; figure 2.5). Four examples comprise the small and medium canyon and channel group, with three of these examples exhibiting crescentic crests. Similarly, when viewed in cross-section, the small and medium canyon and channel examples display asymmetry in a downslope orientation. The Espirito Santo Basin, Stromboli Volcano and San Mateo bedforms are confined to a small-scale (<10 km) canyon and channel environments yet they have much larger dimensions (200-1100 m wavelength and 20-50 m wave height) than other examples (100 m wavelength with a wave height of 5 m). Large canyon and channel bedforms reach much greater wavelengths than small and medium canyon and channel bedforms (700-5000 m) with wave heights from 5 m to 30 m (red area; figure

2.5). No single planform crest shape defines the large canyon and channel bedforms but cross-sectional shape is typically asymmetrical, however no information is provided on whether asymmetry is upslope or downslope.

2.3.4   Bedform classification

By combining both crest shape and environment based on descriptions above, we are able to define the following single classification scheme:

i. small-scale sediment waves with mixed relief in confined settings and small-scale systems

ii. large-scale sediment waves with mixed relief in relatively unconfined settings

iii. large-scale scours that comprise enclosed depressions.

2.3.5   Support of bedform groups - cluster analysis

A cluster analysis of the logarithmic maximum wavelength versus wave height plots, using the Gaussian Finite Mixture Model, confirms three groups based on the Bayesian Information Criterion plot (figure 2.6a), with the position of the clusters represented in figure 2.6b. The dashed line on figure 2.6a highlights the minimum Bayesian Information Criterion value that shows the strongest support of three clusters; coinciding with clusters that are modelled as spherical, equal shape, and either variable or equal volume. The first group encompasses the small-scale sediment waves in a range of settings: delta and confined continental slope settings (blue group; figure 2.4). The mean value of the wavelength and wave height for this small-scale sediment wave group ellipse is 80 m and 2.5 m respectively. The ellipse ranges from 41 to 130 m wavelength and 1.3 to 4.5 m wave height (figure 2.6b). The second statistically recognised group comprises bedforms from the open continental slope, large canyon and channel, and large-scale scours (green group; figure 2.4). The mean value of the wavelength and wave height for this large-scale sediment wave group ellipse is 1600 m and 16 m respectively. The ellipse ranges from 700 to 3500 m wavelength 7 to 38 m wave height (figure 2.6b).
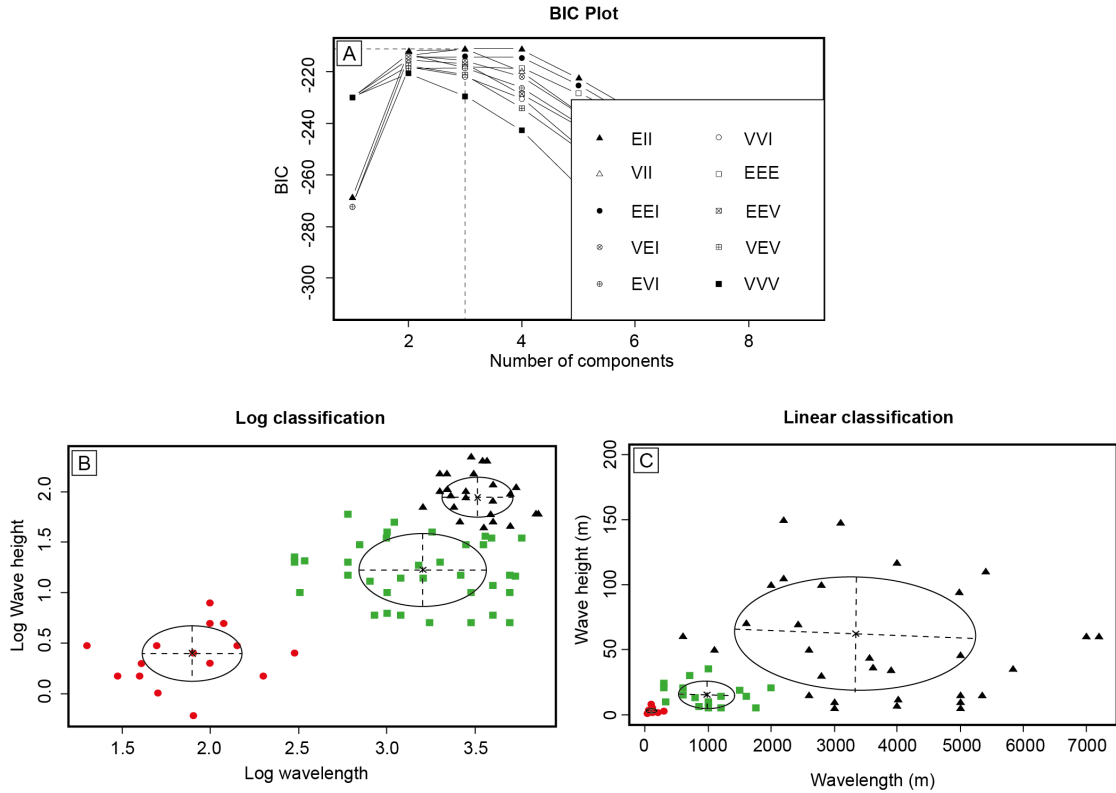
Figure 2.6: (A) Bayesian Information Criterion plot that shows the best fit of the data is to either a EII model (clusters that are spherical, equal volume, equal shape) or VII model (clusters that are spherical, variable volume, equal shape) with three clusters. (B) Model based cluster analysis on a log-log scale that defines three groups based on data distribution. (C) Model based cluster analysis on a linear scale defines three groups based on data distribution despite the visual difference to the log-log cluster analysis.

The third statistical group comprises the largest dimension bedforms and is primarily the largest open slope bedforms and large-scale scours (red group; figure 2.4). The mean value of the wavelength and wave height for this largest scale bedform group ellipsis is 3200 m and 90 m respectively. The ellipse ranges from 2050 to 5100 m wavelength and 57 to 150 m wave height (figure 2.6b).

There is a data gap (figures 2.4-2.6) that separates small dimension bedforms and larger dimension bedforms. This gap is evident when the data are plotted on a logarithmic scale; the gap is less evident when the data are plotted on a linear scale. However, the presence of the gap is statistically supported on the linear dataset with small-scale mixed relief bedforms statistically recognised on the linear plot (figure 2.6c). Therefore, statistical analysis supports the presence of the data gap and demonstrates

that it is not an artefact of logarithmic scaling as small-scale bedform groups are identified in both the logarithmic and linear plots (figure 2.6).

2.3.6 What are the controlling parameters on cluster groups?

The three clusters identified from the Finite Mixture Model are also distinctly identified when principal components 1 and 2 are cross-plotted (figure 2.7). The clusters are numbered here, from smallest (cluster 1) to largest wavelength and wave height (cluster 3), coinciding with the clusters from the Finite Mixture Model (figure 2.6).

Cluster 1 shows a large variance in principal component 3 (figure 2.7; table 2.2), which is likely to be due to a wide range of grain sizes. Only a small variance is observed in principal component 1, suggesting that wavelength or water depth does not vary greatly. Cluster 2 features a wide variance in principal component 1, but variance
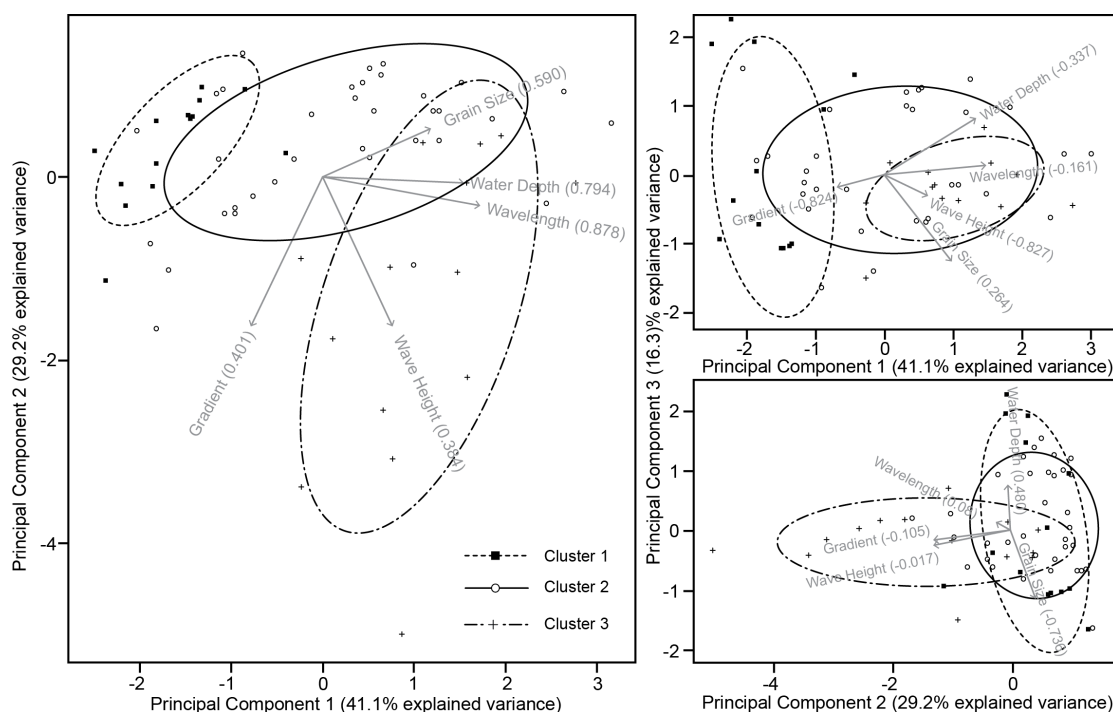
Figure 2.7: Biplots of principal component analysis. Correlation coefficients for variables are highlighted in table 2.2. Clusters determined from the Finite Mixture Model are annotated; where cluster 1 contains the bedforms with the smallest wavelengths and wave heights, and cluster 3 features the largest dimension bedforms. The length of the arrows shows the significance of that component on the principal component, with a correlation coefficient of 1 being perfectly correlated, -1 perfectly negatively correlated, and 0 shows no correlation.

is relatively small for principal component 2 (figure 2.7; table 2.2). Thus, wavelength or water depth are key variables that explain this cluster, whereas, wave height or gradient are less important. Cluster 3 has a wide variance in principal component 2, which primarily reflects a diversity of wave heights and gradients, but a very limited variance is noted for principal component 3 (figure 2.7; table 2.2), indicating a very small grain size range.

2.4 Discussion

Data from 82 seafloor bedform locations were collated in order to attempt to define groups based on key morphological characteristics and environmental settings. In this section we consider whether these morphological and environmental groups are indicative of different formative processes, and whether the classification of deep-water sediment waves by Wynn and Stow (2002) is valid for a much larger dataset and wider range of environments.

2.4.1 Can bedforms be grouped based on key characteristics and/or environment?

We demonstrated using visual inspection and cluster analysis that the bedforms fall into three groups based upon their size (wavelength and wave height), relief and environmental setting (figure 2.8). Our analysis also considered whether crest shape or grain size can be used to determine groups; however, these parameters were not found to be as important as bedform dimensions and environmental setting (water depth), as supported by the principal component analysis. The following groups were determined:

1. small-scale sediment waves with mixed relief in confined settings and small-scale systems (figure 2.9)

2. large-scale sediment waves with mixed relief in relatively unconfined settings (figure 2.10)
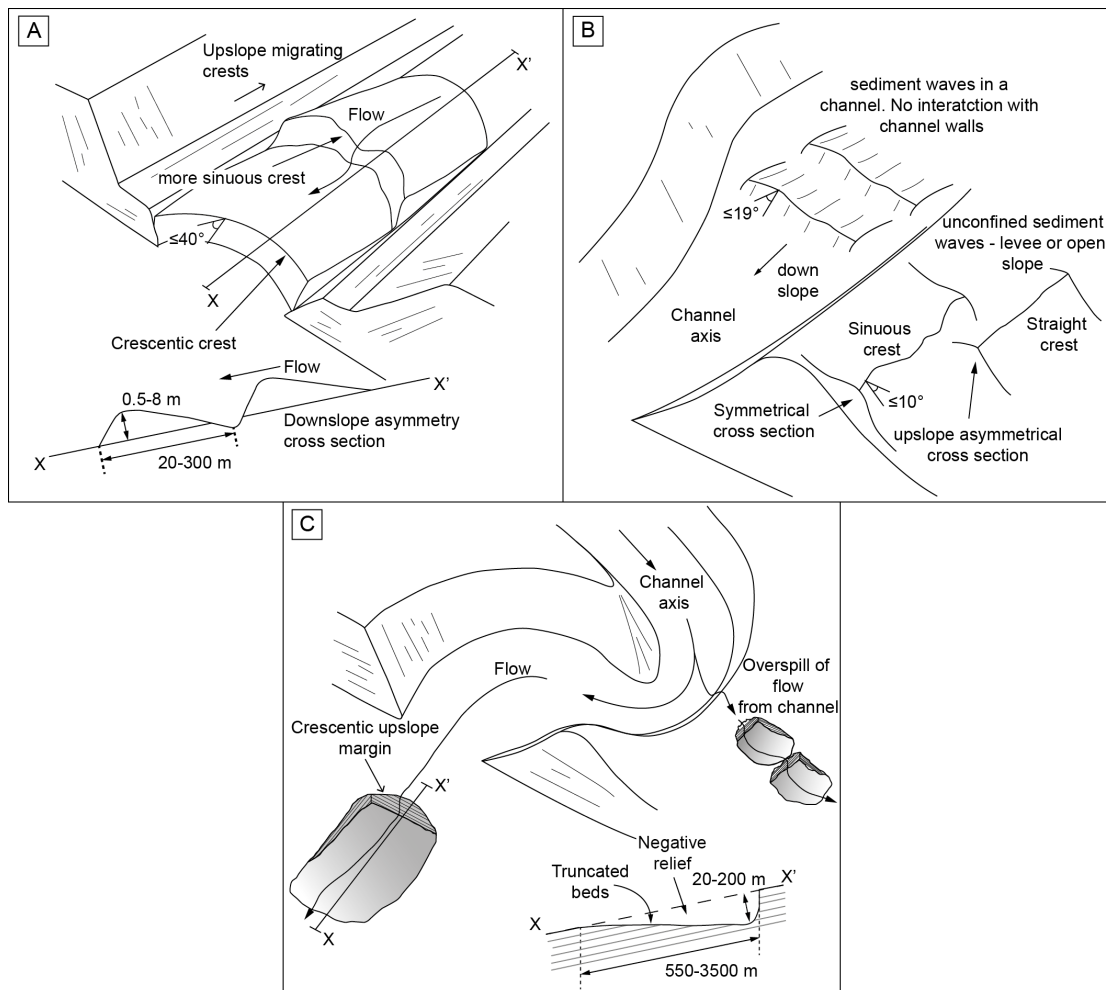
Figure 2.8: Cartoon summary showing the three groups of bedforms defined from morphological and environmental characteristics. (A) Small-scale crescentic bedforms with positive relief in confined settings; referred to as crescent shaped bedforms by some authors. (B) Large-scale crescentic bedforms with negative relief in areas of flow expansion such as channel mouths and overbanks or levees; referred to as scours. (C) Straight to sinuous crested bedforms with positive relief in relatively unconfined settings with some occurrences in channels without bounding wall interaction; typically defined as sediment waves.

3. large-scale scours that comprise enclosed depressions with negative relief (figure 2.11)

We now describe each bedform group and the environments in which it occurs.

Small-scale sediment waves with mixed relief in confined settings and small-scale systems are restricted to delta-front channels and slopes, and small to medium (<10-50 km) scale canyons and channels on the continental shelf. Small-scale sediment waves are composed of up to cobble sized sediment (e.g. Paull et al., 2010a)

and are generally asymmetric in cross-section, such that the steeper flank faces down-slope. These steeper flanks have gradients of up to 40° (Hughes Clarke et al., 2012). Many of the bedforms within this small-scale bedform group, in particular those that occur in a confined setting, have a downslope crescentic crest shape and have been termed crescent-shaped bedforms in recent studies (Paull et al., 2010a). These studies concluded that such crescent-shaped bedforms differ from more widely described sediment waves in particular because of their coarse grain sizes and lack of internal stratigraphy. Subsequently the term crescent shaped bedform has been used more generally to describe any bedform with a crescentic crest, regardless of scale and environment (e.g. Covault et al., 2014; Casalbore et al., 2013; 2014). However, our study does not find crest shape to be a good discriminator between different types of bedform. Indeed the *small-scale bedforms with mixed relief* group contains examples with both downslope crescentic and sinuous crests. Therefore we opt not to use the term crescent-shaped bedform and instead call this group *small (≤300 m wavelength) sediment waves*. We choose to remove relief as a discriminator as it appears that cross-sectional relief is not useful in distinguishing between different bedform groups. Evidence from this study suggests
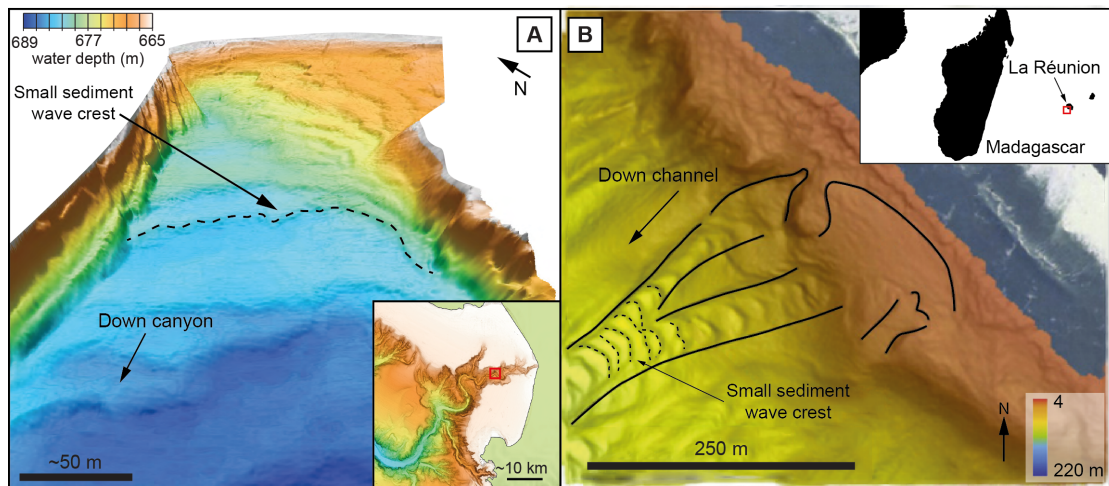
Figure 2.9: Bathymetric examples of the small-scale bedforms with mixed relief in confined settings and small-scale systems with crests of bedforms highlighted in both examples. (A) Perspective view of multi-beam echosounder data from the floor of Monterey Canyon, California. This data was collected using and Autonomous Underwater Vehicle (AUV) between 689 m and 665 m water depth (modified from figure 6 of Paull et al., 2011). (B) Multi-beam echosounder data from 4 - 220 m water depth of seafloor in front of the Saint-Etienne river mouth, La Réunion Island (modified from figure 6 of Babonneau et al., 2013)=).

that bedforms of all scales show varying levels of mixed relief. A potential problem with calling some of these small scale bedforms sediment waves is that they do not have a well-defined internal stratigraphy, which is a feature previously considered characteristic of sediment waves. Although the lack of internal stratigraphy could be a result of the coarse nature of the material causing difficulty in distinguishing internal reflectors using high-frequency sources, sampling of these bedforms highlights the lack of stratification (Paull et al., 2010a). However, as discussed in more depth below, there is evidence to suggest that these small bedforms form by a similar mechanism to other sediment waves that do show internal stratigraphy i.e. from interaction of a turbidity current with the bed (Hughes Clarke et al., 2014). We suggest that it is likely that this lack of internal stratification occurs when the deposit is formed from a very dense and coarse-grained near-bed layer at the base of the gravity current (Cartigny et al., 2013) or as a result of strongly decreased bed traction due to a hydraulic jump (Postma et al., 2009).

Large-scale sediment waves with mixed relief in relatively unconfined settings display a wider range of dimensions and morphologies, and occur in a wider
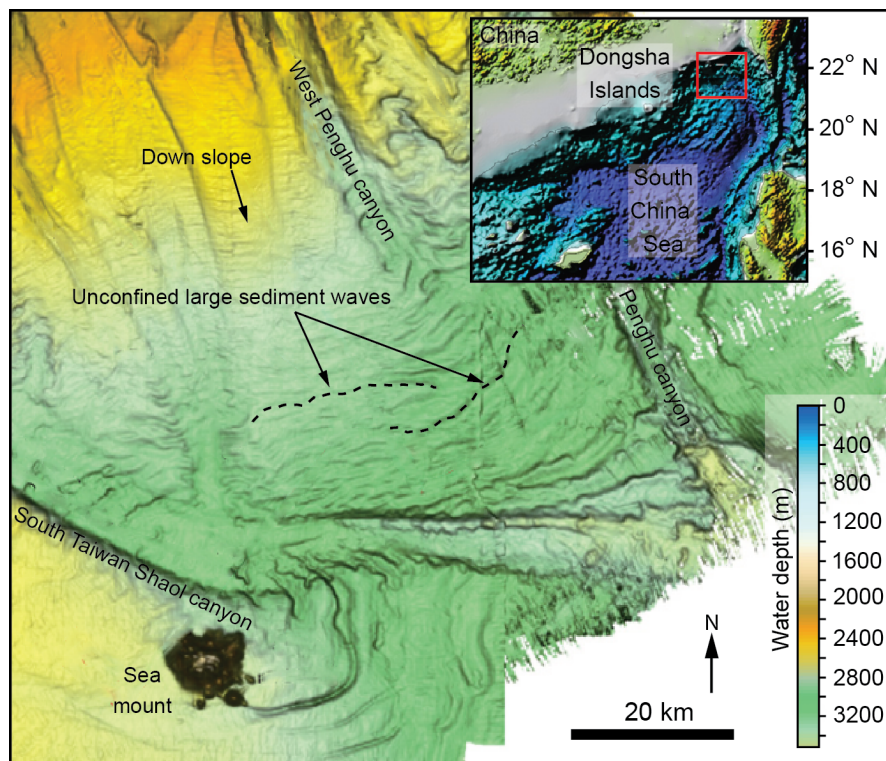
Figure 2.10: Multibeam bathymetric map of sediment waves in the South China Sea. These features comprise large-scale bedforms with mixed relief in relatively unconfined settings (modified from figure 1 of Zhong et al., 2015).

range of water depths than other groups. Large-scale sediment waves are typically found in water depths greater than 500 m. Most sediment waves in this category are straight to sinuous in planform and from symmetrical to asymmetrical in cross-section with lee slopes reaching a maximum angle of 19° in asymmetrical bedforms (within this study; Kostaschuk and Villard, 1996).

Bedforms with a volcanic association (table 2.1), either directly on a volcanic slope, formed through volcanic processes, or inferred to be composed of volcaniclastic grains, fall within this large-scale sediment wave with mixed relief group. Although these volcanic bedforms are arguably in a distinct setting, the dimensions are not distinctive enough from other open slope bedforms for a separate group. The wave height of some volcanic bedforms (e.g. Sumisu Volcano, Macaulay Island, South Candlemas Embayment) is greater than the wave height of other non-volcanic bedforms with the same wavelength. The greater wave height can be explained by the steeper slopes that non-confined volcanic bedforms typically form on compared to non-volcanic slopes. Whilst many other parameters (e.g. trigger processes, flow temperature and clast densities) beyond just slope angle may influence volcanic bedforms and may justify a separate environmental group, the lack of available data for investigating these other parameters means that we incorporate these volcanic bedforms into the large-scale sediment waves with mixed relief in relatively unconfined settings group.

Large-scale sediment waves with mixed relief in relatively unconfined settings can occasionally occur in confined settings (e.g. Lower Nazaré Canyon and Southern Hikurangi Trough; Arzola et al., 2008; Lewis and Pantin, 2002). In these confined cases, bedforms appear to have developed without any interaction with the edges of the container. Authors often refer to these bedforms as sediment waves but we will adopt the term ***large (>300 m wavelength) sediment wave*** to distinguish them from the small-scale sediment waves outlined previously, again removing relief as a discriminator.

Large-scale scours that comprise enclosed depressions with negative relief are characterised by well-developed closed depressions, which are mainly below the level of the surrounding seafloor. We will simply refer to them as ***scours*** in this contribution. These scours can be found in a variety of forms and can therefore be subdivided into three types: isolated scours, fields of scours (i.e. multiple scours that do

not form a linear train), and linear trains of multiple scours (figure 2.11). It is unclear whether the process that forms the scours forms a continuum with sediment waves, i.e. it is the erosive end member, or alternatively that scours result from erosion into pre-existing seafloor topography.

Scours are found in the following settings: on levees due to flow stripping at channel bends (Fildani et al., 2006), on canyon floors where the canyon goes around a bend (Lamb et al., 2008; Covault et al., 2014), at canyon mouths (Macdonald et al., 2010), in fan valleys and on continental slopes (Shor et al., 1990; Macdonald et al., 2010). Linear trains of scours may also extend up canyon thalwegs (Covault et al., 2014; Zhong et al., 2015).
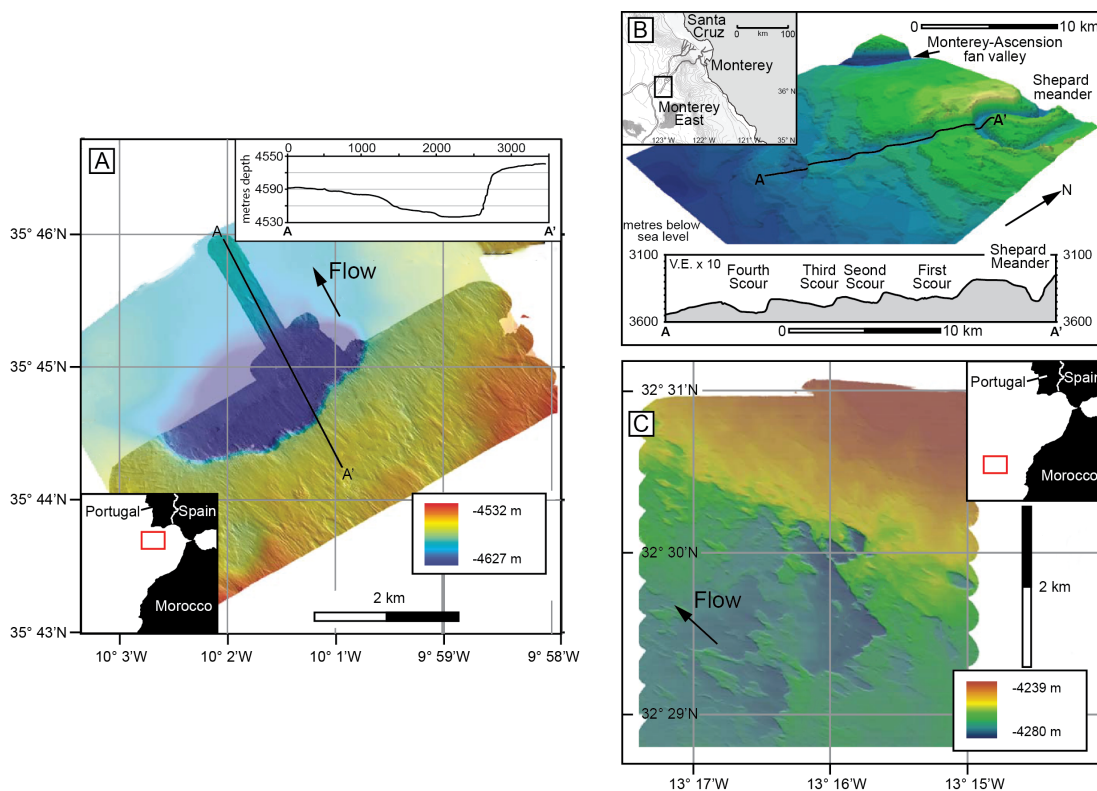
Figure 2.11: Bathymetric examples of large-scale bedforms that comprise enclosed depressions with negative relief (scours). (A) An Autosub6000 image of a single isolated scour in the Horseshoe Valley, offshore southwest Portugal, with depth information derived from autonomous underwater vehicle (AUV) depth profiler data. Inset shows cross-sectional profile of the scour (vertical exaggeration = 11x) (modified from figure 4 of Macdonald et al., 2011). (B) High-resolution Autosub6000 image of a complex field of scours at the Agadir Canyon mouth, offshore northwest Morocco. (C) Shaded relief image (constructed from multibeam bathymetric data) of a linear train of large-scale scour features at Monterey East (modified from figure 4 and 5 of Fildani et al., 2006).

2.4.2   Is the data gap in wavelength and amplitude real?

A statistically significant gap exists between small-scale sediment waves and large-scale sediment waves (figures 2.4-2.6). An important question is whether this data gap occurs because of a sampling bias due to our current methods for collecting seafloor bathymetry or whether there are a range of bedform dimensions that do not exist in nature.

Deep-water bedforms plot largely to the right of the data gap (longer wavelength and wave height) and shallow-water bedforms to the left (shorter wavelength). Therefore, it is possible that the data gap is a result of a sampling bias in which certain water depths have not been sampled. Additionally, the data gap may be a result of current seafloor mapping capabilities, in that we do not capture small-scale bedforms in deeper water due to resolution limitations. Most of the longer wavelength bedforms within this dataset are found in deeper waters (e.g. 3000 m), identified from hull mounted multibeam sonars. The achievable horizontal and vertical resolution of typical sonar systems is ~3.5-20% of water depth and ~0.2-0.8% of water depth respectively (Hughes Clarke, 1998), therefore an achievable lower resolution limit within 3000 m of water is bedforms with 90-600 m wavelength and 6-24 m wave height. These dimensions fall within the data gap and suggests that there may well be a population of bedforms at this scale and have not been resolved yet. With the onset of Autonomous Underwater Vehicle (AUV) based surveys, it may well be that if these surveys begin to explore deeper waters; bedforms of the data gap dimensions may be discovered.

However, plotting the water depth that bedforms occur in against wavelength reveals a continuous distribution with no gap in water depth (figure 2.12). Thus, it is unlikely that the data gap results entirely from sampling bias. Instead we suggest that seafloor bedforms have dimensions that cluster into two modes and that bedforms with wavelengths of 200-300 m coupled with wave heights of 3-10 m are unusual in nature. It may be that the environmental conditions (i.e. confinement) that would lead to bedforms with these dimensions are uncommon in nature (discussed further in section 2.4.4).
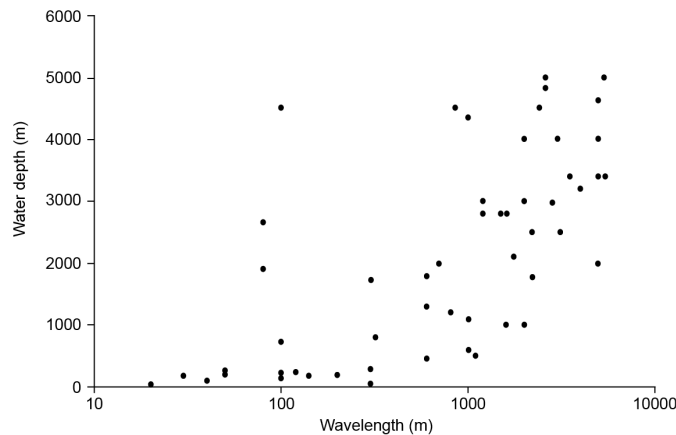
Figure 2.12: Plot of maximum wavelength of bedforms and maximum water depth occurrence. The plot shows a general trend of larger bedforms as water depth increases.

2.4.3   What can the bedforms tell us about flow processes?

We now explore how the three groups of bedforms originate, and what their occurrence reveals about flow processes, including whether the parent flow was subcritical or supercritical.

2.4.3.1   Origin of small sediment waves

The group of small sediment waves includes eight examples that have downslope crescent-shaped crests. The formation of bedforms with crescent-shaped crests has received discussion in the literature (Paull et al., 2010a; Kostic, 2011; Cartigny et al., 2011; Talling et al., 2013). The first hypothesis is that small sediment waves within Monterey Canyon were formed by internal tides (Xu et al., 2008). However, the measured flow speeds (<80 cm/s) (Xu et al., 2008) associated with internal tides would be insufficient to move the sediment sizes found within bedforms at this location, and therefore this hypothesis has thus been discarded.

The second hypothesis is that small sediment waves are generated by liquefaction of the axial channel sediment, and episodic slumping of this coarse channel-fill associated with concave-upwards fault scarps (figure 2.13a; Paull et al., 2010a). It is typical for concave-upward, listric type faults to be arcuate in planform view (Martel, 2004) and therefore provide a crescent-shaped expression (figure 2.13a(i)). The

migration direction for crescent-shaped bedforms has either been demonstrated to be up-current (Hughes Clarke et al., 2014) or is unknown. The problem with invoking just slumping for these bedforms alone is that slumping would cause the bedform crests to migrate downslope under gravity whereas this type of bedform has only been observed to migrate upslope (Smith et al., 2007; Conway et al., 2012; Hughes Clarke et al., 2014). A third hypothesis is that small sediment waves are supercritical-flow bedforms termed cyclic steps (Parker, 1996; Taki and Parker 2005). Cyclic steps are a series of bedform undulations where each undulation is characterised by supercritical flow on their lee side and subcritical flow on their stoss side. Flows are supercritical when inertia dominates over gravity, expressed by the *Froude Number* ($Fr = U/(\sqrt{RCgh})$) exceeding unity (Fr > 1), where U is flow velocity, R is the submerged specific gravity of suspended sediment, C is the layer-averaged volume of suspended sediment concentration, h is flow depth, and g is the acceleration of gravity (Parker, 1996). The subcritical flow on the
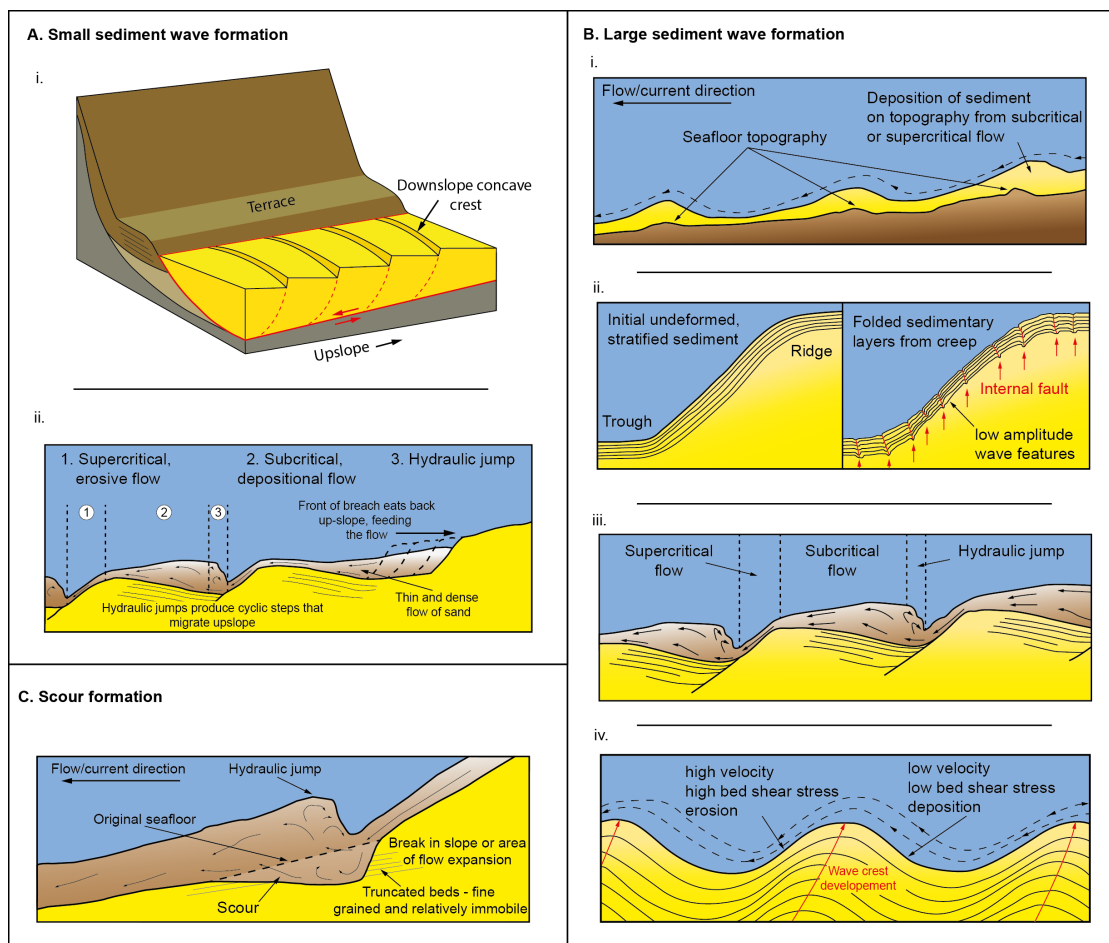
Figure 2.13: (Caption next page.)

Figure 2.13: *(Previous page)* Cartoons of possible mechanisms for bedform formation. (A) Small sediment wave formation. (i) Slumping of channel fill along listric faults could generate asymmetrical bedform shapes with crescentic crests (modified from figure 12 of Paull et al., 2010a). (ii) Asymmetric, small sediment waves can be formed by the upslope migration of cyclic steps. The origin of the thin and dense flow of sediment is from failure on a master scarp (modified from figure 2 of Cartigny et al., 2011 and figure 3 of Van den Berg et al., 2002). (B) Proposed ideas for the formation of sediment waves. (i) The lee wave model (modified from Flood, 1988). Sedimentation from a stratified flow over undulating topography would lead to preferential deposition on the upstream flank. (ii) Kubo and Nakajima (2002) suggest that the formation and migration of small sediment wave fields is a result of topographic effects and possible from subcritical flow, not purely supercritical flow. (iii) Broad crested and narrow troughed wavy stratified sediment can be formed from sediment creep and deformation, with internal faults common in troughs. Sediment creep is initiated on gentle slopes ($<0.5°$) from external triggers such as earthquakes (modified from Lee and Chough, 2001). (iv) Sediment waves are cyclic steps, generated from a thick and tranquil flow (subcritical) on the upslope limb and a swift, shallow flow (supercritical) eroding the downslope limb, bounded by a hydraulic jump (modified from figure 2 of Cartigny et al., 2011). (C) Scour formation. Scours could be generated by erosion due to a hydraulic jump that forms because of flow expansion or a break in slope.

upstream side of the step is thick, tranquil and depositional in contrast to the supercritical flow on the downstream side where the flow is swift, shallow and erosional. The transition from super to subcritical flow is made by a hydraulic jump in the trough of the undulation (Parker, 1996; Taki and Parker, 2005) (figure 2.13a(ii)). Experimental and numerical work have shown how these supercritical flow processes are Froude-scalable between open-channel settings studied by the early workers (Parker, 1996; Taki and Parker; 2005) and turbidity current settings (Kostic and Parker, 2006; Fildani et al., 2006; Spinewine et al., 2009). Later numerical studies have also argued a cyclic step interpretation for what is here defined as small sediment waves (Cartigny et al., 2011; Kostic, 2011). Some authors have gone on to suggest that the turbidity currents must be stratified to explain how thick flows observed in canyons and channels can generate small dimension sediment waves (Talling et al., 2013; Postma and Cartigny, 2014). As stated earlier, the presence of such dense near-bed layers may explain the lack of internal stratification that has been observed in some small-scale sediment waves.

It has also been suggested that the small sediment waves are associated with slope failure, to account for pronounced (master) head scarps seen at the upper end of individual trains of bedforms (Paull et al., 2013). These master headscarps may be

linked to liquefaction of loosely compacted (contractant) sand. Such liquefaction has been seen using remotely operated vehicles (ROVs) and in older studies by divers (Dill, 1964; Paull et al., 2010a; 2014 see supplementary video). Alternatively, more densely packed (dilatant) sand may be linked to up-slope migrating slope failures that are termed breaches (Van den Berg et al., 2002). Indeed, slope failures due to either liquefaction or breaching may generate supercritical sediment flows that create the bedforms as up-slope migrating cyclic steps (Masterbergen and Van den Berg, 2003; figure 2.13a(ii)), in keeping with observations of up-current migrating bedforms at Squamish Delta (Hughes Clarke et al., 2014). Breaching could produce the unusually steep lee faces that small sediment waves exhibit (up to 40°), and has been seen to occur below supercritical flows on lee sides of cyclic steps (Cartigny et al., 2014). Preserving slope angles greater than the angle of repose (~30°) in a non-cohesive sediment is possible if erosion is being limited by breaching (Van den Berg et al., 2002; Cartigny et al., 2011). Talling (2014) suggested that a combination of slope failure, and resulting cyclic steps in supercritical flows, produce small sediment waves.

Eight of the small sediment waves have a sinuous crest. This sinuous crest shape is inconsistent with a slope failure model; therefore it seems most likely that small sediment waves form from the migration of cyclic steps beneath supercritical flows.

2.4.3.2 Origin of large sediment waves

It has been suggested that sediment waves formed beneath turbidity currents or bottom currents can result from the interaction of the flow with pre-existing irregular topography (Cattaneo et al., 2004) such as dunes (Migeon et al., 2001; Nakajima and Satoh, 2001), or hummocky submarine slides (Ercilla et al., 2002). In this model the sediment waves simply exploit and exaggerate this topography, regardless of whether the transporting flow is subcritical or supercritical (Kubo and Nakajima, 2002) (figure 2.13b(i)).

More recently it has been proposed that although pre-existing topography can influence the formation of these turbidity current bedforms, it is not required. Experimental (Spinewine et al., 2009) and numerical work (Kostic and Parker, 2006) have

shown that sustained density flows are prone to form antidunes and cyclic steps without the need for pre-existing topography.

Wave-like topography can also result from soft sediment deformation. This deformation tends to occur where slope gradients and sedimentation rates are high (Lee and Chough, 2001; Wynn and Stow, 2002; Gong et al., 2012). Such deformation may be triggered by a variety of mechanisms, including slope failure, shear force instabilities, earthquake shaking, gravitational instabilities, and gas escape (Faugères et al., 2002; Holbrook et al., 2002; Lee et al., 2002; Gong et al., 2012; Heifetz et al., 2005; Covault et al., 2014) (figure 2.13b(ii)).

Alternatively large sediment waves have been interpreted as supercritical flow bedforms, such as antidunes (Normark et al., 1980) or cyclic steps (Kostic, 2011; Cartigny et al., 2011) (figure 2.13b(iii)). Recent work shows that antidunes and cyclic steps might occur simultaneously, where the antidunes are of a shorter wavelength and symmetrical, superimposed on longer and often more asymmetric undulations that form the cyclic steps (Cartigny et al., 2014; Kostic, 2014; Zhong et al., 2015). Deposition occurs dominantly on the upslope flank and erosion occurs on the downslope flank, resulting in up-current migration of the crest of the bedform (Cartigny et al., 2011). The unconfined setting make these cyclic steps more prone to form a more positive relief in contrast to the small-scale, confined sediment waves, where erosion is thought to play a larger role.

Although, the above mechanisms is appropriate for turbidity currents, large-scale sediment waves formed by weaker and more linear stratified bottom currents have been proposed to be the result of lee-waves triggered by sediment wave crests (Flood, 1988; Blumsack and Weatherly, 1989; Blumsack, 1993). The lee-waves trigger higher bottom current flow velocities on the lee slopes of the sediment waves than those on the stoss slopes results in in development and migration of the sediment waves (or aggradation if velocities are below <9 cm/s) (figure 2.13b(iv)). In contrast to the cyclic step hypothesis where the flow dynamics are controlled by a Froude number and therefore by the flow depth and the average density, the dynamics of lee waves are controlled by the height of the sediment waves and the density gradient (Castro and Snyder, 1993). Lee-waves have also been observed to occur in combination with hydraulic jumps (Hiscott et al., 2013), which might hint at a gradual transition between cyclic steps and lee

waves depending on the nature of the density stratification. A lee-wave model seems a more suitable for large sediment wave generation in areas where weakly stratified bottom currents are prevalent such as the bedforms (in this study) from the Gardar Drift (Manley and Caress, 1994), Gulf of Cadiz (Habgood et al., 2003), Zapiola Drift (Flood and Shor, 1988).

2.4.3.3   Origin of seafloor scours

It is unclear whether isolated scours (figure 2.11a), trains of scours (figure 2.11b) and fields of scours (figure 2.11c) form by similar processes to one another. It is also unclear whether scours are the erosive end members of a continuous process that also forms sediment waves as the depositional end member. Therefore we present two hypotheses that remain to be tested. The first hypothesis is that scours simply form by excavation of an initial bed defect, which may explain the apparently unstructured distribution of some fields of scours. This model does not require the flow to be supercritical, and would most likely involve flows that are thicker than the scour depth. The second hypothesis is that scours are associated with supercritical flows, with isolated scours forming where there is an individual hydraulic jump caused by flow expansion or a break in slope (figure 2.13c); and trains of scours forming from cyclic steps. In this case flows are thought to be smaller or of a similar thickness to the scour in order to induce a hydraulic jump or breaking lee-waves within the scour (Hiscott et al., 2013). Fields of scours are harder to explain with this model. However, it has been suggested that a field of scours may form from flows that are only weakly supercritical which causes a field of hydraulic jumps to form rather than an individual hydraulic jump or linear trains of cyclic steps (Sumner et al., 2013; Hiscott et al., 2013).

2.4.4   Does the data gap result from bimodality in the confinement of different environments?

The distribution of the bedform groups appears to be partly controlled by confinement (figure 2.5), although the possibility that the data gap is a result of data resolution is also considered (see section 2.4.2). Bedforms in the small sediment waves

group are mostly found in canyons and channels, and small scale systems while bedforms in the large sediment waves group are unconfined with no interaction with any lateral container walls (figure 2.5). This confinement also defines what grain sizes are most likely to be found; with coarse sediment (sand and gravel) associated with small sediment waves (Paull et al., 2010a) in confined systems; and fine grain sizes (mud and silt) found in unconfined settings. Previously, it has been hypothesised that the gap between small and large sediment waves is related to flow stratification (Postma and Cartigny, 2014), which builds on an established relationship between supercritical flow discharge and cyclic step lengths (Cartigny et al., 2011; Kostic, 2011). Small discharges associated with just the denser basal layer would form small sediment waves, while in a flow without the denser basal layer it is the full discharge of the much larger dilute flow that dictates the cyclic step length, thereby resulting in large sediment waves.

It therefore appears that small sediment waves are probably mainly formed by stratified flows in confined setting, and internally consist of coarse sediment and massive facies that are deposited from dense basal layers. Large sediment waves form in dilute unstratified flows in unconfined setting, where grain sizes are much finer and internal structures can develop due to turbulent tractional sediment transport.

2.4.5   How widespread are supercritical flows?

Up-current migration is typical of bedforms generated by supercritical flows. Other mechanisms such as slumping and subcritical flow would tend to produce down current migrating bedforms (e.g. Carling and Shvidchenko, 2002). Supercritical flows are typically associated with confined systems whereas subcritical flows are associated with more open systems. Therefore it might be assumed that the small sediment wave group results from supercritical flows, whereas the large sediment waves result from subcritical flows, reflecting the bimodality in confinement between the bedform environments. However, figure 2.14 shows a surprisingly widespread distribution of bedforms with up-current migrating crests, identified from the subsurface expression of crest position over time on seismic images. The identification of widespread up-current migrating crests in multiple environments and between bedform groups suggests that supercritical
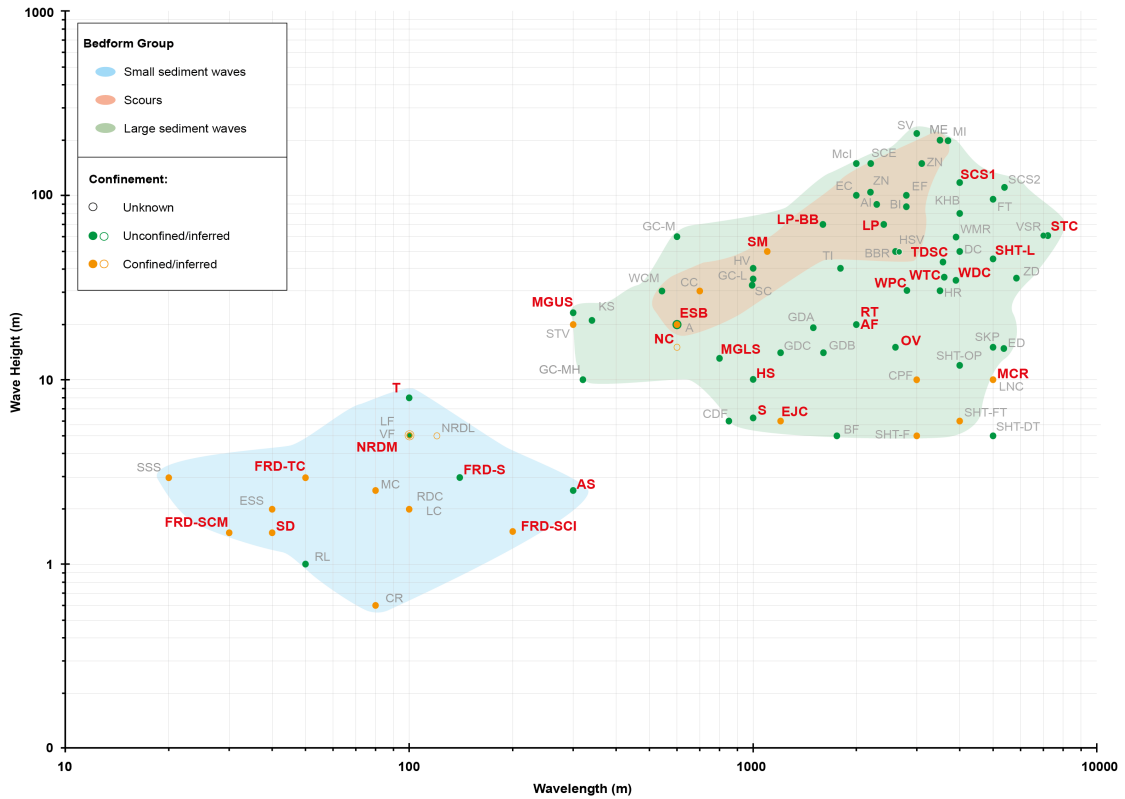
Figure 2.14: Plot of wavelength versus amplitude of bedforms with logarithmic axes. Bold red labels highlight the bedforms that exhibit upslope migrating crests.

bedforms may be more prevalent than previously thought. However, we note that we do not have migration direction for 53 of our cases and furthermore there are cases where up-current migration would be unlikely – e.g. for large sediment-waves formed beneath bottom currents. However, the data suggests a possible continuum of supercritical bedforms over a range of environments; this is supported in specific locations (e.g. Monterey Canyon) where small sediment waves are seen to evolve into large sediment waves down system in response to channel broadening (figure 2.15).

2.4.5.1 Do small sediment waves, large sediment waves and scours form a continuum of supercritical bedforms?

Given that supercritical flows appear to be widespread between different environments and bedform types, an even broader continuum of bedform types that include small sediment waves, large sediment waves, and some of the linear trains of scours could exist (figure 2.11b). The small and large sediment waves can be formed by the interplay

of erosion and deposition over a cyclic step, being either transportational (Parker and Izumi, 2000) or net-depositional (Kostic, 2011). Additionally, bedforms associated with cyclic steps in supercritical flows can be net erosional, as seen in rivers and laboratory experiments (Parker and Izumi, 2000; Fagherazzi and Sun, 2003; Kostic and Parker, 2006; Kostic et al., 2010), therefore extending the cyclic step hypothesis into cyclic scours. Here we group such continuum of depositional, transportational and erosional cyclic steps under the wider term ***supercritical flow bedforms*** (figure 2.16) that also includes antidunes, and seem closely related to the lee-wave processes described for weakly stratified bottom currents.

A more conservative view leave scours out of the supercritical flow continuum because their migration direction is either unknown (Shor, 1990; Macdonald et al., 2010) or ambiguous from the data that is available (Covault et al., 2014). Albeit the limited
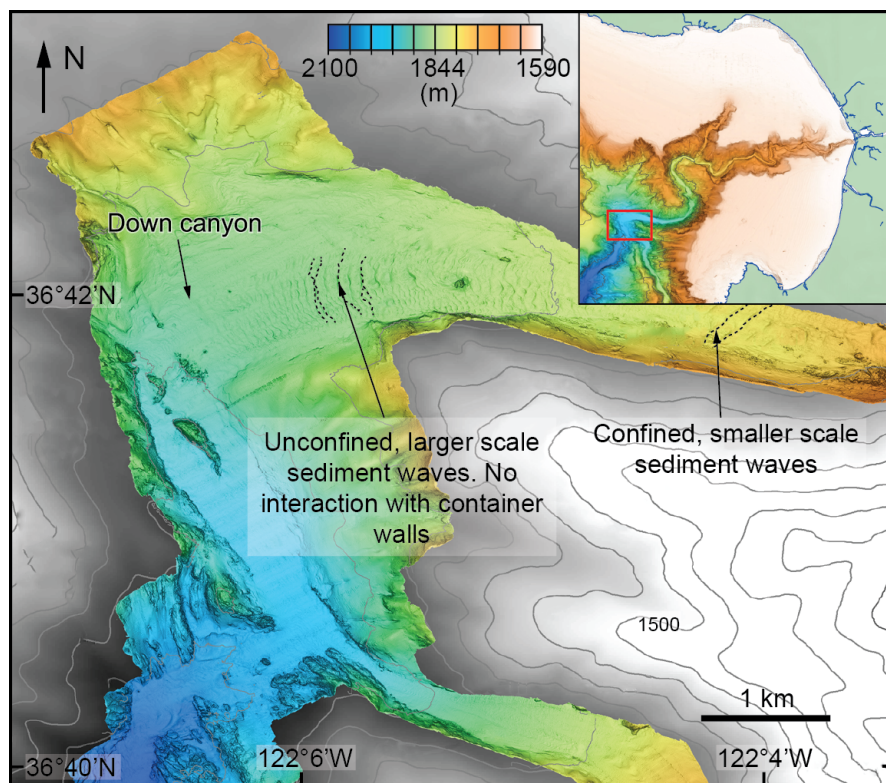
Figure 2.15: Map showing multibeam data from Monterey Canyon between 1723 m and 2066 m water depth that was collected using an autonomous underwater vehicle (AUV). The image shows that where the axial channel broadens from ∼350 m to ∼1000 m the bedforms increase in size and their crest shape changes because they are no longer confined by the channel (modified from figure 11 of Paull et al., 2011).

amount of data available for scours from direct field measurements and laboratory experiments shows scours to be associated with hydraulic jumps and thus supercritical flows (e.g. Hiscott et al., 2013; Sumner et al., 2013). Of the various types of scours, linear trains of depressions are most easily linked to cyclic steps in supercritical flow but may similarly result from excavation of initial bed defects by a subcritical flow with high enough shear stresses. So it is again uncertain whether the trains of scours are a signature of supercritical flows and cyclic steps.

2.4.5.2 Origin of different bedform groups – a summary

Statistical analysis confirms that bedforms tend to cluster within three morphological groups (figure 2.6). These groups comprise small sediment waves, large sediment waves, and scours. There is a data gap within the wavelength and wave height of these
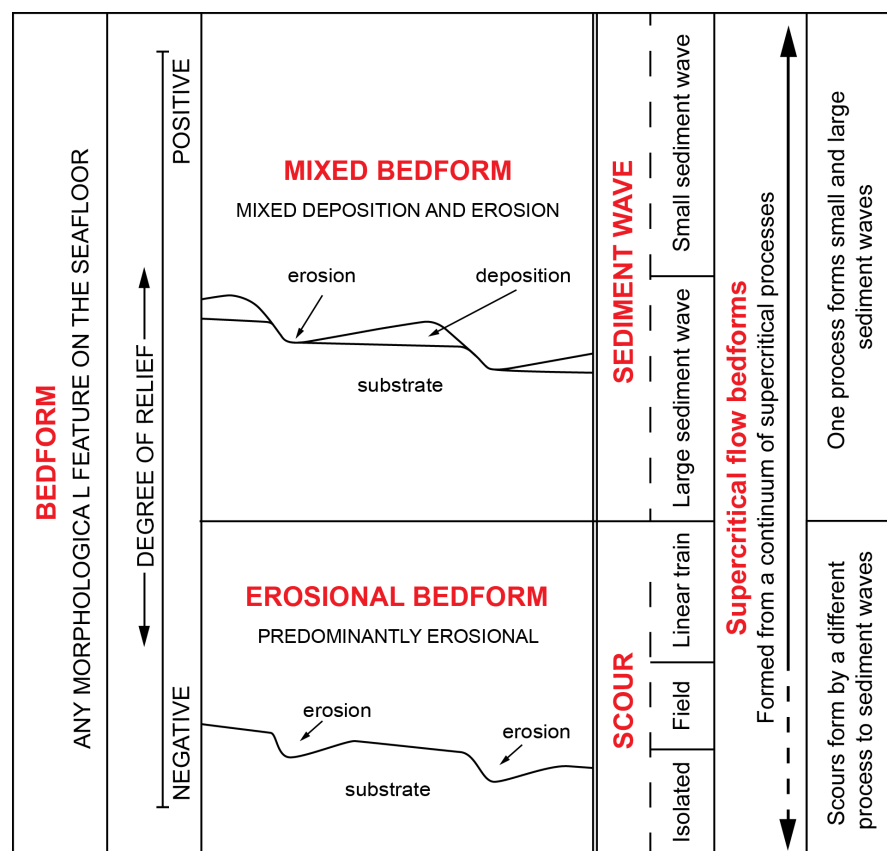
Figure 2.16: Classification of seafloor bedforms with the new terminology introduced in this study. A continuum of supercritical bedforms is shown along with an alternative hypothesis whereby the mechanism for scour formation is unknown and may result from process other than supercritical flows.

bedforms, which separates the first group (small sediment waves) from the second and third groups (large sediment waves and scours). Our analysis suggests that this gap most likely results from bimodality in container shape such that flows are either confined or unconfined.

Up-current migration of bedforms most likely results from supercritical flow. Our study shows that up-current migrating bedforms are common and widespread, and comprise both the smaller and larger modes of wavelength and wave height. This suggests that supercritical flow can be associated with generating individual bedforms in both the small sediment wave and large sediment wave groups, although we do not dismiss other formative mechanisms for individual bedforms. The migration direction of scours is not known, and it is therefore harder to assess whether they area always associated with supercritical flow.

2.4.6   Are the conclusions of Wynn and Stow (2002) still valid?

This study of 82 examples from a wide range of settings and water depths broadly supports the observations and conclusions made by Wynn and Stow (2002). Coarse-grained turbidity current sediment waves have maximum wavelengths of 1000 m and maximum wave heights of 10 m as outlined by Wynn and Stow (2002). Coarse-grained systems plot to the left of the data gap and fine-grained systems plot largely to the right of the data gap, thus the distributions of this study largely agree with Wynn and Stow (2002). More data was available for this study than was available to Wynn and Stow (2002) a decade ago, which has resulted in a much wider range of bedforms (small and larger sediment waves, scours), from different environments and water depths being included. By proposing a correlation between confinement and the scale of sediment waves we are able to suggest why the bedforms cluster in to two distinct scales, a step that Wynn and Stow (2002) were unable to take. The increase in examples has also enabled us to identify a small number of outliers that do not conform with the boundaries defined by Wynn and Stow (2002) for coarse-grained turbidity current sediment waves, and thus extending their coarse-grained turbidity current formed sediment wave maximum wavelengths from 1000 m to 4000 m.

2.5   Conclusions

Three statistically significant groups of bedforms are recognised in our analysis of a global dataset of 82 examples, taking into consideration bedform morphology and environment:

i. ***Small sediment waves*** are small-scale (<300 m wavelength and <8 m wave height) bedforms with mixed relief, and are restricted to confined settings (channels and canyons). They tend to have downslope crescentic crests, are formed of coarse grains (sand-gravel) and can lack internal stratigraphy.

ii. ***Large sediment waves*** are the most wide-ranging bedforms in dimension (up to 7200 m wavelengths and 220 m wave heights) and exhibit mixed relief compared to the overall slope. Large sediment waves are typically located in relatively unconfined settings where they are characterised by straight to sinuous crests. Large sediment waves tend to be composed of fine-grained but mobile sediment. Additional large sediment waves with more crescentic crests are observed in confined settings.

iii. ***Scours*** are large-scale (up to 3000 m long and 200 m deep) bedforms with negative relief, which have well developed enclosed depressions that lie below the height of the surrounding seafloor. They often occur in areas of flow expansion and have eroded into cohesive, fine-grained sediment.

Our study shows that bedform dimensions (wavelength and wave height) have two modes with an intervening data gap (figure 2.4-2.5). This bimodality appears to result mainly from container shape, such that bedforms with smaller dimensions occur in confined settings (canyons and channels) whilst larger bedforms occur on open slopes. Bedforms that migrate up-current most likely result from supercritical flows and have been shown to be widespread across a range of scales and settings suggesting a continuum of process; it remains unclear whether scours also form part of this continuum.

This review of a novel global database of seafloor bedforms broadly agrees with the conclusions of a previous study on deep-sea seafloor bedforms (Wynn and Stow, 2002) but may stimulate further work that takes advantage of new mapping and flow

monitoring techniques to test these competing hypotheses.

Chapter 3

A new model for turbidity current behaviour based on integration of flow monitoring and precision coring in a submarine canyon

Symons, W.O[1]., Sumner, E.J[1]., Paull, C.K[2]., Cartigny, M.J.B[3]., Xu, J[4]., Maier, K.L[5]., Lorenson, T.D[5]., Talling, P.J[3]., 2017. A new model for turbidity current behavior based on integration of flow monitoring and precision coring in a submarine canyon. Geology 45, 367-370.

[1]*School of Ocean and Earth Science, University of Southampton*
[2]*Monterey Bay Aquarium Research Institute*
[3]*Departments of Earth Science and Geography, University of Durham*
[4]*College of Marine Geosciences, Ocean University of China*
[5]*United States Geological Survey*

Abstract

Submarine turbidity currents create some of the largest sediment accumulations on Earth, yet there are few direct measurements of these flows. Instead, most of our

understanding of turbidity currents results from analysing their deposits in the sedimentary record. However, the lack of direct flow measurements means that there is considerable debate regarding how to interpret flow properties from ancient deposits. This novel study combines detailed flow monitoring with unusually precisely located cores at different heights, and multiple locations, within Monterey Submarine Canyon. Dating demonstrates that the cores include the time interval that flows were monitored in the canyon, albeit individual layers cannot be tied to specific flows. There is good correlation between grain sizes collected by traps within the flow and grain sizes measured in cores from similar heights on the canyon walls. Synthesis of flow and deposit data suggests that turbidity currents sourced from the upper reaches of Monterey Canyon comprise three flow phases. Initially, a thin (38-50 m) powerful flow in the upper canyon can transport, tilt and break the most proximal moorings and deposit chaotic sands and gravel on the canyon floor. The initially thin flow front then thickens and deposits interbedded sands and silty-muds on the canyon walls up to 62 m above the canyon floor. Finally, the flow thickens along its length thus lofting silty mud and depositing it at greater altitudes than the previous deposits and in excess of 70 m altitude above the local thalweg.

3.1   Introduction

Turbidity currents are energetic gravity-driven flows that dominate sediment transport across large expanses of seafloor and play an important role in global carbon burial. Turbidity currents can break seafloor cables (e.g. Grand Banks (Heezen and Ewing, 1952; Piper et al., 1999)) and pipelines, resulting in millions of dollars being spent rerouting pipelines (e.g. Cooper at al., 2012). The fundamental nature of turbidity currents is poorly understood because of a paucity of direct observations which results from difficulties in measuring these often destructive flows (Xu, 2010; Liu et al., 2012). As a result, most of our understanding of turbidity currents results from interpreting the deposits that they leave behind in the sedimentary record (e.g. Pirmez and Imran, 2003; Talling et al., 2012; Hubbard et al., 2014). However, the validity of such interpretations remains controversial, due to a lack of field datasets that include both flow and deposit

measurements (e.g. Puig et al., 2003; Khripounoff et al., 2009).

This study is novel because it combines some of the most detailed direct measurements from turbidity currents (Xu et al., 2004, 2014) with a new set of precisely located core transects through their deposits. We extend the previous analysis of monitoring data by Xu et al. (2004, 2014) by also documenting patterns of mooring tilt and movement. We show that the new cores contain the monitored flows, although age control does not allow individual deposits to be linked to specific flows. The aims of this study are to evaluate how well deposits record flow properties, and produce a new model of turbidity current evolution that combines both flow measurements and deposits.
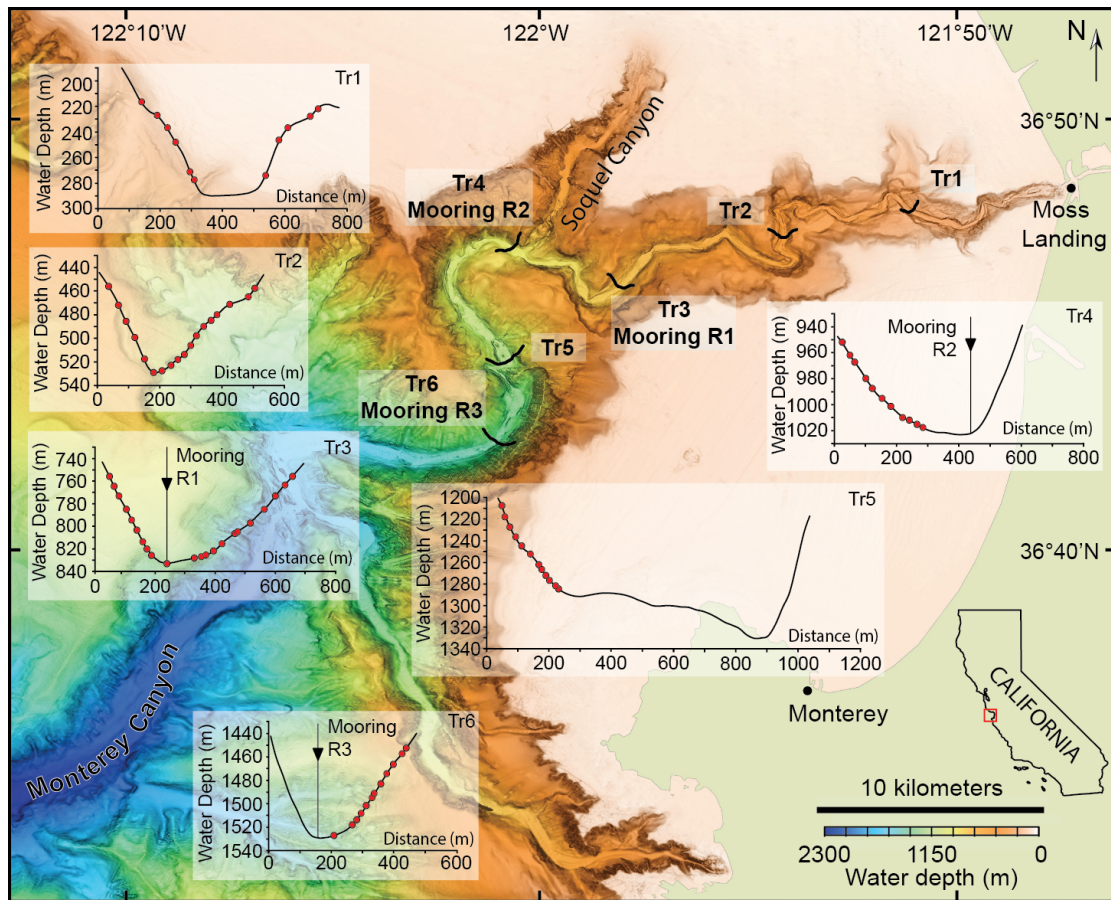
Figure 3.1: Map showing the bathymetry of Monterey Bay and Monterey Canyon (Modified after Paull et al., 2010a). Included are the cross-sections (looking down-canyon) of Monterey Canyon at Tr1-6 and their positions within the canyon. On each cross-sectional profile is the position of each core on the canyon wall used in the study (red dot). On Tr3, Tr4, and Tr6 is the approximate position of the USGS sediment trap (black triangle).

3.1.1 Characteristics of turbidity currents in Monterey Canyon based on monitoring studies

Multiple turbidity currents occur in Monterey Canyon each year (Xu et al. 2004; Paull et al., 2010a). It is rare for turbidity currents in this canyon to extend beyond 2000 m water depth (Xu, 2011), with the last event to pass Shepard Meander (3400 m water depth, 36°13'00"N, 122°52'00"W) occurring 150 years ago (Johnson et al., 2005). Most flows have not been monitored in detail but instead are known to have occurred because they damaged seafloor equipment (e.g. Paull et al., 2010a). Only four turbidity currents have been previously monitored in detail and at multiple locations in Monterey Canyon (Xu et al. 2004, 2014; Xu 2010). These turbidity currents were monitored using three U.S. Geological Survey (USGS) moorings located in the canyon thalweg at water depths of 820 m (R1), 1020 m (R2), and 1445 m (R3) that were deployed from December 2002-November 2003 (figure 3.1; table 3.1) (Xu et al., 2004). Whilst the instruments were only deployed for 12 months, this is the best available dataset to assess the characteristics of turbidity currents in Monterey Canyon and how much variability exists among flows. These datasets are probably typical of the frequency of small events that fill the canyon; larger flows must occasionally occur that flush sediments onto the submarine fan.

Three of the four turbidity currents originated in Monterey Canyon, and one flow was sourced from Soquel Canyon (figure 3.1). The turbidity current from Soquel Canyon exhibits different characteristics (Xu et al., 2004; 2014), probably because Soquel Canyon is finer-grained than Monterey Canyon (Paull et al., 2005). We therefore focus our analyses on the three turbidity currents sourced from Monterey Canyon. All of these three turbidity currents had a thin flow front at the shallowest mooring and thickened through time and downstream as shown by Xu (2010). The thin flow front was evident at the second mooring but not at the deepest mooring. The longevity of this thin flow front varied from 1 to 6 hours among the different flows (table 3.2). The maximum thickness of the flows was 48 to 59 m. The three turbidity currents had broadly comparable maximum hourly velocities of 1-2 m s^{-1} at each mooring (table 3.2). The run out distances of the turbidity currents are variable: two of the flows pass all moorings, whereas the second Monterey Canyon flow did not reach the deepest mooring.

Mooring	Water depth	Latitude	Longitude
R1	820	36.77167	121.9632
R2	1020	36.78033	122.0135
R3	1445	36.7195	122.0125

Table 3.1: Table of US Geological Survey moorings placed within Monterey Canyon in 2002.

We now focus on the second turbidity current (TC2) from Monterey Canyon because it was the only event captured at all three moorings and is the only event from Monterey Canyon with grain size data from sediment traps. This turbidity current is intermediate in thickness between the two other flows. The speeds and dimensions of the other two flows are summarized in table 3.2.

Turbidity current	Date	Source	Trigger	Mooring R1			Mooring R2			Mooring R3		
				Time (hr)	Thickness (m)	Max speed (cm/s)	Time (hr)	Thickness (m)	Max speed (cm/s)	Time (hr)	Thickness (m)	Max speed (cm/s)
TC1	17/12/2002	Soquel canyon	Storm activity that caused failure of the canyon floor or wall	*Not recorded at mooring as Soquel tributary intersects Monterey Canyon downstream of R1*			1	30.2	60	4	57.1	75
							2	24.2		5	50.2	
							3	34.6		6	48.2	
							4	39.7		7	54.7	
							5	27.2		8	39.8	
										9	26.7	
TC2	20/12/2002	Monterey Canyon	Storm activity transported large amounts of sediment to the canyon head which failed under wave loading	1	23.9	190	1	37.5	160	2	31.1	180
				2	33.0		2	38.2		3	55.6	
				3	35.1		3	43.2		4	58.1	
				4	34.1		4	48.5		5	52.5	
				5	29.2		5	51.3		6	55.1	
				6	38.2		6	33.1		7	53.5	
				7	51.4					8	53.5	
				8	55.5					9	37.0	
										10	25.8	
TC3	14/03/2003	Monterey Canyon	Anthropogenic. Dredged material dumped at the head of Monterey Canyon	1	32.4	160	2	32.2	105	*Turbidity current did not reach mooring*		
				2	33.6		3	32.3				
				3	39.9		4	42.5				
				4	38.2		5	45.9				
				5	45.6		6	47.7				
				6	53.7							
TC4	19/11/2003	Monterey Canyon	Unknown	*Turbidity current broke mooring*			1	41.8	155	3	46.3	110
							2	46.5		4	56.0	
							3	49.7		5	58.0	
							4	51.9		6	58.5	
							5	52.4				
							6	52.9				
							7	49.3				

Table 3.2: Characteristics of the four monitored turbidity currents (Xu et al., 2004; Xu 2010). Flow thicknesses were determined from the ADCP velocity profiles (Xu, 2010).

3.2 Methods

3.2.1 Core collection

In April and October 2014, core transects were collected in Monterey Canyon at water depths of 275 m (Tr1), 530 m (Tr2), 830 m (Tr3), 1020 m (Tr4), 1280 m (Tr5), and 1525 m (Tr6) (figure 3.1). Data were collected using a 25 cm long push corer deployed from Monterey Bay Aquarium Research Institute's remotely operated vehicle (ROV) *Doc Ricketts*. This ROV-deployed coring system enables location of cores at different heights above the thalweg to a level of precision that cannot be achieved using traditional wireline coring techniques. Across canyon transects comprised up to 12 push cores and included samples from the thalweg, terraces (raised plateaus between the incised thalweg and canyon wall), and the canyon walls up to an altitude of 70 m above local thalweg (m-alt) (figure 3.1). The facies in the push cores were visually analyzed and then sampled for grain-size and ^{210}Pb analyses. Grain-size analyses were conducted using the same laser particle size analyser used for the 2002 sediment trap data (Xu et al. 2014).

Table 3.3: Table of push cores used with altitude on the canyon wall and geographical location.

Transect	Core number	Altitude (m)	Latitude	Longitude
Tr1 north wall	DR681 PsC 53	0.03	36.794487	121.844739
	DR681 PsC 42	27.76	36.794934	121.844696
	DR681 PsC 54	36.59	36.795153	121.844639
	DR681 PsC 67	44.56	36.795684	121.844428
	DR681 PsC 57	53.26	36.796102	121.844332
	DR681 PsC 70	57.10	36.797717	121.843964
Tr1 south wall	DR683 PsC 57	0.01	36.792304	121.845408
	DR683 PsC 63	6.85	36.792202	121.845399
	DR683 PsC 58	30.59	36.791763	121.845488
	DR683 PsC 75	41.30	36.791545	121.845518
	DR683 PsC 42	51.15	36.791294	121.845608
	DR683 PsC 52	62.19	36.79068	121.845698

Table 3.3 – *Continued from previous page*

Transect	Core number	Altitude (m)	latitude	Longitude
Tr2 north wall	DR677 PsC 78	0.01	36.788592	121.902991
	DR677 PsC 54	7.76	36.788581	121.903618
	DR677 PsC 43	17.07	36.788658	121.904332
	DR677 PsC 70	30.77	36.788602	121.904764
	DR678 PsC 43	46.14	36.788549	121.90533
	DR678 PsC 78	59.45	36.788628	121.906063
	DR678 PsC 72	71.98	36.788588	121.907336
Tr2 south wall	DR687 PsC 58	0.00	36.788719	121.9029
	DR687 PsC 47	13.05	36.788624	121.902603
	DR687 PsC 64	30.99	36.788799	121.902321
	DR687 PsC 74	44.32	36.788723	121.901854
	DR687 PsC 56	59.20	36.788789	121.901603
	DR687 PsC 45	72.91	36.788781	121.901226
Tr3 north wall	DR585 PsC 64	1.37	36.76513	121.969405
	DR585 PsC 79	7.74	36.765919	121.969977
	DR585 PsC 74	21.91	36.766338	121.970698
	DR586 PsC 56	35.07	36.767173	121.971071
	DR586 PsC 67	56.76	36.767823	121.971461
	DR586 PsC 60	74.93	36.768652	121.971543
Tr3 south wall	DR685 PsC 49	0.01	36.764466	121.968944
	DR685 PsC 64	8.20	36.764101	121.968603
	DR680 PsC 47	11.68	36.764026	121.968444
	DR680 PsC 64	28.96	36.763797	121.96822
	DR685 PsC 77	49.44	36.763424	121.967913
	DR685 PsC 51	70.26	36.763126	121.967586
	DR685 PsC 80	78.38	36.762994	121.967471
Tr4 north wall	DR589 PsC 77	2.00	36.781507	122.016136
	DR589 PsC 75	4.36	36.781083	122.016472
	DR589 PsC 71	15.51	36.780547	122.016652
	DR590 PsC 75	28.67	36.779837	122.017104
	DR590 PsC 51	36.59	36.779565	122.017242
	DR590 PsC 52	48.64	36.779321	122.017397
	DR590 PsC 62	64.44	36.77891	122.017268
Tr5 south wall	DR591 PsC 47	9.83	36.734525	122.013342
	DR591 PsC 43	13.32	36.734721	122.013248
	DR591 PsC 75	0.41	36.734157	122.014367
	DR592 PsC 56	38.70	36.735102	122.012422

Continued on next page

Table 3.3 – *Continued from previous page*

Transect	Core number	Altitude (m)	latitude	Longitude
	DR592 PsC 44	53.58	36.735316	122.01206
	DR592 PsC 55	71.81	36.735545	122.01179
Tr6 north wall	DR679 PsC 64	0.00	36.702313	122.02049
	DR679 PsC 79	5.33	36.702505	122.020895
	DR679 PsC 63	11.49	36.702728	122.021185
	DR679 PsC 76	21.37	36.703056	122.021483
	DR682 PsC 76	44.09	36.703305	122.021926
	DR682 PsC 46	58.08	36.703521	122.022221
	DR682 PsC 41	74.55	36.703783	122.022662

3.2.2 Flow thickness

Data from the USGS mooring (Xu et al. 2004, 2014; Xu, 2010) was used to characterise spatial and temporal changes in the thickness and grain size of sediment in the flow. We use the flow thicknesses calculated by Xu (2010) (table 3.2).

3.2.3 Grain-size analysis

Two samples were taken from each push core: (i) the slice with the coarsest material and (ii) the slice that visually appeared to contain the finest sediment. Grain-size analysis was conducted on a sub-sample of the 1 cm push core slices.

To ensure that the results of this study were directly comparable to those within Xu et al (2014), grain-size analysis was undertaken on the same Beckman Coulter LS230 laser diffraction particle size analyser, located at the USGS field office in Santa Cruz, California. Sample preparation also followed the same process used by Xu et al. (2014) and is outlined below.

Approximately 20 g of sediment was placed into individual 1000 mL beakers where 10 mL of 35% hydrogen peroxide (H_2O_2) was added along with sufficient distilled (DI) water to make a 300 mL solution. This solution was left overnight in order to remove organics and begin the process of sample dispersion. The following day, the

samples were placed onto a hotplate set at 250-300°C for 2-3 hours, or until the solution was concentrated to 200 mL: this ensures that any hydrogen peroxide was removed. Following this, each beaker was placed into an ultrasonic bath for 10 minutes to continue the disaggregation of fine mud particles.

The removal of soluble salts required two runs in a centrifuge. Samples were transferred into 250 mL centrifuge bottles. The bottles were weighed and in pairs, topped up with DI water to within 0.1 g of each other. Each bottle within a pair was placed opposite each other within the centrifuge to ensure it was correctly balanced. Samples were centrifuged initially for 1 hour at 1700 rpm. After this initial run, samples were removed and the supernate removed without losing sample before samples were re-weighed while adding DI water for a second 30 minute run at 1700 rpm. Following this, each sample had 5 mL of sodiumhexametaphosphate (calgon) added to disperse negatively charged clay particles. To ensure the weight of the calgon was accounted for, three aluminium trays were weighed before 5 mL of calgon was added and left to dry overnight in the oven.

Wet sieving was used to separate the sand and silt (2000-63 μm) fraction from the fines and mud fraction (<63 μm). Samples were washed: sand and silt sized grains were trapped in the sieve stack. Sand and silt were washed from the sieve and transferred into a crucible and then dried in an 80-110°C oven overnight. Each graduated cylinder was topped up with DI water to 1000 mL and left overnight.

The weight of each sample (both the dried sand and silt weight and the fines) was determined. The dry sand and silt were weighed and recorded. The dried weight of 20 mL of the fines solution was determined by drying the solution in an oven overnight and deducting the known weight of the calgon.

The Coulter counter was operated using the same protocol and parameters as described in Xu et al (2014). Approximately 1-2 g of sample was needed, with finer - grained samples requiring less sediment to achieve the correct light obscuration. If the sample exceeded this 1-2 g guide, then it was split using a sand splitter before being added to the Coulter chamber. Most samples were run using an obscuration of ~30%. It was necessary to run some samples with an obscuration as low as 4%. For the fine samples, the sample was transferred to a beaker and agitated using a motorised

stirrer in order to achieve a homogeneous suspension. After two minutes of stirring a sample was taken using a pipette and added into the Coulter chamber. Each sample was passed through the counter three times, although the first run was discarded, because air bubbles were often present. The second and third runs were compared and if similar, then results were averaged. Between each run, the system was flushed to ensure no residual grains from the previous sample remained in the system. The coarse and fine samples, from a single grain-size sample (i.e. one push core slice), were combined using the bespoke USGS software, pc SDSZ, at the end of each run.

3.2.4 ^{210}Pb analysis

The flow measurements and samples were collected 12 years apart. We do not aim to identify the precise deposits laid down by the flows in 2002/2003. Instead we use ^{210}Pb analysis to assess whether the time interval represented by the cores encompasses the time period from 2002 to 2003 and note that deposit characteristics are consistent throughout the depth of each core.

Sediment accumulation rates and ages were constrained by analysing for unsupported (excess) ^{210}Pb. ^{210}Pb is a naturally occurring radionuclide of the ^{238}U radioactive decay chain. Supported ^{210}Pb is derived from its parent radionuclide, ^{226}Ra ($t_{1/2} = 1600$ years), within the sediment and is in secular equilibrium with its precursors in the ^{238}U decay series. In contrast, unsupported ^{210}Pb is formed by the decay of atmospheric ^{222}Ra ($t_{1/2} = 3.8$ days) and accumulates in sediments through adsorption on suspended particulates (Swarzenski, 2014). ^{210}Pb has a half-life of 22.3 years and can therefore be used to establish sediment accumulation rates over the past 100-150 years.

The ^{210}Pb activity of samples was measured using gamma spectrometry at the USGS laboratories in Menlo Park, California. A 1 cm slice from the highest altitude push core ($\sim$70 m altitude) at each transect was used for the ^{210}Pb analysis. In the laboratory the samples where dried in an oven at 55°C over five days. The samples were weighed before and after drying to determine wet and dry sample weight, and sample porosity. Each dried sample was pulverized by hand using a ceramic mortar and pestle. The resulting powered-sediment was transferred to a scintillation vial and sealed, with

the mass also noted.

1 or 2 centimeter intervals of sediment were counted in a calibrated high-purity Ge well-type gamma detector using the 46.52 keV (^{210}Pb), 351.87 and 609.31 keV (^{226}Ra) and the 661.6 keV (^{137}Cs) gamma energies. Precision in the activities of ^{210}Pb, ^{226}Ra, and ^{137}Cs were better than 5%. Excess ^{210}Pb derived geochronologies were calculated by deriving the inventories (I) of ^{210}Pb$_{xs}$, ^{137}Cs, and ^{226}Ra using the following relationship:

$$I(dpm.cm^{-2}) = An.M \tag{3.1}$$

where M is the cumulative mass (sum of mass depth in each layer) for each depth interval (g cm^{-2}), and An is the activity of each nuclide (i.e., ^{210}Pb$_{xs}$, ^{137}Cs, or ^{226}Ra) per cumulative mass. The cumulative mass was calculated by adding the mass from each layer equivalent to the mass depth. Further details of these methods can be found in Swarzenski et al., 2006.

As several samples were taken at different depths within a core, sedimentation rates were calculated using a constant rate of supply method (Appleby and Oldfield, 1978), and is defined by:

$$C_d = C_0 e^{-kt} \tag{3.2}$$

Where Cd is the activity of ^{210}Pb at depth d, C_0 is the activity of ^{210}Pb at the core top (i.e. initial concentration of unsupported ^{210}Pb), k is the decay constant for ^{210}Pb (0.031), and t is the sedimentation rate. Least squares regression was used to establish the sedimentation rate of Ln(^{210}Pb$_{xs}$) as a function of depth.

3.3   Results

3.3.1   Sedimentary facies

The push cores contain five different sedimentary facies (figure 3.2):

i. **Indurated substrate:** *Indurated Substrate* is firm mud that may be homogeneous or contain rip-up clasts.

ii. **Chaotic sand and gravel:** This facies comprises poorly sorted clean sands and gravel overlain with a drape of soft mud.

iii. **Clean sand:** These are moderately to well sorted fine-medium sands that may be ungraded or normally graded (figure 3.2a).

iv. **Interbedded sand and silty mud:** This facies comprises fine sands interbedded with silty mud, the sand laminae/beds range in thickness from 5 mm to 6 cm (figure 3.2b).

v. **Silty mud:** Silty mud comprises homogeneous or bioturbated silty mud (figure 3.2c).
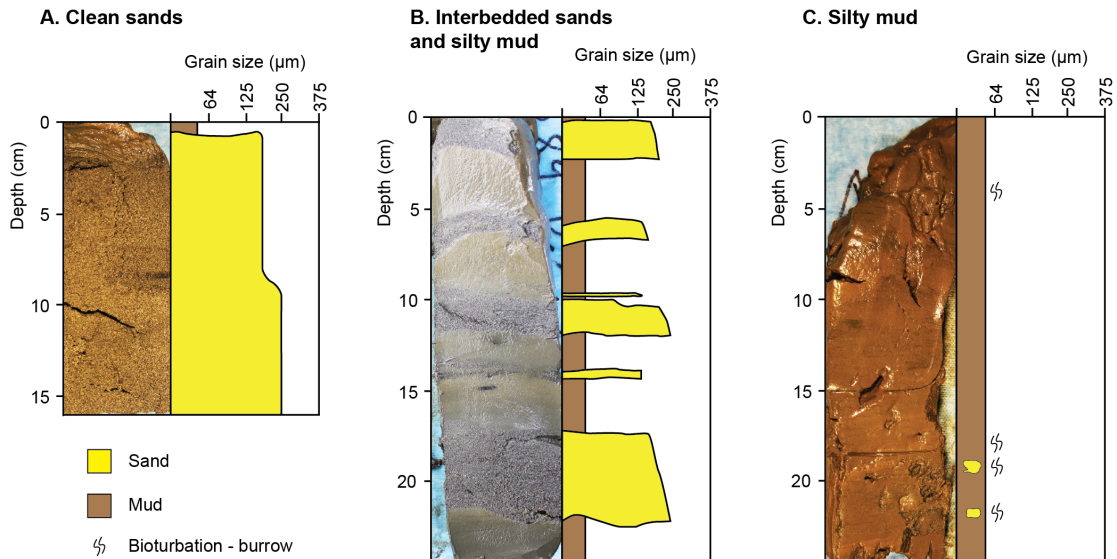
Figure 3.2: Graphical logs and images of three facies collected from Monterey Canyon

3.3.2 Facies distribution per transect

We now describe the lithofacies seen in transects (Tr) of cores collected along canyon floors and walls. (figure 3.3).

Tr1 No recent deposits are seen below 40 m-alt, instead indurated substrate is recorded on the steep (∼27°) canyon walls; silty mud crops out 40 m-alt (figures 3.3b). The maximum grain size recorded on the canyon walls is 200 μm. Previous studies have identified chaotic sand and gravel within the thalweg (Paull et al., 2010a).

Tr2 - Clean sands with grain sizes up to 500 μm crop out up to 6 m-alt; above 6 m-alt interbedded sand and silty mud crops out with silty mud >29 m-alt (figure 3.3b).

Tr3 - This is the first location where coincident flow measurements and deposit samples exist. Chaotic sand and gravel and clean sand, with grain sizes up to 600 μm, crop out up to 1.5 and 7.5 m-alt respectively. Above this interbedded sand and silty mud crops out up to 35 m-alt with silty mud reaching 75 m-alt (figure 3.3b).

Tr4 - Chaotic sand and gravel and clean sand, with grain sizes up to 500 μm crop out at 2 and 4.5 m-alt respectively. Above this, interbedded sand and silty mud crops out 48.5 m-alt; above which silty mud crops out (figure 3.3b).

Tr5 - At Tr5 there are no chaotic sand and gravel or clean sand facies. Interbedded sand and silty mud with a maximum grain size of 300 μm crops out 62 m-alt. Above this, silty mud crops out (figure 3.3b).

Tr6 - At the most distal transect (Tr6), no coarse-grained facies are present. Interbedded sand and silty mud with a maximum grain size of 200 μm crops out 30 m-alt with silty mud above this up to 74 m-alt (figure 3.3b).

3.3.3   Do the push cores contain deposits from the 2002 flow events?

^{210}Pb dating was used to establish the time interval represented by deposits in the push cores. Most ^{210}Pb profiles show non-steady-state deposition; where steady-state does occur (Tr4) a sedimentation rate of 0.24 cm yr^{-1} is calculated (figure 3.4). Identifying specific turbidity current deposits from 2002/2003 in the cores is beyond the resolution of the dating technique. However, based on sedimentation rates, the sediments in these cores include the time period between 2002 and 2003. Furthermore, these cores have similar characteristics throughout their depth.

3.3.4   Comparison of grain sizes in sediment traps and canyon-wall deposits

At the two deeper moorings (R2; Tr4 and R3; Tr6) the sediment trap and push cores from 70 m-alt show similar grain sizes: (i) the R2 sediment trap contains grains
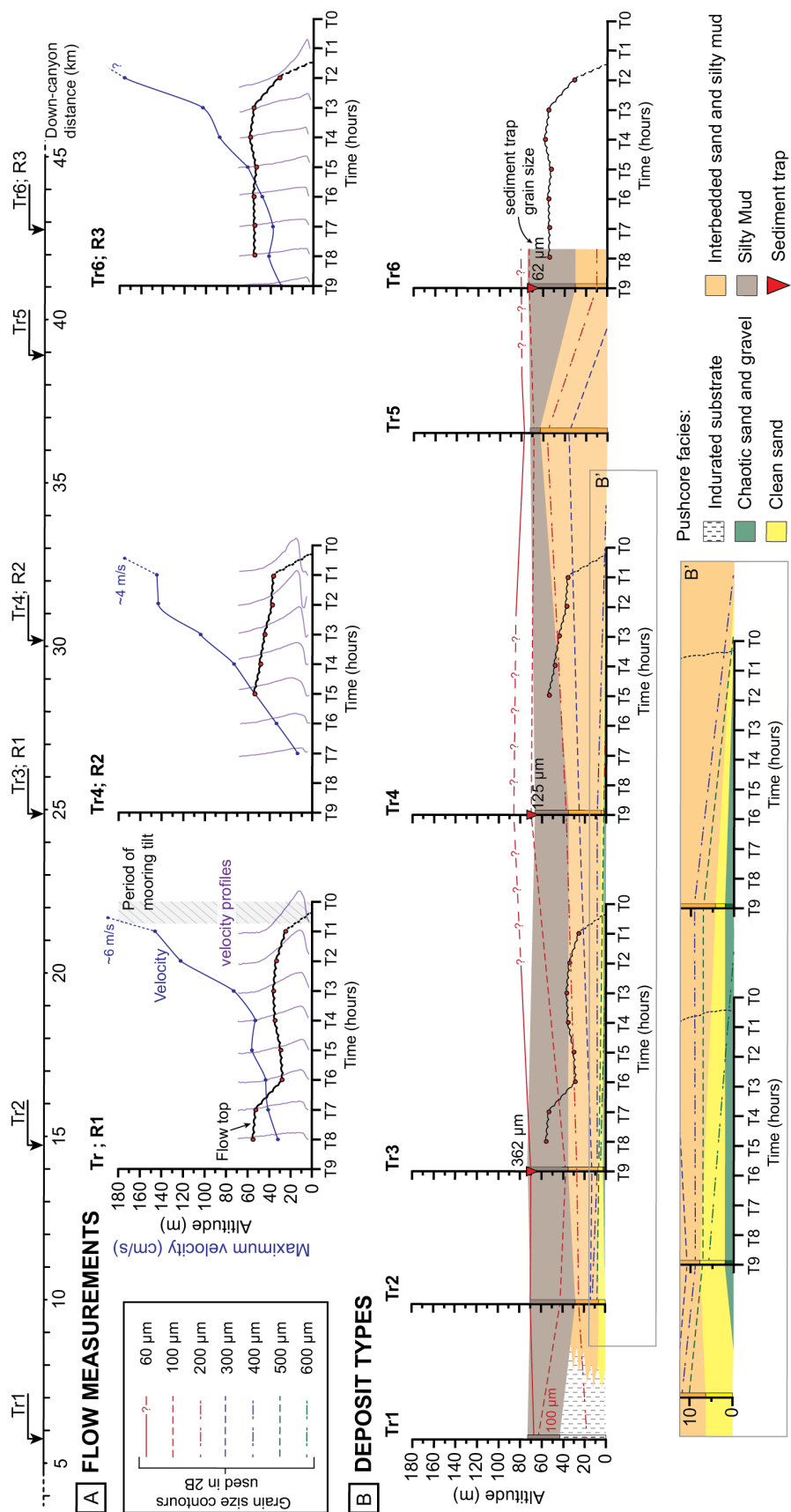
Figure 3.3: (Caption next page.)

Figure 3.3: *(Previous page)* Summary plots for flow monitoring data and grain size and facies data. (A) Flow monitoring data for transects Tr3, Tr4, and Tr6. The turbidity current thickness (black line) as defined by the velocity profiles (purple profiles) and transmissometer data. The maximum velocity for each measurement (blue line) shows the decay of velocity over time with the maximum frontal velocity stated based on arrival times at each mooring. Proximally, the flow starts as a thin, high velocity flow, which rapidly expands and continues to thicken down-system. (B) Grain size and facies distribution for the six transects. Grain sizes are shown by the dashed lines and show strong correlation with the facies distribution both in altitude and down-system. The facies reaching higher altitudes and the coarse facies being deposited at shallower transects represent the expansion of the flow. B′ highlights the facies and grain sizes in the bottom 10 m of the canyon.

up to 125 μm and the canyon wall has grains up to 100 μm; (ii) the R3 sediment trap contains grains up to 62 μm and the canyon wall has grains up to 100 μm. However at the shallow mooring (R1; Tr3) there is a discrepancy between grain sizes in the sediment trap versus in the push core at 70 m altitude; the sediment trap contains grains up to 362 μm from TC2, whereas the canyon wall has grains up to 60 μm.

3.3.5   Tilting and movement of the sediment trap and its implications

Here we demonstrate that during the first ∼15 minutes of TC2, the shallow mooring (R1; Tr3) was severely tilted and therefore collected coarse sediment from lower parts of the flow, explaining the disparity between grain sizes in the sediment trap and the canyon wall at Tr3. During the first 20 minutes of TC2 the pressure recorded on the mooring at 170 m above seafloor (masf) increased from 657 dbar to 675 dbar where it then remained. This pressure increase represents the mooring moving ∼580 m down the canyon at ∼0.5 m s^{-1} (figure 3.5), despite having a 1,000 kg anchor (Xu et al., 2004). To further investigate the movement of the mooring we analyzed the temperature sensors, which have a higher sampling resolution (5 minutes) than the pressure sensors (20 minutes). At the onset of TC2 there was an ∼15 minute decrease in temperature at sensors located at 170 and 300 masf, implying that both sensors were exposed to deeper, colder water. The measured decrease in temperature suggests that the sediment trap located at 70 masf experienced a depth increase of ∼37 m, allowing it to sample lower, coarser parts of the turbidity current. Thus the mooring appears to have tilted and then
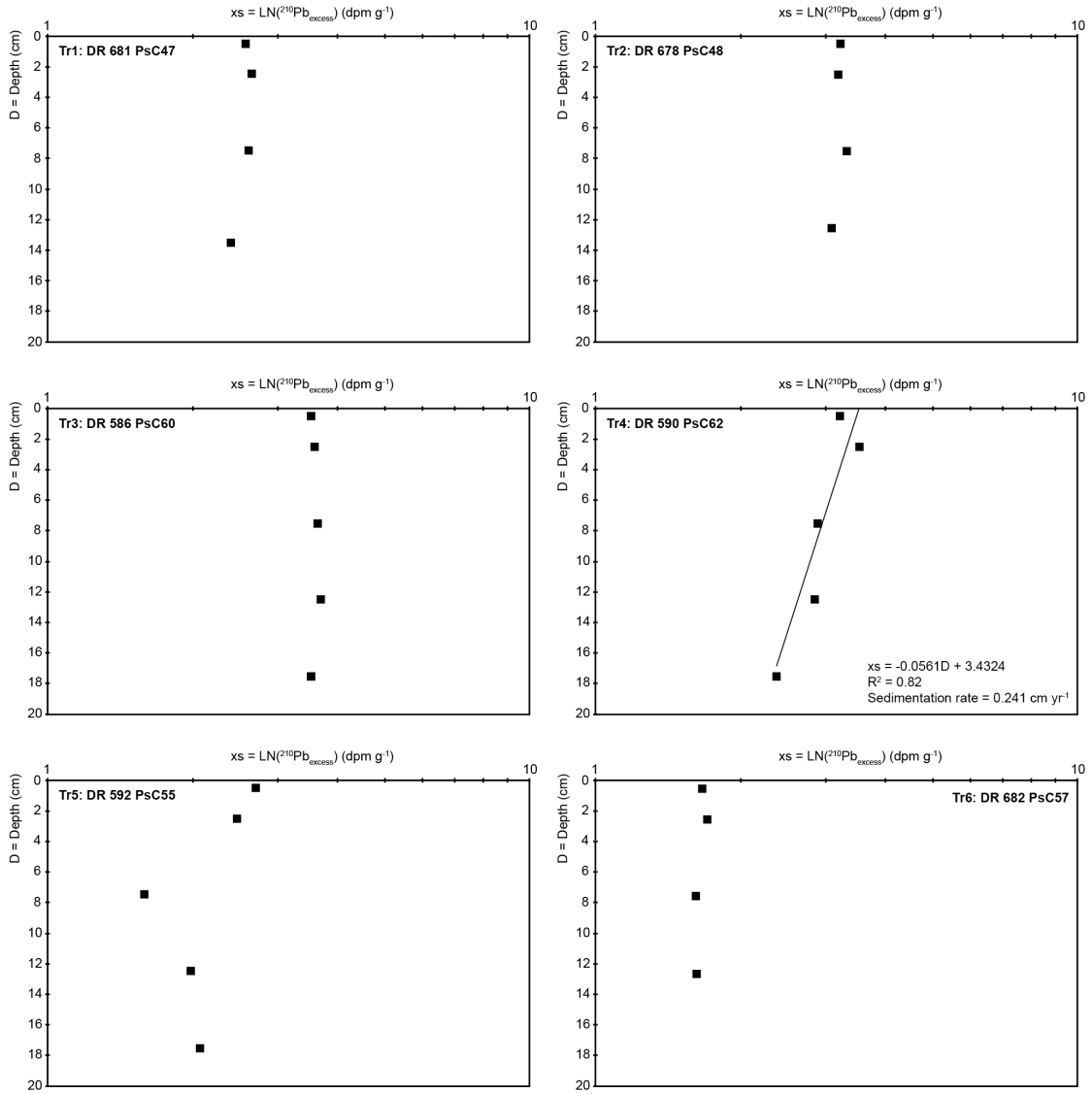
Figure 3.4: Excess down-core ^{210}Pb (^{210}Pb$_{xs}$) in disintegrations per minute (dpm). Each plot represents a different 70 m altitude core at a different transect (Tr1-6). Summary parameters of the linear regression (equation, R^2 value and sedimentation rate) are included for Tr4.

returned to an upright position during the first 15 minutes of the flow, which is prior to the first measurement by the ADCP (sampling at an hourly rate); as a result ADCP measurements used to define the flow structure are not compromised. The pressure and temperature sensors on moorings R2 and R3 show no evidence for tilting.

A

B

C

Based on the temperature data, the 300 m altitude temperature sensor (blue) dips down to the level of the 170 m altitude sensor (red). This tilt lasts for a maximum of 15 minutes.

The sediment trap dipped enough to be within the body of the flow. This is thought to be the minimum amount of tilt (see zoomed section of B above)
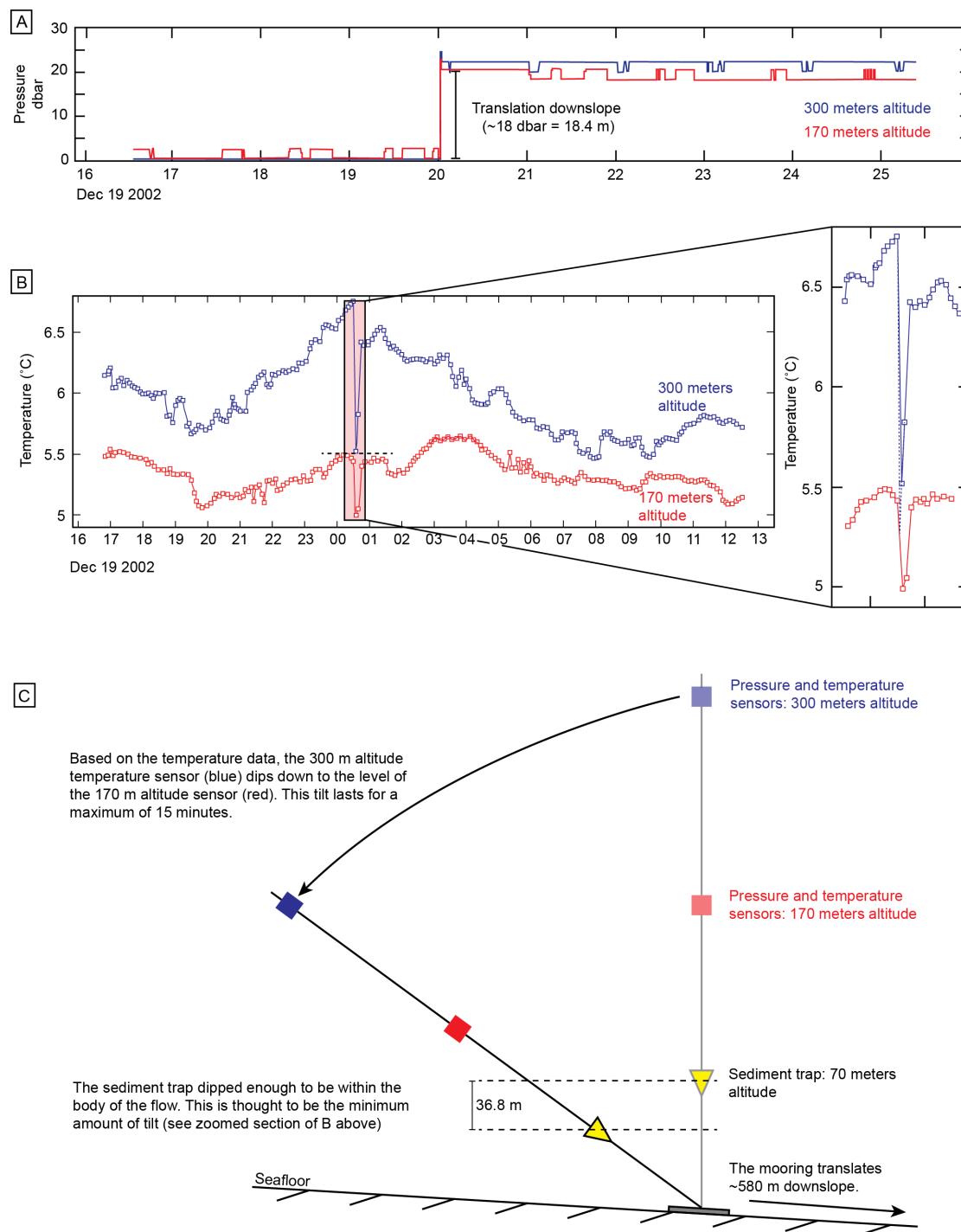
Figure 3.5: (Caption next page.)

Figure 3.5: *(Previous page)* Pressure, temperature, and schematic plots to highlight the translation and tilt of mooring R1. (A) Pressure measurements at 170 (red) and 300 (blue) meters above seafloor. The increase in pressure signifies the onset of the turbidity current. The 20 minute measurement resolution of the pressure sensor means that the tilt is not record with these instruments (tilt lasts for <15 minutes) but the translation downslope, which occurs within 20 minutes, is highlighted by the pressure remaining at an elevated level. An ~18.4 dbar increase equates to ~18 m water depth increase. With an average slope of 1.8° and an 18 m depth increase, this equates to the mooring having travelled ~180 m down-canyon. (B) Temperature plots at 170 (red) and 300 (blue) meters above seafloor. The temperature drop between 00 and 01 highlights the length and amount of mooring tilt. The 300 m temperature sensor drops to measure levels of the 170 m sensor indicates the amount of tilt on the mooring. The measurements are taken every five minutes. Three intervals during the temperature drop suggest the mooring was tilted for up to 15 minutes. The zoomed sections shows that the amount of tilt is the minimum amount of tilt. The mooring could have tilted more (dashed line) but not be recorded as the sensors only record every five minutes. (C) Schematic representation of the mooring tilt. The 300 m sensors (blue) tilts to the level of the 170 m sensors (red). At the level of the sediment trap (70 meters), this tilt equates to 36.8 m depth increase. During this tilting the mooring is also translating down canyon.

3.4 Discussion

3.4.1 Linkage between flow structure and deposits

We now examine the distribution of facies and relate them to different flow phases. Chaotic sands and gravels are present at very low altitudes above the thalweg (<7.5 m-alt) at Tr 1-4; they are not found at Tr 5. Chaotic sands and gravels pinch out at a similar location to where the flows change from having a thin flow to a thick flow front (Fig. 3). They are therefore most likely linked to a high-energy, high-concentration flow phase responsible for moving the mooring. Previous studies (e.g., Paull et al., 2005) that used longer cores have shown that these coarser facies are found at deeper depths beneath the seafloor both here and downstream, demonstrating that larger flows, have not occurred in the past 12 years, can produce this facies at this location and downstream.

Interbedded sand and silty muds are encountered at transects 2-5. The height at which this facies is recorded on the canyon walls progressively increases from 29 m to 62 m-alt between transects 2 and 5. This is coincident with where the turbidity currents

expand and become more dilute. These deposits are indicative of a turbulent flow phase that is sufficiently dilute to enable grain segregation. These results suggest that key features of turbidity currents, such as changes in flow thickness and concentration, are faithfully recorded by their deposits.
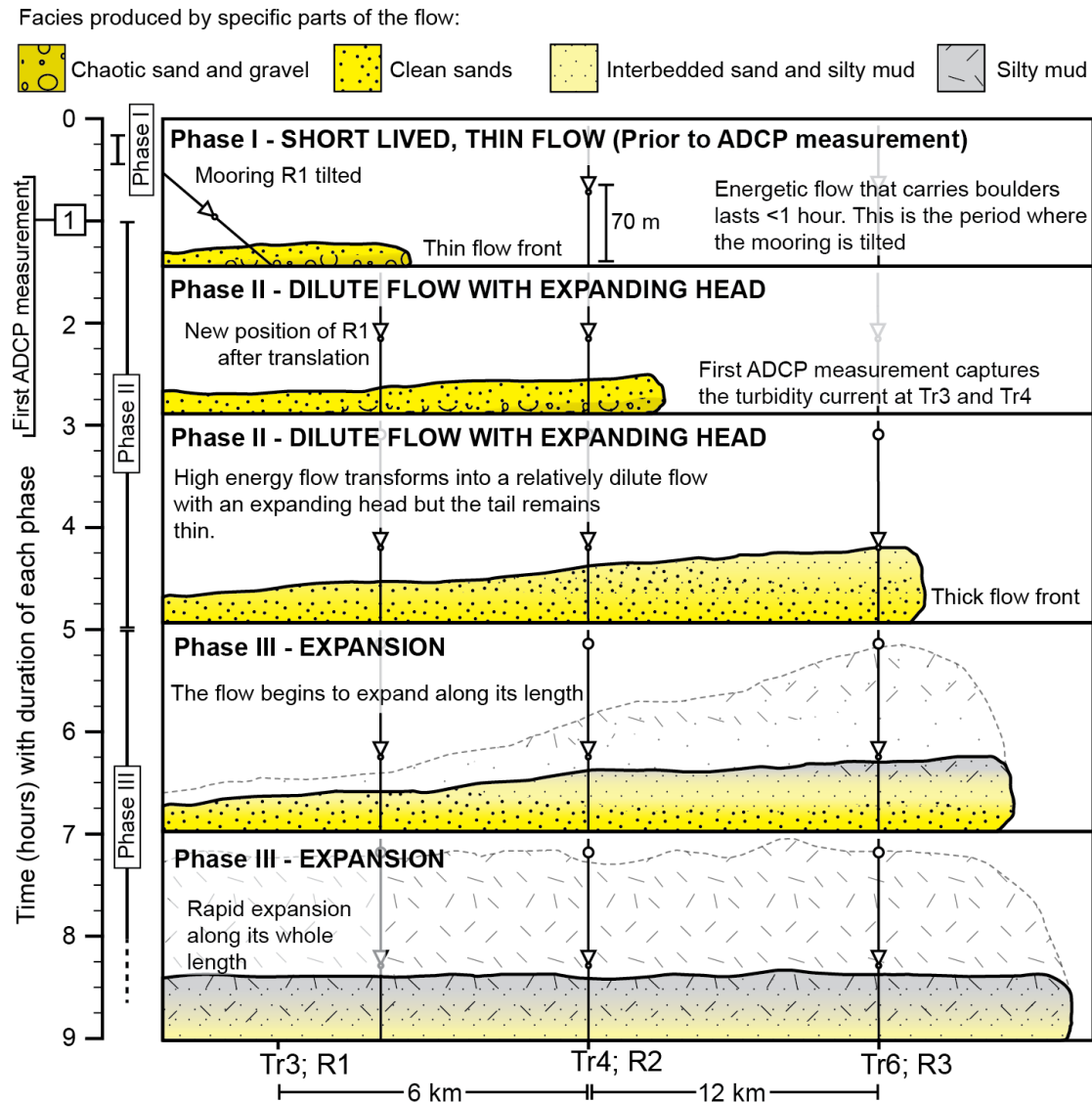
Figure 3.6: Interpretive diagram showing the evolution of flow structure and composition among the three moorings. Each panel shows a snapshot in time constructed using the flow thickness and facies from figure 3.3. Dashed gray line on the phase III panels represents the possible extent of suspended fine-grained material from saturation of transmissometers suspended at 170 m above seafloor on each mooring. ADCP-acoustic Doppler current profiler.

3.4.2 Summary model: evolving flow structure and resulting deposits

We provide flow and deposit data for field-scale turbidity currents from the same location. The combined flow data (Xu et al. 2014) and deposit data suggest that there is a strong link between changes in facies and grain size on the canyon walls and measured changes in the flow structure. Additionally, the combined data provide valuable insights into the dynamics of turbidity currents (figure 3.6). Monterey Canyon turbidity currents begin as thin, high concentration highly energetic flows that deposit chaotic sand and gravel and clean sand facies (figure 3.6). This flow phase lasts for a maximum of 1 h but is most energetic during the first 15 min when it has an estimated velocity of 4-6 m s^{-1} (based on turbidity current arrival times at each mooring (Xu et al., 2014)), which is sufficient to move a 1,000 kg mooring down the canyon. This highly-energetic, high-concentration phase transforms into a more dilute flow phase over the first ∼30 km of the canyon and deposits interbedded sand and silty mud facies (figure 3.6). As the dilute flow travels down canyon the head of the flow progressively thickens resulting in interbedded sand and silty mud facies being deposited at increasingly high altitudes on the canyon walls (figure 3.6). Finally, after 5-6 hours the flows rapidly thicken along their whole length, lofting and depositing silty mud (figure 3.6).

3.5   Conclusions

Broadly comparable grain sizes in sediment traps located within the flow, and in cores from similar heights on the canyon walls, increase confidence in reconstructions of flow properties from deposit textures. A novel combination of direct measurements and cored deposits provide a new three-part model of turbidity current behaviour: 1) they begin as a short-lived (at least 15 minutes) but highly energetic, high-concentration, thin flows; 2) they evolve into a dilute flow with an expanding head capable of transporting sand for 1-5 hours; 3) finally they experience expansion along their whole length, lofting silt and depositing it high on the canyon walls. This new model has important wider implications as it suggests the initial period of powerful flow that is most hazardous for seafloor pipelines and cable may be of limited (15-60 minutes) duration.

Chapter 4

The influence of turbidity currents on bioturbating communities in submarine canyons

Symons, W.O[1,2]., Sumner, E.J[1]., Minter, N.J[3]., Paull, C.K[4]., Clare, M.A[2]., 2017. The influence of turbidity currents on bioturbating communities in submarine canyons.

[1]*School of Ocean and Earth Science, University of Southampton*
[2]*National Oceanography Centre, Southampton*
[3]*University of Portsmouth*
[4]*Monterey Bay Aquarium Research Institute*

The deposit data for this article were collected by Paull assisted by Symons and Sumner. The analysis for this chapter was carried out by Symons. This article was written by Symons with general comments, suggestions and editing by Sumner, Minter, Clare and Paull.

Abstract

Submarine canyons can be biodiversity hotspots; yet any life in submarine canyons is subject to episodic, highly energetic sediment transport events such as turbidity currents. This study considers the effects of turbidity currents on benthic communities, by analysing the traces that these organisms leave behind in the sedimentary record. Monterey Canyon is probably the best-understood submarine canyon on Earth in terms of sedimentary processes because it has been the subject of several direct flow monitoring campaigns in recent years. For this study, six systematic transects comprising a

total of 87 precisely located vibracores were collected from Monterey Canyon using a remotely operated vehicle (ROV) to enable (i) a better understanding of how bioturbating communities are responding to disturbance by turbidity currents of known characteristics; and (ii) validation of models involving biogenic sedimentary structures that are used to interpret ancient submarine canyons. Statistical analysis reveals that altitude above the local thalweg is the primary control for lithofacies and bioturbation index distribution, whereas water depth controls the distribution of specific biogenic sedimentary structures and their relational associations (ichnofabrics). The water depth control on the distribution of ichnofabrics probably results from the availability of dissolved oxygen and the frequency of energetic turbidity currents. Community responses to the higher frequency of turbidity currents in shallow water and a reduced colonisation window results in opportunistic species generating simple traces whereas a lower frequency of turbidity currents in deeper water creates a longer colonisation window with climax communities generating complex burrow systems. Understanding the factors that control the distribution of benthic communities in a modern submarine canyon also enables validation and explanation of ichnological models that are used for palaeoenvironmental reconstruction within ancient submarine canyon systems by alluding to both proximity within a system and altitude above the local thalweg.

4.1   Introduction

Submarine canyons are among the most dramatic geomorphic features that occur along continental margins and act as conduits for sediment transport from the shelf to the deep sea. (Puig et al., 2003). The complex yet dynamic interplay of hydrodynamic processes (e.g. tidal currents, internal waves, and sediment gravity flows) and strong chemical gradients (e.g. oxygen and carbon concentration, nutrient availability) that are a result of confinement, are identified as key controls of the benthic ecosystems found within submarine channels and canyons (Callow et al., 2014). Turbidity currents are the dominant sediment transport process in submarine canyons, yet remarkably few direct observations of such active flows exist. This is due to their often destructive nature, coupled with difficulties in accessing the deep-sea locations where they occur. As

a result, most of our knowledge about turbidity currents in submarine canyons comes from outcrop studies, scaled-down laboratory experiments, and numerical modelling (e.g. Heezen and Ewing, 1952; Piper et al., 1999; Kneller and Buckee, 2000; Pirmez and Imran, 2003; Liu et al., 2012; Talling et al., 2012; Cooper at al., 2013; Cartigny et al., 2014; Hubbard et al., 2014). New technological advances have enabled the active monitoring of flows in submarine canyons in recent years; including repeat mapping of the seafloor, sampling of the seafloor and water column, and flow monitoring efforts, are beginning to reveal the dynamics of turbidity currents that shape these complex and heterogeneous environments (e.g. Khripounoff et al., 2003; Puig et al., 2004; Xu et al., 2004; Liu et al., 2012; Cooper et al., 2013; Hughes-Clarke, 2016).

Submarine canyon topography and the interplay of oceanographic and sedimentological processes make submarine canyons an important location for biological activity. Oceanic currents often enhance productivity (Ryan et al., 2005), making submarine canyons hotspots for faunal activity in the deep-sea (De Leo et al., 2010; Fernandez-Arcaya et al., 2017). The complex topography that submarine canyons exhibit typically makes them undesirable for seafloor exploitation through activities such as bottom-trawl fishing (Puig et al., 2012; Wrtz, 2012; Fernandez-Arcaya et al., 2017); however, they are not untouched by anthropogenic influences, with inputs such as pollutants (e.g. Gwiazda et al., 2015), litter (e.g. Schlining et al., 2013) and mine tailings (e.g. Hughes et al., 2015) commonly reported. The assemblage of seafloor species can provide insight into the interaction between sedimentological and biological processes. For example, turbidity currents can result in unstable sediments, making unfavourable colonisation conditions for many species (Romano et al., 2013). An additional consequence of flow processes on benthic fauna is the periodic cycles of disturbance, recolonisation and recovery of these communities (McClain and Schlacher, 2015). As a result, organisms with opportunistic life strategies are often abundant in submarine canyons (e.g. Gambi and Danovaro, 2016; Fernandez-Arcaya et al., 2017). Some authors have used the cycles of disturbance to better understand the physical impacts and recolonisation strategies of benthic community structures within submarine canyons (e.g. Hess et al., 2005; Paterson et al., 2011; Fernandez-Arcaya et al., 2017). By assessing the faunal elements on the seafloor and then comparing how similar they are to down-core faunal assemblages associated

with turbidites, the stage of recolonisation by seafloor fauna can be assessed (e.g. Hess et al., 2005). Whilst these studies identify the importance of sedimentological processes on deep-sea fauna, they often lack any data characterising the flows. Submarine canyon deposits have the potential to reveal details about the sedimentological processes that occur within submarine canyons but also the resilience of benthic communities to these processes.

Ichnology, the study of biogenic sedimentary structures formed by the activity of an organism (Bromley, 1996), and the intensity of bioturbation within sediments are important tools that when integrated with sedimentological data can offer unique insights for palaeoenvironmental reconstructions. Trace-making organisms (and subsequently their behaviour and intensity of bioturbation) are reliant on a number of dynamic controls (substrate, nutrient supply, oxygenation, hydrodynamic energy, sedimentation rate, salinity, and chemical toxicity (Frey et al., 1990; Taylor et al., 2003; Gingras et al., 2008; Heard and Pickering, 2008, McIlroy, 2008; Heard et al., 2014)), which therefore makes trace fossils good environmental indicators. Previous studies have also used ichnological data to infer information about depositional processes in submarine canyon systems (Heard et al., 2014), including: 1) primary consistency of the sedimentary substrate (e.g. Ekdale and Bromley, 1991; Gingras et al., 2011), 2) process of deposition (e.g. Frey and Goldring, 1992), 3) information about the water column (oxygen levels, trophic state etc) (e.g. Savrda and Bottjer, 1986; Wignall, 1991; Wetzel and Uchman, 1998), 4) palaeoflow direction (e.g. Monaco, 2008), and 5) stratigraphic discontinuity surfaces resulting from cessation of flows (e.g. Hubbard and Shultz, 2008; Knaust, 2009).

4.1.1   Ichnology of ancient deep marine settings

In the last decade our understanding of deep-water ichnology has advanced as studies are more commonly integrating sedimentology and ichnology into their palaeoenvironmental reconstructions (e.g. Martin and Pollard, 1996; McIlroy, 2004; Shultz and Hubbard, 2005; Kane et al., 2007; Heard and Pickering, 2008; Hubbard and Shultz, 2008; Wetzel, 2008; Knaust, 2009; Monaco et al., 2010; Cummings and Hodgson, 2011; Phillips et al., 2011; Hubbard et al., 2012; Callow et al., 2013a,b; Heard et al., 2014).

A number of these studies have focused on confined turbidite channel and canyon systems from the shelf to deep-sea fans (e.g. Kane et al., 2007; Heard and Pickering 2008; Knaust, 2009; Cummings and Hodgson, 2011; Phillips et al., 2011; Hubbard et al., 2012; Callow et al., 2013a,b; Heard et al., 2014; Knaust et al., 2014). The focus on these environments is typically driven by the economic importance of turbidite plays in hydrocarbon exploration.

As more studies use both sedimentological and ichnological datasets in their analyses, despite different oceanographic settings, similar trends in trace fossil distributions across submarine channel and canyon environments are becoming evident (Callow et al., 2014). The most consistent trends that are evident from ichnological studies of channelised systems are of increasing bioturbation intensity and ichnodiversity moving from the channel axis towards off-axis and overbank environments (e.g. Uchman et al., 2004; Heard and Pickering, 2008; Knaust, 2009; Cummings and Hodgson, 2011; Phillips et al., 2011; Callow et al., 2013a; Heard et al., 2014). More specifically, particular traces are seen to characterise different (cross-sectional) areas of these environments. A number of studies have all identified *Ophiomorpha* as characteristic of channel axis deposits, occasionally associated with Phycosiphoniform burrows and *Chondrites* (e.g. Uchman et al., 2004; Knaust, 2009; Cummings and Hodgson, 2011; Phillips et al., 2011; Callow et al., 2013a; Heard et al., 2014). These studies also identify ichnofabrics associated with firmgrounds (stiff but uncemented sediment exposed at the surface after erosion of upper layers (Drosser et al., 2002), e.g. *Thalassinoides*) in channel axis and off-axis environments (Heard et al., 2014). In more marginal and levee-overbank environments, *Scolicia*, *Nereites*, *Planolites* and *Skolithos* are characteristic (Knaust, 2009; Uchman et al., 2004; Callow et al., 2013a; Heard et al., 2014).

Much of our understanding of ichnology in ancient deep marine systems comes from outcrop but recently more studies are utilising core material in ichnological assessments. There are some known difficulties in analysing trace fossils in cores rather than outcrop. Traces from deep-marine, turbidite-dominated environments (e.g. graphoglyptids) tend to be cast by sand-rich turbidite deposits parallel to bedding planes (Wetzel and Uchman, 1998; Knaust, 2009), which are not well exposed in core. Therefore, the

suites of traces typically identified in core are limited to those that vertically penetrate the sediment. Further complications arise from not being able to view the three-dimensional structure of a trace, making ichnotaxonomic identification more difficult; although the use of advanced techniques such as 3D CT-scanning of core material are becoming more prevalent (Knaust, 2017). This has led to differences in the ichnological classification schemes as ichnotaxonomically determinable traces of particular subenvironments differ between outcrop and core. There are also advantages of analysing trace fossils in core rather than outcrop, such as lack of weathering, the vertical continuity of sections (Knaust, 2009), and better detail for burrow boundaries and walls (Pickering and Hiscott, 2016). There are two different approaches to ichnological analysis (McIlroy, 2008; Pickering and Hiscott, 2016): 1) ichnofacies analysis, typically employed by outcrop studies, where individual ichnotaxa are identified and assemblages of these trace fossils and bioturbation intensity highlight environmental variation (e.g. Seilacher, 1967; Uchman, 2001; Heard and Pickering, 2008), and 2) the ichnofabric approach where sedimentary fabric, traces and bioturbation are studied simultaneously, typically quantifying the intensity of bioturbation and cross-cutting and tiering relationships of traces. Those analysing trace fossils within core often adopt the ichnofabric approach, where identification of individual ichnotaxa can be limited (e.g. Ekdale and Bromley, 1983; Taylor and Goldring, 1993; McIlroy, 2008; Knaust. 2009; Callow et al., 2013b).

Despite the value of ichnology to deep-sea sedimentological studies, ichnological studies in modern deep-sea settings are rare compared to shallow-water studies (Knaust 2009; Callow et al., 2014; Knaust et al., 2015). This lack of modern ichnological analyses from deep-water turbidite settings likely stems from the complexities in accessing and often hazardous nature of deep-water environments.

4.1.2 Aims

Despite multiple studies proposing the link between ichnology and sedimentary facies (Callow et al., 2014), the conclusion that trace fossils vary according to the exact location with a submarine canyon or channel (e.g. thalweg, terrace, over-bank) remains

untested in a modern, active system. Therefore, there is a lack of validation for ichnological models being used to make inferences on palaeoenvironment, and thus there is a need to ground-truth these interpretations. This study aims to provide the first high spatial resolution calibration of ichnofabric variation using systematically collected, precisely located vibracores within an active system, integrating knowledge of sedimentological processes to unravel the controls on the observed ichnofabric distributions and understand the effects of turbidity currents on bioturbating marine communities. This aim will be achieved by testing the hypotheses that (i) lithofacies, (ii) bioturbation index, and (iii) ichnofabrics vary with altitude above the canyon thalweg and down-system (water depth).

4.1.3 Monterey Canyon: An active laboratory for understanding biology and sedimentology

Monterey Canyon is probably one of the best-studied submarine canyons in the world and provides a natural laboratory to analyse canyon processes and deposits (Fildani, 2017), with results applicable to many other similar sized submarine canyons globally. The canyon head is only 10 m from the shore (Okey, 1997) in the littoral zone, and can be traced for more than 400 km seaward to water depths >4000 m (Paull et al., 2011). Two main tributaries, Soquel Canyon and Carmel Canyon, join Monterey Canyon at water depths of 980 m and 1970 m respectively. Approximately ~400,000 m^3 of sand is transported through the canyon each year by regular, sub-annual turbidity currents in water depths of up to 1850 m (Paull et al., 2003, Xu et al., 2004, 2014; Talling et al., 2013). These active flows have been a focus of recent studies that analyse sedimentological processes (in particular turbidity currents) within submarine canyons (e.g. Paull et al., 2003, 2005, 2010a; Smith et al., 2005, 2007; Xu et al., 2014; Symons et al., 2017), providing unique insights to support the assessment of biological response to energetic turbidity currents.

Monterey Canyon lies within a major coastal upwelling system in which productivity is enhanced by upwelled nutrients (Ryan et al., 2005). As a result Monterey
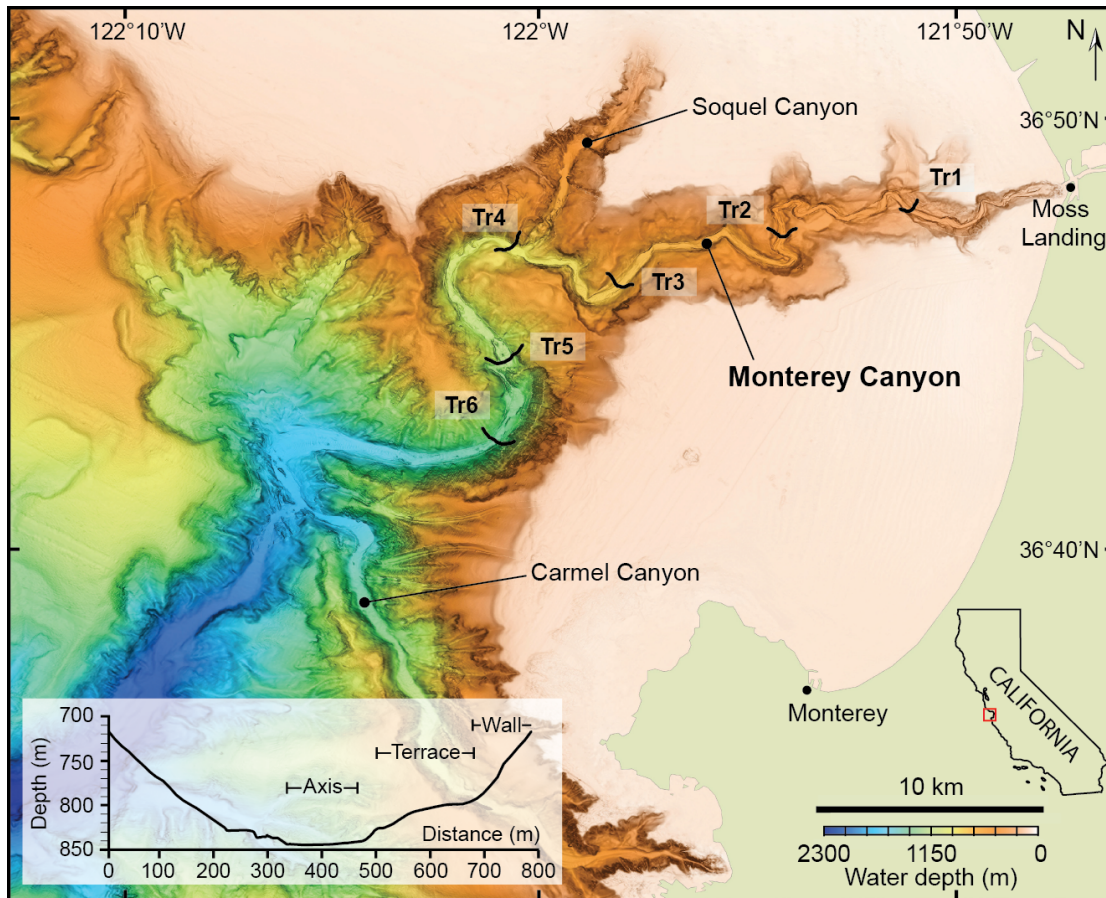
Figure 4.1: Map showing the bathymetry of Monterey Bay (Modified after Paull et al., 2010a). Included are the locations of the six core transects (Tr1-6) within Monterey Canyon. The cross-canyon profile highlights the different elements of the canyon profile (axis, terrace and wall). The inset map shows the location of Monterey Bay in relation to California (red box).

Canyon is rich in benthic biological activity with many studies focussing on the biological communities that inhabit Monterey Canyon (e.g. Barry et al., 1996; Goffredi et al., 2004; Lundsten et al., 2010; Robison et al., 2010), with some integrating the response of biological communities to sedimentological processes (e.g. Okey, 1997; Paull et al., 2010b).

4.2 Methods

4.2.1 Core collection and logging

In April and October 2014, dives of the Monterey Bay Aquarium Research Institutes remotely operated vehicle (ROV) *Doc Ricketts* were conducted in the upper reaches of Monterey Canyon to systematically collect cores in order to test the responses of lithofacies and bioturbation to position within the canyon. Data were collected using an ROV-mounted vibracore system capable of collecting up to six 2 m-long and 7.65 cm-diameter cores in aluminium tubes. This ROV-deployed coring system enabled location of cores at different altitudes above the thalweg to a level of precision that cannot be achieved using traditional wireline coring techniques. The position of the ROV was continuously tracked using an ultrashort baseline system. Additional instrumentation included a conductivity-temperature-depth (CTD) sensor with transmissometer and oxygen sensor. Systematic across canyon transects were collected, comprising up to 12 vibracores per wall and included cores from the thalweg, and the canyon walls up to an altitude of ~70 m above local thalweg (m-alt). These transects were at water depths of 300 m (Tr1), 530 m (Tr2), 833 m (Tr3), 1018 m (Tr4), 1280 m (Tr5), and 1525 m (Tr6) (figure 4.1). The vibracores were logged for p-wave velocity and γ-attenuation with a GEOTEK multisensor core logger, split, photographed with a GEOTEK digital line-scanning camera, and archived at the U.S. Geological Survey (USGS) in Menlo Park, California. The cores were visually sedimentologically logged with grain sizes measured using a hand lens and grain-size comparator.

Table 4.1: Table of vibracores used with altitude on the canyon wall and geographical location.

Transect	Core number	Altitude (m)	Latitude	Longitude
Tr1 north wall	DR681 VC-437	15.8	36.794481	-121.844734
	DR681 VC-438	43.5	36.794937	-121.844701
	DR681 VC-439	52.4	36.795154	-121.844645
	DR681 VC-440	60.3	36.795672	-121.844442
	DR681 VC-441	69.	36.796099	-121.844341
	DR681 VC-442	72.3	36.797711	-121.844012

Table 4.1 – *Continued from previous page*

Transect	Core number	Altitude (m)	latitude	Longitude
Tr1 south wall	DR683 VC-449	11.9	36.794481	-121.845375
	DR683 VC-450	18.3	36.794937	-121.845399
	DR683 VC-451	42	36.795154	-121.845483
	DR683 VC-452	52.9	36.795672	-121.845515
	DR683 VC-453	62.5	36.796099	-121.84559
	DR683 VC-454	73.8	36.797711	-121.845707
Tr2 north wall	DR677 VC-415	0	36.792308	-121.903232
	DR677 VC-416	5.7	36.792197	-121.90364
	DR677 VC-417	10.4	36.791763	-121.903933
	DR677 VC-418	15	36.791546	-121.904326
	DR677 VC-419	22	36.791299	-121.904574
	DR677 VC-420	28.8	36.790686	-121.904762
	DR678 VC-421	37.7	36.788568	-121.905036
	DR678 VC-422	44.1	36.78858	-121.905318
	DR678 VC-423	49	36.788594	-121.905662
	DR678 VC-424	57.4	36.788682	-121.906067
	DR678 VC-425	63.6	36.788618	-121.906753
	DR678 VC-426	70	36.788609	-121.907322
Tr2 south wall	DR687 VC-466	0	36.788537	-121.902894
	DR687 VC-467	13.4	36.788561	-121.902595
	DR687 VC-468	31	36.7886	-121.902303
	DR687 VC-469	44.4	36.788618	-121.901841
	DR687 VC-470	59.3	36.788593	-121.901597
	DR687 VC-471	73	36.788582	-121.901226
Tr3 north wall	DR585 VC-331	0	36.788728	-121.969199
	DR585 VC-332	1.36	36.788643	-121.969435
	DR585 VC-333	3.57	36.788801	-121.969557
	DR585 VC-334	7.73	36.788731	-121.969973
	DR585 VC-335	13.47	36.788794	-121.970345
	DR585 VC-336	21.92	36.788796	-121.970663
	DR586 VC-337	24.07	36.764819	-121.970579
	DR586 VC-338	35.09	36.765156	-121.971075
	DR586 VC-339	45.37	36.765555	-121.971158
	DR586 VC-340	56.76	36.765921	-121.97144
	DR586 VC-341	66.11	36.766184	-121.971287
	DR586 VC-342	74.94	36.766354	-121.971557
Tr3 south wall	DR685 VC-455	0	36.766712	-121.968948

Table 4.1 – *Continued from previous page*

Transect	Core number	Altitude (m)	latitude	Longitude
	DR685 VC-456	8.2	36.767172	-121.968608
	DR680 VC-433	11.6	36.767558	-121.968444
	DR680 VC-434	19.3	36.767826	-121.968374
	DR680 VC-435	29	36.768319	-121.968174
	DR680 VC-436	39.8	36.768654	-121.968009
	DR685 VC-457	49	36764465	-121.96789
	DR685 VC-458	60.2	36.764094	-121.967721
	DR685 VC-459	70.2	36.764036	-121.967589
	DR685 VC-460	78.3	36.76396	-121.967476
Tr4 south wall	DR589 VC-348	0	36.763823	-122.016094
	DR589 VC-349	1.96	36.763641	-122.016172
	DR589 VC-350	4.33	36.763483	-122.01646
	DR589 VC-351	7.93	36.763344	-122.016626
	DR589 VC-352	15.41	36.763124	-122.016655
	DR589 VC-353	23.15	36.762999	-122.01683
	DR590 VC-354	28.63	36.781886	-122.017118
	DR590 VC-355	36.58	36.781522	-122.017249
	DR590 VC-356	48.62	36.781089	-122.017398
	DR590 VC-357	56.68	36.780965	-122.017297
	DR590 VC-359	64.4	36.780545	-122.017264
Tr5 south wall	DR591 VC-365	0.38	36.780213	-122.014369
	DR591 VC-364	0	36.7798339	-122.013934
	DR591 VC-360	4.08	36.779569	-122.013576
	DR591 VC-361	9.85	36.779323	-122.01334
	DR591 VC-363	13.33	36.779081	-122.013247
	DR591 VC-362	20.74	36.7789	-122.013035
	DR592 VC-366	29.99	36.734151	-122.012852
	DR592 VC-367	38.75	36.734343	-122.01242
	DR592 VC-368	44.79	36.734546	-122.012213
	DR592 VC-369	53.66	36.734517	-122.012056
	DR592 VC-370	62.62	36.734709	-122.011949
	DR592 VC-371	72.28	36.734657	-122.011791
Tr6 north wall	DR679 VC-427	0	36.734739	-122.020496
	DR679 VC-428	5.3	36.735091	-122.020862
	DR679 VC-429	9.8	36.735125	-122.021142
	DR679 VC-430	15.5	36.735317	-122.021335
	DR679 VC-431	21.4	36.735439	-122.02136
	DR679 VC-432	30.2	36.735525	-122.021694
	DR682 VC-443	34.1	36.702325	-122.02172

Table 4.1 – *Continued from previous page*

Transect	Core number	Altitude (m)	latitude	Longitude
	DR682 VC-444	44.1	36.702514	-122.021908
	DR682 VC-445	51.7	36.702663	-122.022089
	DR682 VC-446	58.3	36.763742	-122.022264
	DR682 VC-447	67.1	36.702799	-122.022433
	DR682 VC-448	74.1	36.702953	-122.022683

4.2.2   Ichnological analysis

Bioturbation intensity is a major component of ichnofabric analysis and provides insight into the duration of colonisation events (Pickering and Hiscott, 2016). To define the amount of bioturbation (bioturbation index), the scheme of Taylor and Goldring (1993) was adopted, which is well suited to core studies (Pickering and Hiscott, 2016). The degree of bioturbation was defined in terms of burrow density and sharpness of the original sedimentary fabric. Cores were visually divided into 5 cm intervals, or by bed thickness if bed thickness was <5 cm. Each interval was assigned a grade from 0 (no bioturbation) to 6 (complete bioturbation) (figure 4.2). There is debate about whether structureless surficial deposits exhibit no bioturbation, or may have been completely bioturbated (e.g. Lowemark, 2007; Wetzel, 2010). The most surficial deposits within the vibracores typically display no sedimentary structures and appear as homogenous mud; occasional sand filled burrows are present. Some authors describe these sediments as within the mixed-layer (thickness of 9.8 ± 4.5 cm (Uchman and Wetzel, 2011)) where bioturbation is so effective that no structures remain. In this study, the consistent view that all sediment has passed through the mixed layer and has subsequently had the chance to be bioturbated is used. Therefore, if no discrete bioturbation structures were seen then it was assumed there was zero bioturbation (as opposed to completely bioturbated and homogenised). Where surficial deposits do exhibit sand filled burrows, these were determined to be primary bioturbation (i.e. not burrows penetrating an already completely homogenised layer). Furthermore, previous workers suggest that modern abyssal sediments are completely bioturbated as a result of the low energy and

sedimentation rates (Wetzel, 2010). As this study focuses on a high-energy submarine canyon, it is not unreasonable to assume a much lower level of bioturbation of surficial sediments.

In contrast to outcrop studies that are often afforded a three-dimensional view, trace fossils in core are typically studied in two dimensions. In modern sediment cores, only a few taxa can reliably be ichnotaxonomically identified; the most useful being small-sized burrows and those that have characteristic geometries or distinct internal
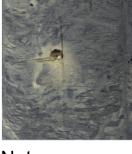
Bioturbation Index	Description	Bioturbation (%)	Example
0	No bioturbation	0	
1	Sparse bioturbation, bedding distinct, few discrete traces and/or escape structures	1-4	
2	Low bioturbation, bedding distinct, low trace density, escape structures often common	5-30	
3	Moderate bioturbation, bedding boundaries sharp, traces discrete, overlap rare	31-60	
4	High bioturbation, bedding boundaries indistinct, high trace density with overlap common	61-90	
5	Intense bioturbation, bedding completely disturbed (just visible), limited reworking, later burrows discrete	91-99	
6	Complete bioturbation, sediment reworking due to repeated overprinting	100	Not seen

Figure 4.2: Bioturbation Index (BI) classification table (after Taylor and Golding, 1993). Each grade (0-6) is determined by the sharpness of the original sedimentary fabric and burrow abundance. Percentage of bioturbation is used as a guide and not as an absolute grade division. An example of each grade (except 6) is included.

structures (Wetzel, 2010). Biological traces were therefore considered at the ichnogeneric level due to the difficulty in identifying ichnospecies in vertical cross-sections. Whilst there is inconsistency when naming ichnofabrics in the literature, the ichnofabrics were named with reference to the most abundant or most characteristic traces; following the protocol of recent workers (e.g. Pollard et al., 1993; Taylor and Goldring, 1993; Taylor et al., 2003; McIlroy 2004, 2007). Identification of traces was primarily from key morphological features following the hierarchical scheme of Knaust (2017), where orientation, branching, shape, fill and lining are the main diagnostic criteria. Previous studies that classified traces from core material have presented visual and descriptive accounts of observed traces (e.g. McIlroy, 2004; Heard et al., 2014; Knaust et al., 2009; Knaust, 2017). This set of key ichnotaxonomically determinable traces from previous studies was used as a reference for identifying specific traces in the Monterey Canyon cores.

4.2.3 Testing the effects of altitude and water depth on lithofacies and ichnofabric distribution

One of the primary aims of this study was to test the response of deposits and organisms and their behaviours to active processes and morphology of an active submarine canyon. This was achieved by statistically testing the response of (1) lithofacies, (2) bioturbation index (BI), and (3) ichnofabrics to different altitudes and water depths. All statistical analyses were carried out in IBM SPSS 24.0. Altitude above the local thalweg was sorted into 10 m bins (10-80 m) and water depth was taken as the maximum water depth at each transect (Tr1 = 300 m; Tr2 = 530 m; Tr3 = 833 m; Tr4 = 1018 m; Tr5 = 1280 m; Tr6 = 1525 m):

i. **Lithofacies**: A multinomial logistic regression was used to test the hypothesis that altitude and water depth (continuous independent variables) have overall significant effects on lithofacies (nominal dependent variable). Silty mud was used as the reference category as it has the most widespread distribution, and therefore acts as the null case for comparison whereby there is no effect of altitude and water depth on lithofacies distribution.

ii. **Bioturbation Index**: An ordinal logistic regression was used to test the hypothesis that altitude and water depth (continuous independent variables) have overall significant effects on bioturbation index (ordinal dependent variable). A Kruskal-Wallis test was also used to test the effects of lithofacies (independent variable) on the distribution of bioturbation index (response variable).

iii. **Ichnofabrics**: A multinomial logistic regression was used to test the hypothesis that altitude and water depth (continuous independent variables) have significant effects on ichnofabrics (nominal dependent variable). None was chosen as the reference category because areas of no bioturbation occur in cores at all altitudes and water depths and therefore acts as the null case.

4.3   Results

4.3.1   Lithofacies
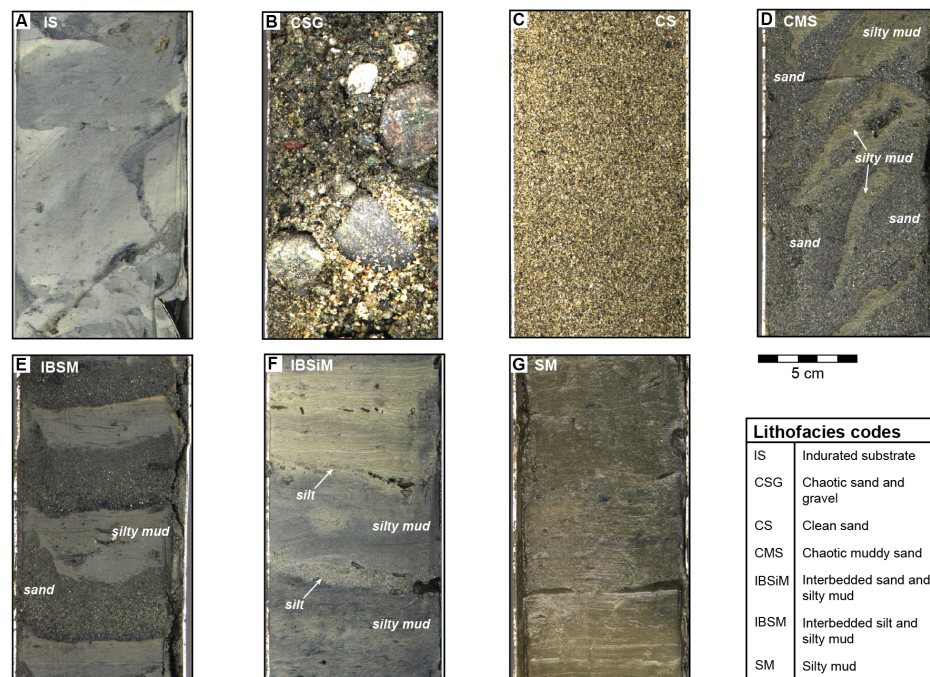
Figure 4.3: Photographs of split ROV-collected vibracores collected from the thalweg, terraces and walls of Monterey Canyon that highlight the lithofacies variability. (A) Indurated substrate, (B) chaotic sand and gravel, (C) clean sand, (D) chaotic muddy sand, (E) interbedded sand and silty mud, (F) interbedded silt and silty mud, (G) silty mud.

The facies scheme developed for this study was based on deposits from the vibracores collected within Monterey canyon (figure 4.3). These facies have been adapted from a facies scheme devised for shorter push cores collected from the same locations (Symons et al., 2017) and supports previous facies identification undertaken in Monterey Canyon (Paull et al., 2005, 2006, 2010a, 2011). Each lithofacies is described and their altitude and transect distributions outlined in table 4.2 and figures 4.4-4.18.

Table 4.2: Lithofacies identified with the Monterey Canyon vibracores.

Facies	Facies code	Description	Grading	Sorting	Grain size range	Max facies thickness (cm)	Max bed thickness (cm)	Altitude range (m)	Canyon location	Transect distribution
Indurated substrate	IS	Pale grey to dark grey firm mud that crops out on steep (∼19-27°) canyon walls at the most proximal transect (Tr1). Found beneath coarse-grained deposits at more distal transects (Tr2 and Tr3). Comprised of homogenous mud or contains rip-up material of previous mud deposits. Some softer mud clasts are found within this facies suggesting clasts of more recent deposition are included	Ungraded	Very well sorted	Mud	96	96	0 - 18.3	Thalweg and canyon terraces	TR1, Tr2, Tr3
Chaotic sands and gravel	CSG	Poorly sorted clean sands and gravels restricted to the canyon thalweg. Lithic clasts dominate but cohesive clay-clasts are sometimes present. Typically massive but sand matrix occasionally shows normal grading towards top of unit. Can be clast supported at base of unit. Most prominent at shallower transects (Tr2-4) and fines down-system. Tr1 does not sample the canyon thalweg but previous studies (e.g. Paull et al., 2005, 2010a) have described this facies in the thalweg at Tr1	Weak grading of sand matrix.	Poorly sorted	Matrix: 187 μm - granules. Clasts: 0.5 - 7 cm	54	32	0 - 3.6	Thalweg	Tr1 (inferred), Tr2, Tr3, Tr4, Tr5, Tr6

Table 4.2 – *Continued from previous page*

Facies	Facies code	Description	Grading	Sorting	Grain size range	Max facies thickness (cm)	Max bed thickness (cm)	Altitude range (m)	Canyon location	Transect distribution
Clean sands	CS	Clean yellow-brown sand that exhibits normal grading or is ungraded. Seen in conjunction with other coarse-grained facies (CSG, CMS) at shallower transects (Tr2-4) and is the primary coarse facies at more distal transects (Tr4-6). Straight to slightly wavy laminations at the base of some normally graded units	Normal or ungraded	Moderately to well sorted	187 - 1500 μm	91	76	0 - 22	Thalweg, terraces and walls	Tr2, Tr3, Tr4, Tr5, Tr6
Chaotic muddy sands	CMS	Grey-brown sand with clasts or contorted horizons of soft to moderately-stiff brown mud. Always sharp contacts between the sand and mud components. With exception to Tr4, always sampled along with clean sand	Ungraded	Poorly sorted	63 - 375 μm *(sand: 187-375 um)*	31	31	5.7-28.6	Terraces and lower levels of the canyon walls	Tr2, Tr3, Tr4, Tr5
Interbedded sands and silty muds	IBSM	Very fine to coarse sand, typically graded, interbedded with silty mud. Sand-laminae/-beds range in thickness from 0.4-15.5 cm. Straight laminations found at the base of some thicker graded units. The silty mud component is often bioturbated. No distinction able to be made between possible turbidite mud and hemipelagic mud. Sand bed thickness decreases with altitude. Sand beds become more discontinuous and bioturbated with increasing altitude from the local thalweg	Sand beds either ungraded or normally graded	Sands moderately to well sorted	Sand: 187 - 750 μm	103	15.5	0-74	Thalweg, terraces and walls	Tr1, Tr2, Tr3, Tr4, Tr5, Tr6

Table 4.2 – *Continued from previous page*

Facies	Facies code	Description	Grading	Sorting	Grain size range	Max facies thickness (cm)	Max bed thickness (cm)	Altitude range (m)	Canyon location	Transect distribution
Interbedded silt and silty muds	IBSiM	Brown-grey silty muds separated by distinct silt-laminae/-beds. Silt-laminae/-beds range in thickness from 0.1-2 cm. Some weak grading event in thicker horizons but no other discernable structure. Silt beds get thinner with greater altitude above the local thalweg. Silt beds are increasingly bioturbated with greater altitude above the thalweg. The interbedded silty mud is often strongly bioturbated, more so at greater altitudes. No distinction able to be made between possible turbidite mud and hemipelagic mud. Presence increases with greater altitudes	Typically ungraded, rare normal grading	Individual mud and silt component well sorted	63 μm	38	2.1	4-74	Terraces and walls	Tr1, Tr2, Tr3, Tr4, Tr5, Tr6
Silty mud	SM	Brown to grey structureless silty mud. Distinguishable from IBSM and IBSiM in that the silt component is distributed throughout the mud and not in distinct laminae/beds. Silty mud is often strongly bioturbated and can contain organic material (twigs, shells). Above the thalweg and terraces, silty mud typically makes up most of the surficial deposits	Ungraded	Well sorted	Mud with minor silt component	166	166	0-74	Canyon terraces and walls	Tr1, Tr2, Tr3, Tr4, Tr5, Tr6

Figure 4.4: Graphical sedimentary logs, bioturbation index, lithofacies, and ichnofabric distribution for the north and south wall of Tr1. Included is a cross section profile of the canyon showing the location of each core within the transect. Mu - *Multina*, N - *Nereites*, Op - *Ophiomorpha*, Pa - *Palaeophycus*, Pl - *Planolites*, Th - *Thalassinoides*, Z - *Zoophycos*.

Figure 4.5: High-resolution core photos from Tr1. Included is a cross section profile of the canyon showing the location of each core within the transect.

Figure 4.6: Graphical sedimentary logs, bioturbation index, lithofacies, and ichnofabric distribution for the north wall of Tr2. Included is a cross section profile of the canyon showing the location of each core within the transect. As - *Asterosoma*, Mu - *Multina*, N - *Nereites*, Op - *Ophiomorpha*, Pl - *Planolites*, Th - *Thalassinoides*, Z - *Zoophycos*.

Figure 4.7: High-resolution core photos from the north wall of Tr2. Included is a cross section profile of the canyon showing the location of each core within the transect.

Figure 4.8: Graphical sedimentary logs, bioturbation index, lithofacies, and ichnofabric distribution for the south wall of Tr2. Included is a cross section profile of the canyon showing the location of each core within the transect. As - *Asterosoma*, Mu - *Multina*, N - *Nereites*, Op - *Ophiomorpha*, Pl - *Planolites*, Th - *Thalassinoides*, Z - *Zoophycos*.

Figure 4.9: High-resolution core photos from the south wall of Tr2. Included is a cross section profile of the canyon showing the location of each core within the transect.
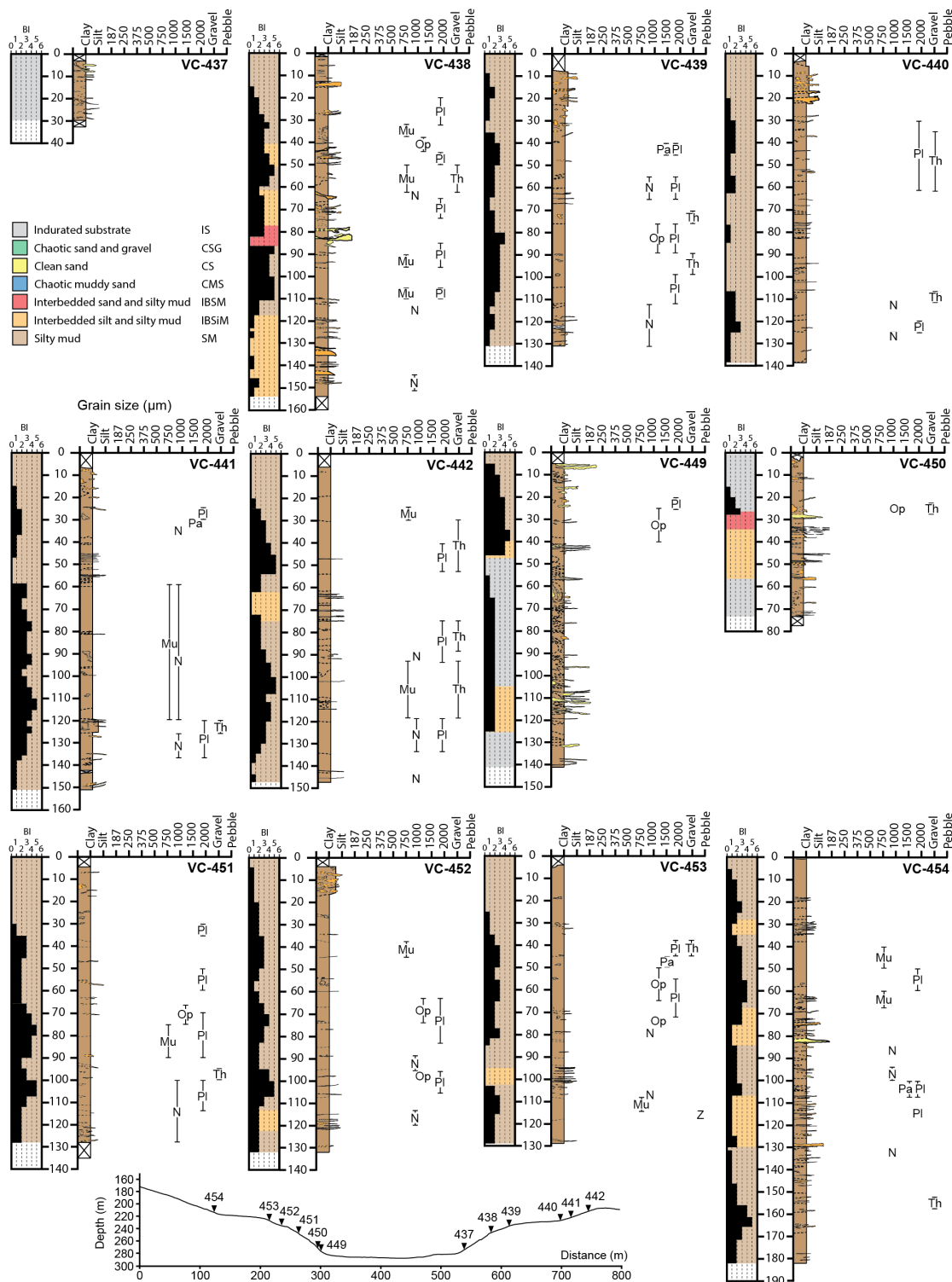
Figure 4.10: Graphical sedimentary logs, bioturbation index, lithofacies, and ichnofabric distribution for the north wall of Tr3. Included is a cross section profile of the canyon showing the location of each core within the transect. Ar - *Arenicolites*, As - *Asterosoma*, N - *Nereites*, Op - *Ophiomorpha*, Pa - *Palaeophycu*s, Pl - *Planolites*, Sk - *Skolithos*, Th - *Thalassinoides*.

Figure 4.11: High-resolution core photos from the north wall of Tr3. Included is a cross section profile of the canyon showing the location of each core within the transect.
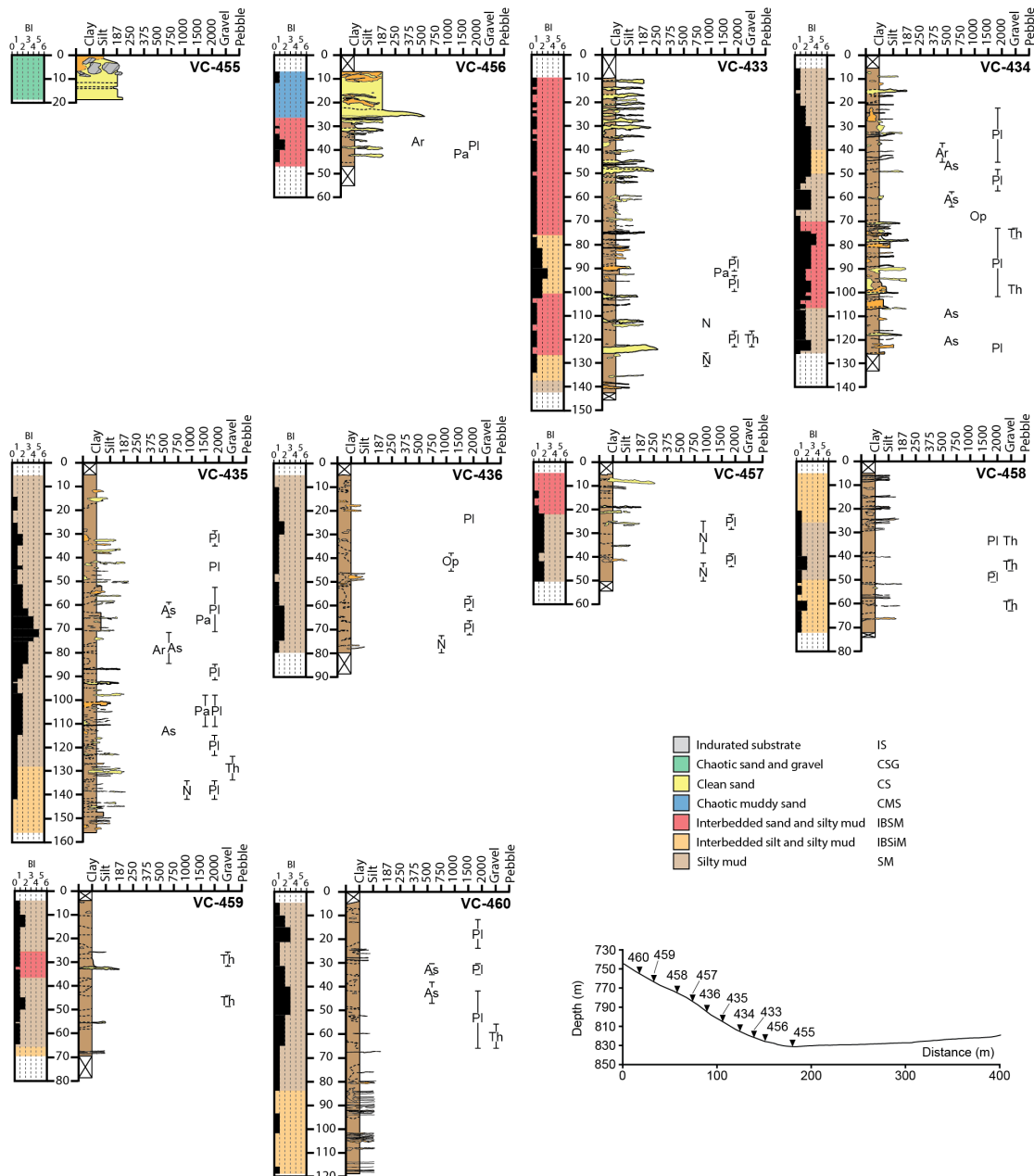
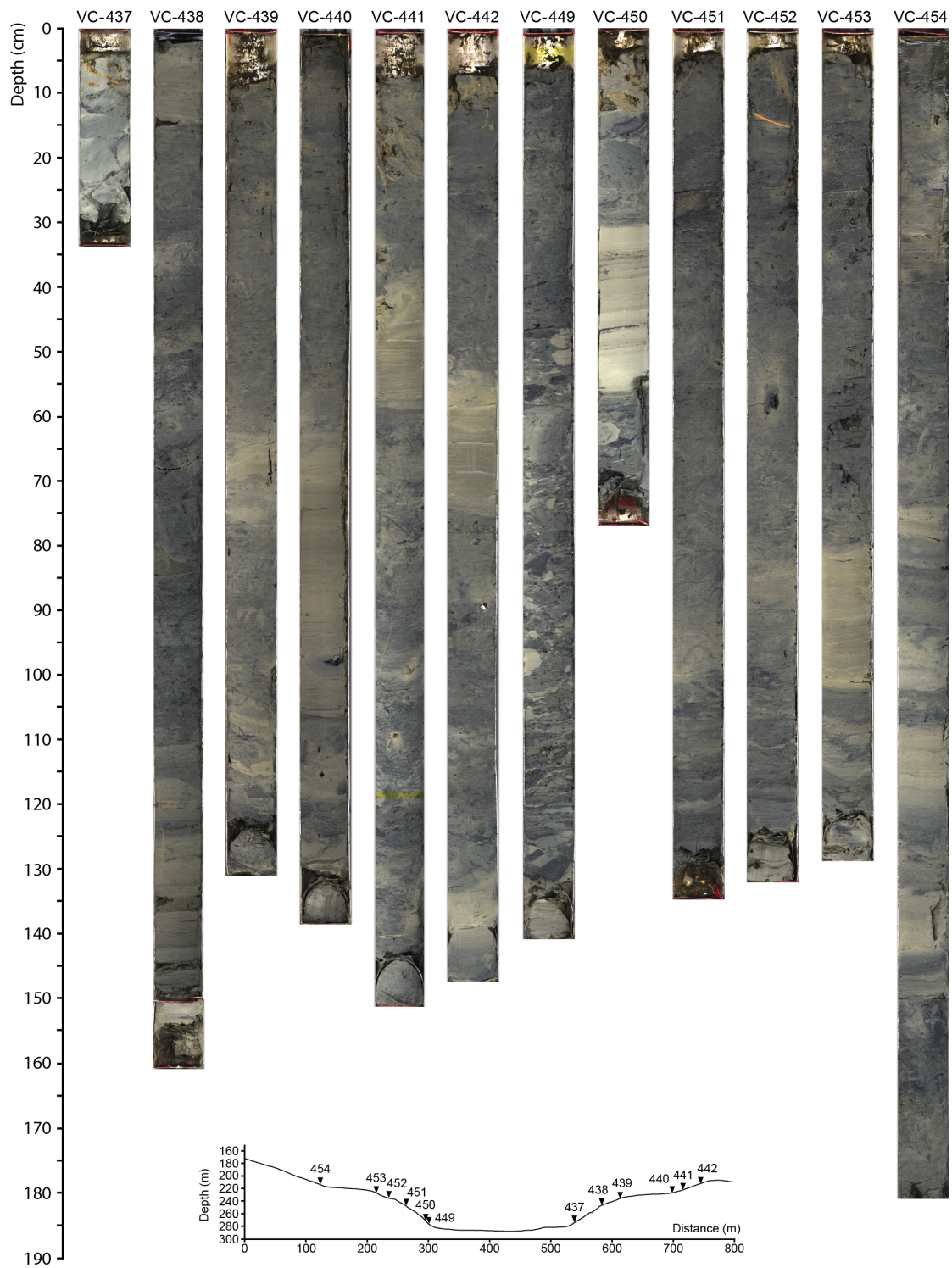Figure 4.12: Graphical sedimentary logs, bioturbation index, lithofacies, and ichnofabric distribution for the south wall of Tr3. Included is a cross section profile of the canyon showing the location of each core within the transect. Ar - *Arenicolites*, As - *Asterosoma*, N - *Nereites*, Op - *Ophiomorpha*, Pa - *Palaeophycus*, Pl - *Planolites*, Sk - *Skolithos*, Th - *Thalassinoides*.
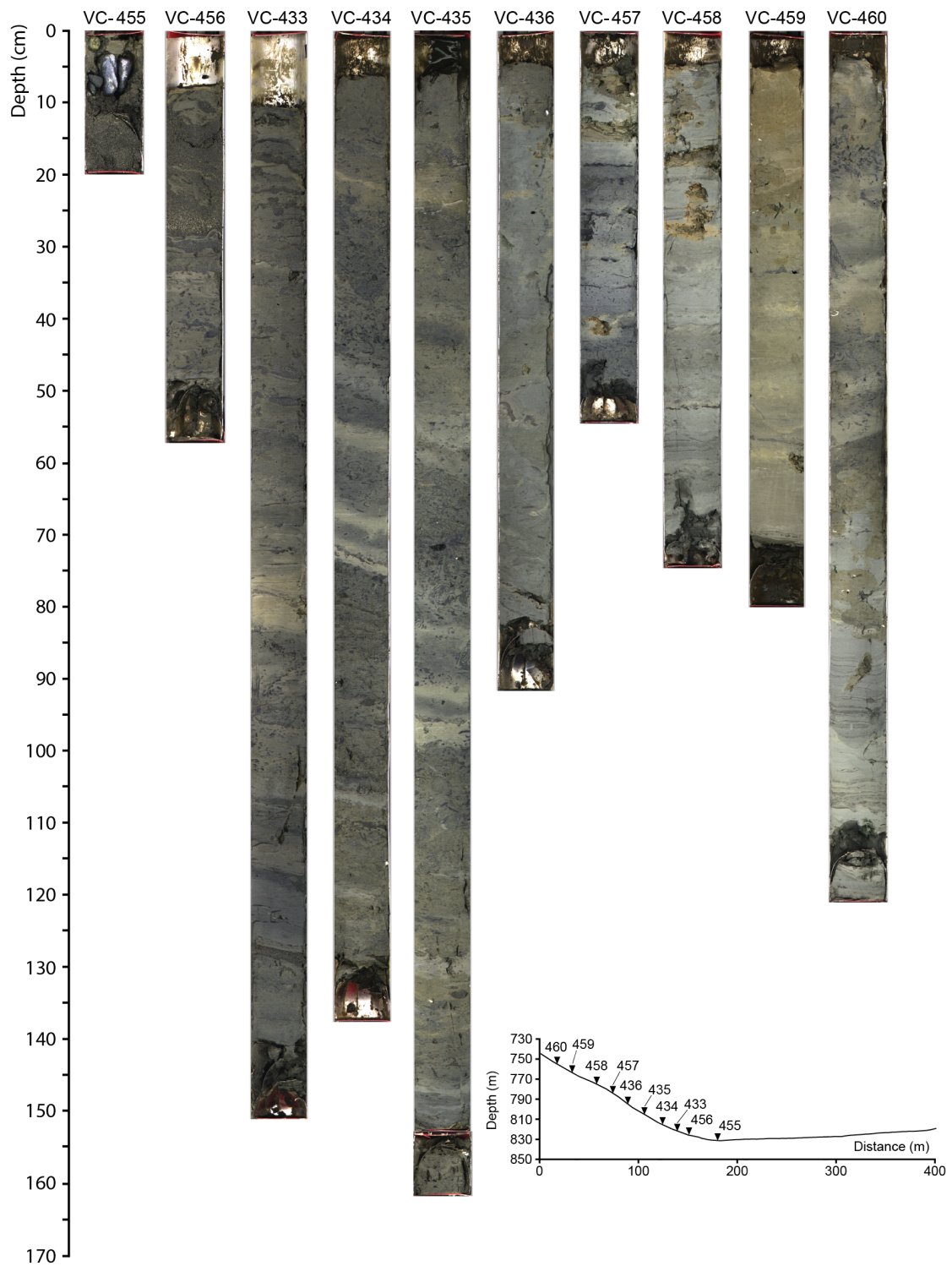
Figure 4.13: High-resolution core photos from the south wall of Tr3. Included is a cross section profile of the canyon showing the location of each core within the transect.
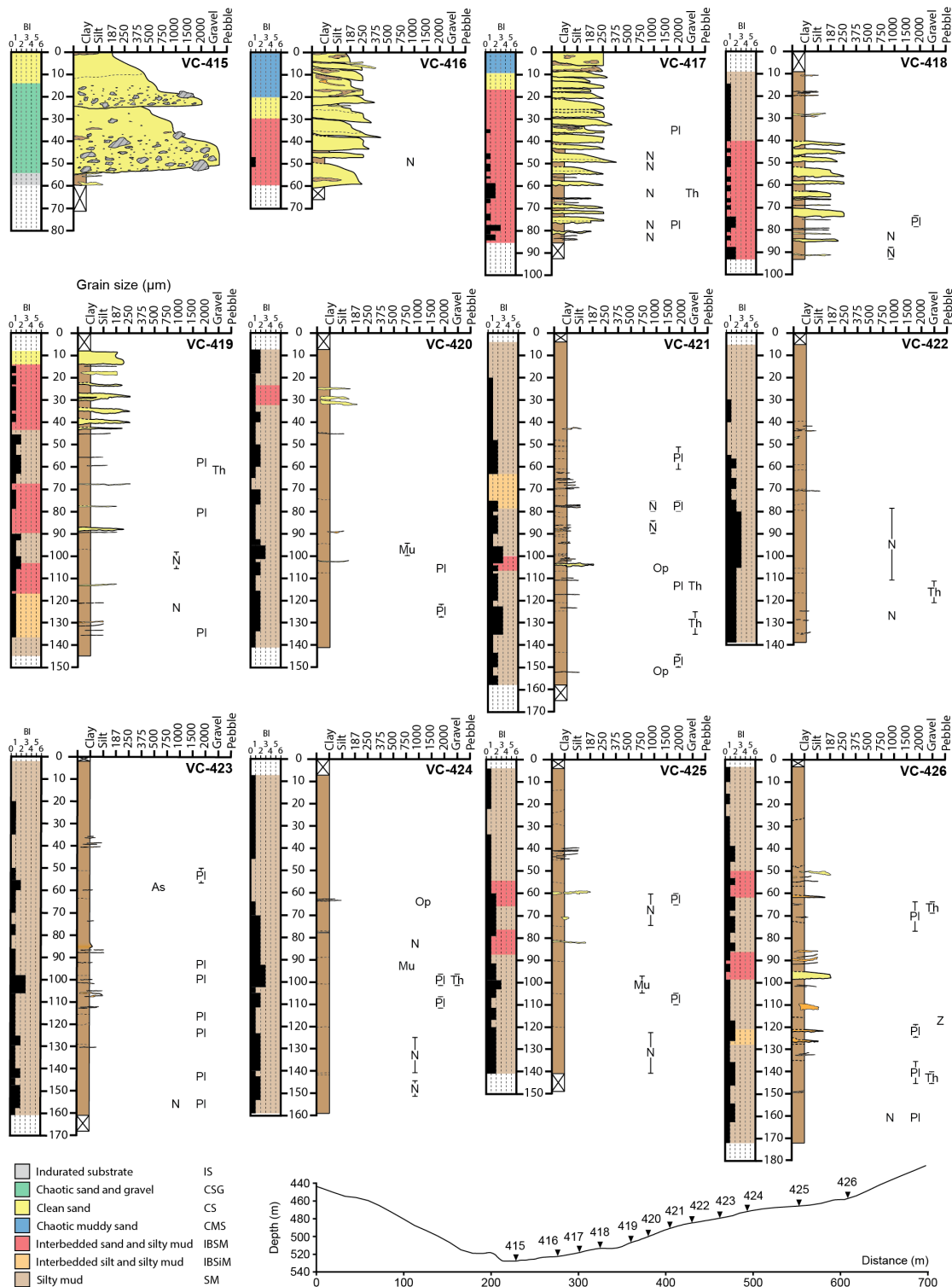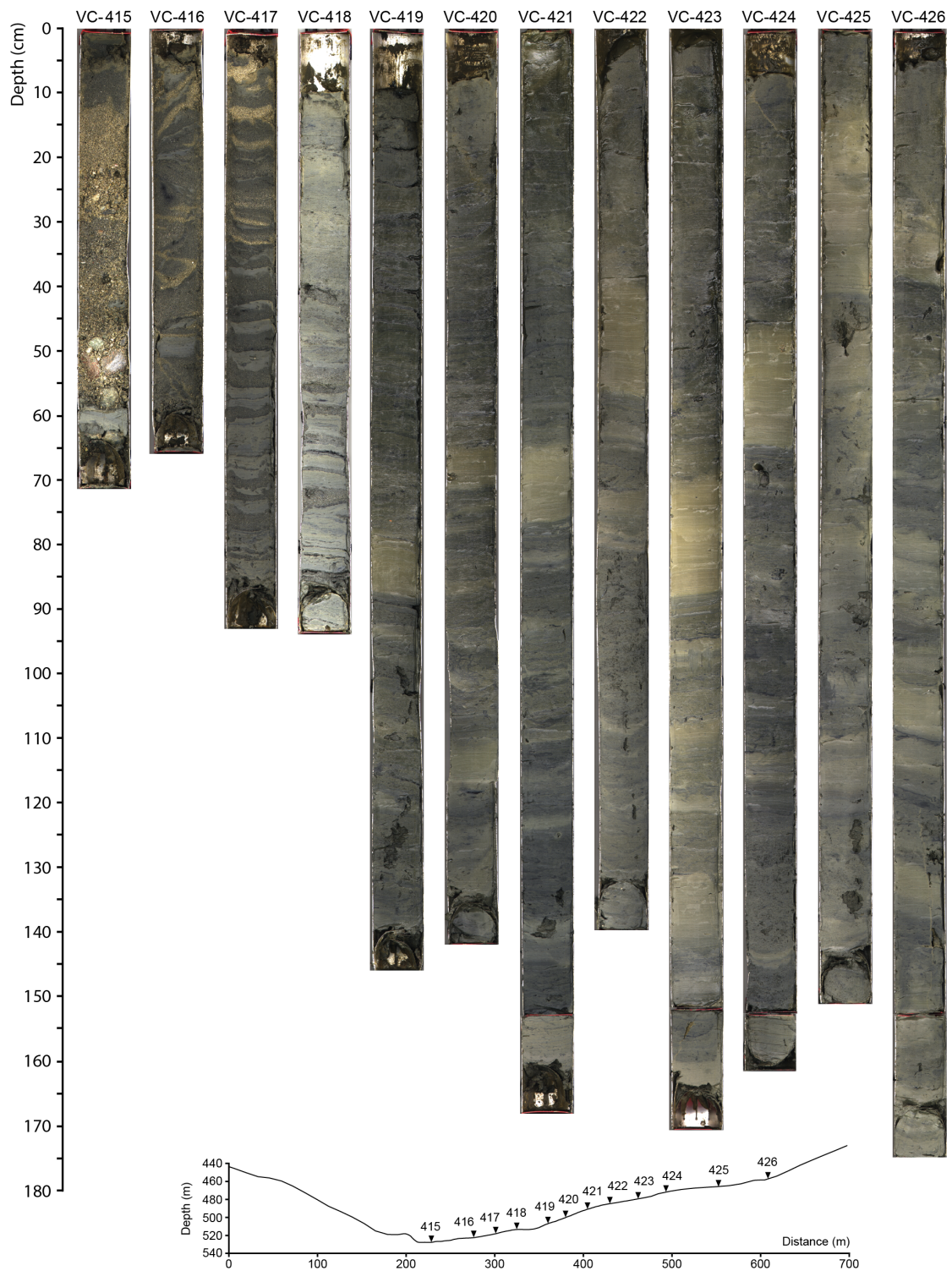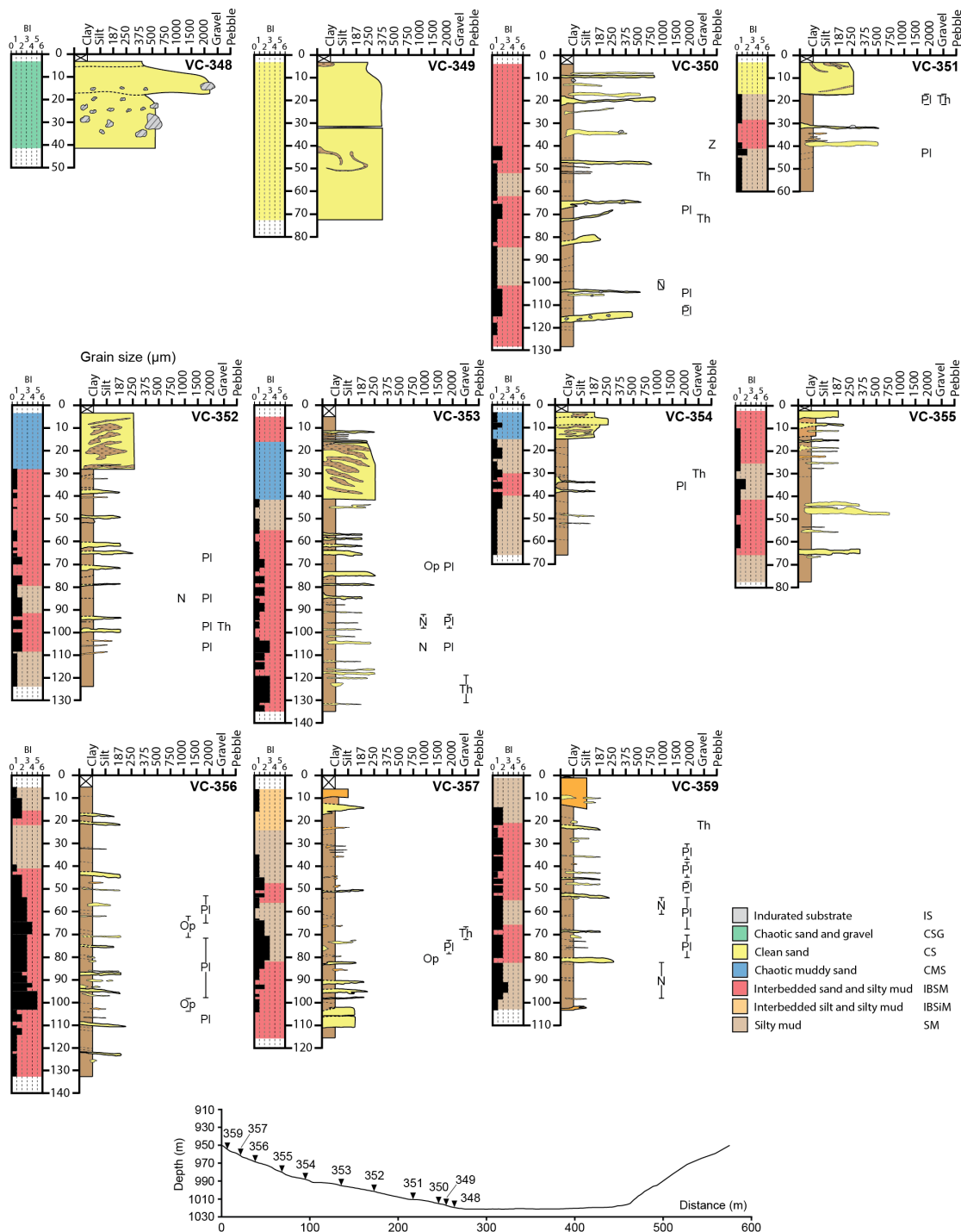
Figure 4.14: Graphical sedimentary logs, bioturbation index, lithofacies, and ichnofabric distribution for the south wall of Tr4. Included is a cross section profile of the canyon showing the location of each core within the transect. N - *Nereites*, Op - *Ophiomorpha*, Pl - *Planolites*, Th - *Thalassinoides*, Z - *Zoophycos*.
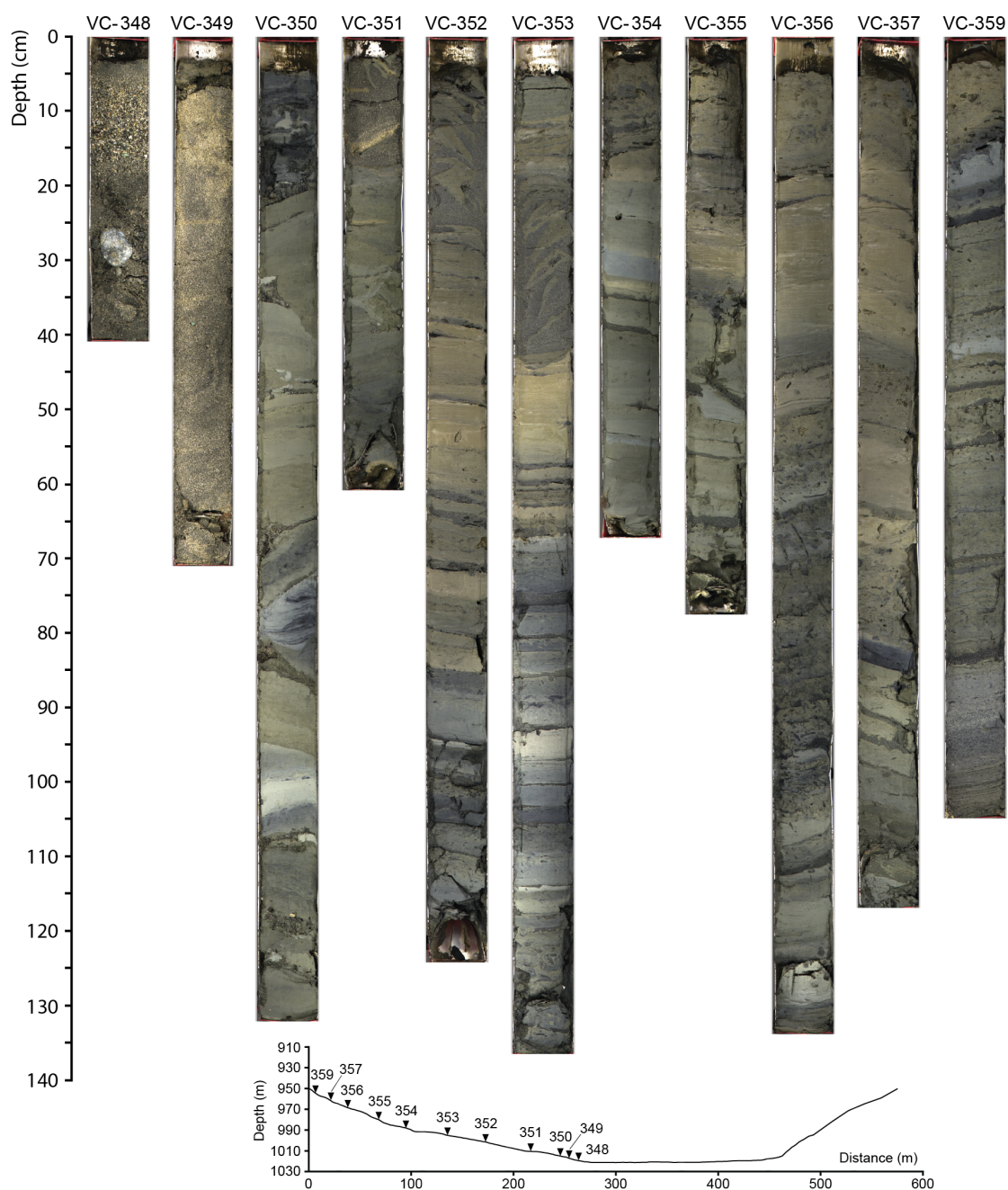
Figure 4.15: High-resolution core photos from Tr4. Included is a cross section profile of the canyon showing the location of each core within the transect.
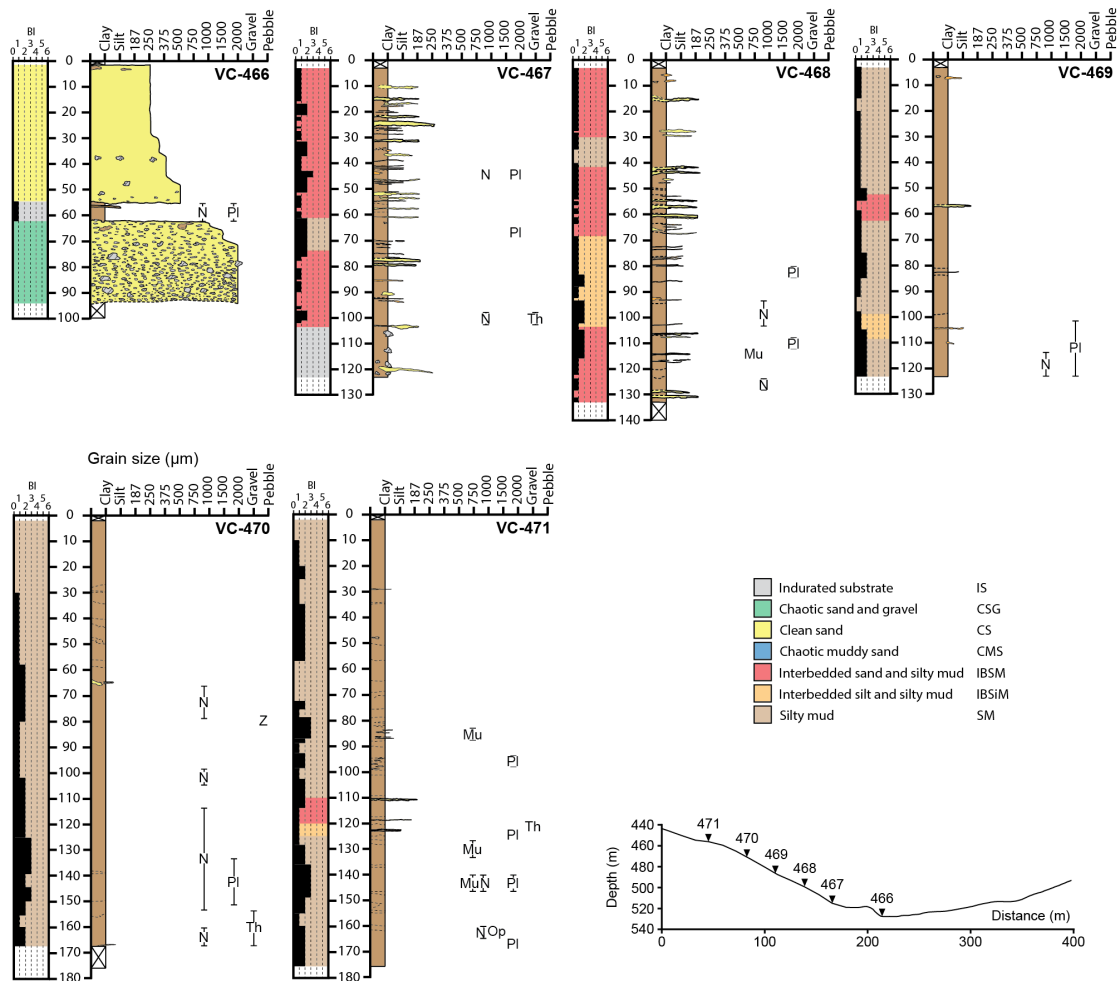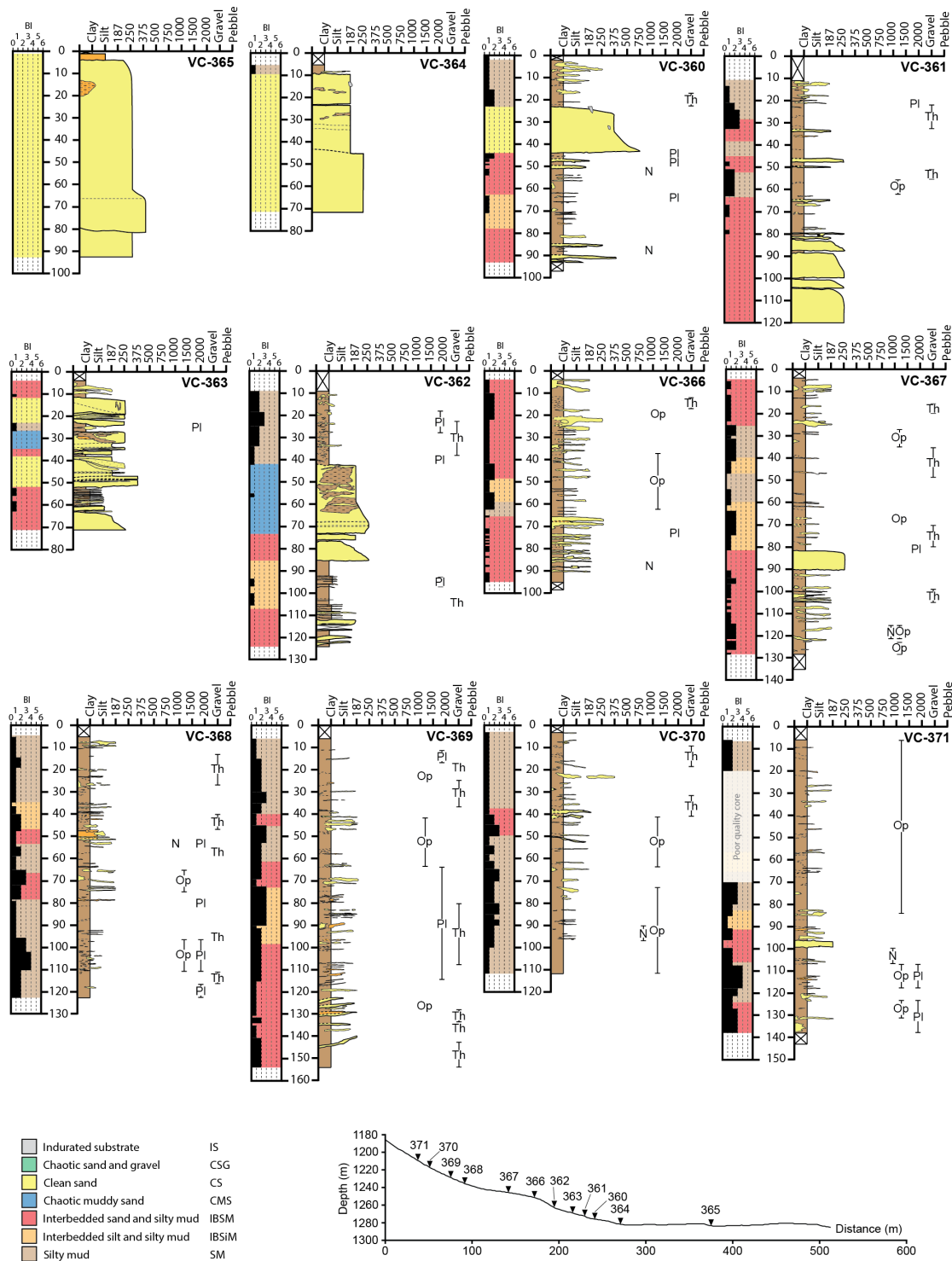
Figure 4.16: Graphical sedimentary logs, bioturbation index, lithofacies, and ichnofabric distribution for the south wall of Tr5. Included is a cross section profile of the canyon showing the location of each core within the transect. N - *Nereites*, Op - *Ophiomorpha*, Pl - *Planolites*, Th - *Thalassinoides*.
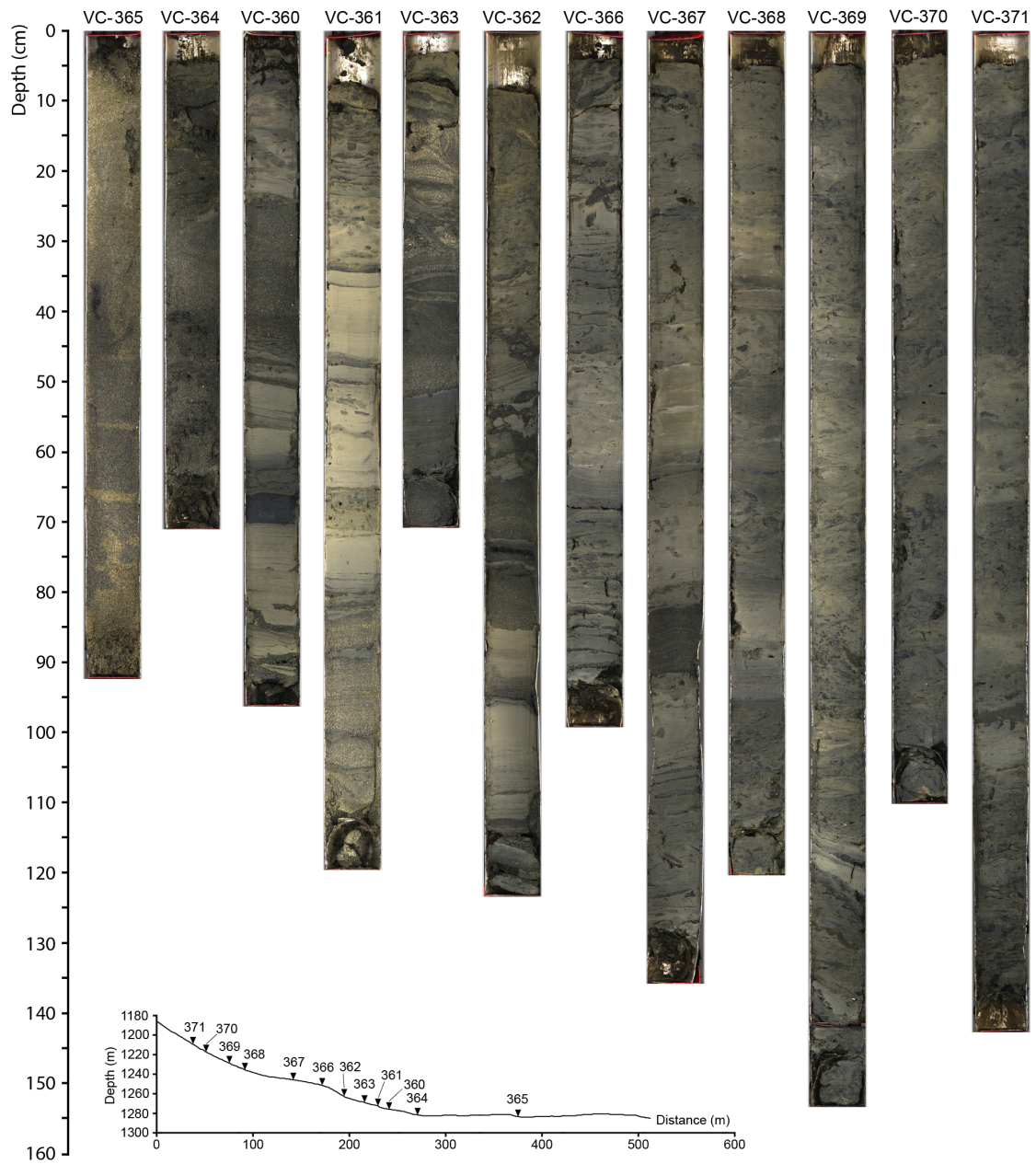
Figure 4.17: High-resolution core photos from Tr5. Included is a cross section profile of the canyon showing the location of each core within the transect.
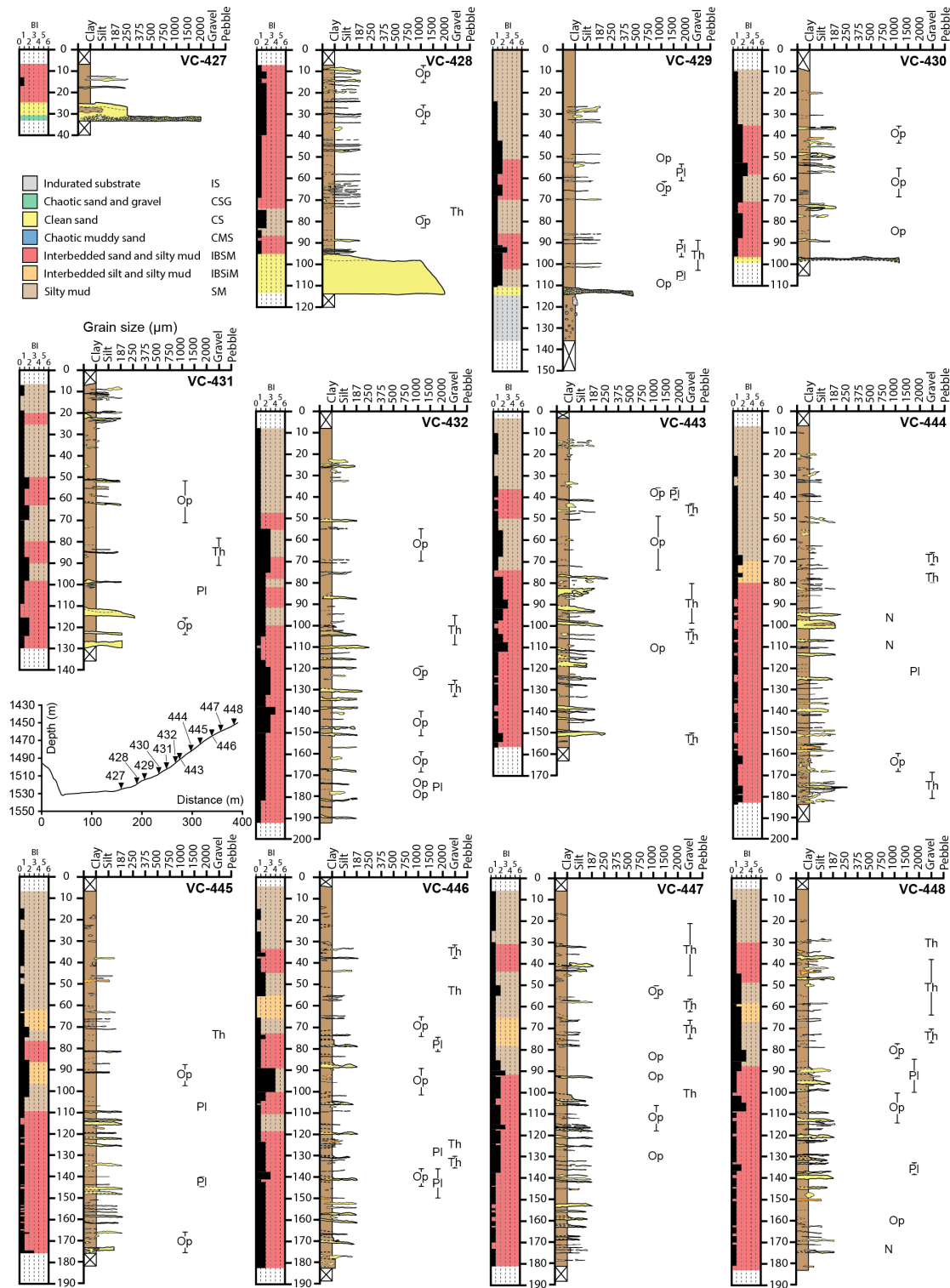
Figure 4.18: Graphical sedimentary logs, bioturbation index, lithofacies, and ichnofabric distribution for the north wall of Tr6. Included is a cross section profile of the canyon showing the location of each core within the transect. N - *Nereites*, Op - *Ophiomorpha*, Pl - *Planolites*, Th - *Thalassinoides*.
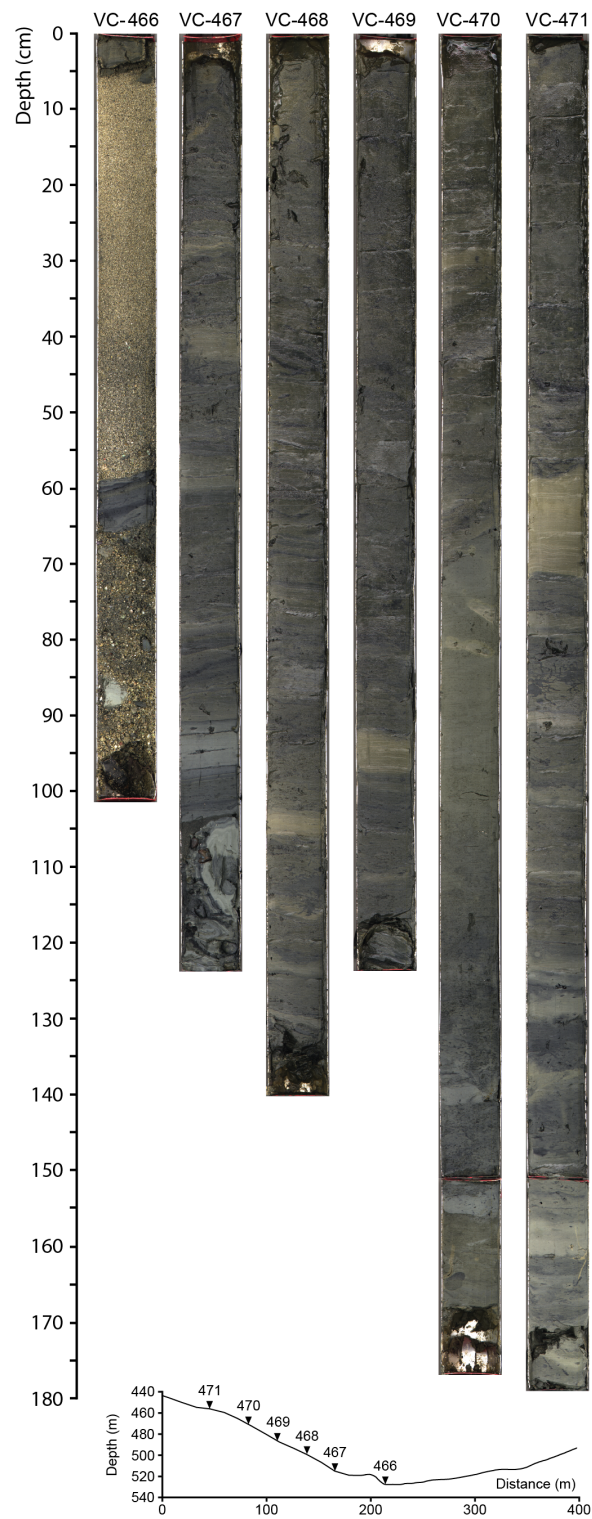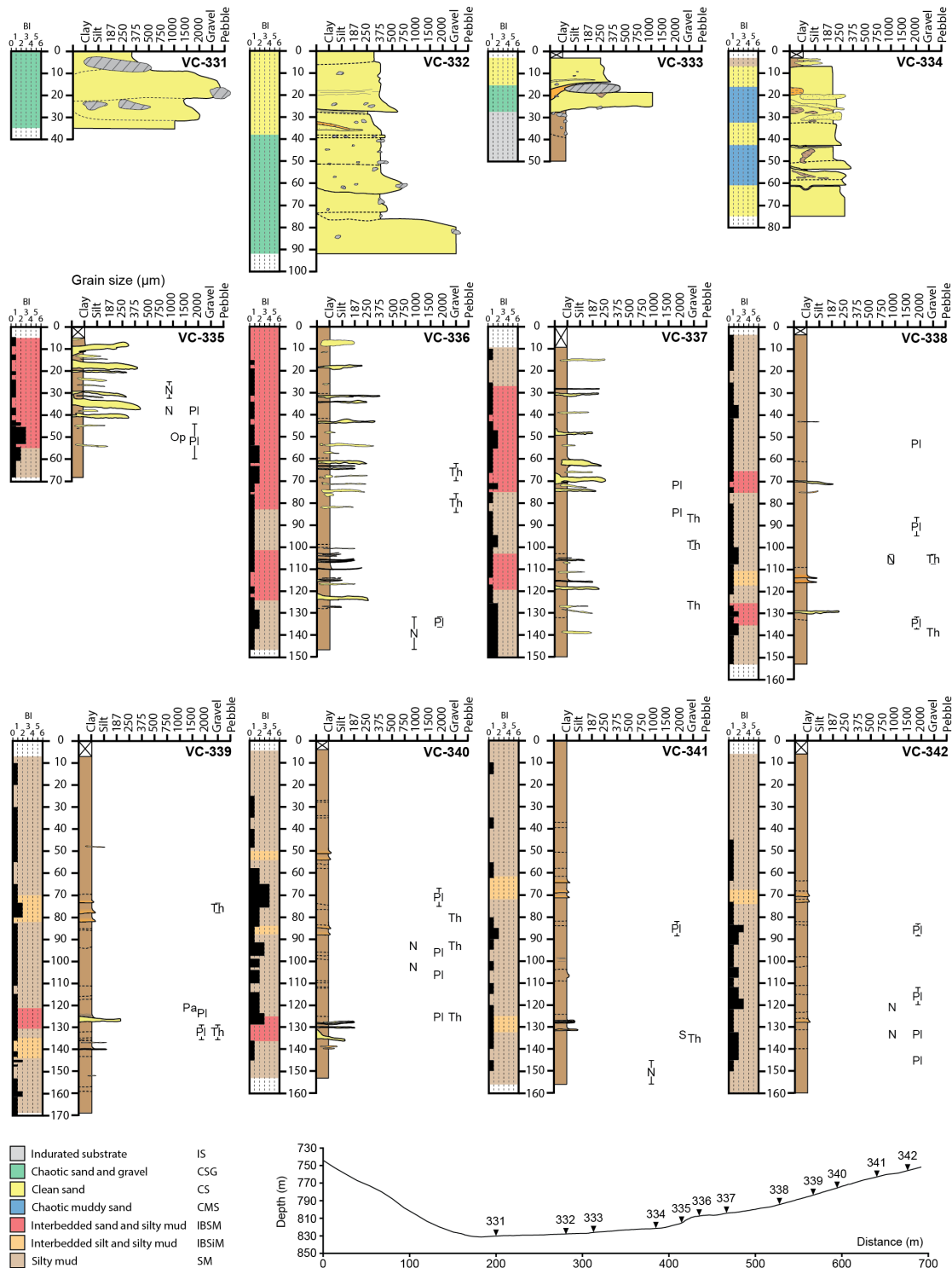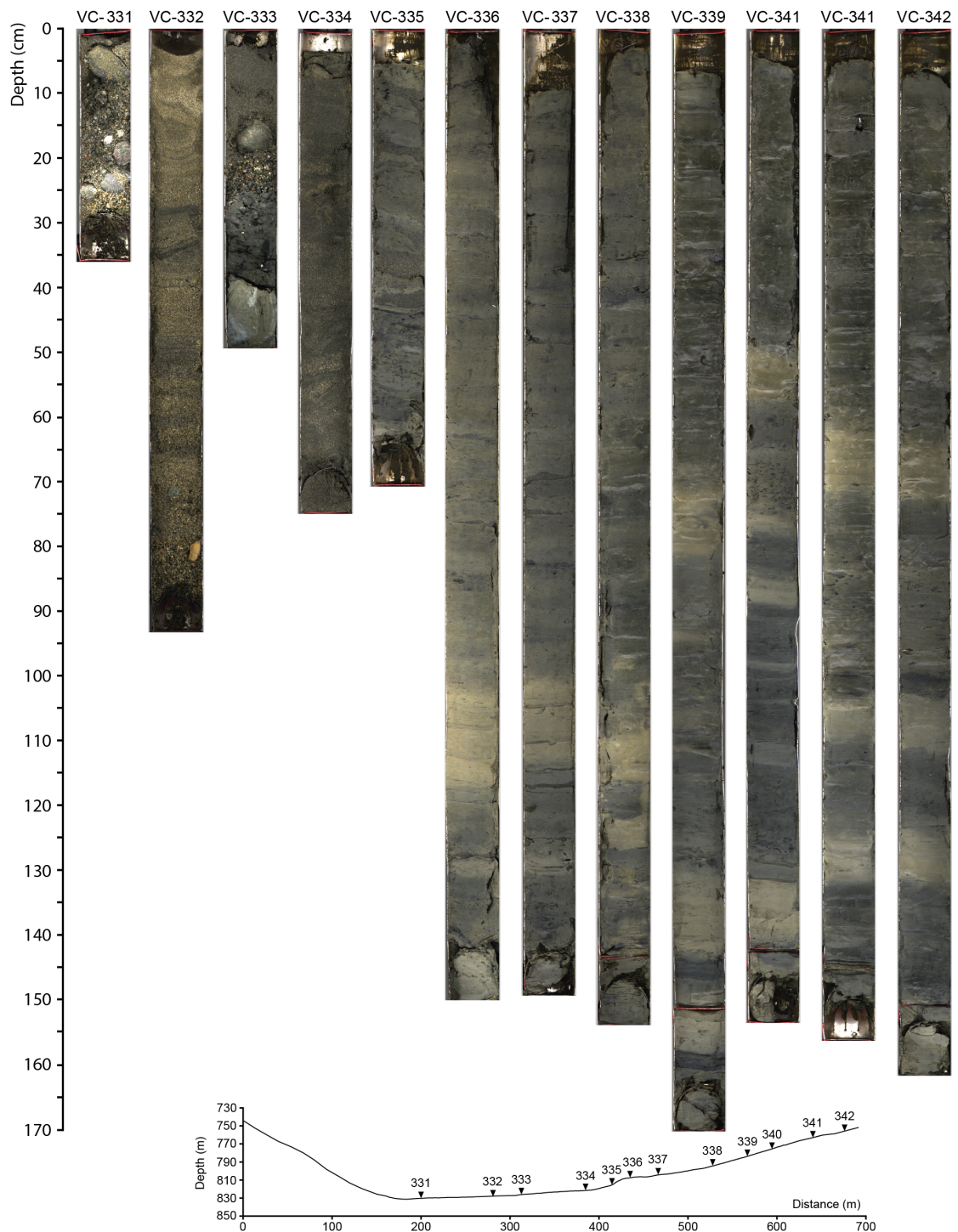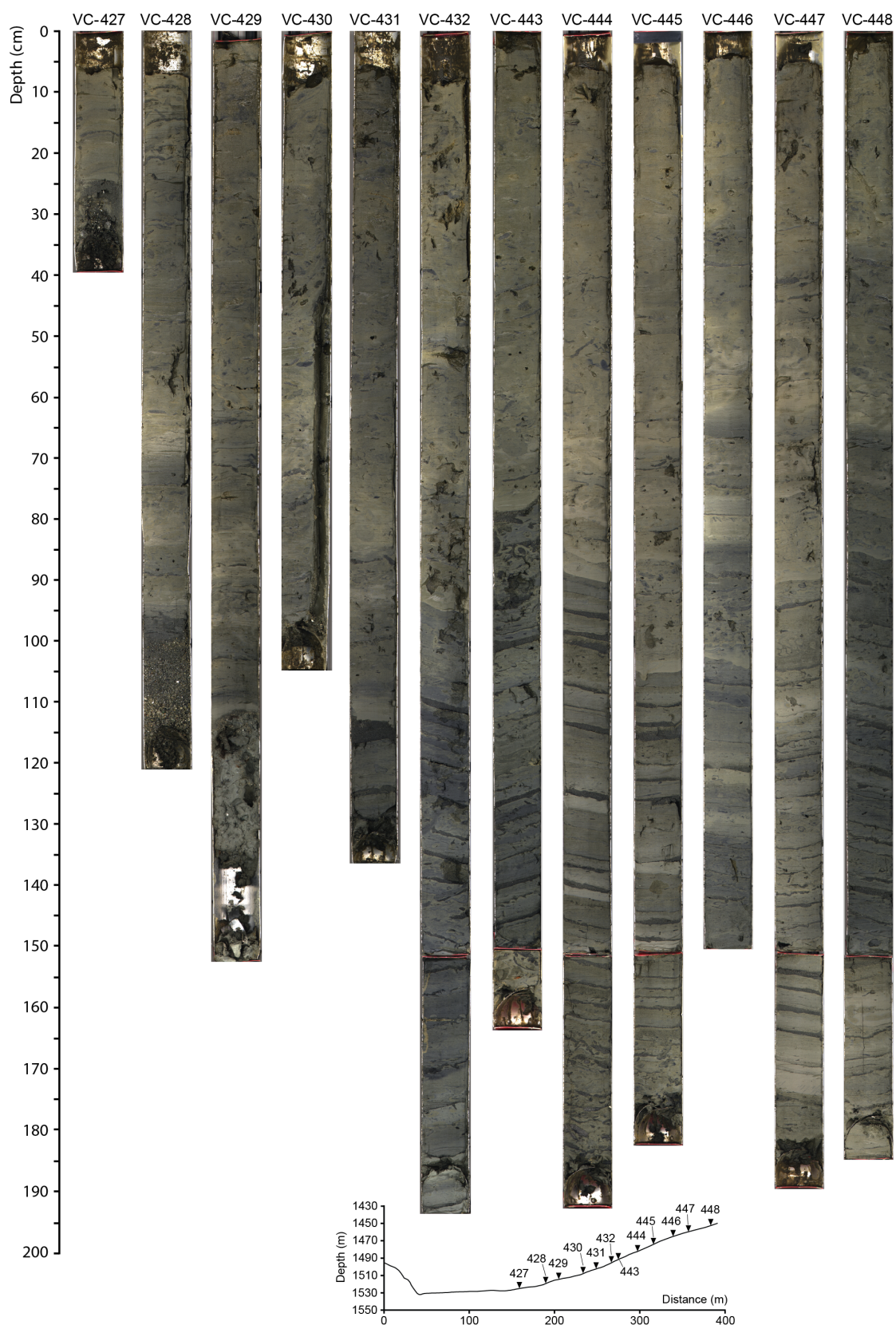
Figure 4.19: High-resolution core photos from Tr6. Included is a cross section profile of the canyon showing the location of each core within the transect.

4.3.2   Ichnofabrics

Traces were identified in vertical cross-section and defined at the ichnogenus level. The overall trace fossil assemblage is comparable to assemblages described from similar channelised turbidite settings (e.g. Heard and Pickering 2008; Callow et al., 2013a,b; Heard et al., 2014). Primary traces identified were *Arenicolites*, *Asterosoma*, *Multina*, *Nereites*, *Ophiomorpha*, *Palaeophycus*, *Planolites*, *Skolithos*, *Thalassinoides*, and *Zoophycos* (figure 4.20). Here we outline each ichnogenus with visual descriptions,

Ichnofabric codes	
Ar	*Arenocolites*
As	*Asterosoma*
Mu	*Multina*
N	*Nereites*
Op	*Ophiomorpha*
Pa	*Palaeophycus*
Pl	*Planolites*
Sk	*Skolithos*
Th	*Thalassinoides*
Z	*Zoophycos*
Bs	*Biodeformed substrate*
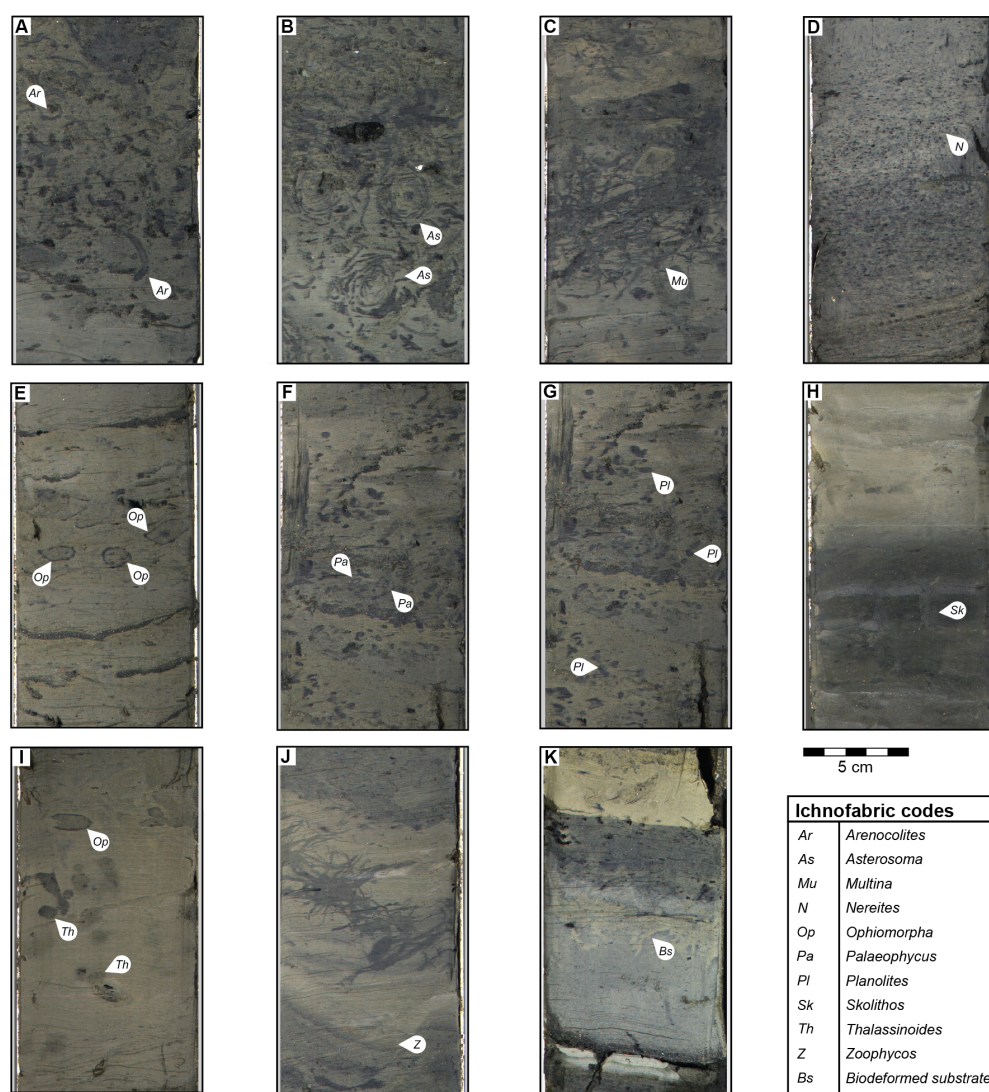
Figure 4.20: Photographs of split ROV-collected vibracores collected from the terraces and walls of Monterey Canyon that highlight the observed ichnological traces. (A) *Arenicolites*, (B) *Asterosoma*, (C) *Multina*, (D) *Nereites*, (E) *Ophiomorpha*, (F) *Palaeophycus*, (G) *Planolites*, (H) *Skolithos*, (I) *Thalassinoides*, (J) *Zoophycos*, (K) Biodeformed substrate.

typical known depositional environments, and distribution and associated ichnogenera within Monterey Canyon. Together, these are used to define ichnofabrics. Although multiple taxa may be present within a specific interval, no crosscutting relationships were able to be determined for analysis of tiering. Detailed taxonomic descriptions are beyond the scope of this paper, but notable features are outlined in table 4.3.

Table 4.3: Ichnofabrics identified with the Monterey Canyon vibracores.

Ichnogenus	Code	Description	Typical depositional environment	Distribution	Associated ichno-genera	Ichnofabric
Arenicolites	Ar	Unbranched U-shaped burrow typically with mud lining (some examples unlined) that have been passively filled. Tube diameter 2-4 mm. Complete burrows not observed with J-shaped, elliptical (typically elongate), and circular forms typical depending on orientation of core (vertical vs. sub-vertical)	Known from a wide range of continental to deep-marine environments, and commonly with high-energy deposition. Mass occurrence in low diversity is indicative of stressed environments e.g. reduced or fluctuating salinity	Only occurrence is at Tr3 (833 m water depth) and at low altitudes (<30 m-alt)	*Planolites,* *Asterosoma*	*Arenicoloites,* ***Arenicolites-Planolites***
Asterosoma	As	Overall circular trace of concentric (incomplete) mud filled traces surrounding a central, often somewhat twisted axis. Overall trace up to 4 cm in diameter with individual concentric tube diameter of 1-3 mm	Commonly reported from marginal-to deep-marine environments. May have the potential to identify well-oxygenated settings (Uchman and Wetzel, 2011) close to the axis of turbidity current and sediment gravity flows (Callow et al., 2013a). Recently reported in deep-marine settings associated with thin-bedded turbidite facies (Phillips et al., 2010)	Restricted to Tr2 and Tr3 (530 and 833 m) with main occurrence at 20 and 30 m. Individual occurrences seen at 50 m and 80 m (altitude bin)	*Arenicolites,* *Planolites*	*Asterosoma,* ***Asterosoma-Arenicolites****,* *Asterosoma-Planolites*
Multina	Mu	Irregular, cylindrical, horizontal to sub-horizontal, mud filled, unlined burrow network. Variable, but typically high density of overlapping between branches to form large areas of amalgamated burrows. Individual burrow diameters range from <1-3 mm	Commonly recorded in shallow marine deposits but more recently occurrence is seen in deeper-marine environments (Buatois et al., 2009), in very fine to fine-grained, low energy systems	Restricted to Tr1 and Tr2 (300 and 530 m). Not found at lower altitudes but spans altitudes from 30-80 m-alt (lower energy as per environmental considerations)	*Planolites,* *Thalassinoides,* *Planolites-Nereites*	*Multina,* ***Multina-Planolites****,* *Multina-Thalassinoides,* ***Multina-Planolites-Nereites***

Table 4.3 – *Continued from previous page*

Ichnogenus	Code	Description	Typical depositional environment	Distribution	Associated ichno-genera	Ichnofabric
Nereites	N	Occurs as a mass of horizontal burrows (typically as circular cross-sections), <1 mm in diameter. Primarily identified by the halo of reworked sediment around the primary burrow	A typical element of deep-sea deposits, in sediment deposited under moderate energy (Wetzel, 2002). Does occur in shallow water also, e.g. sandy estuarine deposits. Forms within oxygenated sediment	Found at all transects (Tr1-6) and all altitudes (up to 80 m-alt)	*Ophiomorpha, Planolites, Thalassinoides, Multina-Planolites*	*Nereites*
Ophiomorpha	Op	0.5-2 cm diameter circular to cylindrical (in cross section) burrows; more elongate when seen longitudinally. Occasional vertical sections seen that branch out into horizontal burrow system. Passive burrow fill is the same material as the host sediment and is structureless. The walls of the cylindrical trace are smooth and mostly completely lined with pelletoidal sediment. Typically complex burrow systems with multiple traces but occasional single, simple traces are present	A common trace that can appear in a wide range of environments. Although not exclusively, a typically component of high-energy environments, both in shallow- and deep-marine settings. Considered diagnostic of sand-rich turbidite systems, from axial, terrace, and levee settings (Callow et al., 2013b)	Found at all transects (Tr1-6) and all altitudes (up to 80 m-alt)	*Nereites, Planolites*	*Ophiomorpha,* **Ophiomorpha-Nereites***, Ophiomorpha-Planolites*
Palaeophycus	Pa	Horizontal to sub-horizontal, and circular or elliptical in cross-section, unbranched burrows with a lining and passive fill. Ranges in size from 3-8 mm. Typically occur as a small number (<5) or single burrows	Occurs in both marine and continental environments, and is reported from marginal-marine, through continental slopes, to deep-sea fans	Restricted to Tr1 and Tr3 (300 and 833 m), and from 30-70 m-alt	*Planolites*	*Palaeophycus*

Continued on next page

Table 4.3 – *Continued from previous page*

Ichnogenus	Code	Description	Typical depositional environment	Distribution	Associated ichnogenera	Ichnofabric
Planolites	Pl	Typically observed in cross-section and is circular to elliptical. When observed longitudinally, Planolites is horizontal. A simple unlined and unbranched burrow with a different, unstructured muddy fill to the host sediment. Diameter of trace ranges from 1-5 mm	Observed in all aquatic environments, with abundance closely linked to how well bottom waters are oxygenated. A very abundant trace in most Ichnofacies not considered useful as a palaeoenvironmental indicator (Callow et al., 2013b)	The most abundant ichnofabric observed in this system and found at all transects and altitudes	*Multina*, *Multina-Nereites*, *Ophiomorpha*, *Nereites*, *Palaeophycus*, *Thalassinoides*	*Planolites*, ***Planolites-Nereites***, *Planolites-Palaeophycus*, ***Planolites-Thalassinoides***
Skolithos	Sk	Unbranched, vertical, unlined burrow with a curved (concave) base. Passively infilled with mud. Ranges from 0.3-1 cm wide and 0.6-2 cm deep	A common indictor of relatively high-energy environments, from shallow-water to marginal-marine environments. Also common in deep-marine submarine channels and canyons	Restricted to Tr3 (833 m) and to <30 m-alt	None	*Skolithos*
Thalassinoides	Th	Similar to Ophiomorpha but lacking burrow lining. Burrows are circular to elliptical in cross-section with a smooth wall. Burrows range in diameter from 4-12 mm and typically occur as a dense network of burrows and occasionally as a single burrow	Most common in, but not limited to, shallow-marine environments, with examples also observed in deep-marine channel and fan systems (e.g. Heard and Pickering, 2008)	Found at all transects (Tr1-6) and all altitudes (up to 80 m-alt)	*Multina*, *Planolites*, *Nereites*	*Thalassinoides*, ***Thalassinoides-Nereites***
Zoophycos	Z	In cross-section, appears as 0.5-1.3 cm (diameter) horizontal to sub-horizontal burrow. Poorly preserved internal laminae preserve the previous position of the active burrow	Observed in deposits from shallow shelf to deep basin floor and can be common in turbidites	Observed at Tr1, Tr2 and Tr4 (300, 533, 1018 m) but restricted to greater altitudes (70-80 m-alt)	None	*Zoophycos*

4.3.3 Controls on lithofacies distribution

Altitude has the strongest statistical significance on the distribution of litho-facies (multinomial logistic regression, $p < 0.001$ for all lithofacies). Coarse-grained facies (CSG, CS) are restricted primarily to the thalweg of the canyon and terraces. As altitude above the thalweg increases, deposits become finer until silty mud deposition dominates. Indurated substrate is found at lower altitudes on the canyon wall despite being fine-grained. Water depth is not statistically significant in the distribution of lithofacies except for two cases: indurated substrate (multinomial logistic regression, $p = 0.04$) and interbedded sand and silty mud (multinomial logistic regression, $p = 0.009$) (figure 4.21). As lithofacies is shown to be influenced by altitude, lithofacies will not be used in conjunction with altitude in further statistical tests.
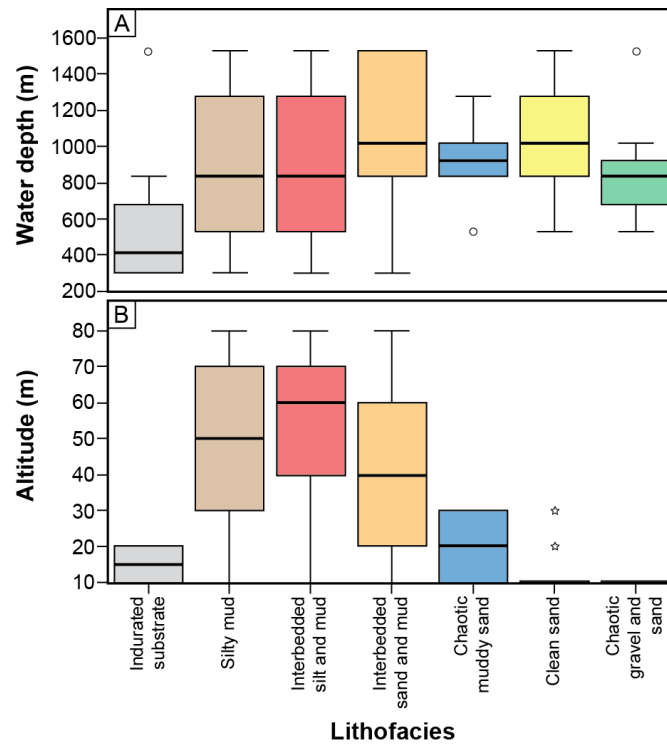
Figure 4.21: Plots showing the distribution of lithofacies across (A) water depth and (B) altitude. The extent of each box defines the 25th percentile (bottom) and 75th percentile (top), with the solid black line defining the median value. The whiskers define 1.5 times the interquartile range (IQ). Outliers (circles; 1.5-3 times IQ) and extreme outliers (stars; >3 times IQ) are shown. Colours used for the lithofacies here are consistent throughout all figures.

4.3.4   Controls on bioturbation index distribution

Altitude has the strongest statistical significance on the distribution of bioturbation index (ordinal logistic regression, $p < 0.001$), whereas water depth is not controlling on bioturbation index (ordinal logistic regression, $p = 0.515$) (figure 4.22). As altitude above the thalweg increases, the intensity of bioturbation increases, whereas bioturbation index appears consistent across all water depths, apart from the highest category seen (5), which primarily occurs in shallower water depths. Lithofacies is also seen to have a significant effect on the distribution of bioturbation index (Kruskal-Wallis test, $p < 0.001$), indicating that the two co-vary and are both affected by altitude.
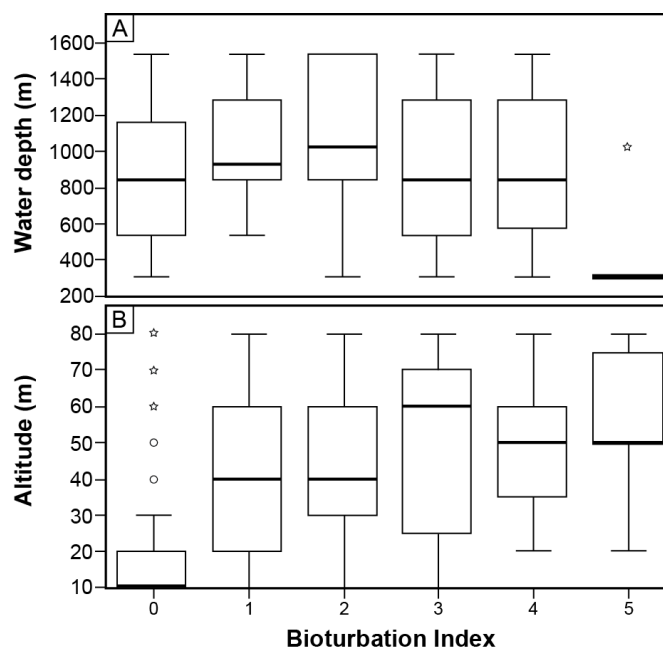
Figure 4.22: Plots showing the distribution of Bioturbation Index across (A) water depth and (B) altitude. The extent of each box defines the 25th percentile (bottom) and 75th percentile (top), with the solid black line defining the median value. The whiskers define 1.5 times the interquartile range (IQ). Outliers (circles; 1.5-3 times IQ) and extreme outliers (stars; >3 times IQ) are shown.

4.3.5   Controls on ichnofabric distribution

The statistical analysis into the control on the distribution of ichnofabrics by altitude and water depth is not as conclusive as the statistical analysis of lithofacies
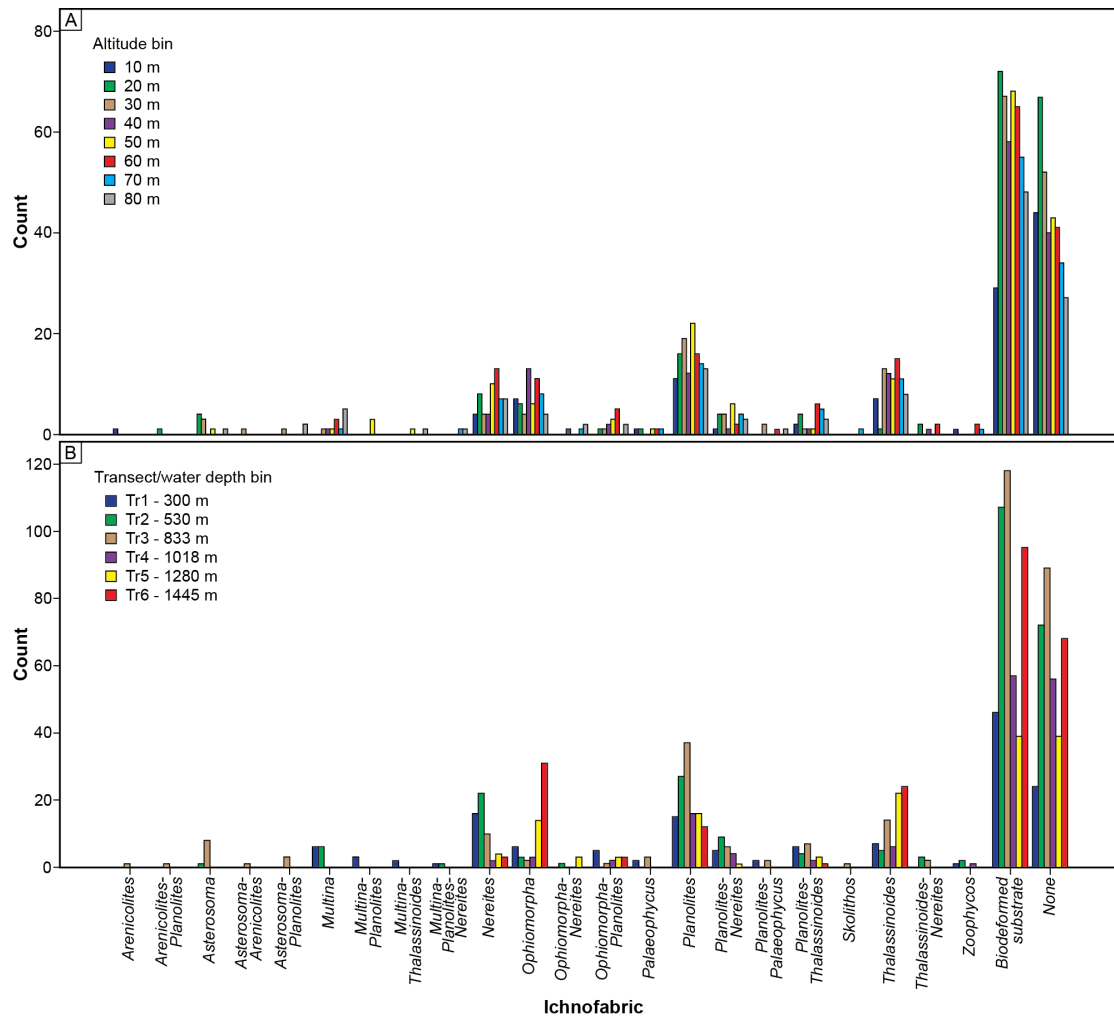
Figure 4.23: Plots showing the distribution of all ichnofabrics and associations for (A) altitude and (B) transect/water depth. Altitudes have been grouped into 10 m bins. Water depth was taken as the deepest point of a given transect.

and bioturbation index. The large number of identified traces and subsequent ichnofabrics has resulted in a small count number for most ichnofabrics (e.g., for *Arenicolites-Planolites*, *n*=1) (figure 4.23). To provide a more detailed statistical analysis on the controls of ichnofabric distribution, the total number occurrences counted had to be 12 or greater for inclusion in the statistical analysis (*n*=12 is 1% of total trace count). The ichnofabrics taken forward into the statistical analysis are *Nereites*, *Ophiomorpha*, *Ophiomorpha-Planolites*, *Planolites*, *Planolites-Nereites*, *Planolites-Thalassinoides*, and *Thalassinoides*.

Statistical analysis (Multinomial logistic regression) into the distribution of the
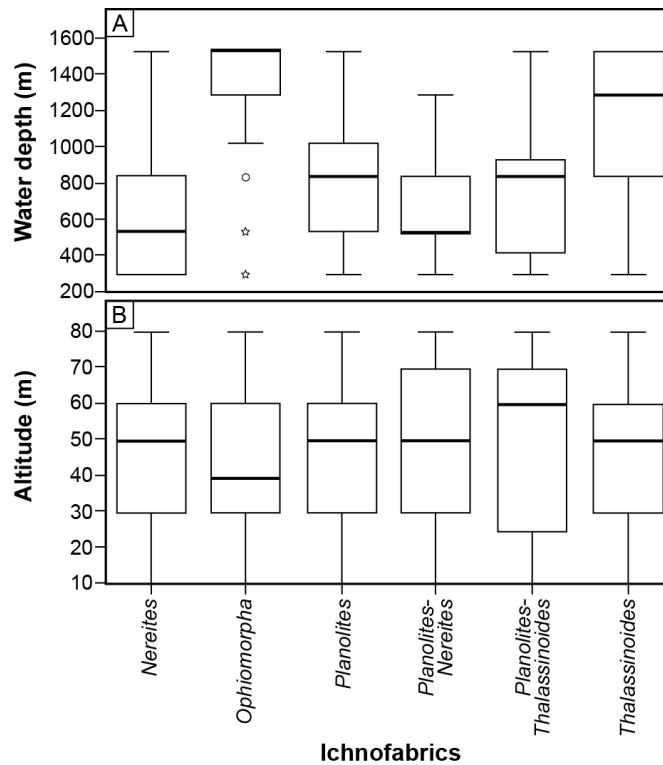
Figure 4.24: Plots showing the distribution of the most abundant ichnofabrics and associations across (A) water depth and (B) altitude. The extent of each box defines the 25th percentile (bottom) and 75th percentile (top), with the solid black line defining the median value. The whiskers define 1.5 times the interquartile range (IQ). Outliers (circles; 1.5-3 times IQ) and extreme outliers (stars; >3 times IQ) are shown.

above ichnofabrics with regards to altitude and water depth show that water depth is statistically significant ($p < 0.001$) for analysed ichnofabrics, except for the *Ophiomorpha-Planolites* ichnofabric ($p = 0.09$). Altitude is not statistically significant in the distribution of ichnofabrics (figure 4.24). Due to the significance of water depth, the distribution and abundance of each ichnofabric is summarised below (see table 4.3 for details of both water depth and altitude):

i. The *Nereites* ichnofabric is found at all water depths and is most abundant at proximal transects (Tr1 and Tr2) with a general decrease in abundance with increasing water depth.

ii. The *Ophiomorpha* ichnofabric is found at all water depths and increases in abundance with increasing water depth.

iii. The *Planolites* ichnofabric is the most abundant and is found at all water depths. Whilst more abundant at shallower transects, abundance peaks at Tr3 (and to a lesser extent Tr2). The *Planolites-Nereites* ichnofabric decreases in abundance with water depth and is not observed at the deepest transect (Tr6). The *Planolites-Thalassinoides* ichnofabric is observed at all transects with a decrease in abundance with increasing water depth.

iv. The *Thalassinoides* ichnofabric is observed at all transects with a general trend of increasing abundance with increasing water depth.

4.4   Discussion

Altitude is shown to be the primary control on the distribution of lithofacies and bioturbation index, and water depth is the significant controlling factor for ichnofabric distribution. Here, the sedimentary processes operating in Monterey Canyon are used to explain the potential controlling factors on the distribution of sedimentary deposits and biological structures.

4.4.1   Why is altitude a significant control on the distribution of lithofacies and bioturbation index?

It is unsurprising that lithofacies and bioturbation index are controlled by altitude, as there is a statistical dependence on the distribution of bioturbation index by lithofacies (Kruskal-Wallis test, $p < 0.001$). This significance is expected, as the traces identified throughout the cores are restricted to the fine, mud-rich deposits.

To understand the observed facies and bioturbation distribution the specifics of turbidity current transformation through Monterey Canyon are considered. The distribution of sediment within confined systems is strongly governed by the evolution of the flows that transport the sediment, typically turbidity currents (e.g. Pirmez et al., 2003; Symons et al., 2017). Turbidity currents monitored in Monterey Canyon (Xu et al., 2004) begin as thin, highly energetic flows that transport coarse-grained facies (CSG, CS) (Symons et al., 2017). These facies are restricted to low altitudes and are comprised

of sand and gravel with no mud content in the resultant deposits, therefore limiting the bioturbation potential at low altitudes. As the flow evolves both in time and space, the head gradually thickens, depositing the individual beds of the interbedded units (IBSM, IBSiM) at increasingly higher altitudes on the canyon walls (Symons et al., 2017). The increasing presence and thickness of mud-rich horizons at greater altitude above the local thalweg provides suitable sediment for colonisation and therefore a greater intensity of bioturbation between sandy flow deposits. The final stage of evolution for these confined flows is expansion along the length of the turbidity current, depositing silty mud up to the highest altitudes sampled (Symons et al., 2017). The small-scale deposit architecture within a confined turbidite system is predominantly controlled by the vertical structure of the parent flow, in particular grain size segregation (e.g. Pirmez and Imran, 2003; Jobe et al., 2010; Symons et al., 2017). Whilst water depth does result in differences between proximal and distal occurrences of the same facies (e.g. distally, sand facies are finer), each facies is present throughout the system.

A primary control on bioturbation is the substrate, with greater levels of bioturbation occurring in fine-grained deposits, and hence at lower energy levels. The distribution of silty mud at high altitudes above the local thalweg by an expanding turbidity current provides a more hospitable environment for benthic biological activity. Coupled with this are the energy conditions experienced at different altitudes, linked to the turbidity current velocities. The acoustic Doppler current profiler (ADCP) velocity profiles of turbidity currents in Monterey Canyon show peak velocities of 1.9 m/s at ~6-12 m-alt (Xu, 2010; Xu et al., 2014; Symons et al., 2017). It is suggested however that these stated velocities may be an underestimate, as instrument limitations (sampling resolution and lack of penetration to the seafloor) means the fastest part of the flow (possibly up to 6 m/s) is not captured (Xu et al., 2014; Symons et al., 2017). These high velocities allow for the coarse sediment to be transported and deposited but also result in a more hostile environment for biological activity compared to higher altitudes where turbidity current velocities are much lower (e.g. 0.2-0.3 m/s), which are similar to background tidal current values. Additionally, previous studies have shown that despite the peak velocities being above the canyon floor, the thalweg is highly energetic with heavy (>1000 kg) instruments moved and broken without leaving the seafloor (Paull et

al., 2003; 2010a).

4.4.2 Why is water depth a significant control on the distribution of ichnofabrics?

An important factor to consider when examining the effects of water depth is the specific ichnofabric. The six ichnofabrics whose abundance are significantly controlled by water depth are *Nereites*, *Ophiomorpha*, *Planolites*, *Planolites-Nereites*, *Planolites-Thalassinoides* and *Thalassinoides*. These six ichnofabrics can be divided into two groups based on their changing abundance in relation to water depth; *Nereites*, *Planolites*, *Planolites-Nereites* and *Planolites-Thalassinoides* are more abundant in shallower water (<800 m), whereas *Ophiomorpha* and *Thalassinoides* are more abundant in deep water (>800 m). Taylor et al. (2003) suggest that grain size, nature of the substrate, oxygenation, sedimentation rate, nutrient levels, and colonisation window are variables that contribute to ichnofabric distributions; each of these factors are also linked to water depth. The distribution of the above ichnofabrics and possible processes and factors that contribute to the observed distributions are now outlined.

One of the key effects on ichnofabric distribution that can be examined in detail here is the colonization window (Pollard et al., 1993). Over recent years, studies on the processes that occur within Monterey Canyon have revealed important insights into turbidity current behaviour (e.g. Garfield et al., 1994; Greene et al., 2002; Paull et al., 2003, 2005; Xu et al., 2004, 2014; Xu, 2010; Johnson et al., 2005; Smith et al., 2005; Symons et al., 2017). Multiple turbidity currents occur within Monterey Canyon each year (Xu et al., 2004; Paull et al., 2010a) but it is rare for these flows to extend beyond 2000 m water depth (Xu, 2011). The last event to pass Shepard Meander (3400 m water depth, 36°13'00"N, 122°52'00"W) occurred c.150 years ago (Johnson et al., 2005). Some monitored events do not exceed 1500 m water depth (e.g. Xu et al., 2004) and highlights that the most proximal transects in this study may be exposed to a higher frequency of turbidity currents than the more distal transects. A limited time for organisms to colonise the seafloor in between high-energy turbidity currents would better suit opportunistic colonisers (Taylor et al., 2003). *Nereites* and *Planolites*, likely

formed by vermiform (worm-like) organisms (Mangano et al., 2000; Pemberton et al., 2001; Phillips et al., 2010; Knaust 2017), are considered to be the traces of opportunistic organisms favouring well-oxygenated sediments (Pervesler et al., 2008). The distribution of these ichnofabrics is therefore likely governed by the relatively high frequency of turbidity currents in the upper reaches of Monterey Canyon, as the colonization window is restricted. The frequency of turbidity currents can also be linked to the abundance of deep-tier traces (e.g. *Ophiomorpha* and *Thalassinoides*) in deeper water. A lower frequency of turbidity currents reaching these more distal sites favours the more stable and mature climax communities (Taylor et al., 2003), as environmental stability is greater and favours the complex burrow networks created by the *Ophiomorpha* and *Thalassinoides* trace makers. Longer residence time of sediments at the surface also leads to the development of firmground substrates in which *Thalassinoides* may be excavated. The distributions of traces with Monterey Canyon broadly show a typical response of organisms to turbidity currents, supporting previous studies that have used ichnofabrics and traces to indicate relative depositional energy and their position within the system (e.g. Kane et al., 2007; Heard and Pickering, 2008; Knaust et al., 2014).

Turbidity current processes in Monterey Canyon are also responsible for other factors that are suggested to govern ichnofabric distribution, such as the grain size and nature of the substrate (Taylor et al., 2003). For example, as turbidity currents travel down system into deeper water, they become more dilute (Xu et al., 2014; Symons et al., 2017), and deposit finer grains (Symons et al., 2017); preferred by different organisms. It is difficult to fully examine the response of ichnofabrics to these factors in this study, as traces are restricted to fine-grained mud. Additional studies should not overlook these factors as a greater diversity of traces could be observed in multiple lithofacies and therefore gain further insights into biological responses to turbidity current activity.

Modern submarine channel and canyon systems contain a greater faunal diversity than the adjacent non-channel regions, primarily due to oxygen and nutrient enrichment (e.g. Griggs et al., 1969; Gardner, 1989; Kane et al., 2007). Previous workers have used bioturbation and traces to recognise variable bottom-water conditions (e.g. Follmi and Grimm, 1990; Wetzel, 1991; Taylor and Goldring, 1993; Ekdale and Mason, 1998; Callow et al., 2014). For example, Vetter and Dayton (1998) show that in La Jolla

canyon (offshore southern California), at 500 m water depth within the canyon, dissolved oxygen levels are significantly higher than at the same water depth in non-canyon areas. By analysing the dissolved oxygen content of the water column from the ROV dives, a trend of decreasing oxygen with water depth occurs until ~800 m. At 800 m water depth the dissolved oxygen content begins to increase with depth (figure 4.25). The lowest dissolved oxygen concentration layer, between ~500-1000 m water depth, defines the oxygen minimum zone (<0.5 ml/L dissolved O_2; Levin, 2003) (figure 4.25). The oxygen minimum zone is present due to oxygen consumption by macro- and microorganisms in the water column (Callow et al., 2014), and is an area with reduced biodiversity. The increase in dissolved oxygen below the oxygen minimum zone is due to the influx of oxygenated waters originating from deep water currents and coastal downwelling of surface waters, coupled with low rates of biological consumption at depth (Seibel, 2011; Callow et al., 2014). The distribution of ichnofabrics within Monterey Canyon somewhat reflect
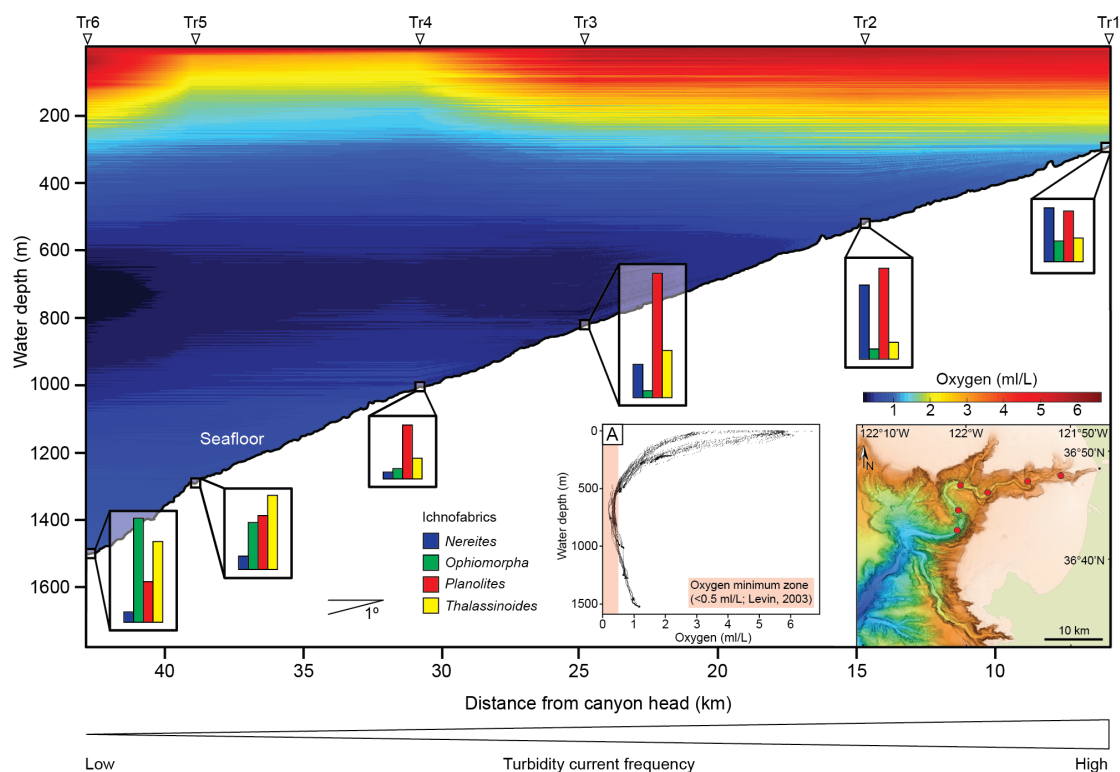
Figure 4.25: Dissolved oxygen concentration contour plot (ml/L) that highlights the oxygen minimum zone with longitudinal thalweg profile. Included are the key ichnofabrics with relative abundance that highlight variation in response to the oxygen minimum zone. The dive profiles (A) highlight the oxygen minimum zone (<0.5 ml/L) between ~500-100 m water depth. The inset map of Monterey Canyon shows each transects location.

the distribution of dissolved oxygen within bottom waters. Callow et al. (2014) suggest that dissolved oxygen concentration is likely a major control on the distribution of large, arthropod traces such as *Ophiomorpha*. *Ophiomorpha* is least abundant at Tr3, Tr4 and Tr5, all of which sit within, or at the boundary of the oxygen minimum zone (530 m, 833 m, and 1018 m water depth respectively). *Nereites* also reflects oxygenation with trace makers preferring well-oxygenated sediment (Knaust, 2017). This is reflected by the distribution of the ichnofabric with the greatest abundance of *Nereites* at Tr1 and Tr2 (300 m and 530 m water depth), where dissolved oxygen concentration is highest. Similarly, the presence of *Planolites* is closely linked to bottom water oxygenation, with an abundance of *Planolites* indicative of well-oxygenated waters (Bromley 1996; Phillips et al., 2010). An abundance of *Planolites* observed at the well oxygenated shallower-water transects shows that the trace making organism is responding to available oxygen within Monterey Canyon.

4.4.3　What does analysis of a modern system reveal about integrating ichnology and sedimentology for palaeoenvironmental reconstruction?

Recent studies have employed a more integrated ichnological and sedimentological approach to deep-water studies by combing knowledge of channel architectures and environmental variables to predict likely faunal, and thus ichnological assemblages expected in different canyon subenvironments (e.g. Kane et al., 2007; Wetzel et al., 2007; Heard and Pickering 2008; Knaust 2009; Hubbard et al., 2012; Phillips et al., 2011; Callow et al., 2013a, 2014; Heard et al., 2014). The significance that this study presents in altitude controlling the distribution of lithofacies and bioturbation index; and water depth in controlling ichnofabrics highlights that integrating ichnological and sedimentological datasets is invaluable for determining specific palaeoenvironments (e.g. height above the thalweg and proximity within the system) in canyon systems. These relationships also highlight that ichnological trends within modern systems can be used for ground-truthing ichnological models from the geological record.

4.4.4 Is Monterey Canyon an accurate representation of ichnological trends globally?

The traces identified within this study are comparable to traces identified from other, albeit ancient submarine canyon systems. The traces identified in this study are distributed across a wide range of altitudes and water depths. These distributions could suggest multiple organisms are producing a single trace (especially for *Planolites*; Pemberton and Frey, 1982) or a single trace-making organism occupies wide water depth ranges. The lack of trace making organisms visible on the seafloor (either because of poor visibility due to turbid water or no organisms present) seen from ROV video footage makes this difficult to determine. The observed distributions may also come from the tolerances of trace makers to environmental variation. Many previous studies analyse a complete system, from channel axis, external levees, and deep-sea fans (e.g. Heard and Pickering, 2008; Callow et al., 2013a; Heard et al., 2014). These studies show distinct ichnological assemblages from these different subenvironments within channel and/or canyon systems. Despite the high resolution transects collected for this study, the restricted environmental variation (relative to the outlined studies above) perhaps limits the ichnological diversity that previous studies of ancient systems have found. The lack of traces within sand horizons has meant that limited comparisons can be made with previous studies of ancient systems. The axial channel of Monterey Canyon is active (Paull et al., 2005), so benthic organisms are unlikely to inhabit the axial channel, and if traces were made, the preservation potential is extremely low. Other, perhaps less active systems would be more likely to exhibit a more complete suite of deep-marine ichnofabrics and be more comparable to previous outcrop studies.

This study has presented the highest resolution study of submarine canyon deposits to date. Monterey Canyon was chosen due to the wealth of existing data on the dynamic processes that occur within this system, and these processes are shown to be vital in interpreting the distribution of lithofacies and ichnofabrics. Canyon systems globally are diverse and complicated systems and the results presented for Monterey Canyon may be very different for other canyons, where sedimentological processes and tidal currents are different. It would be beneficial to pursue the systematic, high-resolution

approach within other modern systems to accurately compare with the results from studies that focus on outcrop from ancient systems, particularly considering variability of sedimentological processes in submarine canyons.

4.5   Conclusions

The distributions of lithofacies, bioturbation index and ichnofabrics have been analysed systematically in a modern submarine canyon; including the axial channel, terraces and canyon walls. A statistical relationship is shown between the distribution of both lithofacies and bioturbation index (itself controlled by lithofacies) and altitude. This relationship is governed by the transformation of turbidity currents through Monterey Canyon as height above the canyon floor dictates velocity and subsequently the grain-size carried and deposited. The low energy levels and muddy substrates that are found at high altitudes above the canyon thalweg are key in promoting a higher level of bioturbation.

The ichnofabrics identified in this study are *Nereites*, *Ophiomorpha*, *Ophiomorpha-Planolites*, *Planolites*, *Planolites-Nereites*, *Planolites-Thalassinoides*, and *Thalassinoides*. These ichnofabrics (except *Ophiomorpha-Planolites*) show a statistically significant response to water depth with regards to their distribution. The frequency of turbidity currents controls ichnofabric distribution. Lower turbidity current frequency and longer residence time of surficial sediments in deep waters promotes an abundance of deep-tier traces compared to higher-frequency turbidity currents and shorter residence times in shallow waters where the colonisation window is reduced, promoting an abundance of opportunistic species. Additionally, traces are seen to respond to oxygen availability with reduced ichnodiversity within the oxygen minimum zone.

For an accurate interpretation of submarine canyon deposits in the geological record, an integrated sedimentological and ichnological approach is needed so that altitude above thalweg and distance down system can be inferred. Studies such as this, and the continuing focus on deep-marine ichnology, have the ability to enhance our understanding of deep-sea turbidite systems from outcrop, and the interplay of dynamic sedimentological and ecological processes within submarine canyons.

Chapter 5

Conclusions

The overall purpose of this PhD was to analyse seafloor deposits in order to better understand the processes, specifically turbidity currents, which transport sediment through submarine canyons. This was achieved through (i) compiling a comprehensive database of modern seafloor bedforms, (ii) combining the most complete monitoring data of natural turbidity currents and an unusually high-resolution dataset of remotely operated vehicle (ROV) collected sediment cores, and (iii) integrating ichnological and sedimentological datasets. The systematic nature of the core transects resulted in the ability to analyse turbidity current deposits in an unparalleled manner, allowing the nature of turbidity currents in Monterey Canyon to be inferred directly from their deposits.

The three overarching questions that this thesis aimed to answer were:

1. What do the morphological characteristics of seafloor bedforms reveal about the turbidity currents that created them?

2. How accurately do deposits represent the spatial and temporal evolution of turbidity currents?

3. What are the primary controls on the distribution of lithofacies and bioturbation within a submarine canyon?

The following sections address each of these questions with reference to the relevant thesis chapter.

5.1   What do the morphological characteristics of seafloor bedforms reveal about the turbidity currents that created them?

Bedforms are an important tool for inferring turbidity current dynamics as their morphological expression is directly related to the flow that generates them. Chapter 2 of this thesis presented a global database of bedforms from the modern seafloor with analysis of their morphology (crest shape and cross-sectional expression) and environmental constraints (e.g. confinement versus open slope). This evaluation was timely as it had been over a decade since the last attempt at classifying sediment waves (Wynn and Stow, 2002); and recent advances in seafloor mapping capabilities have subsequently revealed previously unresolvable bedforms.

The database was analysed visually and statistically by plotting wavelength against wave height. This analysis revealed three distinct groups of bedforms:

1. Small sediment waves (<300 m wavelength and <8 m wave height) that have mixed relief, and are restricted to confined settings (channels and canyons). They tend to have downslope crescentic crests, are formed of coarse grains and can lack internal stratigraphy.

2. Large sediment waves (up to 7200 m wavelengths and 220 m wave heights) exhibit mixed relief compared to the overall slope and are in relatively unconfined settings. They are characterised by straight to sinuous crests and are typically composed of fine-grained but mobile sediment. Additional large sediment waves with more crescentic crests are observed in confined settings.

3. Scours are large-scale (up to 3000 m long and 200 m deep) bedforms with negative relief, which have well developed enclosed depressions that lie below the height of the

surrounding seafloor. They often occur in areas of flow expansion and have eroded into cohesive, fine-grained sediment.

A number of formative mechanisms had previously been suggested for bedforms in each of the above three groups. In this chapter, analysis of published seismic images was used to infer bedform migration direction by tracing the position of the bedform crest between different reflectors. In all cases, where data was available (29 out of 82 examples including small and large sediment waves), the bedforms were inferred to migrate up-current. Up-current migration is indicative of supercritical flow; thus this data suggests that supercritical flows operate in a wide range of environments and can generate both small and large sediment waves. More specifically, the identification of small-scale sediment waves in the axis of submarine canyons suggests that supercritical turbidity currents are prevalent in these environments.

5.2 How accurately do deposits represent the spatial and temporal evolution of turbidity currents?

Most of our understanding of turbidity currents comes from the deposits that they leave behind. However, interpretations of flow dynamics based on deposits remain largely untested against the real world because of the lack of direct monitoring of turbidity currents combined with sampling of their deposits in the same location. In chapter 3 a detailed flow monitoring data set, previously collected by the USGS (Xu et al., 2004), coupled with an unusually high-resolution, systematic and precise set of core transects from the same location that were collected for this PhD.

The monitoring data of Xu et al. (2004) was used to constrain the thickness, velocity and duration of turbidity currents within Monterey Canyon, with estimated concentrations from backscatter values (Xu et al., 2014). By directly comparing lithofacies and grain sizes to direct measurements of the turbidity currents, a new three-part model of turbidity current behavior in Monterey Canyon was presented:

1. Flows begin as thin, high-concentration highly energetic flows that deposit coarse-grained facies in the canyon thalweg. This phase lasts for up to one hour and is probably most energetic in the first 15 minutes, during which time monitoring equipment was tilted and moved.

2. The flow transforms from this high-concentration phase into a more dilute phase over the first 30 km of the canyon, depositing classic interbedded turbidites. During this phase the head of the turbidity current is expanding, which lasts for 1-5 hours.

3. The final phase is a rapid thickening of the turbidity current along its entire length, which causes lofting and deposits silt and mud.

Seafloor deposits provide an accurate representation of how turbidity currents within Monterey Canyon evolve both spatially and temporally and therefore demonstrates that it is appropriate to use deposits (e.g. the distribution of facies and grain size) to reconstruct flow characteristics.

5.3   What are the primary controls on the distribution of lithofacies and bioturbation within a submarine canyon?

Submarine canyons can be biodiversity hotspots; yet any life in submarine canyons is subject to episodic, highly energetic sediment transport events such as turbidity currents. Previous studies from ancient outcrop have developed ichnological models that use the distribution of specific trace fossils for palaeoenvironmental reconstructions. The aim of chapter 4 was to analyse six transects (87 cores) of precisely located cores to consider the affects of turbidity currents on the distribution of benthic communities in Monterey Canyon, ultimately in order to ground-truth ichnological models based on outcrop.

There is a statistical relationship between the distribution of both lithofacies and bioturbation index (itself controlled by lithofacies) and altitude. The new three-part model for turbidity current behaviour in Monterey Canyon (from the previous chapter) was used to explain these distributions. The low energy levels and muddy substrates

that are found at high altitudes above the canyon thalweg from the final stage expansion of the turbidity currents are key in promoting a higher level of bioturbation.

The distribution of ichnofabrics is governed by water depth, with the frequency of turbidity currents determining trace type. The higher frequency of turbidity currents in shallow water results in a reduced colonisation window and opportunistic species generating simple traces; whereas the lower frequency of turbidity currents in deeper water creates a longer colonisation window with climax communities generating complex burrow systems. Additionally, traces are seen to respond to oxygen availability with reduced ichnodiversity within the oxygen minimum zone.

For an accurate interpretation of submarine canyon deposits in the geological record, an integrated sedimentological and ichnological approach is needed so that altitude above thalweg and distance down system can be inferred.

5.4 Future work

The compilation of seafloor bedforms presented in chapter 2 is not an exhaustive list of all bedforms presented in the literature and the database should therefore be viewed as a starting point. As seafloor mapping capabilities increase and higher resolution is achieved, bedforms of different scales and in different environments should further populate this database. New data points will likely support the view that a continuum of supercritical processes generate and maintain bedforms at all water depths and the bimodal nature of the data is a result of confined versus unconfined systems. Workers should also consider the possibility that bedforms of the data gap dimensions may be discovered as high-resolution Autonomous Underwater Vehicle (AUV) surveys in deeper waters become more common.

Monterey Canyon is one of the best-studied submarine canyons on earth. The wealth of data available, from deposit, biological, and monitoring data, make Monterey Canyon an ideal test site for better understanding sedimentological processes. The work presented in the thesis is the precursor for a large, international effort that was led by the Monterey Bay Aquarium Research Institute (MBARI). Developing on previous monitoring efforts by the USGS (presented in chapter 3), this coordinated effort had

instrumentation (including ADCPs, sediment traps and current meters) deployed at multiple depths from ~300 m to ~2000 m. These instruments were deployed for three-years and had a high-resolution sampling rate, resolving features of Monterey Canyon turbidity currents not resolved by previous efforts. Coupled with the direct monitoring was continued coring and mapping of the canyon floor and walls. These coring efforts were undertaken shortly after turbidity currents were monitored. This short time period between the flow and coring will better constrain which deposits were created by a specific flow, thus better linking flows to their deposits. The wealth of data collected during this large-scale effort will allow for development and refinement of the turbidity current model presented in this thesis as well as better understanding triggers and frequency between proximal and distal sites of these turbidity currents.

The analysis of ichnofabrics (chapter 4) provided an initial look into directly comparing modern seafloor ichnofabrics to ichnological models derived from ancient outcrop. Studies that use ichnological models are typically assessing outcrops or deposits from a wide range of canyon sub-environments (e.g. thalweg, terraces, levees, fans). Whilst this study provided an important step in ground-truthing ichnological models, the restrictions with regards to canyon sub-environment in this study limited the ichnodiversity of observed traces. To develop the study further, a wider range of canyon sub-environments should be studied (e.g. levees and more distal parts of the system such as submarine fans and channels) in order to accurately compare to and ground-truth previous outcrop studies.

The heterogeneous and complex nature of submarine canyons means that whilst the conclusions drawn from this study are applicable to many systems, the details that set other systems apart (e.g. triggering mechanisms, canyon head position relative to shelf and shoreline, river versus wave fed systems), may result in different turbidity current behaviour. Monitoring of submarine canyons and turbidity currents is expensive and challenging, with no guarantee of success. Whilst the direct monitoring of turbidity provide insight into aspects of the turbidity currents that deposits are unable to (e.g. velocities), high-resolution sampling of seafloor deposits is cheaper and can therefore be conducted more widely. Additionally, a number of studies, including this thesis, have demonstrated the ability to sample deposits from locations in submarine canyons where

the flows would be too big and destructive to monitor. The accuracy of the deposits in recording the evolution of a turbidity current shows that the high-resolution systematic approach to understanding turbidity current dynamics in submarine canyons is hugely beneficial and where possible, should be utilised in other systems.

List of appendices

Appendix A   Database of seafloor bedforms used in chapter 2 and additional plots for minimum and measured bedform dimensions. The main database is on the first tab of the spreadsheet. Subsequent tabs have figures of the bedforms (where possible) from the article the data were extracted from.

Appendix B   Push core photos from Monterey Canyon used in Chapter 3. The file contains six figures, one for each transect (Tr1-Tr6). Each figure has high-resolution photos of each core in a transect (if present). The different colours of the core photos may relate to different lighting of the photos or different cameras used. The contrast and brightness of the photos have been adjusted to highlight features. Each photo has the lithofacies highlighted. Also included is an across-canyon profile (looking down-canyon) with each push core location.

Appendix C   Shear velocity methods that were considered for chapter 3. Numerical modelling was undertaken to understand the grain sizes that theoretically could have been supported by the measured flows within Monterey Canyon. The document provides the methods used for these calculations and tables of results.

Appendix D   The file contains three spreadsheets that contain data for: 1) vibracore lithofacies, 2) Bioturbation Index, and 3) Ichnofabrics, that were all used in chapter 4.

Bibliography

Amy, L.A., Talling, P.J., 2006. Anatomy of turbidites and linked debrites based on long distance (120 x 30 km) bed correlation, Marnoso Arenacea Formation, Northern Apennines, Italy. Sedimentology 53, 161-212.

Appleby, P.G., Oldfield, F., 1978. The calculation of lead-210 dates assuming a constant rate of supply of unsupported 210Pb to the sediment. Catena 5, 1-8.

Arzola, R.G., Wynn, R.B., Lastras, G., Masson, D.G., Weaver, P.P.E., 2008. Sedimentary features and processes in the Nazaré and Setúbal submarine canyons, west Iberian margin. Marine Geology 250, 64-88.

Ayranci, K., Lintern, D.G., Hill, P.R., Dashtgard, S.E., 2012. Tide-supported gravity flows on the upper delta front, Fraser River delta, Canada. Marine Geology 326328, 166-170.

Babonneau, N., Delacourt, C., Cancout, R., Sisavath, E., Bachlery, P., Mazuel, A., Jorry, S.J., Deschamps, A., Ammann, J., Villeneuve, N., 2013. Direct sediment transfer from land to deep-sea: Insights into shallow multibeam bathymetry at La Réunion Island. Marine Geology 346, 47-57.

Bagnold, R., 1962. Auto-Suspension of Transported Sediment; Turbidity Currents. Proceedings of the Royal Society of London. Series A, Mathematical and Physical Sciences 265, 315-319.

Barley, B., 1999. Deepwater problems around the world. Leading Edge 18, 488-494.

Barry, J.P., Greene, H.G., Orange, D.L., Baxter, C.H., Robison, B.H., Kochevar, R.E., Nybakken, J.W., Reed, D.L., McHugh, C.M., 1996. Biologic and geologic characteristics of cold seeps in Monterey Bay, California. Deep-Sea Research Part I-Oceanographic Research Papers 43, 1739-1762.

Berner, R.A., 1982. Burial of organic carbon and pyrite sulfur in the modern ocean: Its geochemical and environmental significance. American Journal of Science 282, 451-473.

Blumsack, S.L., 1993. A model for the growth of mudwaves in the presence of time-varying currents. Deep-sea Research II 40, 963-974.

Blumsack, S.L., Weatherly, G.L., 1989. Observations of the nearby flow and a model for the growth of mud waves. Deep-sea Research 36, 1327-1339.

Bornhold, B.D., Prior, B.D., 1990. Morphology and sedimentary processes on the subaqueous Noeick River delta, British Columbia, Canada, in. Colella, A., Prior, D.B (Eds.), Coarse Grained Deltas. Blackwell Scientific Publications., Oxford, pp. 169-185.

Bouma, A.H., 1962. Sedimentology of some Flysch Deposits, Elsevier Pub. Co., 168.

Bromley, R.G., 1996. Trace Fossils. Biology, Taphonomy and Applications: Chapman and Hall, London, 361.

Bromley, R.G., Ekdale, A.A., 1984. Chondrites: A trace fossil indicator of anoxia in sediments. Science 227, 872-874.

Bromley, R.G., Pemberton, S.G., Rahmani, R.A., 1984. A Cretaceous woodground: the Teredolites ichnofacies. Journal of Paleontology 58, 488498.

Bromley, R.G., Ekdale, A.A., 1986. Composite ichnofabrics and tiering of burrows. Geological Magazine 123, 59-65.

Brothers, D.S., ten Brink, U.S., Andrews, B.D., Chaytor, J.D., Twichell, D.C., 2013. Geomorphic process fingerprints in submarine canyons. Marine Geology 337, 53-66.

Buatois, L.A., Mngano, M.G., Brussa, E.D., Benedetto, J.L., Pompei, J.F., 2009. The changing face of the deep: Colonization of the Early Ordovician deep-sea floor, Puna, northwest Argentina. Palaeogeography, Palaeoclimatology, Palaeoecology 280, 291-299.

Cacchione, D.A., Drake, D.E., 1986. Nepheloid layers and internal waves over continental shelves and slopes. Geo-Marine Letters 6, 147-152.

Callow, R.H.T., McIlroy, D., Kneller, B., Dykstra, M., 2013a. Ichnology of Late Cretaceous Turbidites from the Rosario Formation, Baja California, Mexico. Ichnos 20, 114.

Callow, R.H.T., McIlroy, D., Kneller, B., Dykstra, M., 2013b. Integrated ichnological and sedimentological analysis of a Late Cretaceous submarine channel-levee system: The Rosario Formation, Baja California, Mexico. Marine and Petroleum Geology 41, 277-294.

Callow, R.H.T., Kneller, B., Dykstra, M., McIlroy, D., 2014. Physical, biological, geochemical and sedimentological controls on the ichnology of submarine canyon and slope channel systems. Marine and Petroleum Geology 54, 144-166.

Canals, M., Puig, P., de Madron, X.D., Heussner, S., Palanques, A., Fabres, J., 2006. Flushing submarine canyons. Nature 444, 354-357.

Carling, P.A., Shvidchenko, A.B., 2002. A consideration of the dune: antidune transition in fine gravel. Sedimentology 49, 1269-1282.

Carson, B., Baker, E., Hickey, B., Nittrouer, C., DeMaster, D., Thorbjarnarson, K., Snyder, G., 1986. Modern sediment dispersal and accumulation in Quinault submarine canyon - A summary. Marine Geology 71, 1-13.

Carter, L., Burnett, D., Drew, S., Marle, G., Hagadorn, L., Bartlett-McNeil, D., Irvine, N., 2009. Submarine cables and the oceans: Connecting the world [WWW Document]. UNEP-WCMC Biodivers. Ser. 31. ICPC/UNEP/UNEP-WCMC.

Carter, L., Milliman, J.D., Talling, P.J., Gavey, R., Wynn, R.B., 2012. Near-synchronous and delayed initiation of long run-out submarine sediment flows from a record-breaking river flood, offshore Taiwan. Geophysical Research Letters 39, 6-10.

Cartigny, M.J.B., Postma, G., Van den Berg, J., Mastbergen, D.R., 2011. A comparative study of sediment waves and cyclic steps based on geometries, internal structures and numerical modeling. Marine Geology 280, 40-56.

Cartigny, M.J.B., Eggenhuisen, J.T., Hansen, E.W.M., Postma, G., 2013. Concentration-dependent flow stratification in experimental high-density turbidity currents and their relevance to turbidite facies models. Journal of Sedimentary Research 83, 1046-1064.

Cartigny, M.J.B., Ventra, D., Postma, G., Van den Berg, J., 2014. Morphodynamics and sedimentary structures of bedforms under supercritical-flow conditions: New insights from flume experiments. Sedimentology 61, 712-748.

Casalbore, D., Romagnoli, C., Chiocci, F.L., Frezza, V., 2010. Morpho-sedimentary characteristics of the volcaniclastic apron around Stromboli volcano (Italy). Marine Geology 269, 132-148.

Casalbore, D., Romagnoli, C., Bosman, A., Chiocci, F.L., 2013. Small-scale crescent-shaped bedforms in submarine volcanic setting: examples from Stromboli and Salina island (Italy). GeoActa 12, 37-45.

Casalbore, D., Romagnoli, C., Bosman, A., Chiocci, F.L., 2014. Large-scale seafloor waveforms on the flanks of insular volcanoes (Aeolian Archipelago, Italy), with inferences about their origin. Marine Geology 355, 318-329.

Castro, I.P., Snyder, W.H., 1993. Experiments on wave breaking in stratified flow over obstacles. Journal of Fluid Mechanics 255, 195-211.

Cattaneo, A., Correggiari, A., Marsset, T., Thomas, Y., Marsset, B., Trincardi, F., 2004. Seafloor undulation pattern on the Adriatic shelf and comparison to deep-water sediment waves. Marine Geology 213, 121-148.

Cattaneo, A., Babonneau, N., Ratzov, G., Dan-Unterseh, G., Yelles, K., Bracéne, R., Mercier de Lépinay, B., Boudiaf, A., Déverchére, J., 2012. Searching for the seafloor signature of the 21 May 2003 Boumerds earthquake offshore central Algeria. Natural Hazards and Earth System Science 12, 2159-2172.

Cavazza, W., DeCelles, P.G., 1993. Geometry of a Miocene submarine canyon and associated sedimentary facies in south eastern Calabria, southern Italy. Geological Society of America Bulletin 105, 12971309.

Clifton, H.E., Hill, G.W., 1987, Paleocene submarine canyon fill, Point Lobos, California: Geological Society of America Centennial Field Guide, Cordilleran Section, 239244.

Conway, K.W., Barrie, J.V., Picard, K., Bornhold, B.D., 2012. Submarine channel evolution: active channels in fjords, British Columbia, Canada. Geo-Marine Letters 32, 301-312.

Cooper, C., Wood, J., Andrieux, A., 2013. Turbidity current measurements in the Congo Canyon: OTC Abstract 23992, Offshore Technology Conference, 6-9 May, Houston, Texas, 12.

Covault, J.A., Normark, W.R., Romans, B.W., Graham, S.A., 2007. Highstand fans in the California borderland: The overlooked deep-water depositional systems. Geology, 35, 783-786.

Covault, J.A., Kostic, S., Paull, C.K., Ryan, H.F., Fildani, A., 2014. Submarine channel initiation, filling and maintenance from sea-floor geomorphology and morphodynamic modelling of cyclic steps. Sedimentology 61, 1031-1054.

Cummings, J.P., Hodgson, D.M., 2011. Assessing controls on the distribution of ichnotaxa in submarine fan environments, the Basque Basin, Northern Spain. Sedimentary Geology 239, 162-187.

Cunningham, A.P., Barker, P.F., 1996. Evidence for westward-flowing Weddell Sea Deep Water in the Falkland Trough, western South Atlantic. Deep-sea Research 43, 643-654.

De Leo, F.C., Smith, C.R., Rowden, A.A., Bowden, D.A., Clark, M.R., 2010. Submarine canyons: hotspots of benthic biomass and productivity in the deep sea. Proceedings of the Royal Society B: Biological Sciences 277, 2783-2792.

de Stigter, H.C., Boer, W., de Jesus Mendes, P.A., Jesus, C.C., Thomsen, L., van den Bergh, G.D., van Weering, T.C.E., 2007. Recent sediment transport and deposition in the Nazaré Canyon, Portuguese continental margin. Marine Geology 246, 144-164.

Dempster, A., Laird, N., Rubin, D., 1977. Maximum Likelihood from Incomplete Data via the EM Algorithm. Journal of the Royal Statistical Society Series B (Methodological) 39, 1-38.

Di Celma, C., 2011. Sedimentology, architecture, and depositional evolution of a coarse-grained submarine canyon fill from the Gelasian (early Pleistocene) of the Peri-Adriatic basin, Offida, central Italy. Sedimentary Geology 238, 233-253.

Dill, R.F., 1964. Contemporary submarine erosion in Scripps Submarine Canyon head, in. R.L. Miller (Editor). Papers in Marine Geology, Shepard Commemorative Volume, 23-41.

Drake, D.E., Gorsline, D.S., 1973. Distribution and Transport of Suspended Particulate Matter in Hueneme, Redondo, Newport, and La Jolla Submarine Canyons, California. Geological Society of America Bulletin 84, 3949-3968.

Droser, M.L., Jensen, S., Gehling, J.G., 2002. Trace fossils and substrates of the terminal Proterozoic-Cambrian transition: Implications for the record of early bilaterians and sediment mixing. Proceedings of the National Academy of Sciences 99, 12572-12576.

Duarte, J.C., Terrinha, P., Rosas, F.M., Valadares, V., Pinheiro, L.M., Matias, L., Magalhes, V., Roque, C., 2010. Crescent-shaped morphotectonic features in the Gulf of Cadiz (offshore SW Iberia). Marine Geology 271, 236-249.

Durrieu de Madron, X., 1994. Hydrography and nepheloid structures in the Grand-Rhône canyon. Continental Shelf Research 14, 457-477.

Dykstra, M., Kneller, B.C., 2007. Canyon San Fernando, Mexico: a deep-water, channel-levee complex exhibiting evolution from submarine canyon-confined to unconfined. In: Nilsen, T.H., Shew, R.D., Steffens, G.S., Studlick, J.R.J. (Eds.), Atlas of Deep-water Outcrops. American Association of Petroleum Geologists, SG56, CDROM, Chapter 135.

Dykstra, M., Kneller, B., 2009. Lateral accretion in a deep-marine channel complex: Implications for channellized flow processes in turbidity currents. Sedimentology

56, 1411-1432.

Eakins, B.W., Robinson, J.E., 2006. Submarine geology of Hana Ridge and Haleakala Volcanos northeast flank, Maui. Journal of Volcanology and Geothermal Research 151, 229-250.

Ediger, V., Velegrakis, A., Evans, G., 2002. Upper slope sediment waves in the Cilician Basin, northeastern Mediterranean. Marine Geology 192, 321-333.

Ekdale, A.A., Mason, T.R., 1988. Characteristic trace fossils associations in oxygen-poor sedimentary environments. Geology 16, 720-723.

Ekdale, A.A., Bromley, R.G., 1991. Analysis of Composite Ichnofabrics: An Example in Uppermost Cretaceous Chalk of Denmark. Palaios 6, 232-249.

Ercilla, G., Alonso, B., Wynn, R.B., Baraza, J., 2002. Turbidity current sediment waves on irregular slopes: observations from the Orinoco sediment-wave field. Marine Geology 192, 171-187.

Fagherazzi, S., Sun, T., 2003. Numerical simulations of transportational cyclic steps. Computers and Geosciences 29, 1143-1154.

Faugéres, J., Gonthier, E., Mulder, T., Kenyon, N.H., Cirac, P., Griboulard, R., Berne, S., Lesuave, R., 2002. Multi-process generated sediment waves on the Landes Plateau (Bay of Biscay, North Atlantic). Marine Geology 182, 279-302.

Fernandez-Arcaya, U., Ramirez-Llodra, E., Aguzzi, J., Allcock, A.L., Davies, J.S., Dissanayake, A., Harris, P., Howell, K., Huvenne, V.A.I., Macmillan-Lawler, M., Martn, J., Menot, L., Nizinski, M., Puig, P., Rowden, A.A., Sanchez, F., Van den Beld, I.M.J., 2017. Ecological Role of Submarine Canyons and Need for Canyon Conservation: A Review. Frontiers in Marine Science 4, 1-26.

Fildani, A., 2017. Submarine Canyons: A brief review looking forward. Geology 45, 383-384.

Fildani, A., Normark, W.R., Kostic, S., Parker, G., 2006. Channel formation by flow stripping: large-scale scour features along the Monterey East Channel and their relation to sediment waves. Sedimentology 53, 1265-1287.

Flood, R.D., 1988. A lee wave model for deep-sea mudwave activity. Deep-sea Research 35, 973-983.

Flood, R.D., 1994. Abyssal bedforms as indicators of changing bottom current flow: Examples from the U.S. East Coast continental rise. Paleoceanography 9, 1049-1060.

Flood, R.D., Shor, A.N., 1988. Mud waves in the Argentine Basin and their relationship to regional bottom circulation patterns. Deep-sea Research 35, 943-971.

Flood, R.D., Giosan, L., 2002. Migration history of a fine-grained abyssal sediment wave on the Bahama Outer Ridge. Marine Geology 192, 259-273.

Follmi, K.B., Grimm, K.A., 1990. Doomed pioneers: gravity-flow deposition and bioturbation in marine oxygen-deficient environments. Geology 18, 1069-1072.

Fraley, C., Raftery, A.E., Murphy, T.B., Scrucca, L., 2012. Technical Report No. 597 [WWW Document]. Department of Statistics University of Washington.

Frey, R.W., Seilacher, A., 1980. Uniformity in marine invertebrate ichnology. Lethaia 13, 183-207.

Frey, R.W., Pemberton, S.G., Fagerstrom, J.A., 1984. Morphological, ethological, and environmental significance of the ichnogenera Scoyenia and Ancorichnus. Journal of Paleontology 58, 511-528.

Frey, R.W., Pemberton, S.G., Saunders, T.D.A., 1990. Ichnofacies and bathymetry: a passive relationship. Journal of Paleontology 64, 155-158.

Frey, R.W., Goldring, R., 1992. Marine event beds and recolonization surfaces as revealed by trace fossil analysis. Geological Magazine. 129, 325-335.

Gambi, C., Danovaro, R., 2016. Biodiversity and life strategies of deep-sea meiofauna and nematode assemblages in the Whittard Canyon (Celtic margin, NE Atlantic Ocean). Deep-sea Research Part I: Oceanographic Research Papers 108, 13-22.

Garcia, M.H., 1994. Depositional turbidity currents laden with poorly sorted sediment. Journal of Hydraulic Engineering 120, 1240-1263.

Gardner, W.D., 1989. Baltimore Canyon as a modern conduit of sediment to the deep sea. Deep Sea Research Part A, Oceanographic Research Papers 36, 323-358.

Gardner, J. V., 2010. The West Mariana Ridge, western Pacific Ocean: Geomorphology and processes from new multibeam data. Geological Society of America Bulletin 122, 1378-1388.

Garfield, N., Rago, T.A., Schnebele, K.J., Collins, C.A., 1994. Evidence of a turbidity current in Monterey Submarine Canyon associated with the 1989 Loma Prieta earthquake. Continental Shelf Research 14, 673-686.

Giddings, J.A., Wallace, M.W., Haines, P.W., Mornane, K., 2010. Submarine origin for the Neoproterozoic Wonoka canyons, South Australia. Sedimentary Geology 223,

3550.

Gingras, M.K., Dashtgard, S.E., MacEachern, J.A., George Pemberton, S., 2008. Biology of shallow marine ichnology: A modern perspective. Aquatic Biology 2, 255-268.

Gingras, M.K., MacEachern, J.A., Dashtgard, S.E., 2011. Process ichnology and the elucidation of physico-chemical stress. Sedimentary Geology 237, 115-134.

Girardclos, S., Hilbe, M., Corella, J.P., Loizeau, J., Kremer, K., Delsontro, T., Arantegui, A., Moscariello, A., Arlaud, F., Akhtman, Y., Anselmetti, F.S., Lemmin, U., 2012. Searching the Rhone delta channel in Lake Geneva since Franois-Alphonse Forel. Archives Des Sciences 65, 103-118.

Goffredi, S.K., Paull, C.K., Fulton-Bennett, K., Hurtado, L.A., Vrijenhoek, R.C., 2004. Unusual benthic fauna associated with a whale fall in Monterey Canyon, California. Deep-sea Research Part I: Oceanographic Research Papers 51, 1295-1306.

Goldfinger, C., Nelson, C.H., Johnson, J.E., Party, S., 2003. Deep-water turbidites as Holocene earthquake proxies: the Cascadia subduction zone and Northern San Andreas Fault systems. Annals of Geophysics 46, 1169-1194.

Gong, C., Wang, Y., Peng, X., Li, W., Qiu, Y., Xu, S., 2012. Sediment waves on the South China Sea Slope off southwestern Taiwan: Implications for the intrusion of the Northern Pacific Deep Water into the South China Sea. Marine and Petroleum Geology 32, 95-109.

Gordon, R.L., Marshall, N.F., 1976. Submarine canyons: Internal wave traps? Geophysical Research Letters 3, 622-624.

Graham, S.A., 1976. Role of the Salinian block in evolution of San Andreas Fault system, California. American Association of Petroleum Geologists Bulletin 62, 2214-2231.

Greene, H.G., 1977. Geology of the Monterey Bay region. U.S. Geological Survey Open File Report No. 77-718. 347.

Greene, H.G., Hicks, K.R., 1990. Regional tectonics and structural evolution of the Monterey Bay region, central California. In: Garrison, R.E., Greene, H.G., Hicks, K.R., Weber, G.E., Wright, T.L. (Eds.), Geology and tectonics of the central California coastal region, San Francisco to Monterey. Pacific section of the AAPG Guidebook, 31-56.

Greene, H.G., Maher, N.M., Paull, C.K., 2002. Physiography of the Monterey Bay National Marine Sanctuary and implications about continental margin development. Marine Geology 181, 55-82.

Griggs, G.B., Carey Jr., A.G. and Kulm, L.D. 1969. Deep-sea sedimentation and sediment-fauna interaction in Cascadia Channel and on Cascadia Abyssal Plain. Deep-Sea Research 16, 157-170.

Gwiazda, R., Paull, C.K., Ussler, W., Alexander, C.R., 2015. Evidence of modern fine-grained sediment accumulation in the Monterey Fan from measurements of the pesticide DDT and its metabolites. Marine Geology 363, 125-133.

Habgood, E.L., Kenyon, N.H., Asson, D.G.M., Akhmetzhanov, A., Weaver, P.P.E., Gardner, J., 2003. Deep-water sediment wave fields, bottom current sand channels and gravity flow channel-lobe systems: Gulf of Cadiz, NE Atlantic. Sedimentology 50, 483-510.

Harris, P.T., Whiteway, T., 2011. Global distribution of large submarine canyons: Geomorphic differences between active and passive continental margins. Marine Geology 285, 69-86.

Heard, T.G., Pickering, K.T., 2008. Trace fossils as diagnostic indicators of deep-marine environments, Middle Eocene Ainsa-Jaca basin, Spanish Pyrenees. Sedimentology 55, 809-844.

Heard, T.G., Pickering, K.T., Clark, J.D., 2014. Ichnofabric characterization of a deep-marine clastic system: A subsurface study of the Middle Eocene Ainsa System, Spanish Pyrenees. Sedimentology 61, 1298-1331.

Heezen, B.C., Ewing, M., 1952. Turbidity currents and submarine slumps, and the 1929 Grand Banks Earthquake. American Journal of Science 250, 849-873.

Heifetz, E., Agnon, A., Marco, S., 2005. Soft sediment deformation by Kelvin Helmholtz Instability: A case from Dead Sea earthquakes. Earth and Planetary Science Letters 236, 497-504.

Heinio, P., Davies, R.J., 2009. Trails of depressions and sediment waves along submarine channels on the continental margin of Espirito Santo Basin, Brazil. Geological Society of America Bulletin 121, 698-711.

Hess, S., Jorissen, F. J., Venet, V., Abu-Zied, R. 2005. Benthic foraminiferal recovery after recent turbidite deposition in Cap Breton Canyon, Bay of Biscay. Journal of Foraminiferal Research 35, 114-119.

Hill, P., 2012. Changes in submarine channel morphology and slope sedimentation patterns from repeat multibeam surveys in the Fraser River delta, western Canada. International Association of Sedimentologists Special Publication 44, 47-70.

Hiscott, R.N., Aksu, A.E., Flood, R.D., Kostylev, V., Yaar, D., 2013. Widespread overspill from a saline density-current channel and its interaction with topography on

the south-west Black Sea shelf. Sedimentology 60, 1639-1667.

Hodgson, D.M., Di Celma, C.N., Brunt, R.L., Flint, S.S., 2011. Submarine slope degradation and aggradation and the stratigraphic evolution of channel-levee systems. Journal of the Geological Society 168, 625628.

Holbrook, W.S., Lizarralde, D., Pecher, I.A., Gorman, A.R., Hackwith, K.L., Hornbach, M., 2002. Escape of methane gas through sediment waves in a large methane hydrate province. Geology 30, 467-470.

Howe, J.A., 1996. Turbidite and contourite sediment waves in the northern Rockall Trough, North Atlantic Ocean. Sedimentology 43, 219-234.

Hsu, S., Kuo, J., Lo, C., Tsai, C., Doo, W., Ku, C., Sibuet, J., 2008. Turbidity Currents, Submarine Landslides and the 2006 Pingtung Earthquake off SW Taiwan. Terrestrial, Atmospheric and Oceanic Sciences 19, 767-772.

Huang, Z., Nichol, S.L., Harris, P.T., Caley, M.J., 2014. Classification of submarine canyons of the Australian continental margin. Marine Geology 357, 362-383.

Hubbard, S.M., Shultz, M.R. 2008. Deep burrows in submarine fan-channel deposits of the Cerro Toro Formation (Cretaceous), Chilean Patagonia: implications for firmground development and colonization in the deep sea. Palaios, 23, 223-232.

Hubbard, S.M., MacEachern, J.A., Bann, K.L., 2012. Slopes, in Knaust, D., and Bromley, R.G., eds., Trace Fossils as Indicators of Sedimentary Environments: Amsterdam, Elsevier, Developments in Sedimentology 64, pp. 607-642.

Hubbard, S.M., Covault, J.A., Fildani, A., Romans, B.W., 2014. Sediment transfer and deposition in slope channels: Deciphering the record of enigmatic deep-sea processes from outcrop. Geological Society of America Bulletin 126, 857-871.

Hughes, D. J., Shimmield, T. M., Black, K. D., Howe, J. A., 2015. Ecological impacts of large-scale disposal of mining waste in the deep sea. Science Reports 5, 9985.

Hughes Clarke, J.E., 1998. The effect of fine scale seabed morphology and texture on the fidelity of swath bathymetric sounding data: Proceedings Canadian Hydrographic Conference 1998, Victoria, 168-181.

Hughes Clarke, J.E., 2016. First wide-angle view of channelized turbidity currents links migrating cyclic steps to flow characteristics. Nature Communications 7, 11896.

Hughes Clarke, J., Brucker, S., Muggah, J., Church, I., Cartwright, D., Kuus, P., Hamilton, T., Pratomo, D., Eisan, B., 2012. The Squamish ProDelta: Monitoring Active Landslides and Turbidity Currents, in: Canadian Hydrographic Conference 2012.

pp. 1-15.

Hughes Clarke, J., Marques, C.R.V., Pratomo, D., 2014. Imaging active mass-wasting and sediment flows on a fjord delta, Squamish, British Columbia, in: Krastel, S., Behrmann, J.H., Vlker, D., Stipp, M., Berndt, C., Urgeles, R., Chaytor, J., Huhn, K., Strasser, M., Harbitz, C.B. (Eds.), Submarine Mass Movements and Their Consequences, Advances in Natural and Technological Hazards Research, Advances in Natural and Technological Hazards Research. Springer International Publishing, Cham, pp. 249-260.

Huh, C.A., Lin, H.L., Lin, S., Huang, Y.W., 2009. Modern accumulation rates and a budget of sediment off the Gaoping (Kaoping) River, SW Taiwan: A tidal and flood dominated depositional environment around a submarine canyon. Journal of Marine Systems 76, 405-416.

Hung, G.W., Chung, Y.C., 1998. Particulate fluxes, 210Pb and 210Po measured from sediment trap samples in a canyon off northeastern Taiwan. Continental Shelf Research 18, 1475-1491.

Huvenne, V.A.I., McPhail, S.D., Wynn, R.B., Furlong, M., Stevenson, P., 2009. Mapping Giant Scours in the Deep Ocean. Eos (Washington. DC). 90, 274-275.

Huvenne, V.A., Davies, J.S., 2013. Towards a new and integrated approach to submarine canyon research. Deep Sea Research Part II: Topical Studies in Oceanography 104, 1-5.

Inman, D.L., Nordstrom, C.E., Flick, R.E., 1976. Currents in Submarine Canyons: An Air-Sea-Land Interaction. Annual Review of Fluid Mechanics 8, 275-310.

Iverson, R.M., 1997. The physics of debris flows. Reviews of Geophysics 35, 245-296.

Jacobi, R.D., Rabinowitz, P.D., Embley, R.W., 1975. Sediment waves on the Moroccan continental rise. Marine Geology 19, 61-67.

Jobe, Z.R., Bernhardt, A., Lowe, D.R., 2010. Facies and Architectural Asymmetry in a Conglomerate-Rich Submarine Channel Fill, Cerro Toro Formation, Sierra Del Toro, Magallanes Basin, Chile. Journal of Sedimentary Research 80, 1085-1108.

Jobe, Z., Sylvester, Z., Pittaluga, M.B., Frascati, A., Pirmez, C., Minisini, D., Howes, N., Cantelli, A., 2017. Facies architecture of submarine channel deposits on the western Niger Delta slope: Implications for grainsize and density stratification in turbidity currents. Journal of Geophysical Research: Earth Surface 122, 473-491.

Johnson, J.E., Paull, C.K., Normark, W.R., Ussler, W., 2005. Late Holocene turbidity currents in Monterey Canyon and fan channel: Implications for interpreting active margin turbidite records: Eos (transactions, American Geophysical union), 86, abs.

OS21A-1521.

Joliffe, I., 2002. *Principal component analysis.* John Wiley & Sons, Ltd.

Kane, I.A., Kneller, B.C., Dykstra, M., Kassem, A., McCaffrey, W.D., 2007. Anatomy of a submarine channel-levee: An example from Upper Cretaceous slope sediments, Rosario Formation, Baja California, Mexico. Marine and Petroleum Geology 24, 540-563.

Karl, H., Carlson, P., 1982. Large sand waves in Navarinsky Canyon head, Bering Sea. Geo-Marine Letters 2, 157-162.

Kenyon, N.H., Belderson, R.H., 1973. Bedforms of the Mediterranean undercurrent observed with side-scan sonar. Sedimentary Geology 9, 77-99.

Khripounoff, A., Vangriesheim, A., Babonneau, N., Crassous, P., Dennielou, B., Savoye, B., 2003. Direct observation of intense turbidity current activity in the Zaire submarine valley at 4000 m water depth. Marine Geology 194, 151-158.

Khripounoff, A., Vangriesheim, A., Crassous, P., Etoubleau, J., 2009. High frequency of sediment gravity flow events in the Var submarine canyon (Mediterranean Sea). Marine Geology 263, 1-6.

Khripounoff, A., Crassous, P., Lo Bue, N., Dennielou, B., Jacinto, R.S., 2012. Progress in Oceanography Different types of sediment gravity flows detected in the Var submarine canyon (northwestern Mediterranean Sea). Progress in Oceanography 106, 138-153.

Knaust, D., 2009. Characterisation of a Campanian deep-sea fan system in the Norwegian Sea by means of ichnofabrics. Marine and Petroleum Geology 26, 1199-1211.

Knaust, D., 2015. Trace fossils from the continental Upper Triassic Kågeröd Formation of Bornholm, Denmark. Annales Societatis Geologorum Poloniae 85, 481-492.

Knaust, D. 2017. Atlas of Trace Fossils in Well Core: Appearance, Taxonomy and Interpretation. Springer.

Knaust, D., Warchol, M., Kane, I.A., 2014. Ichnodiversity and ichnoabundance: Revealing depositional trends in a confined turbidite system. Sedimentology 61, 2218-2267.

Kneller, B.C., Branney, M.J., 1995. Sustained high-density turbidity currents and the deposition of thick massive sands. Sedimentology 42, 607-616.

Kneller, B., Buckee, C., 2000. The structure and fluid mechanics of turbidity currents: a review of some recent studies and their geological implications. Sedimentology

47, 62-94.

Kneller, B.C., McCaffrey, W.D., 2003. The interpretation of vertical sequences in turbidite beds: the influence of longitudinal flow. Journal of Sedimentary Research 73, 706-713.

Komar, P.D., 1969. The channelized flow of turbidity currents with application to Monterey Deep-Sea Fan Channel. Journal of Geophysical Research 74, 4544-4558.

Komar, P.D., 1985. The hydraulic interpretation of turbidites from their grain sizes and sedimentary structures. Sedimentology 32, 395-407.

Konishi, S., Kitagawa, G., 2008. Bayesian information criteria, in: Konishi, S., Kitagawa (Eds.), Information Criteria and Statistical Modeling. Springer Series in Statistics, 211-237.

Kostaschuk, R., Villard, P., 1996. Flow and sediment transport over large subaqueous dunes: Fraser River, Canada. Sedimentology 43, 849-863.

Kostic, S., 2011. Modeling of submarine cyclic steps: Controls on their formation, migration, and architecture. Geosphere 7, 294-304.

Kostic, S., 2014. Upper flow regime bedforms on levees and continental slopes: Turbidity current flow dynamics in response to fine-grained sediment waves. Geosphere 10, 1094-1103.

Kostic, S., Parker, G., 2006. The response of turbidity currents to a canyon-fan transition: internal hydraulic jumps and depositional signatures. Journal of Hydraulic Research 44, 631-653.

Kostic, S., Sequeiros, O.E., Spinewine, B., Parker, G., 2010. Cyclic steps: A phenomenon of supercritical shallow flow from the high mountains to the bottom of the ocean. Journal of Hydro-environment Research 3, 167-172.

Kuang, Z., Zhong, G., Wang, L., Guo, Y., 2014. Channel-related sediment waves on the eastern slope offshore Dongsha Islands, northern South China Sea. Journal of Asian Earth Sciences 79, 540-551.

Kuenen, P.H., Migliorini, C.I., 1950, Turbidity currents as a cause of graded bedding: Journal of Geology 58, 91-127.

Kubo, Y., Nakajima, T., 2002. Laboratory experiments and numerical simulation of sediment-wave formation by turbidity currents. Marine Geology 192, 105-121.

Kunze, E., Rosenfeld, L.K., Carter, G.S., Gregg, M.C., 2002. Internal Waves in Monterey Submarine Canyon. Journal of Physical Oceanography 32, 1890-1913.

Lamb, M.P., Parsons, J.D., Mullenbach, B.L., Finlayson, D.P., Orange, D.L., Nittrouer, C.A., 2008. Evidence for superelevation, channel incision, and formation of cyclic steps by turbidity currents in Eel Canyon, California. Geological Society of America Bulletin 120, 463-475.

Lastras, G., Arzola, R.G., Masson, D.G., Wynn, R.B., Huvenne, V.A.I., Hühnerbach, V., Canals, M., 2009. Geomorphology and sedimentary features in the Central Portuguese submarine canyons, Western Iberian margin. Geomorphology 103, 310-329.

Leat, P.T., Tate, A.J., Tappin, D.R., Day, S.J., Owen, M.J., 2010. Growth and mass wasting of volcanic centers in the northern South Sandwich arc, South Atlantic, revealed by new multibeam mapping. Marine Geology 275, 110-126.

Leat, P.T., Day, S.J., Tate, A.J., Martin, T.J., Owen, M.J., Tappin, D.R., 2013. Volcanic evolution of the South Sandwich volcanic arc, South Atlantic, from multibeam bathymetry. Journal of Volcanology and Geothermal Research 265, 60-77.

LeBas, E., Le Friant, A., Boudon, G., Watt, S.F.L., Talling, P.J., Feuillet, N., Deplus, C., Berndt, C., Vardy, M.E., 2011. Multiple widespread landslides during the long-term evolution of a volcanic island: Insights from high-resolution seismic data, Montserrat, Lesser Antilles. Geochemistry, Geophysics, Geosystems 12, 1-20.

Lee, S.H., Chough, S.K., 2001. High-resolution (2-7 kHz) acoustic and geometric characters of submarine creep deposits in the South Korea Plateau, East Sea. Sedimentology 48, 629-644.

Lee, H.J., Syvitski, J.P.M., Parker, G., Orange, D., Locat, J., Hutton, E.W.H., Imran, J., 2002. Distinguishing sediment waves from slope failure deposits: field examples, including the "Humboldt slide", and modelling results. Marine Geology 192, 79-104.

Levin, L., 2003. Oxygen minimum zone benthos: adaptation and community response to hypoxia. Oceanography and Marine Biology: an Annual Review 41, 1-45.

Lewis, K.B., Collot, J., Lallemand, S.E., 1998. The dammed Hikurangi Trough: a channel-fed trench blocked by subducting seamounts and their wake avalanches (New Zealand France GeodyNZ Project). Basin Research 10, 441-468.

Lewis, K.B., Pantin, H.M., 2002. Channel-axis, overbank and drift sediment waves in the southern Hikurangi Trough, New Zealand. Marine Geology 192, 123-151.

Liu, J.T., Wang, Y.-H., Yang, R.J., Hsu, R.T., Kao, S.J., Lin, H.L., Kuo, F.H., 2012. Cyclone-induced hyperpycnal turbidity currents in a submarine canyon. Journal of

Geophysical Research 117, C04033.

Lonergan, L., Jamin, N.H., Jackson, C.A.-L., Johnson, H.D., 2013. U-shaped slope gully systems and sediment waves on the passive margin of Gabon (West Africa). Marine Geology 337, 80-97.

Lonsdale, P., Malfait, B., 1974. Abyssal dunes of foraminiferal sand on the Carnegie Ridge. Geological Society of America Bulletin 85, 1697-1712.

López-Gamundí, O.R., 1993. Pebbly mudstones in the Cretaceous Pigeon Point Formation, western California: a study in the transitional stages from submarine slumps to cohesive debris flows. Sediment. Geol. 84, 3750.

Lowe, D.R., 1982. Sediment gravity flows: II. Depositional models with special reference to the deposits of high-density turbidity currents. Journal of Sedimentary Research 52, 279-297.

Lowe, D.R., Guy, M., 2000. Slurry-flow deposits in the Britannia Formation (Lower Cretaceous), North Sea: a new perspective on the turbidity current and debris flow problem. Sedimentology 47, 31-70.

Löwemark, L., 2007. Importance and usefulness of trace fossils and bioturbation in paleoceanography. In: Miller III, W. (Ed.), Trace Fossils. Concepts, Problems, Prospects. Elsevier,Amsterdam 413427.

Lundsten, L., Schlining, K.L., Frasier, K., Johnson, S.B., Kuhnz, L.A., Harvey, J.B.J., Clague, G., Vrijenhoek, R.C., 2010. Time-series analysis of six whale-fall communities in Monterey Canyon, California, USA. Deep-sea Research Part I: Oceanographic Research Papers 57, 1573-1584.

Macdonald, H.A., Wynn, R.B., Huvenne, V.A.I., Peakall, J., Masson, D.G., Weaver, P.P.E., McPhail, S.D., 2011. New insights into the morphology, fill, and remarkable longevity (>0.2 m.y.) of modern deep-water erosional scours along the northeast Atlantic margin. Geosphere 7, 845-867.

Mángano, M.G., Buatois, L. a, Maples, C.G., West, R.R., 2000. A new ichnospecies of Nereites from Carboniferous tidal-flat facies of Eastern Kansas, USA: Implications for the Nereites-Neonereites debate. Journal of Paleontology 74, 149-157.

Manley, P.L., Caress, D.W., 1994. Mudwaves on the Gardar Sediment Drift, NE Atlantic system. Paleoceanography 9, 973-988.

Martel, S., 2004. Mechanics of landslide initiation as a shear fracture phenomenon. Marine Geology 203, 319-339.

Martin, M.A., Pollard, J.E., 1996. The role of trace fossil (ichnofabric) analysis in the development of depositional models for the Upper Jurassic Fulmar Formation of the Kittiwake Field (Quadrant 21 UKCS.), in: Hurst, E.A. (Ed.), Geology of the Humber Group: Central Graben and Moray Firth, UKCS. pp. 163-184.

Mastbergen, D.R., Van den Berg, J., 2003. Breaching in fine sands and the generation of sustained turbidity currents in submarine canyons. Sedimentology 50, 625-637.

May, J.A., Warme, J.E., 2007. An ancient submarine canyon, Blacks Beach, La Jolla, California, USA. In: Nilsen, T.H., Shew, R.D., Steffens, G.S., Studlick, J.R.J. (Eds.), Atlas of deep-water outcrops: AAPG Studies in Geology 56, CD-ROM, 20 p.

McClain, C.R., Schlacher, T.A., 2015. On some hypotheses of diversity of animal life at great depths on the sea floor. Marine Ecology 36, 849-872.

McIlroy, D., 2004. Some ichnological concepts, methodologies, applications and frontiers. In: McIlroy, D. (Ed.), The Application of Ichnology to Palaeoenvironmental and Stratigraphic Analysis, vol. 228. Special Publication of the Geological Society, London, 3-29.

McIlroy, D., 2007. Lateral variability in shallow marine ichnofabrics: implications for the ichnofabric analysis method. Journal of the Geological Society of London 164, 359-369.

McIlroy, D., 2008. Ichnological analysis: The common ground between ichnofacies workers and ichnofabric analysts. Palaeogeography, Palaeoclimatology, Palaeoecology 270, 332-338.

Meiburg, E., Kneller, B., 2010. Turbidity Currents and Their Deposits. Annual Review of Fluid Mechanics 42, 135-156.

Menard, H. W., 1964. Marine Geology of the Pacific, McGraw-Hill, New York, Chap. 9, 191-222.

Middleton, G.V., Hampton, M.A., 1973. Sediment gravity flows: mechanics of flow and deposition. In: Middleton, G.V., Bouma, A.H. (Co-Chairmen), Turbidites and Deep Water Sedimentation. Soc. Econ. Paleontol. Mineral., Pac. Sect., Short Course, pp. 1-38.

Migeon, S., Savoye, B., Faugres, J., 2000. Quaternary development of migrating sediment waves in the Var deep-sea fan: distribution, growth pattern, and implication for levee evolution. Sedimentary Geology 133, 265-293.

Migeon, S., Savoye, B., Zanella, E., Mulder, T., Fauge, J., Weber, O., 2001. Detailed seismic reflection and sedimentary study of turbidite sediment waves on the Var

Sedimentary Ridge (SE France): significance for sediment transport and deposition and for the mechanisms of sediment-wave construction. Marine and Petroleum Geology 18, 179-208.

Migeon, S., Mulder, T., Savoye, B., Sage, F., 2012. Hydrodynamic processes, velocity structure and stratification in natural turbidity currents: Results inferred from field data in the Var Turbidite System. Sedimentary Geology 245-246, 48-62.

Monaco, P., 2008. Taphonomic Features of Paleodictyon and Other Graphoglyptid Trace Fossils in Oligo-Miocene Thin-Bedded Turbidites, Northern Apennines, Italy. Palaios 23, 667-682.

Monaco, P., Milighetti, M., Checconi, A., 2010. Ichnocoenoses in the Oligocene to Miocene foredeep basins (Northern Apennines, central Italy) and their relation to turbidite deposition. Acta Geologica Polonica 60, 53-70.

Moore, J.G., Normark, W.R., Holcomb, R.T., 1994. Giant Hawaiian Landslides. Annual Review of Earth and Planetary Sciences 22, 119-144.

Morris, W.R., Busby-Spera, C.J., 1990. A submarine-fan valley-levee complex in the Upper Cretaceous Rosario Formation: implication for turbidite facies model. Geological Society of America Bulletin 102, 900914.

Mulder, T., Syvitski, J.P.M., 1995. Turbidity currents generated at river mouths during exceptional discharges to the world oceans. The Journal of Geology 103, 285-299.

Mulder, T., Savoye, B., Syvitski, J.P.M., 1997. Numerical modelling of a mid-sized gravity flow: the 1979 Nice turbidity current (dynamics, processes, sediment budget and seafloor impact). Sedimentology 44, 305-326.

Mulder, T., Alexander, J., 2001. The physical character of subaqueous sedimentary density flows and their deposits. Sedimentology 48, 269-299.

Mulder, T., Syvitski, J.P.M., 2003. Marine hyperpycnal flows: initiation, behavior and related deposits. A review. Marine and Petroleum Geology 20, 861-882.

Mullenbach, B.L., Nittrouer, C.A., Puig, P., Orange, D.L., 2004. Sediment deposition in a modern submarine canyon: Eel Canyon, northern California. Marine Geology 211, 101-119.

Nakajima, T., Satoh, M., 2001. The formation of large mudwaves by turbidity currents on the levees of the Toyama deep-sea channel, Japan Sea. Sedimentology 48, 435-463.

Normandeau, A., Lajeunesse, P., Stonge, G., 2015. Geomorphology Submarine canyons and channels in the Lower St . Lawrence Estuary (Eastern Canada): Morphology, classification and recent sediment dynamics. Geomorphology 241, 1-18.

Normark, W.R., Hess, G.R., Stow, D.A. V, Bowen, A.J., 1980. Sediment waves on the Monterey fan levee: A preliminary physical interpretation. Marine Geology 37, 1-18.

Normark, W.R., Piper, D.J.W., 1991. Initiation processes and flow evolution of turbidity currents: Implications for the depositional record, in Osborne, R.H., ed., From shoreline to abyss; contributions in marine geology in honor of Francis Parker Shepard: SEPM (Society for Sedimentary Geology) Special Publication 46, 207-230.

Normark, W.R., Damuth, J.E., 1997. Sedimentary facies and associated depositional elements of the Amazon Fan. In: Flood, R.D., Piper, D.J.W., Klaus, A., and Peterson, L.C. (Eds.), Proceedings of the Ocean Drilling Program. Scientific Results, 155: College Station, TX (Ocean Drilling Program), 611-651.

Normark, W.R., Piper, D.J.W., Posamentier, H., Pirmez, C., Migeon, S., 2002. Variability in form and growth of sediment waves on turbidite channel levees. Marine Geology 192, 23-58.

Normark, W.R., Piper, D., Covault, J.A., Romans, B.W., Dartnell, P., Covault, J.A., Dartnell, P., Sliter, R.W., 2009. Submarine canyon and fan systems of the California Continental Borderland. Geological Society of America Bulletin 454, 141-168.

Okey, Thomas, A., 1997. Sediment flushing observations, earthquake slumping, and benthic community changes in Monterey Canyon head. Continental Shelf Research 17, 877-897.

Page, B.M., Englebretson. D.C., 1984. Correlation between the geologic record and computed plate motions for central California. Tectonics 3, 133-155.

Palanques, A., Garc, E., Marcos, M., Pascual, A., Puig, P., Gili, J., Emelianov, M., Monserrat, S., Guilln, J., Tintore, J., Segura, M., Jordi, A., Ruiz, S., Basterretxea, G., Font, J., Blasco, D., Pages, F., 2005. Progress in Oceanography General patterns of circulation, sediment fluxes and ecology of the Palamos (La Fonera) submarine canyon, northwestern the Palamo Mediterranean. Progress in Oceanography 66, 89-119.

Palanques, A., Durrieu de Madron, X., Puig, P., Fabres, J., Guilln, J., Calafat, A., Canals, M., Heussner, S., Bonnin, J., 2006. Suspended sediment fluxes and transport processes in the Gulf of Lions submarine canyons. The role of storms and dense water cascading. Marine Geology 234, 43-61.

Palanques, A., Puig, P., Latasa, M., Scharek, R., 2009. Deep sediment transport induced by storms and dense shelf-water cascading in the northwestern Mediterranean basin.

Deep-sea Research Part I: Oceanographic Research Papers 56, 425-434.

Parker, G., 1982. Conditions for the ignition of catastrophically erosive turbidity currents. Marine Geology 46, 307-327.

Parker, G., 1996. Some speculations on the relation between channel morphology and channel-scale flow structures. Coherent Flow Structures in Open Channels, 423-458.

Parker, G., Izumi, N., 2000. Purely erosional cyclic and solitary steps created by flow over a cohesive bed. Journal of Fluid Mechanics 419, 203-238.

Paterson, G.L.J., Glover, A.G., Cunha, M.R., Neal, L., de Stigter, H.C., Kiriakoulakis, K., Billett, D.S.M., Wolff, G.A., Tiago, A., Ravara, A., Lamont, P., Tyler, P., 2011. Disturbance, productivity and diversity in deep-sea canyons: A worm's eye view. Deep-sea Research Part II: Topical Studies in Oceanography 58, 2448-2460.

Paull, C.K., Ussler III, W., Greene, H.G., Keaten, R., Mitts, P., Barry, J., 2003. Caught in the act: the 20 December 2001 gravity flow event in Monterey Canyon. Geo-Marine Letters 22, 227-232.

Paull, C.K., Mitts, P., Ussler III, W., Keaten, R., Greene, H.G., 2005. Trail of sand in upper Monterey Canyon: Offshore California. Geological Society of America Bulletin 117, 1134.

Paull, C.K., Ussler III, W., Mitts, P.J., Caress, D.W., West, G.J., 2006. Discordant 14C-stratigraphies in upper Monterey Canyon: A signal of anthropogenic disturbance. Marine Geology 233, 21-36.

Paull, C.K., Caress, D.W., Ussler III, W., Lundsten, E., Thomas, H., 2008. Axial channel morphology fill and movement within submarine canyons off California: American Geophysical Union Fall Meeting Proceedings, OS54A-01.

Paull, C.K., Ussler III, W., Caress, D.W., Lundsten, E.M., Covault, J.A., Maier, K.L., Xu, J.P., Augenstein, S., 2010a. Origins of large crescent-shaped bedforms within the axial channel of Monterey Canyon, offshore California. Geosphere 6, 755-774.

Paull, C.K., Schlining, B., Ussler III, W., Lundsten, E., Barry, J.P., Caress, D.W., Johnson, J.E., McGann, M., 2010b. Submarine mass transport within Monterey Canyon: benthic disturbance controls on the distribution of chemosynthetic biological communities. In: Mosher, D.C., Shipp, R.C., Moscardelli, L., Chaytor, J.D., Baxter, C.D.P., Lee, H.J., Urgeles, R. (Eds.), Submarine Mass Movements and Their Consequences, Advances in Natural and Technological Hazard Research, Springer, London. 4th International Symposium on Submarine Mass Movements and Their Consequences, 28. Springer, London, 229-247.

Paull, C.K., Caress, D.W., Ussler III, W., Lundsten, E.M., Meiner-Johnson, M., 2011. High-resolution bathymetry of the axial channels within Monterey and Soquel submarine canyons, offshore central California. Geosphere 7, 1077-1101.

Paull, C.K., Caress, D.W., Lundsten, E.M., Gwiazda, R., Anderson, K., McGann, M., Conrad, J., Edwards, B., Sumner, E.J., 2013. Anatomy of the La Jolla Submarine Canyon system; offshore southern California. Marine Geology 335, 16-34.

Paull, C.K., McGann, M., Sumner, E.J., Barnes, P.M., Lundsten, E.M., Anderson, K., Gwiazda, R., Edwards, B., Caress, D.W., 2014. Sub-decadal turbidite frequency during the early Holocene: Eel Fan, offshore northern California. Geology 42, 855-858.

Pemberton, S.G., Spila, M., Pulham, A.J., Saunders,T., Maceachern, J.A., Robbins, D., Sinclair, I.K., 2001. Ichnology and Sedimentology of Shallow to Marginal Marine Systems: Geological Association of Canada Short Course Notes, 15, 343.

Pervesler, P., Uchman, A., Hohenegger, J., 2008. New methods for ichnofabric analysis and correlation with orbital cycles exemplified by the Baden-Sooss section (Middle Miocene, Vienna Basin). Geologica Carpathica 59, 395-409.

Petruncio, E.T., Rosenfeld, L.K., Paduan, J.D., 1998. Observations of the internal tide in Monterey Canyon. Journal of Physical Oceanography 28, 1873-1903.

Phillips, C., McIlroy, D., Elliott, T., 2011. Ichnological characterization of Eocene/Oligocene turbidites from the Gres d'Annot Basin, French Alps, SE France. Palaeogeography, Palaeoclimatology, Palaeoecology. 300, 67-83.

Pickering, K.T., Hodgson, D.M., Platzman, E., Clark, J.D., Stephens, C., 2001. A new type of bedform produced by backfilling processes in a submarine channel, Late Miocene, Tabernas-Sorbas Basin SE Spain. Journal of Sedimentary Research 71, 692-704.

Pickering, K.T., Hiscott, R.N., 2015. Deep Marine Systems: Processes, Deposits, Environments, Tectonics, and Sedimentation: American Geophysical Union, Wiley, 672.

Piper, D.J.W., Shor, A.N., Farre, J.A., Connell, S.O., Jacobi, R.D., 1985. Sediment slides and turbidity currents on the Laurentian Fan: Sidescan sonar investigations near the epicenter of tlhe 1929 Grand Banks earthquake. Geology 13, 538-541.

Piper, D.J.W., Savoye, B., 1993. Processes of late Quaternary turbidity current flow and deposition on the Var deep-sea fan, north-west Mediterranean Sea. Sedimentology 40, 557-582.

Piper, D.J.W., Cochonat, P., Morrison, M.L., Marines, Â., 1999. The sequence of events around the epicentre of the 1929 Grand Banks earthquake: initiation of debris flows

and turbidity current inferred from sidescan sonar. Sedimentology 46, 79-97.

Piper, D.J.W., Normark, W.R., 2009. Processes that initiate turbidity currents and their influence on turbidites: A marine geology perspective. Journal of Sedimentary Research 79, 347-362.

Pirmez, C., Imran, J., 2003. Reconstruction of turbidity currents in Amazon Channel. Marine and Petroleum Geology 20, 823-849.

Postma, G., Nemec, W., Kleinspehn, K.L., 1988. Large floating clasts in turbidites: a mechanism for their emplacement. Sedimentary Geology 58, 47-61.

Postma, G., Cartigny, M.J.B., Kleverlaan, K., 2009. Structureless, coarse-tail graded Bouma Ta formed by internal hydraulic jump of the turbidity current? Sedimentary Geology 219, 1-6.

Postma, G., Cartigny, M.J.B., 2014. Super- and subcritical turbidity currents and their deposits - a synthesis. Geology 42, 987-990.

Posamentier, H.W., Erksine, R.D., Mitchum, R.M., Jr., 1991, Submarine fan deposition within a sequence stratigraphic framework. In: Welmer, B., Link, M.H. (Eds.), Seismic facies and sedimentary processes of submarine fans and turbidite systems, New York, SpringerVerlag, 127136.

Puig, P., 2004. Storm-induced sediment gravity flows at the head of the Eel submarine canyon, northern California margin. Journal of Geophysical Research 109, C03019.

Puig, P., Palanques, A., 1998. Temporal variability and composition of settling particle fluxes on the Barcelona continental margin (Northwestern Mediterranean). Journal of Marine Research 56, 639-654.

Puig, P., Ogston, A.S., Mullenbach, B.L., Nittrouer, C.A., Sternberg, R.W., 2003. Shelf-to-canyon sediment-transport processes on the Eel continental margin (northern California). Marine Geology 193, 129-149.

Puig, P., Palanques, A., Guilln, J., El Khatab, M., 2004. Role of internal waves in the generation of nepheloid layers on the northwestern Alboran slope: Implications for continental margin shaping. Journal of Geophysical Research 109, 1-11.

Puig, P., Palanques, A., Orange, D.L., Lastras, G., Canals, M., 2008. Dense shelf water cascades and sedimentary furrow formation in the Cap de Creus Canyon, northwestern Mediterranean Sea. Continental Shelf Research 28, 2017-2030.

Puig, P., Canals, M., Company, J.B., Martin, J., Amblas, D., Lastras, G., Palanques, A., Calafat, A., 2012. Ploughing the deep sea floor. Nature 489, 286-289.

Puig, P., Palanques, A., Martn, J., 2014. Contemporary sediment-transport processes in submarine canyons. Annual Review of Marine Science. 6, 53-77.

Robison, B.H., Sherlock, R.E., Reisenbichler, K.R., 2010. The bathypelagic community of Monterey Canyon. Deep-sea Research Part II: Topical Studies in Oceanography. 57, 1551-1556.

Romano, C., Coenjaerts, J., Flexas, M.M., Ziga, D., Vanreusel, A., Company, J.B., Martin, D., 2013. Spatial and temporal variability of meiobenthic density in the Blanes submarine canyon (NW Mediterranean). Progress in Oceanography 118, 144-158.

Ryan, J.P., Chavez, F.P., Bellingham, J.G., 2005. Physical-biological coupling in Monterey Bay, California: Topographic influences on phytoplankton ecology. Marine Ecology Progress Series 287, 23-32.

Sanchez-Cabeza, J.A., Masqué, P., Ani-Ragolta, I., Merino, J., Frignani, M., Alvisi, F., Palanques, A., Puig, P., 1999. Sediment accumulation rates in the southern Barcelona continental margin (NW Mediterranean Sea) derived from ^{210}Pb and ^{137}Cs chronology. Progress in Oceanography 44, 313-332.

Satur, N., Kelling, G., Cronin, B.T., Hurst, A., Gurbuz, K., 2005. Sedimentary architecture of a canyon-style fairway feeding a deep-water clastic system, the Miocene Cingöz Formation, southern Turkey: significance for reservoir characterisation and modeling. Sedimentary Geology 173, 91119.

Savrda, C.E., Bottjer, D.J., 1986. Trace-fossil model for reconstruction of paleo-oxygenetation in bottom waters. Geology 14, 3-6.

Schlining, K., von Thun, S., Kuhnz, L., Schlining, B., Lundsten, L., Jacobsen Stout, N., Chaney, L., Connor, J., 2013. Debris in the deep: Using a 22-year video annotation database to survey marine litter in Monterey Canyon, central California, USA. Deep-sea Research Part I: Oceanographic Research Papers 79, 96-105.

Seibel, B.A., 2011. Critical oxygen levels and metabolic suppression in oceanic oxygen minimum zones. Journal of Experimental Biology 214, 326-336.

Seilacher, A., 1964. Biogenic sedimentary structures. In: Imbrie, J., Newell, N. (Eds.), Approaches to Paleoecology. Wiley, New York, 96-316.

Seilacher, A., 1967. Bathymetry of trace fossils. Marine Geology 5, 413-428.

Shanmugam, G., 2000. 50 Years of the Turbidite Paradigm (1950s-1990s): Deep Water Processes and Facies Models - a Critical Perspective. Marine and Petroleum Geology 17, 285-342.

Shepard, F.P., Dill, R.F., 1966, Submarine canyons and other sea valleys: Chicago, Rand McNally, 381.

Shepard, F., Buffington, E., 1967. La Jolla submarine fan-valley. Marine Geology 6, 107-143.

Shepard, F.P., 1975. Progress of internal waves along submarine canyons. Marine Geology 19, 131-138.

Shepard, F.P., 1981. Submarine Canyons: Multiple Causes and Long-Time Persistence. American Association of Petroleum Geologists Bulletin 5, 1062-1077.

Shepard, F.P., Dill, R.F., Von Rad, U., 1969. Physiography and sedimentary processes of La Jolla submarine fan and fan-valley, California. American Association of Petroleum Geologists Bulletin 53, 390-420.

Shepard, F.P., Marshall, N.F., McLoughlin, P.A., Sullivan, G.G., 1979. Currents in submarine canyons and other sea valleys: American Association of Petroleum Geologists Study in Geology 8, 173.

Shor, A.N., Piper, D.J.W., Clarke, J.E.H., Mayer, L.A., 1990. Giant flute-like scour and other erosional features formed by the 1929 Grand Banks turbidity current. Sedimentology 37, 631-645.

Shultz, M.R., Hubbard, S.M., 2005. Sedimentology, stratigraphic architecture, and ichnology of gravity-flow deposits partially ponded in a growth-fault-controlled slope minibasin, Tres Pasos Formation (Cretaceous), southern Chile. Journal of Sedimentary Research 75, 440-453.

Silver, E., Day, S.J., Ward, S., Hoffmann, G., Llanes, P., Driscoll, N., Appelgate, B., Saunders, S., 2009. Volcano collapse and tsunami generation in the Bismarck Volcanic Arc, Papua New Guinea. Journal of Volcanology and Geothermal Research 186, 210-222.

Sisavath, E., Babonneau, N., Saint-Ange, F., Bachlery, P., Jorry, S.J., Deplus, C., De Voogd, B., Savoye, B., 2011. Morphology and sedimentary architecture of a modern volcaniclastic turbidite system: The Cilaos fan, offshore La Réunion Island. Marine Geology 288, 1-17.

Smith, D.P., Ruiz, G., Kvitek, R., Iampietro, P.J., 2005. Semiannual patterns of erosion and deposition in upper Monterey Canyon from serial multibeam bathymetry. Geological Society of America Bulletin 117, 1123-1133.

Smith, D.P., Kvitek, R., Iampietro, P.J., Wong, K., 2007. Twenty-nine months of geomorphic change in upper Monterey Canyon (2002-2005). Marine Geology 236, 79-94.

Spinewine, B., Sequeiros, O.E., Garcia, M.H., Beaubouef, R.T., Sun, T., Savoye, B., Parker, G., 2009. Experiments on Wedge-Shaped Deep Sea Sedimentary Deposits in Minibasins and/or on Channel Levees Emplaced by Turbidity Currents. Part II. Morphodynamic Evolution of the Wedge and of the Associated Bedforms. Journal of Sedimentary Research 79, 608-628.

Stow, D.A.V., Shanmugam, G., 1980. Sequence of Structures in Fine-Grained Turbidite - Comparison of Recent Deep-sea and Ancient Flysch Sediments, Sedimentary Geology, 25, 23-42.

Stow, D.A.V., Reading, H.G., Collinson, J.D., 1996. Deep Seas, in H.G. Reading (ed), Sedimentary Environments: Processes, Facies and Stratigraphy, 3rd edn., Blackwell Science Ltd., Oxford.

Sumner, E.J., Amy, L.A., Talling, P.J., 2008. Deposit Structure and Processes of Sand Deposition from Decelerating Sediment Suspensions. Journal of Sedimentary Research 78, 529-547.

Sumner, E.J., Peakall, J., Parsons, D.R., Wynn, R.B., Darby, S.E., Dorrell, R.M., McPhail, S.D., Perrett, J., Webb, A., White, D., 2013. First direct measurements of hydraulic jumps in an active submarine density current. Geophysical Research Letters 40, 5904-5908.

Sumner, E.J., Paull, C.K., 2014. Swept away by a turbidity current in Mendocino submarine canyon, California. Geophysical Research Letters 41, 7611-7618.

Swarzenski, P., Baskaran, M., Rosenbauer, R., Orem, W., 2006. Historical trace element distribution in sediments from the Mississippi River delta. Estuaries and Coasts 29, 1094-1107.

Swarzenski, P. W. 2014, ^{210}Pb dating, in Rink, W.J., and Thompson, J., eds., Encyclopedia of Scientific Dating Methods,. Springer-Verlag, Berlin, 626-632.

Symons, W.O., Sumner, E.J., Talling, P.J., Cartigny, M.J.B., Clare, M.A., 2016. Large-scale sediment waves and scours on the modern seafloor and their implications for the prevalence of supercritical flows. Marine Geology 371, 130-148.

Symons, W.O., Sumner, E.J., Paull, C.K., Cartigny, M.J.B., Xu, J.P., Maier, K.L., Lorenson, T.D., Talling, P.J., 2017. A new model for turbidity current behavior based on integration of flow monitoring and precision coring in a submarine canyon. Geology 45, 367-370.

Taki, K., Parker, G., 2005. Transportational cyclic steps created by flow over an erodible bed. Part 1. Experiments. Journal of Hydraulic Research, 43, 488-501.

Talling, P.J., 2014. On the triggers, resulting flow types and frequencies of subaqueous sediment density flows in different settings. Marine Geology 352, 155-182.

Talling, P.J., Amy, L.A., Wynn, R.B., Peakall, J., Robinson, M., 2004. Beds comprising debrite sandwiched within co-genetic turbidite: origin and widespread occurrence in distal depositional environments. Sedimentology 51, 163-194.

Talling, P.J., Wynn, R.B., Masson, D.G., Frenz, M., Cronin, B.T., Schiebel, R., Akhmetzhanov, A., Dallmeier-Tiessen, S., Benetti, S., Weaver, P.P.E., Georgiopoulou, A., Zhlsdorff, C., Amy, L.A., 2007. Onset of submarine debris flow deposition far from original giant landslide. Nature 450, 541-544.

Talling, P.J., Masson, D.G., Sumner, E.J., Malgesini, G., 2012. Subaqueous sediment density flows: Depositional processes and deposit types. Sedimentology 59, 1937-2003.

Talling, P.J., Paull, C.K., Piper, D.J.W., 2013. How are subaqueous sediment density flows triggered, what is their internal structure and how does it evolve? Direct observations from monitoring of active flows. Earth-Science Reviews 125, 244-287.

Talling, P.J., Clare, M.A., Urlaub, M., Pope, E., Hunt, J.E., Watt, S.F.L., 2014. Large Submarine Landslides on Continental Slopes Geohazards, Methane Release, and Climate Change. Oceanography 27, 32-45.

Talling, P.J., Allin, J., Armitage, D.A., Arnott, R.W., Cartigny, M.J., Clare, M.A., Felletti, F., Covault, J.A., Girardclos, S., Hansen, E., Hill, P.R., Hiscott, R.N., Hogg, A.J., Hughes Clarke, J., Jobe, Z.R., Malgesini, G., Mozzato, A., Naruse, H., Parkinson, S., Peel, F.J., Piper, D.J.W., Pop, E., Postma, G., Rowley, P., Sguazzini, A., Stevenson, C.J., Sumner, E.J., Sylvester, Z., Watts, C., and Xu, J., 2015. Key Future Directions for Research on Turbidity Currents and Their Deposits. Journal of Sedimentary Research 85, 153-169.

Tani, K., Fiske, R.S., Tamura, Y., Kido, Y., Naka, J., Shukuno, H., Takeuchi, R., 2007. Sumisu volcano, Izu-Bonin arc, Japan: site of a silicic caldera-forming eruption from a small open-ocean island. Bulletin of Volcanology 70, 547-562.

Taylor, A.M., Goldring, R., 1993. Description and analysis of bioturbation and ichnofabric. Journal of the Geological Society London. 150, 141-148.

Taylor, A., Goldring, R., Gowland, S., 2003. Analysis and application of ichnofabrics. Earth-Science Reviews 60, 227-259.

Terrinha, P., Matias, L., Vicente, J., Duarte, J.C., Lus, J., Pinheiro, L.M., Loureno, N., Diez, S., Rosas, F.M., Magalhes, V., Valadares, V., Zitellini, N., Roque, C., Vctor, L.M., 2009. Morphotectonics and strain partitioning at the Iberia-Africa plate boundary from multibeam and seismic reflection data. Marine Geology 267, 156-174.

Trincardi, F., Normark, W.R., 1988. Sediment waves on the Tiber prodelta slope: Interaction of deltaic sedimentation and currents along the shelf. Geo-Marine Letters 8, 149-157.

Tubau, X., Paull, C.K., Lastras, G., Caress, D.W., Canals, M., Lundsten, E.M., Anderson, K., Gwiazda, R., Amblas, D., 2015. Submarine canyons of Santa Monica Bay, Southern California: Variability in morphology and sedimentary processes. Marine Geology 365, 61-79.

Twichell, D.C., Roberts, D.G., 1982. Morphology, distribution, and development of submarine canyons on the United States Atlantic continental slope between Hudson arid Baltimore Canyons Morphology, distribution, and development of submarine canyons on the United States Atlantic continent. Geology 10, 408-412.

Uchman, A., 2001. Eocene flysch trace fossils from the Hecho Group of the Pyrenees, northern Spain. Beringeria 15, 3-41.

Uchman, A., Janbu, N.E., Nemec, W., 2004. Trace fossils in the Cretaceous-Eocene flysch of the Sinop-Boyabat Basin, Central Pontides, Turkey. Annales Societatis Geologorum Poloniae 74, 197-235.

Uchman, A., Wetzel, A., 2011. Deep-sea ichnology: The relationships between depositional environment and endobenthic organisms. In Huneke, H. and Mulder, T. (eds.). Deep-Sea Sediments. Developments in Sedimentology, 63. Elsevier, Amsterdam, 517-556.

Van den Berg, J., Van Gelder, A., Mastbergen, D.R., 2002. The importance of breaching as a mechanism of subaqueous slope failure in finne sand. Sedimentology 49, 81-95.

Van Weering, T.C.E., De Stigter, H.C., Boer, W., De Haas, H., 2002. Recent sediment transport and accumulation on the NW Iberian margin. Progress in Oceanography 52, 349-371.

Vetter, E., Dayton, P., 1998. Macrofaunal communities within and adjacent to a detritus-rich submarine canyon system. Deep-sea Research Part II 45, 25-54.

Walker, R.G., 1975. Upper Cretaceous resedimented conglomerates at Wheeler Gorge, California: description and field guide. Journal of Sedimentary Petrology 45, 105112.

Wetzel, A., 1991. Ecologic interpretation of deep sea trace fossil communities. Paleogeography, Paleoclimatology, Paleoecology 85, 47-69.

Wetzel, A., 2002. Modern Nereites in the South China Sea ecological association with redox conditions in the sediment. Palaios 17, 507-515.

Wetzel, A., 2008. Recent Bioturbation In The Deep South China Sea: A Uniformitarian Ichnologic Approach. Palaios 23, 601-615.

Wetzel, A., 2010. Deep-sea ichnology: Observations in modern sediments to interpret fossil counterparts. Acta Geologica Polonica 60, 125-138.

Wetzel, A., Uchman, A., 1998. Deep-Sea Benthic Food Content Recorded by Ichnofabrics: A Conceptual Model Based on Observations from Paleogene Flysch, Carpathians. Palaios 13, 533-546.

Wetzel, A., Blechschmidt, I., Uchman, A., Matter, A., 2007. A Highly Diverse Ichnofauna in Late Triassic Deep-Sea Fan Deposits of Oman. Palaios 22, 567-576.

Wignall, P.B., 1991. Dysaerobic trace fossils and ichnofabrics in the Upper Jurassic Kimmeridge clay of southern England, UK. Palaios 6, 364-270.

Wright, I.C., Worthington, T.J., Gamble, J.A., 2006. New multibeam mapping and geochemistry of the 30°-35° S sector, and overview, of southern Kermadec arc volcanism. Journal of Volcanology and Geothermal Research 149, 263-296.

Würtz, M., 2012. Mediterranean Submarine Canyons: Ecology and Governance. Gland; Málaga: IUCN.

Wynn, R.B., Huvenne, V.A.I., Le Bas, T.P., Murton, B.J., Connelly, D.P., Bett, B.J., Ruhl, H.A., Morris, K.J., Peakall, J., Parsons, D.R., Sumner, E.J., Darby, S.E., Dorrell, R.M., Hunt, J.E., 2014. Autonomous Underwater Vehicles (AUVs): Their past, present and future contributions to the advancement of marine geoscience. Marine Geology 352, 451-468.

Wynn, R.B., Masson, D.G., Stow, D.A.V, Weaver, P.P.E., 2000a. Turbidity current sediment waves on the submarine slopes of the western Canary Islands. Marine Geology 163, 185-198.

Wynn, R.B., Weaver, P.P.E., Ercilla, G., Stow, D.A.V, Masson, D.G., 2000b. Sedimentary processes in the Selvage sediment-wave field, NE Atlantic: new insights into the formation of sediment waves by turbidity currents. Sedimentology 47, 1181-1197.

Wynn, R.B., Stow, D.A.V, 2002. Classification and characterisation of deep-water sediment waves. Marine Geology 192, 7-22.

Wynn, R.B., Piper, D.J.W., Gee, M.J., 2002. Generation and migration of coarse-grained sediment waves in turbidity current channels and channel-lobe transition zones. Marine Geology 192, 59-78.

Xu, J.P., 2010. Normalized velocity profiles of field-measured turbidity currents. Geology 38, 563-566.

Xu, J.P., 2011. Measuring currents in submarine canyons: Technological and scientific progress in the past 30 years. Geosphere 7, 868876.

Xu, J.P., Noble, M.A., Eittreim, S.L., Rosenfeld, L.K., Schwing, F.B., Pilskaln, C.H., 2002. Distribution and transport of suspended particulate matter in Monterey Canyon, California. Marine Geology 181, 215-234.

Xu, J.P., Noble, M.A., Rosenfeld, L.K., 2004. In-situ measurements of velocity structure within turbidity currents. Geophysical Research Letters 31, 1-4.

Xu, J.P., Wong, F.L., Kvitek, R., Smith, D.P., Paull, C.K., 2008. Sandwave migration in Monterey Submarine Canyon, Central California. Marine Geology 248, 193-212.

Xu, J.P., Swarzenski, P.W., Noble, M.A., Li, A.C., 2010. Event-driven sediment flux in Hueneme and Mugu submarine canyons, southern California. Marine Geology 269, 74-88.

Xu, J.P., Sequeiros, O.E., Noble, M.A., 2014. Sediment concentrations, flow conditions, and downstream evolution of two turbidity currents, Monterey Canyon, USA. Deep Sea Research Part I: Oceanographic Research Papers 89, 11-34.

Zecchin,M., Caffau, M., Roda, C., 2011. Relationships between high-magnitude relative sealevel changes and filling of a coarse-grained submarine canyon (Pleistocene, Ionian Calabria, Southern Italy). Sedimentology 58, 10301064.

Zhang, H.P., King, B., Swinney, H.L., 2008. Resonant generation of internal waves on a model continental slope. Physical Review Letters 100, 1-4.

Zhong, G., Cartigny, M.J.B., Kuang, Z., Wang, L., 2015. Cyclic steps along the South Taiwan Shoal and West Penghu submarine canyons on the northeastern continental slope of the South China Sea. Geological Society of America Bulletin 127, 804-824.